

ARSENIC REMOVAL IN GROUNDWATER USING ENGINEERED MAGHEMITE ($\gamma\text{-Fe}_2\text{O}_3$) NANOPARTICLES

Ph.D. THESIS

by

AJAY KUMAR



DEPARTMENT OF HYDROLOGY
INDIAN INSTITUTE OF TECHNOLOGY ROORKEE
ROORKEE-247667 (INDIA)
MARCH, 2019



ARSENIC REMOVAL IN GROUNDWATER USING ENGINEERED MAGHEMITE (γ -Fe₂O₃) NANOPARTICLES

A THESIS

*Submitted in partial fulfilment of the
requirements for the award of the degree*

of

DOCTOR OF PHILOSOPHY

in

HYDROLOGY

by

AJAY KUMAR



**DEPARTMENT OF HYDROLOGY
INDIAN INSTITUTE OF TECHNOLOGY ROORKEE
ROORKEE – 247 667 (INDIA)
MARCH, 2019**



**©INDIAN INSTITUTE OF TECHNOLOGY ROORKEE, ROORKEE-2019
ALL RIGHTS RESERVED**



INDIAN INSTITUTE OF TECHNOLOGY ROORKEE ROORKEE

CANDIDATE'S DECLARATION

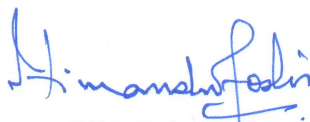
I hereby certify that the work which is being presented in the thesis entitled **“ARSENIC REMOVAL IN GROUNDWATER USING ENGINEERED MAGHEMITE (γ -Fe₂O₃) NANOPARTICLES”** in partial fulfilment of the requirements for the award of the degree of **DOCTOR OF PHILOSOPHY** and submitted in the Department of Hydrology of the Indian Institute of Technology Roorkee, Roorkee is an authentic record of my own work carried out during a period from January, 2013 to March, 2019 under the supervision of Dr. Himanshu Joshi, Professor, Department of Hydrology and Dr. Anil Kumar, Professor, Department of Chemistry, Indian Institute of Technology Roorkee, Roorkee.

The matter presented in this thesis has not been submitted by me for the award of any other degree of this or any other institution.

(AJAY KUMAR)

This is to certify that the above statement made by the candidate is correct to the best of our knowledge.

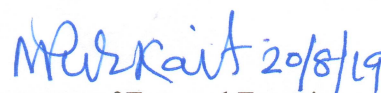
Dated:


(Himanshu Joshi)
Supervisor

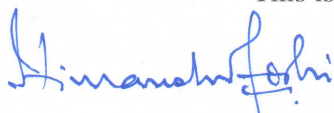
(Anil Kumar)
Supervisor

The Ph.D. Viva-Voce examination of **Mr. Ajay Kumar**, Research Scholar, has been held on 20/08/2019

Chairman, SRC


Signature of External Examiner

This is to certify that the student has made all the corrections in the thesis.



Signature of Supervisor

Head of the Department

Abstract

Arsenic has a global concern as a groundwater contaminant due to its potential for fatal health consequences. The long term consumption of arsenic contaminated water and food results in damage to the liver, kidney and gall bladder. Both developed and developing countries are under a potential threat of groundwater arsenic contamination. To combat the problems related to its contamination, WHO and USEPA have set the standard limit of $10 \mu\text{g L}^{-1}$ for drinking water since the year of 2006. Its removal employing nanoadsorbents has gained considerable attention through both *ex-situ* and *in-situ* techniques among the scientific groups since last two and half decades. Moreover, nanotechnology based water treatment systems in general are also finding favour due to better resource and energy efficiency.

Several metallic nanoadsorbents including oxides of iron, aluminium, cerium, copper, zirconium, titanium alongwith their functionalized nanostructures have been reportedly developed for arsenic removal. In recent years, metallic iron/iron oxides based nanoadsorbents have been widely explored due to their significant affinity towards arsenic and easy availability. Among various polymorphs, nZVI (nano-scale zero-valent iron) has been extensively studied in literature both at the laboratory and pilot scale studies. These nanoparticles, however, are unstable in natural environmental conditions and prone to get oxidized into iron oxides/hydroxides, a fact which limits their application for pilot scale studies effectively.

The aim of present study is to develop the maghemite ($\gamma\text{-Fe}_2\text{O}_3$) nanoparticles and their nanohybrids while also exploring the use of industry waste as one of a precursor material. The $\gamma\text{-Fe}_2\text{O}_3$ is FDA approved iron oxide phase and considered to have high magnetization, bio-compatible and non-toxic nature. At nanoscale, this phase is considered as the most stable polymorph of iron^{III} oxides. Further, the as-synthesized nanoparticles have been explored for arsenic removal as adsorbents, anticipating their application as *ex-situ* and/or *in-situ* remediation materials. To achieve the goal in the present study, several tasks have been performed. The entire study has been divided into 7 chapters.

Chapter 1 presents the introduction of the research work. The research goal, objectives and hypothesis have been stated alongwith the justification for conducting the research. Strategic approach highlights the tasks identified in different domains extending from synthesis, characterisation to batch and continuous remediation experiments.

Chapter 2 highlights the worldwide scenario of arsenic contamination and the mechanisms of its release in groundwater. An overview of the employed treatment technologies adopted at small and large scales have been presented. The issues and scope for increasing the efficacy of already existing arsenic removal units based on adsorption technology have been examined. Further gaps pertaining to the development of nanoadsorbents and their application in batch/continuous scale studies alongwith the fabrication of columns are discussed. Possible scope of *in-situ* arsenic sequestration and need of upgradation of the technologies in this regard have also been included in this section.

Chapter 3 presents the development of methodology for synthesis of bare maghemite (BIO) nanoparticles and functionalized (BIO-DW) nanostructures using chemical approach. Their physio-chemical characterization has been examined for electronic spectroscopy (UV-Visible, XRD, Raman, FTIR and XPS), magnetic characteristics (VSM and SQUID), surface (FE-SEM, HR-TEM, zeta-potential) and physical (DTA-TGA, BET surface area) properties. A fundamental approach in this task has been to develop a method to maintain the yield of nanostructured adsorbents by conserving the maghemite phase of iron^{III} oxides during the formation of nanohybrids. The phase identification has been confirmed using the analysis such as X-ray diffraction (XRD), Raman and X-ray photoelectron (XPS) spectroscopy. In nanohybrids, the results indicate a decrease of 13.2 % in the average particle size (nm) and an increase of 39.6 % in the surface area have been observed which are beneficial characteristics in providing more reactive sites to arsenic species for electrostatic interactions. An increase in the colloidal stability in BIO-DW nanoparticles as compared to BIO nanoparticles have been observed through zeta potential measurements, which are determined to be -21.0 and -27.3 mV at pH 7, respectively. Demonstration of super-paramagnetic behaviour is quite apparent with the magnetic moment (emu g⁻¹) value of 72.7 and 67.5 observed for bare and functionalized nanoparticles, respectively.

Chapter 4 presents the batch experiments to analyse the sorption kinetics and removal characteristics of targeted arsenic specie (+5) as well as in multi-constituent matrix (associated with other constituents simulating real life scenario) for both as-synthesized nanoadsorbents. The adsorbate-adsorbent reactions are illustrated through various models viz. empirical, chemical and surface complexation models. Optimization of the contact time for As^V removal has been worked out simultaneously maximizing adsorption capacity and minimizing amount of dose for the near neutral pH conditions. This study utilizes the CCD (central composite design) to employ RSM (response surface methodology) for optimization procedure. The modeling of the removal kinetics

for the adsorbent dose concentration ranging from 0.15 – 0.45 g L⁻¹ follows pseudo-second-order kinetics and intra-particles diffusion models. Further, the equilibrium isotherms models have been examined for concentrations of As^V (5 - 125 mg L⁻¹) and dose (0.30 and 0.40 g L⁻¹) at the physical variables representing for the treatment of groundwater. The Langmuir constant (unit less), Tempkin constant (J mol⁻¹) and mean free energy (KJ mol⁻¹) from these examinations have been found to be 0.034 - 0.393, 18.036 - 30.775 and 0.707- 1.0, respectively. These studies indicated that the removal process involves both partial physisorption as well as partial chemisorption.

Chapter 5 presents the batch experiments which were extended to examine the removal capabilities of as-synthesized nanoparticles for the real world applications by formulating synthetic water at laboratory scale representing the concentration of elements equivalent to those of samples collected and analyzed from arsenic effected Ballia district, Ultra-Pradesh, India. Taguchi's design of experimental methodology has been explored to evaluate the possible effects of process parameters such as initial arsenic concentration, total dissolved solids (TDS), shaking speed, temperature, pH, dose and contact time. Out of these, two-parametric interactions (arsenic concentration x TDS, arsenic concentration x shaking speed, TDS x shaking speed) have also been investigated to explore their effects on As^V removal. The geochemical code Visual MINTEQ has been utilized for surface complexation modeling (SCMs) to understand the adsorption mechanism. The charge distribution multi-sites complexation (CD-MUSIC) model alongwith 2pk-Three-Plane-Model (TPM) and Diffuse Layer Model (DLM) have been examined for this purpose. Further, the ANN model is trained to evaluate the Taguchi's outcomes using MATLAB neural network tool.

Chapter 6 presents the details of the experiments conducted on the fixed bed 1-dimensional column(s) and sand-tank model to explore the arsenic removal under the dynamic flow environment similar to real world scenario. Design and fabrication of columns have been carried out by considering the factors such as height of reactive zone, column with constant porosity and their correlation with the required mass of adsorbents. Analytical grade sand soil of particles size ranging from 0.05 - 0.5 µm has been used as a supporting material alongwith as-synthesized nanoparticles in all the experimental runs. The Bed-Depth-Service-Time (BDST) model has been employed to determine the breakthrough (T_b) and exhaustion time (T_e) at different bed height and flow rate values. A percent increase in breakthrough and exhaustion time (min) with the values of 22.9 % and 10.3 % have been observed for functionalized nanostructures as compared to bare maghemite nanoparticles. Further, the breakthrough curve data have also been fitted using

Thomas, Yoon-Nelson and Adam-Bohart models to understand the removal characteristics under continuous mode of experiments.

Further, to overcome the limitations of *ex-situ* treatment technologies such as high operational cost and generation of toxic sludge, a laboratory scale 3-D sand tank (60 cm x 30 cm x 50 cm) model has been developed to explore the possible factors that may affect the *in-situ* addition of developed nanoparticles and visualising injection of nanomaterials into the aquifer systems contaminated with arsenic. The efficacy assessment for *in-situ* employment of developed nanoparticles representing Direct Injection mode of application has been investigated through sand-tank experiments for As^{III} removal. The COMSOL Multiphysics software (subsurface flow module) has also been employed to simulate fluid flow below ground during the assessment of arsenic sequestration. Tracer experiments have been performed using molar solution of sodium chloride. The possibilities of recontamination have also been investigated after the arsenic sequestration under variable flow rate.

Finally, Chapter 7 summarizes the research work and presents the conclusions drawn based on the research outcomes. It also presents the possible future perspectives of studies based on investigations carried out in the thesis.

ACKNOWLEDGEMENTS

This thesis could not have been in its present form without the assistance and support of many people who deserve special mention. I would like to thank my supervisors, Prof. Himanshu Joshi and Prof. Anil Kumar for their guidance, encouragement, constructive suggestions and continuous involvement during this research work. Their constant encouragement and stimulating discussions were helpful in taking this research to its fruitful ending.

I express my sincere gratitude to present and former Head of Department, Prof. M. K. Jain and Prof. D. S Arya for providing all necessary facilities for completion of this research work and for all the considerations and timely interventions rendered by them. I am thankful to Prof. N. K. Goel, Prof. M. Perumal, Prof. Pradeep Kumar, and Prof. B. K. Yadav, the members of my research committee for their encouragement from time to time and constructive suggestions. My sincere thanks are also to Dr. Sumit Sen, and Dr. J. Khanna, Faculty members of Department of Hydrology, Indian Institute of Technology Roorkee, for their moral support.

I also express my sincere thanks to my seniors Dr. Manoj Kumar, Dr. Pinky Sharma, Dr. Ajay Ahirwar, Dr. Litan Kr. Ray, my friends Dr. Vikram Kumar, Dr. Harvijay Jahar, Dr. Pankaj Kumar, Jagdish, Sahil, Sunil, Rajesh for their interaction and association during my stay at IIT Roorkee.

I am thankful to lab technician Deepak for making arrangement of chemicals and equipment required for my research work. My special thanks goes to Shyam, Lab Assistant, for his helping hand during all my lab works. I would also like to thank all my lab-mates for their help during the experiments and encouragement during my research work.

I feel profound privilege in expressing my heartfelt reverence to my parents Mrs. Veena Sharma and Mr. Jagdish Chand Sharma for their assistance in various ways. This study would not be possible without the loving support of my wife, Manisha Kaushik. I appreciate her love and patience during all the years. To my beloved sons Kartikeya Vashisht and Vinayak Vashisht, I would like express my thanks for being spending their childhood days in my absence.

Last but not the least; my sincere thanks are due to all those who helped me directly or indirectly to complete this research work successfully.

Ajay Kumar



Table of Contents

CANDIDATE'S DECLARATION	iii
Abstract	v
Acknowledgments	ix
Table of Contents	xi
List of Figures	xix
List of Tables	xxv
Acronyms and Notations	xxvii
Chapter 1. Introduction	1
1.1 Problem statement	1
1.1.1 Outline of arsenic pollution in groundwater and its health consequences	1
1.1.2 Nanostructured adsorbents in arsenic removal	3
1.1.3 Sub-surface sequestration of arsenic	3
1.2 Research goal and objectives	4
1.3 Justification for research	4
1.3.1 Intellectual merit	4
1.3.2 Broader impacts	5
1.4 Strategic approaches	5
1.4.1 Task I: Synthesis of maghemite nanoparticles along with their engineered nanostructures utilizing industry waste	5
1.4.2 Task II: Physio-chemical characterization of as-synthesized nanoparticles	6
1.4.3 Task III: Adsorption isotherm and sorption kinetic modeling of arsenic removal through batch experiments	6
1.4.4 Task IV: Statistical approach for arsenic removal using Response Surface and Taguchi's design of experimental methodology	7
1.4.5 Task V: Understanding the removal mechanisms through surface complexation models and predictive modeling of outcomes using MATLAB	7

1.4.6	Task VI: Evaluating the efficiency of developed nanoadsorbents in arsenic through fixed bed reactors systems (1-D column experiments)	8
1.4.7	Task VII: <i>In-situ</i> efficacy assessment of developed nanomaterials through laboratory scale 3-D sand tank model representing Direct Injection mode of application	8
1.5	Thesis organization	9
Chapter 2.	Literature Review	11
2.1	Sources of arsenic in subsurface environment	11
2.2	Geochemical mechanisms of its release in groundwater	11
2.2.1	Reductive dissolution	11
2.2.2	Alkali desorption	12
2.2.3	Geothermal trigger	12
2.3	Arsenic speciation and its aqueous chemistry	12
2.4	Global scenario of arsenic contamination in groundwater	13
2.5	Employed technologies for its removal in groundwater	15
2.5.1	Coagulation/flocculation	15
2.5.2	Ion-exchange resins	16
2.5.3	Membrane processes	16
2.5.4	Oxidation and adsorption	17
2.5.5	Relevance of adsorption technology	17
2.6	<i>Ex-situ</i> mode of remediation technique	18
2.6.1	Adoption of technology at rural scale	18
2.6.1.1	Domestic or household treatment systems	19
2.6.1.2	Community based removal systems	20
2.7	<i>In-situ</i> mode of remediation technique	20
2.7.1	Technology advantages	20
2.7.2	Methods of treatment	21
2.7.2.1	Permeable reactive barriers (PRBs)	21
2.7.2.2	<i>In-situ</i> chemical treatment	21
2.7.3	Concerns associated to technology	22
2.7.4	Scope of futuristic studies	22
2.8	Metallic nano absorbents for arsenic removal	23

2.8.1	Ti, Al, Zr, Ce, Zn and Cu based nanomaterials	23
2.8.2	Fe based nano particles	26
2.8.2.1	Nano scale zero valent iron (nZVI)	26
2.8.2.2	Di-valent iron nanostructures	27
2.8.2.3	Iron ^{II, III} oxides nanostructured phases	28
2.8.2.4	Iron(oxy)hydroxides nanostructured phases	29
2.9	Maghemite nanoparticles	31
2.9.1	Bare and functionalized nanostructures	31
2.9.2	Scope of development	33
2.10	Gaps pertaining to laboratory scale studies	36
2.10.1	Fabrication of columns	36
2.10.2	Studies representing real world conditions	36
2.10.3	Cost evaluation of nanomaterials production	37
2.11	Summary and scope of research	37
Chapter 3.	Maghemite nanoparticles and their engineered nanostructures: Synthesis and characterization	39
3.1	Chapter abstract	39
3.2	Materials and reagents	40
3.3	Instrumentation	40
3.4	Methodology and operating conditions	41
3.4.1	Chemical co-precipitation mode NPs synthesis	41
3.4.2	Analysis employing inductively coupled plasma-mass spectrometry (ICP-MS)	41
3.4.3	Evaluation for the cost of nano materials production	42
3.4.4	Analysis employing UV-visible spectrophotometer	43
3.4.5	Analysis employing X-ray diffractometer (XRD)	43
3.4.6	Analysis employing Raman spectrometer	44
3.4.7	Analysis employing X-ray photoelectron microscopy (XPS)	44
3.4.8	Analysis employing field emission scanning electron microscopy (FE-SEM)	44
3.4.9	Analysis employing Transmission electron microscopy (TEM)	45
3.4.10	Brunauer–Emmett–Teller (BET) surface area	45
3.4.11	Thermo-gravimetric analysis (TGA/DTA)	45

3.4.12	Analysis employing Vibrating sample magnetometer (VSM)	46
3.4.13	Analysis employing Superconducting quantum interface device (SQUID)	46
3.4.14	Analysis employing Fourier Transform infrared spectrophotometer (FTIR)	46
3.4.15	Analysis employing Zetasizer	47
3.5	Synthesis of maghemite nanostructures and their nanohybrids	47
3.6	Results and discussion	47
3.6.1	Determination of iron content in as-synthesized nanomaterials	47
3.6.2	Cost estimation of as-synthesized nanomaterials	47
3.6.3	UV-Vis spectra	49
3.6.4	XRD diffraction patterns	50
3.6.5	RAMAN spectroscopy	51
3.6.6	XPS spectroscopy	54
3.6.7	Field emission scanning electron microscopy (FE-SEM)	55
3.6.8	Transmission electron microscopy (TEM)	56
3.6.9	Brunauer–Emmett–Teller (BET) surface area	57
3.6.10	Thermo-gravimetric analysis (TG)	57
3.6.11	Vibrating sample magnetometer (VSM) analysis	58
3.6.12	SQUID analysis (M-H curve)	59
3.6.13	Zero-field-cooled (ZFC) and Field-cooled measurements	62
3.6.14	FTIR spectra	62
3.6.15	Zeta-potential measurements	65
Chapter 4.	Batch experiments for arsenic removal and modeling for adsorption isotherms and kinetics	67
4.1	Chapter Abstract	67
4.2	Materials and reagents	68
4.3	Methodology	68
4.3.1	Experimental design, model fitting and statistical analysis	68
4.3.2	Predictive modelling using Response Surface Methodology	69
4.3.3	Desirability function	70
4.3.4	Determination of arsenic concentration	71
4.3.5	Calculation of arsenic removal capacity	72
4.3.6	Kinetic models	72
4.3.6.1	Pseudo-first order model	73

4.3.6.2	Pseudo-Second order model	73
4.3.6.3	Intra-particle diffusion	74
4.3.6.4	Elovich kinetic model	75
4.3.7	Equilibrium Isotherm models	75
4.3.7.1	Freundlich adsorption isotherm	76
4.3.7.2	Langmuir adsorption isotherm	76
4.3.7.3	Tempkin adsorption isotherm	77
4.3.7.4	Dubinin-Radushkevich adsorption isotherm	78
4.4	Results and Discussion	79
4.4.1	Response surface modelling and ANOVA analysis	79
4.4.2	Optimization of arsenic removal	79
4.4.2.1	Effect of process variables	79
4.4.2.2	Statistical analysis and fitting of second order polynomial equation	81
4.4.2.3	Multiple response optimisation	88
4.4.3	Analysis of As ^V removal employing different kinetic models	89
4.4.4	Isotherm modeling using Langmuir, Freundlich, SIPS, DR-Model, Redlich Peterson adsorption models	94
4.5	Leaching test for the determination of secondary pollution	102
Chapter 5.	Batch removal experiments to simulate the usage of developed nanoadsorbents in real world applications: Taguchi's design of experimental methodology	105
5.1	Chapter Abstract	105
5.2	Materials and instrumentation	106
5.3	Methodology	106
5.3.1	Study area, sample collection and their preparation	106
5.3.2	Artificial water formulation (AWF)	107
5.3.3	Analysis for different elemental ions	109
5.3.4	Taguchi's design of experimental methodology	110
5.3.5	Artificial Neural network (ANN), for predicting modelling	118
5.4	Result and Discussion	119
5.4.1	Physio-chemical characterization of collected groundwater samples	119
5.4.2	Effect of process parameters on As ^V removal in multi-ionic system	121
5.4.2.1	Effect of shaking speed, temperature, contact time	121
5.4.2.2	Effects of Arsenic initial concentration, TDS, pH	123

5.4.3	Analysis of inter-parametric interaction	127
5.4.4	Identification of optimal level and estimation of optimum response characteristics	134
5.4.5	Conformation experiments	138
5.4.6	Understanding of adsorption behaviour using surface complexation models (SCMs)	139
5.4.7	Predicting modelling of Arsenic removal using multilayer concept of artificial neural network	142
Chapter 6.	Continuous flow reactive modeling using 1D columns and sand-tank experiments for arsenic removal	145
6.1	Chapter abstract	145
6.2	Materials and equipment	146
6.3	Methodology	146
6.3.1	Mathematical equation for design of columns (1-D) for lab studies	146
6.3.2	Fabrication of sand tank model for lab studies	148
6.3.3	Characteristics of consolidated material	149
6.3.4	Columns (1-D) adsorption experiments	150
6.3.4.1	Analysis of breakthrough curves	150
6.3.4.2	Adam-Bohart model	152
6.3.4.3	Thomas model	152
6.3.4.4	BDST model	153
6.3.4.5	Yoon-Nelson model	153
6.3.5	Sand-tank experiments	155
6.3.5.1	Sand packing	155
6.3.5.2	Preliminary experiments	155
6.4	Results and Discussion	156
6.4.1	Column studies (1-D)	156
6.4.1.1	Evaluation of fix bed parameters for As ^V adsorption	156
6.4.1.2	Empty bed contact time (EBCT) and usage rate of adsorbent (U _r)	159
6.4.1.3	Breakthrough model analysis	161
6.4.2	Sand tank studies (3-D)	170
6.4.2.1	Batch adsorption experiments for As ^{III} removal	170
6.4.2.2	Tracer transport experiments	171
6.4.2.3	Determination of retardation coefficient of nanoparticles	172

6.4.2.4	Governing equation, boundary conditions and input parameters for nanoparticles transport modelling	172
6.4.2.5	Simulations of nanoparticles transport in homogeneous fully saturated media	177
6.4.2.6	Arsenic removal experiments in 3-D sand tank model	177
Chapter 7.	Conclusions and recommendations	181
7.1	Outcomes of the study	181
7.2	Recommendation for further study	183
References	185
Work Recognition	217





LIST OF FIGURES

Figure No.	Title	Page No.
Figure 1.1	Representation of possible causes of arsenic pollution in groundwater	2
Figure 1.2	An overview of arsenic health consequences a. Skin lesions b. Skin cancer c. Blackfoot disease	2
Figure 2.1	Pictorial representation of percent distribution of arsenic species under variable pH and E _h conditions	13
Figure 2.2	World location map showing arsenic contaminated groundwater states in both developed and developing countries	14
Figure 2.3	Overview of molecular model depicts (a) Monolayer adsorption (b) Multilayer adsorption	18
Figure 2.4	An overview of PRB based technique representing remediation of arsenic in shallow groundwater system	21
Figure 2.5	An overview of injection based technique representing remediation of arsenic in deep aquifer system	23
Figure 2.6	Schematic showing mechanism adsorption of arsenic by nanoscale titanium oxides	24
Figure 2.7	Picture representing crystal structures phases of zirconium oxides nanoparticles (a) monoclinic (b) tetragonal (c) cubic	25
Figure 2.8	Picture representing crystal structures phases of (a) Copper ^I (b) Copper ^{II} oxides nanoparticle	26
Figure 2.9	Schematic showing adsorption mechanism of arsenic on nZVI	27
Figure 2.10	Crystal structure of divalent Iron ^{II} compounds a. Wustite b. Mackinawite	27
Figure 2.11	Crystal structure of magnetite nanoparticles	28
Figure 2.12	Schematic showing the proposed redox reaction on the surface of magnetite nanoparticles during adsorption under (a) anoxic (b) oxic environment	29
Figure 2.13	The schematic represents the occurrence of possible electronic interactions and type of adsorption on the surface of engineered nanoadsorbents	33
Figure 3.1	UV-visible absorption spectra of as-synthesized (a) BIO NPs and (b) BIO-DW nanohybrids. Inset: depicting the absorption spectrum in larger wavelength	50
Figure 3.2	XRD diffraction patterns of as-synthesized (a) BIO NPs and (b) BIO-DW nanohybrids	51
Figure 3.3	Raman spectra of as-synthesized (a) BIO NPs and (b) BIO-DW nanohybrids	52
Figure 3.4	Spectra of XPS representing survey scan for (a) BIO NPs and (b) BIO-DW nanohybrids	54

Figure 3.5	XPS spectra of BIO NPs (a-b) and BIO-DW nanohybrids (a'-b'): narrow scan of Fe2p (a and a'); O1s (b and b')	55
Figure 3.6	SEM images of BIO NPs and BIO-DW nanohybrids (100 nm scale)	56
Figure 3.7	TEM images of BIO NPs and BIO-DW nanohybrids (50 nm scale)	56
Figure 3.8	Thermo-gravimetric curves (I) a. BIO NPs b. BIO-DW nanohybrids c. distillery waste (II).; Full range: Distillery waste	57
Figure 3.9	DTA curves of as-synthesized nanomaterials (a) BIO NPs and (b) BIO-DW nanohybrids	58
Figure 3.10	M-H curves of BIO NPs and BIO-DW nanohybrids (a and b) at ambient temperature	59
Figure 3.11	M-H curves of BIO NPs at 5K, 150 K and 300 K	60
Figure 3.12	M-H curves of BIO-DW nanohybrids at 5K, 150 K and 300 K	60
Figure 3.13	Temperature dependence of the magnetization for ZFC (zero-field-cooled) and FC (field-cooled) for (a) BIO NPs and (b) BIO-DW nanohybrids in a range of 5 to 300 K at applied field H= 800 O _e	62
Figure 3.14	FTIR spectra of as-synthesized NPs (a) BIO (b) BIO-DW and Industry waste (c) DW (distillery waste)	63
Figure 3.15	Zeta potential (ζ) measurement of as-synthesized (a) BIO NPs and (b) BIO-DW nanohybrids	65
Figure 4.1	Response surface plots showing the effect of different input variables on removal capabilities of As ^V using BIO NPs (a-c) and BIO-DW (a'-c') nanohybrids	83
Figure 4.2	Response surface plots showing the effect of different input variables on removal capabilities of As ^V using BIO NPs (d-f) and BIO-DW (d'-f') nanohybrids	84
Figure 4.3	Correlation of actual and predicted values of As ^V removal capacity for BIO NPs (R ² - 0.9800) and BIO-DW (R ² - 0.9701) nanohybrids	87
Figure 4.4	Optimization process representing the predicted values and desirability function for the removal capacity of As ^V using BIO NPs	88
Figure 4.5	Optimization process representing the predicted values and desirability function for the removal capacity of As ^V using BIO-DW nanohybrids ...	89
Figure 4.6	Graphical representation of First-order kinetics for As ^V adsorption onto (a) BIO NPs. and (b) BIO-DW nanohybrids	90
Figure 4.7	Graphical representation of Pseudo-second-order kinetics for As ^V adsorption onto (a) BIO NPs. and (b) BIO-DW nanohybrids	91
Figure 4.8	Graphical representation of Intra-particle-diffusion kinetic for As ^V adsorption onto (a) BIO NPs. and (b) BIO-DW nanohybrids	92
Figure 4.9	Graphical representation of Elovich model for As ^V adsorption onto (a) BIO NPs. and (b) BIO-DW nanohybrids	92
Figure 4.10	Adsorption isotherm plot for (I) BIO NPs and (II) BIO-DW nanohybrids at dose concentration of 0.30 g L ⁻¹ (a-a') and 0.40 g L ⁻¹ (b-b')	94
Figure 4.11	Graphical representation of Freundlich adsorption isotherms of As ^V removal onto (a) BIO and (a') BIO-DW nanoparticles (Adsorbent dose- 0.30 g L ⁻¹)	95
Figure 4.12	Graphical representation of Freundlich adsorption isotherms of As ^V removal onto (a) BIO NPs and (a') BIO-DW nanohybrids (Adsorbent dose- 0.40 g L ⁻¹)	95

Figure 4.13	Graphical representation of Langmuir adsorption isotherms of As ^V removal onto (a) BIO and (a') BIO-DW nanoparticles (Adsorbent dose- 0.30 g L ⁻¹)	96
Figure 4.14	Graphical representation of Langmuir adsorption isotherms of As ^V removal onto (b) BIO and (b') BIO-DW nanoparticles (Adsorbent dose- 0.40 g L ⁻¹)	96
Figure 4.15	Graphical representation of Tempkin adsorption isotherms of As ^V removal onto (a) BIO and (a') BIO-DW nanoparticles (Adsorbent dose- 0.30 g L ⁻¹)	97
Figure 4.16	Graphical representation of Tempkin adsorption isotherms of As ^V removal onto (a) BIO and (a') BIO-DW nanoparticles (Adsorbent dose- 0.40 g L ⁻¹)	97
Figure 4.17	Graphical representation of Dubinin-Radushkevich adsorption isotherms of As ^V removal onto (a) BIO and (a') BIO-DW nanoparticles (Adsorbent dose- 0.30 g L ⁻¹)	98
Figure 4.18	Graphical representation of Dubinin-Radushkevich adsorption isotherms of As ^V removal onto (a) BIO and (a') BIO-DW nanoparticles (Adsorbent dose- 0.40 g L ⁻¹)	99
Figure 4.19	Graphical representation showing the possibility of secondary pollution through Fe ions during As ^V removal using (a) BIO NPs and (b) BIO-DW nanohybrids	103
Figure 5.1	Map showing location of the groundwater sampling points	107
Figure 5.2	Architecture of ANN model for the prediction of removal efficiency of As ^V using BIO NPs and BIO-DW nanohybrids	118
Figure 5.3	Effect of process parameters (a) shaking speed (b) temperature and (c) contact time on the removal capacity (q _e) and S: N ratio for multicomponent adsorption of As ^V onto BIO NPs	125
Figure 5.4	Effect of process parameters (a') shaking speed (b') temperature and (c') contact time on the removal capacity (q _e) and S: N ratio for multicomponent adsorption of As ^V onto BIO-DW nanohybrids	125
Figure 5.5	Effect of process parameters (d') As ^V conc. (e') TDS and (f') pH on the removal capacity (q _e) and S: N ratio for multicomponent adsorption of As ^V onto BIO NPs	126
Figure 5.6	Effect of process parameters (d') As ^V conc. (e') TDS and (f') pH on the removal capacity (q _e) and S: N ratio for multicomponent adsorption of As ^V onto BIO-DW nanohybrids	126
Figure 5.7	Interactions between parameters arsenic initial concentration (A) and TDS (B) at three levels on the removal capacity (q _e) and S: N ratio for multicomponent adsorption of As ^V onto BIO NPs	128
Figure 5.8	Interactions between parameters arsenic initial concentration (A) and TDS (B) at three levels on the removal capacity (q _e) and S: N ratio for multicomponent adsorption of As ^V onto BIO-DW nanohybrids	128
Figure 5.9	Interactions between parameters arsenic initial concentration (A) and shaking speed (C) at three levels on the removal capacity (q _e) and S: N ratio for multicomponent adsorption of As ^V onto BIO NPs	129

Figure 5.10	Interactions between parameters arsenic initial concentration (A) and shaking speed (C) at three levels on the removal capacity (q_e) and S: N ratio for multicomponent adsorption of As^V onto BIO-DW nanohybrids.	129
Figure 5.11	Interactions between parameters arsenic TDS (B) and shaking speed (C) at three levels on the removal capacity (q_e) and S: N ratio for multicomponent adsorption of As^V onto BIO NPs	130
Figure 5.12	Interactions between parameters arsenic TDS (B) and shaking speed (C) at three levels on the removal capacity (q_e) and S: N ratio for multicomponent adsorption of As^V onto BIO-DW nanohybrids	130
Figure 5.13	Percent contribution of various parameters for q_e for As^V adsorption in multi ionic system onto BIO NPs: parameter A, arsenate conc. ($\mu g L^{-1}$); parameter B, TDS ($mg L^{-1}$); parameter C, shaking speed (RPM); parameter D, temp. ($^{\circ}C$); parameter E, pH; parameter F, dose ($g L^{-1}$); parameter E, contact time (min)	133
Figure 5.14	Percent contribution of various parameters for q_e for As^V adsorption in multi ionic system onto BIO NPs: parameter A, arsenate conc. ($\mu g L^{-1}$); parameter B, TDS ($mg L^{-1}$); parameter C, shaking speed (RPM); parameter D, temp. ($^{\circ}C$); parameter E, pH; parameter F, dose ($g L^{-1}$); parameter E, contact time (min)	133
Figure 5.15	Representation of As^V adsorption behaviour onto BIO NPs using surface complexation models (a) location I and (b) location II	141
Figure 6.1	Schematic of fixed column(s) utilized for breakthrough curve analysis using both BIO NPs and BIO-DW nanohybrids	147
Figure 6.2	Details of the sand-tank set up used for the tracer and infection of nanoparticles studies	149
Figure 6.3	Picture showing the location of injection port and sampling ports considered during tracer experiments	156
Figure 6.4	Breakthrough curve of As^V adsorption at different flow rate(s) (a) BIO NPs and (a') BIO-DW nanohybrids	157
Figure 6.5	Breakthrough curve of As^V adsorption for different bed height(s) (a) BIO NPs and (a') BIO-DW nanohybrids	158
Figure 6.6	Breakthrough curve of As^V adsorption at different initial concentration(s) (a) BIO NPs and (a') BIO-DW nanohybrids	159
Figure 6.7	Linear plot of Adam-Bohart model with experimental data at different flow rate(s) for (a) BIO NPs and (a') BIO-DW nanohybrids [$C_0 = 4.0 mg L^{-1}$; $h_{rz} = 29.2 cm$]	161
Figure 6.8	Linear plot of Adam-Bohart model with experimental data at different fixed bed height(s) for (a) BIO NPs and (a') BIO-DW nanohybrids [$C_0 = 4.0 mg L^{-1}$; $F_v = 8.0 ml min^{-1}$]	162
Figure 6.9	Linear plot of Adam-Bohart model with experimental data at different As^V initial concentrations(s) for (a) BIO NPs and (a') BIO-DW nanohybrids [$F_v = 8.0 ml min^{-1}$; $h_{rz} = 29.2 cm$]	162
Figure 6.10	Linear plot of Thomas model with experimental data at different flow rate(s) for (a) BIO NPs and (a') BIO-DW nanohybrids [$C_0 = 4.0 mg L^{-1}$; $h_{rz} = 29.2 cm$]	163
Figure 6.11	Linear plot of Thomas model with experimental data at different fixed bed height(s) for (a) BIO NPs and (a') BIO-DW nanohybrids [$C_0 = 4.0 mg L^{-1}$; $F_v = 8.0 ml min^{-1}$]	164

Figure 6.12	Linear plot of Thomas model with experimental data at different As^V initial concentrations(s) for (a) BIO NPs and (a') BIO-DW nanohybrids [$F_v = 8.0 \text{ ml min}^{-1}$; $h_{rz} = 29.2 \text{ cm}$	164
Figure 6.13	Linear plot of Yoon-Nelson model with experimental data at different flow rate(s) for (a) BIO NPs and (a') BIO-DW nanohybrids [$C_0 = 4.0 \text{ mg L}^{-1}$; $h_{rz} = 29.2 \text{ cm}$]	165
Figure 6.14	Linear plot of Yoon-Nelson model with experimental data at different fixed bed height(s) for (a) BIO NPs and (a') BIO-DW nanohybrids [$C_0 = 4.0 \text{ mg L}^{-1}$; $F_v = 8.0 \text{ ml min}^{-1}$]	166
Figure 6.15	Linear plot of Yoon-Nelson model with experimental data at different As^V initial concentrations(s) for (a) BIO NPs and (a') BIO-DW nanohybrids [$F_v = 8.0 \text{ ml min}^{-1}$; $h_{rz} = 29.2 \text{ cm}$]	166
Figure 6.16	Adsorption isotherm plot for As^{III} onto BIO NPs and BIO-DW nanohybrids	170
Figure 6.17	Tracer breakthrough curve (longitudinal) observed at constant head and flow conditions	171
Figure 6.18	A fine mesh of 3-D model for simulation of nanoparticles transport in homogenous saturated porous media	173
Figure 6.19	Diagrams showing the zero flow, no flow and out flow boundary conditions for simulation experiments	173
Figure 6.20	Predictive analysis of nanoparticles transport through simulations using COMSOL	177
Figure 6.21	The breakthrough curve for As^{III} removal in sand-tank experiments using as-synthesized BIO NPs	178



LIST OF TABLES

Table No.	Title	Page No.
Table 2.1	Comparison of experimental protocols and arsenic remediation attributes of maghemite nanoadsorbents	35
Table 3.1	Analysis of cost in the production of as-synthesized BIO NPs and BIO-DW nanohybrids	48
Table 3.2	Crystallite size obtained from Scherrer's formula for BIO NPs	53
Table 3.3	Crystallite size obtained from Scherrer's formula for BIO-DW nanohybrids	53
Table 3.4	M-H curve details of BIO NPs and BIO-DW nanohybrids at 300, 150 and 5 K	61
Table 3.5	FTIR data (cm-1) of BIO NPs, BIO-DW nanohybrids and distillery waste.	64
Table 4.1	Range of experimental input variables for As ^V (initial concentration- 4 mg L ⁻¹) removal using BIO NPs and BIO-DW nanohybrids at shaking speed of 250 rpm	70
Table 4.2	Experimental inputs and response of BIO NPs and BIO-DW nanohybrids at As ^V concentration 4 mg L ⁻¹ and 250 rpm	82
Table 4.3	ANOVA for Response surface quadratic model for As ^V removal using BIO NPs	85
Table 4.4	ANOVA for Response surface quadratic model for As ^V removal using BIO-DW nanohybrids	86
Table 4.5	Kinetic parameters obtained during the removal of As ^V by as-synthesized BIO NPs and BIO-DW nanohybrids under different experimental conditions	93
Table 4.6	Parameters for plotting Langmuir, Freundlich, Tempkin and Dubinin-Radushkevich adsorption isotherms of As ^V removal onto BIO nanoparticles (Dose- 0.30 g L ⁻¹) and (Dose- 0.40 g L ⁻¹)	100
Table 4.7	Parameters for plotting Langmuir, Freundlich, Tempkin and Dubinin-Radushkevich adsorption isotherms of As ^V removal onto BIO nanoparticles (Dose- 0.40 g L ⁻¹)	100
Table 4.8	Parameters for plotting Langmuir, Freundlich, Tempkin and Dubinin-Radushkevich adsorption isotherms of As ^V removal onto BIO-DW nanoparticles (Dose- 0.30 g L ⁻¹) and (Dose- 0.40 g L ⁻¹)	101
Table 4.9	Parameters for plotting Langmuir, Freundlich, Tempkin and Dubinin-Radushkevich adsorption isotherms of As ^V removal onto BIO-DW nanohybrids (Dose- 0.40 g L ⁻¹)	101
Table 4.10	Isotherm constant parameters and correlation coefficients calculated for the adsorption of As ^V onto BIO and BIO-DW nanoparticles	102
Table 5.1	Elements contributed in the formulation of artificial water	108
Table 5.2	Comparison of ionic concentration between actual groundwater and artificial formulated water	108
Table 5.3	Final amount of salts taken for artificial water formulation	109

Table 5.4	Process parameters for As ^V adsorption study in a multicomponent system onto BIO NPs and BIO-DW nanohybrids using Taguchi's design of orthogonal array (OAs)	111
Table 5.5	Taguchi's orthogonal array (OA) L ₂₇ (3 ¹³) for experimental runs assignment alongwith with three interactions levels (2 nd order) and calculation of adsorption capacity (Q_e) values for As ^V in multicomponent ionic systems using BIO nanoparticles	115
Table 5.6	Taguchi's orthogonal array (OA) L ₂₇ (3 ¹³) for experimental runs assignment alongwith with three interactions levels (2 nd order) and calculation of adsorption capacity (Q_e) values for As ^V in multicomponent ionic systems using BIO-DW nanoparticles	116
Table 5.7	Percent distribution inorganic species (free or complex ions) possibly effecting the As ^V adsorption	120
Table 5.8	Average and main effects of q_e values for BIO nanoparticles: Raw and S: N data	123
Table 5.9	Average and main effects of q_e values for BIO-DW nanohybrids: Raw and S: N data.	123
Table 5.10	ANOVA of Q_e and S: N ratio data for multi-ionic system in the adsorption of As ^V using BIO-NPs	131
Table 5.11	ANOVA of Q_e and S: N ratio data for multi-ionic system in the adsorption of As ^V using BIO-DW nanohybrids	132
Table 5.12	Predicted optimal levels of parameters alongwith adsorption capacity (Q_e) values, confidence intervals, outcomes of conformation experiments and percent variation for location I, location II and experimental design (BIO NPs)	136
Table 5.13	Predicted optimal levels of parameters alongwith adsorption capacity (Q_e) values, confidence intervals, outcomes of conformation experiments and percent variation for location I, location II and experimental design (BIO-DW nanohybrids)	138
Table 5.14	Reactions and parameters of surface complexation modeling for BIO nanoparticles	140
Table 5.15	Optimal values of architecture weights and biases for ANN model using BIO NPs	143
Table 5.16	Optimal values of architecture weights and biases for ANN model using BIO-DW nanohybrids	144
Table 6.1	Physical characteristics of sand used for laboratory experiments.	150
Table 6.2	Experimental parameters of adsorptive removal of As ^V by as-synthesized BIO NPs in the fixed bed system(s)	167
Table 6.3	Experimental parameters for adsorptive removal of As ^V by as-synthesized BIO-DW nanohybrids in the fixed bed system(s)	167
Table 6.4	Breakthrough parameters for various experimental conditions obtained during As ^V adsorption using BIO NPs	168
Table 6.5	Breakthrough parameters for various experimental conditions obtained during As ^V adsorption using BIO-DW nanohybrids	169
Table 6.6	Overview of Boundary Conditions used to simulate arsenic fate and transport in subsurface	174
Table 6.7	Summary of water flow and solute transport parameters used in simulation experiments	176

Acronyms and Notations

Acronyms

ABF	Arsenic bio-sand filter
ANN	Artificial neural network
ANOVA	Analysis of variance
ATR-FTIR	Attenuated total reflectance-Fourier transform infrared spectroscopy
BDST	Bed-Depth Service Time
BIO	Bare iron oxide nanoparticles
BIO-DW	Functionalized iron oxide nanoparticles
BPNN	Back propagation neural network
BTU	Bucket treatment unit
CCD	Central composite design
DF	Diffuse flame
DLM	Diffuse double layer model
DoE	Design of Experiments
EC	Electrical conductivity
EDX	Energy dispersive using X-ray
FE-SEM	Filed emission scanning electron microscopy
FTIR	Fourier transform infrared spectroscopy
FWHM	full width at half maximum
HFO	Hydrated ferric oxides
HL	Hidden layer
IC	Ion chromatography
ICP-MS	Inductive coupled Plasma-mass spectrometry
IDF	Induced Diffusion flame

IL	Input layer
IONP's	Iron oxide nanoparticles
IW	Input weight matrix
JCPDS	Joint Committee on Powder Diffraction Standards
LW	Layer weight matrix
MATLAB	Mathematical Lab
mCFMS	Mini- cryogenic free measurement system
MF	Micro filtration
MPMS	Magnetic Property Measuring System
MSDS	Material safety data sheet
NIST	National institute of standards and technology
NF	Nanofiltration
NTU	Nephelometric turbidity unit
OL	Output layer
PRB's	Permeable reactive barriers
PRU	pathogen removal unit
RO	Reverse osmosis
RMS	Root mean square
RSM	Response surface methodology
SCM	Surface complexation model
TDS	Total dissolved solids
TGA	Thermo-gravimetric
TPM	Three plane model
UF	Ultrafiltration
US EPA	United States Environmental Protection Agency
UV-Vis	Ultra-violet visible spectroscopy
WHO	World Health Organization

XPS	X-ray photoelectron microscopy
XRD	X-ray diffraction analysis

Notations

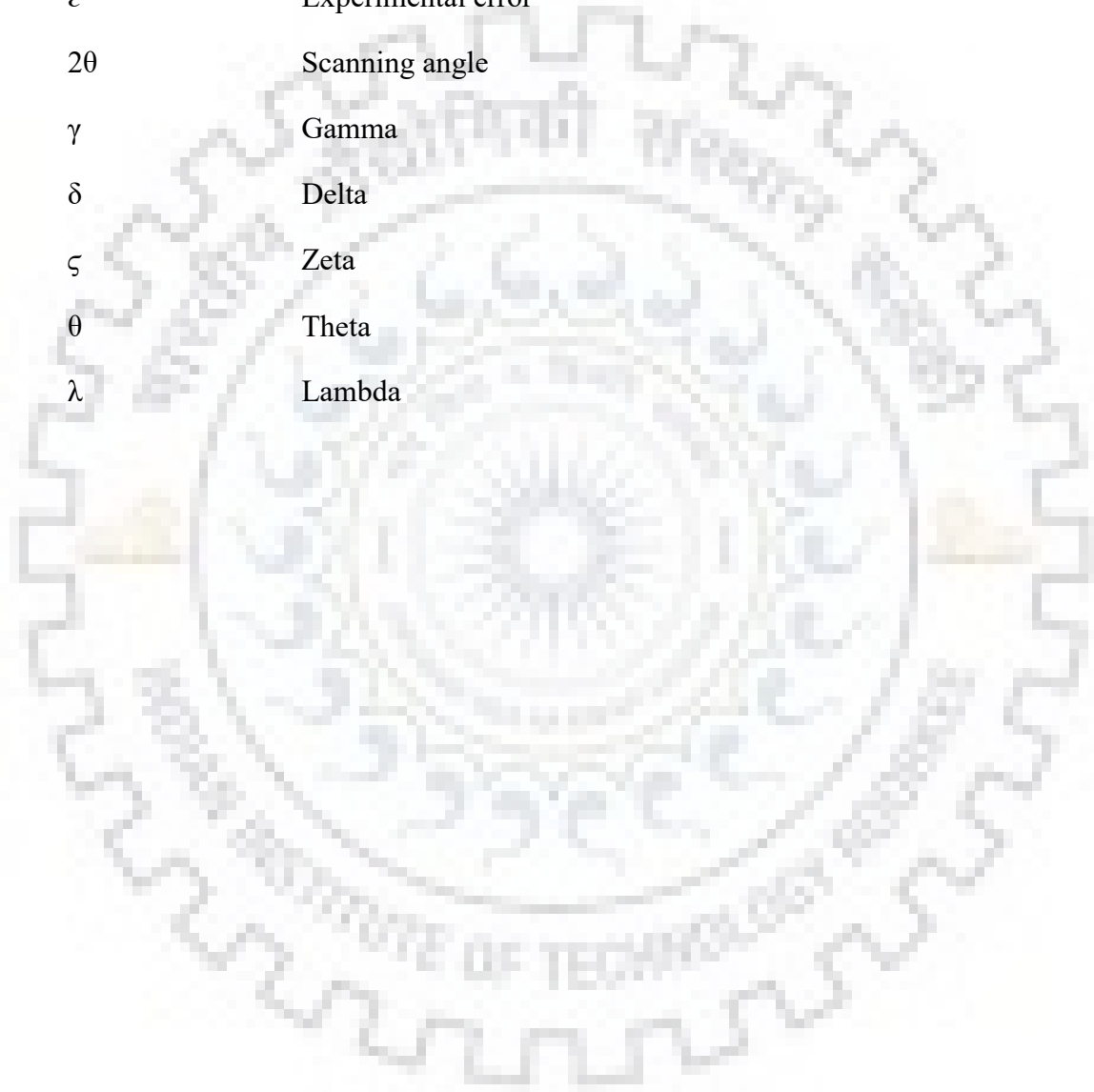
As	Arsenic
Al	Aluminium
b	Bias
C	Carbon
pE	Redox potential
Ca	Calcium
Cl	Chloride
Cr	Chromium
Cu	Copper
emu	Electromagnetic unit
F	Fluoride
FC	Field-cooled
Fe	Iron
K	kelvin
KBr	Potassium bromide
keV	Kilo-electron volt
L_F	Loss-coefficient
logsis	Log sigmoid transfer function
Mg	Magnesium
M-H	Magnetic hysteresis
<i>mm</i>	Millimetre
Mn	Manganese
mV	Millivolt
n	Number of variables

nA	Nano-ampere
nm	nanometer
N	Total number of experiments required
Na	Sodium
NO ₃	nitrate
nZVI	Nanoscale Zero-valent iron
O	Oxygen
OA's	Orthogonal arrays
O_e	Oersted
psi	Pound per square inch
purelin	Linear transfer function
R ²	Coefficient of determination
SO ₄	Sulphate
T	temperature
w	weights
x_i	Coded level of input variables
y	Predicted response
ZFC	Zero-field cooled
Zn	Zinc
1-D	1-Dimensional
3-D	3-Dimensional
μm	micrometre

Greek Symbols

Å	Angstrom
α	Alpha
β	Beta

β_0	Constant term
β_i	Linear regression coefficient
β_{ii}	Quadratic regression coefficient
β_{ij}	Interaction regression coefficient
$^{\circ}\text{C}$	Degree Celsius
ε	Experimental error
2θ	Scanning angle
γ	Gamma
δ	Delta
ζ	Zeta
θ	Theta
λ	Lambda





Introduction

1.1 Problem statement

Arsenic is a toxic, bio-accumulating, redox and pH sensitive element. It is a life threatening contaminant, to which millions are exposed through contaminated groundwater from the beginning of 20th century [1]. The high mobility of arsenic species in aquifer systems is of concern among the scientific communities. Worldwide, about 105 countries and approximately 226 million people are under potential threat of arsenic contamination [2]. Around 90,000 km² area with 50 million people are critically affected by its contamination in Bengal Delta basin comprising Bangladesh [3]. Its contamination in groundwater broadly reported in flood plains of the Ganga River is a subject of concern among the scientific communities across the globe since the last two and half decades due to its high mobility in ecosystem, high toxicity, carcinogenicity to human beings and its bio-magnification characteristics. Both developed and developing countries are under a potential threat of arsenic contaminated groundwater. The menace among the communities across the globe is mainly due to its contamination in groundwater as compared to that of surface water. To combat the problems related to its contamination, WHO and US EPA have set its standard limit as 10 µg L⁻¹ for drinking water since 2006 [4], [5].

1.1.1 Outline of arsenic pollution in groundwater and its health consequences

Most reported arsenic problems (As^{III} species) have been found in groundwater supply systems and are caused primarily by natural processes such as mineral weathering and dissolution resulting from a change in the geo-chemical environment to a reductive condition. Millions of people in West Bengal and Bangladesh had been drinking groundwater from wells contained arsenic concentration ranging from 100 - 3900 µg L⁻¹ with many of them succumbing to diseases caused by it [6], [7]. A pictorial representation of the possible causes of arsenic pollution are shown in Figure 1.1

It may exist as oxyanions in different types of species due to its sensitivity towards redox and pH conditions. At redox potential (pE > 600 mV), HAsO₄²⁻ is a dominant species of As^V in

groundwater between the pH range of 6.5 to 11.5. Below $\text{pH} < 6.5$, it exists as H_2AsO_4^- [8]. However, zero-valent arsenic (As^0) and As^{3-} occur rarely in aquatic environments.

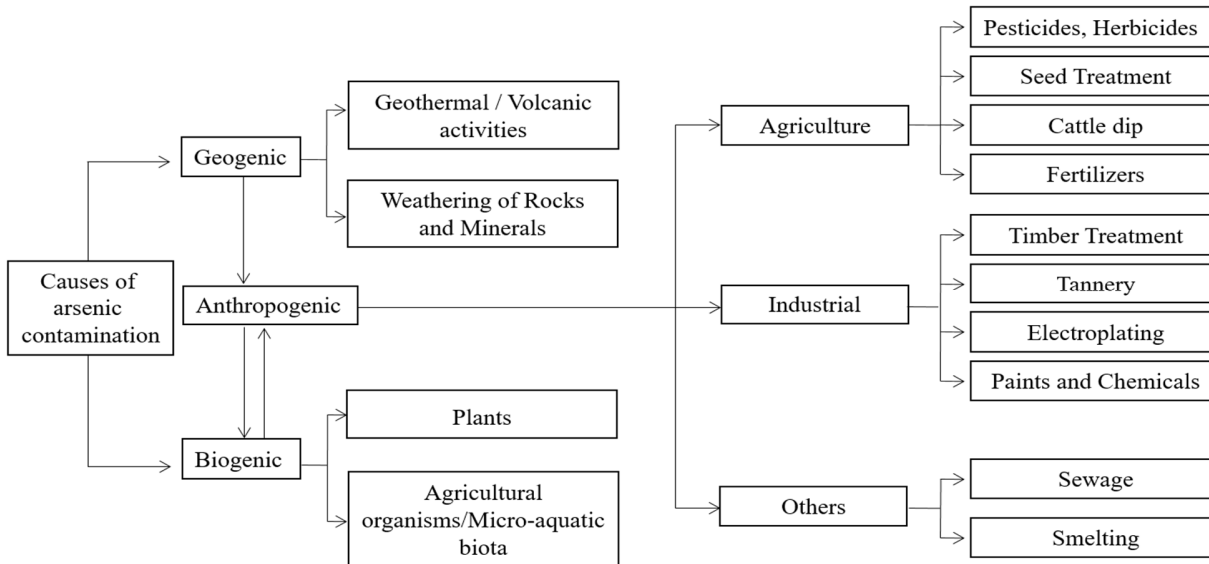


Figure 1.1. Representation of possible causes of arsenic pollution in groundwater [9]–[11].

Early clinical symptoms in acute poisoning are severe nausea and vomiting, weakness, muscular pain and flushing skin, colicky abdominal pain [12]. Chronic exposure is much more insidious in nature and sometimes symptoms appears between 6 months to 2 years, leading to anaemia and leukopenia [13]. The major dermatological diseases such as melano-keratosis, melanosis, spotted melanosis, spotted and diffuse keratosis were reported to affect the human beings. Further, it has been widely reported that the long term consumption of arsenic contaminated water and food results to damage the liver, kidney and gall bladder [14], [15]. Some potential health hazard of arsenic to human beings are highlighted in figure below:



Figure 1.2. An overview of arsenic health consequences a. Skin lesions b. Skin cancer c. Blackfoot disease. [Source: <http://www.sos-arsenic.net/english/contamin/index.html>].

1.1.2 Nanostructured adsorbents for arsenic removal

Nanoadsorbents have gained considerable attention for arsenic removal in groundwater among scientific communities. Nanotechnology based water treatment systems are logical choice in respect to resource and energy efficiency [16]. The literature is widely replete in cases of development of different nanoadsorbents which have been explored for arsenic removal [17]. From past two decades, several metallic nanoadsorbents including oxides of iron, aluminium, cerium, copper, zirconium and titanium have been reported to developed for arsenic removal [18]. Metallic iron based nanoadsorbents have been widely explored due to their strong affinity towards arsenic and ecological-friendly nature.

Development of several polymorphs of metallic iron nanostructures such as nZVI, iron^{III} oxides (α -Fe₂O₃, β - Fe₂O₃, γ - Fe₂O₃) iron^{III} (oxy) hydroxides (α -FeOOH, β -FeOOH, γ -FeOOH) and iron^{II,III} oxides (magnetite) is also reported in the literature for arsenic removal. Among different polymorphs of iron, nZVI (nanoscale zero-valent iron) has been extensively explored in the literature both at laboratory and pilot scale studies. These nanoparticles are unstable in natural environmental conditions and prone to oxidize into iron oxides/hydroxides after oxidation which limit its application for pilot scale studies significantly [19].

1.1.3 Sub-surface sequestration of arsenic

Generally, removal of arsenic from the contaminated systems have been categorised into: *ex-situ* (pump and treat) and *in-situ* (underground treatment) processes. Till now, pump and treat remediation has been practiced on large scale in providing arsenic free water to the affected population [20]. However, such technologies have several disadvantages like high operational cost and generation of toxic sludge [21]. The advantages of *in-situ* removal of contaminants compared to *ex-situ* technologies include such as: natural treatment of groundwater and low operational cost. Moreover, the sequestration of groundwater contaminants using *in-situ* technologies have been considered among sustainable approaches [22]. Therefore, the development of technologies to sequester the arsenic in the subsurface are gaining a considerable attention. From last two decades, *in-situ* technologies such as: biosorption, permeable reactive barriers, chemical oxidation, natural attenuation are being developed. Among these, PRB's (permeable reactive barrier's), because of its convenient operation and compactness makes it easy to manage for remediation and has been considered as a promising technology [20][23].

1.2 Research goal and objectives

Since the large two and half decade continuous efforts have been made by scientific communities in developing the efficient and sustainable arsenic removal technologies.

The focus of the present research has been to explore further one of the widely employed technology due to its cost-effectiveness and easy operational characteristics, i.e. adsorption. The goal of this work is to reduce the risk of arsenic contamination in groundwater through improved understanding and improvement of present nanotechnology based arsenic removal processes on one hand, as well as attempting resource recovery in the industrial waste(s) by employing the same in nanoparticle synthesis. To this end, this research has four objectives: -

1. To improve understanding about the process of arsenic removal employing nanoadsorbents and explore knowledge gaps.
for arsenic removal and exploring the gaps that could be sustainable in their applications.
2. To develop a novel approach to address twin problems, (a) arsenic remediation and (b) utilization of waste as a resource, both at a common platform.
3. Attempting to synthesize the iron based nanomaterials and their functionalized nanostructures by the modification of precursor material employing industry waste.
4. Evaluating the *ex-situ* (above-surface) removal characteristics of developed nanoadsorbents for arsenic removal.
5. Efficacy assessment of generated nanomaterials for *in-situ* (sub-surface) arsenic sequestration through laboratory scale models representing direct injection mode of application.

1.3 Justification for research

1.3.1 Intellectual merits

This study proposes to explore the raw waste of distillery industry, which is rich in a variety of natural organic compounds for the generation of iron oxide nanohybrids under partial hydrolysis (reflux) conditions that could prevent agglomeration of nanoparticles along with the encapsulation of inorganics and putting organic functionalities as surface. The use of economic and non-toxic waste for the generation of nanohybrids could mitigate the expectancy of occupational hazard and health effects as well. Further, a methodology exploring the utilization of waste to nanomaterials production will promote practicability of the technique for industrial resourced communities in

terms of revenue generation. The resulting iron oxide nanoparticles IONP's could be injected around shallow and deeper aquifer groundwater wells for sequestration of arsenic to a considerable extent in sub-surface environment, restoring one of the numerous crippled, yet potential source of drinking water for most of the rural population.

Nonetheless, there are several challenges also that may impede the employment of *in-situ* (sub-surface) application of as-synthesized nanosystems. Although, the as-synthesized nanoparticles have been proven to remove arsenic species significantly in the presence of competing ions and it remains to be seen that long term stability of employed nanoparticles and adsorbed arsenic is established. But, the drawbacks associated with the different types of groundwater conditions may adversely cause the detachment of arsenic species from the surface of these nanoparticles. Also, the variations in the geological formations and microbial environment could lead to increase in possibilities of recontamination with the occurrence of interactions with consolidated materials and interruption in biological life-cycles.

1.3.2 Broader impacts

The findings of this research is expected to help the scientific communities to apply an effective, safer and sustainable removal technology to deal with the problems of arsenic-contaminated groundwater at wider scale. The outcome of the present study may be of significant value not only to the groundwater scientists and engineers, but to the environmental professionals and professional of industry and ultimately in densely populated areas affected with arsenic contaminated groundwater.

1.4 Strategic approaches and tools

While attempting to fulfil the objectives of the present study, several tasks have been performed to develop and critically evaluate the novel treatment media for targeted contaminant removal in both *ex-situ* and *in-situ* application modes.

1.4.1 *Task I*: Synthesis of maghemite nanoparticles along with their engineered nanostructures utilizing industry waste

Task I included the development of methodology in the generation of maghemite nanoparticles and their nanohybrids with the incorporation of industry waste during the synthesis

process under reflux conditions (Chapter 3). Two types of metallic nanoadsorbents have been used in this study in terms of their physio-chemical characteristic features. One type includes the bare maghemite nanoparticles (BIO) and other consists of functionalized phase of these nanoparticles (BIO-DW) encapsulated with the organic surface moieties. A fundamental approach of this task has to develop methods to maintain a good yield of nanostructured adsorbents while conserving the maghemite phase of iron^{III} oxides during the formation of nanohybrids and high surface area that resulted in providing more reactive sites to arsenic species for interactions. The successful completion of Task I, was envisaged to provide a specific methodology that could generate a cost-effective nanoadsorbent material at a significant yield.

1.4.2 *Task II*: Physio-chemical characterization of as-synthesized nanoparticles

In Task II, these nanoparticles have been analyzed in terms of phase identification, crystallinity, magnetic strength, surface features, elemental composition and agglomeration characteristics using several techniques (Chapter 3). The electronic, optical, magnetic and physical characterization of as-synthesized BIO and BIO-DW nanostructured adsorbents have been undertaken employing techniques such as UV-Vis, FTIR, XRD, Raman, FESEM, HRTEM, VSM, SQUID, XPS, DTA-TGA, BET and Zetasizer. These emerging findings are expected to deliver an understanding of possible variations occurred during functionalization of maghemite nanoparticles using organic waste material. This has been employed to establish whether the iron^{III} phase, crystallinity, magnetization remained conserved during the modification of synthesis process for producing BIO-DW nanohybrids. The occurrence of possible variations in average particle size, specific surface area, surface functional moieties, surface characteristics, super-paramagnetic behaviour and thermal features are adequately investigated. The outcomes of all these analyses have been discussed in Chapter 3.

1.4.3 *Task III*: Adsorption isotherm and sorption kinetic modeling of arsenic removal through batch experiments

The Task III elaborates the adsorption experiments, which generated fundamental data to understand the sorption kinetics and removal characteristics of targeted arsenic species by BIO and BIO-DW nanoadsorbents. To predict the sorption behaviour, sorption rates and factors affecting the removal behaviour more accurately, sorption kinetic models have been applied to experimental data

(Chapter 4). In an attempt to explore the efficacy of the developed nanoadsorbents, it is necessary to establish a significant equilibrium correlation between adsorbents and target contaminants. The adsorption reactions of adsorbate were illustrated through empirical, chemical and surface complexation models. These empirical models were expected to deliver the representation of adsorption data without a theoretical basis, whereas chemical models provide a molecular description using equilibrium approach for the adsorption process.

1.4.4 *Task IV*: Statistical approach for arsenic removal using Response Surface and Taguchi's design of experimental methodology

Task IV focused on investigating the adsorption capabilities through experimental design (Chapter 4 and 5), based on mathematical models which are found to be relevant to assess the statistical significance of different factors. As the traditional Design of Experiments (DoE) explains only the effects of design factors on average result level as well as the exploration of interactions between the experimental variables and result outcomes are impractical using one-way classification procedures, therefore, RSM and Taguchi's methodology (robust design) were explored in the present study. These are effective statistical tools in developing a suitable experimental approach for laboratory investigations at optimized parametric levels by selecting a minimum number of experiments. Artificial water having compositions similar to the groundwater in field was prepared and used in experimental runs.

1.4.5 *Task V*: Understanding the removal mechanisms through surface complexation models and predictive modeling of outcomes using MATLAB

The formation of possible competing ion species under different conditions such as pH and variable concentrations range have been identified using Visual MINTEQ, and further explored to understand their effects on As^V adsorption (Chapter 5). Arsenic removal using nanoparticles require a robust methodology for predictive analysis. Artificial neural network tool has been found appropriate for the prediction and estimation of adsorption properties due to its complex non-linear characteristics. This tool has a capability to consider or take into account both the input and output parameters effectively. The tool has also the ability to correlate the input variables with the output adequately in complex conditions. A few authors have explored the predictive modeling for the removal of arsenic onto different adsorbents using ANN. In the present study, the training of ANN

model for Taguchi's data is evaluated using MATLAB neural network tool. An approximation algorithm based on feed-forward back propagation has been applied in which mean square error represents the accuracy index. Three layered architecture of back propagation neural network (BPNN) represented as IL-HL-OL, where IL is input nodes (equal to number of variables in the model), HL is hidden nodes (optimized using runs) and OL is output nodes (based on numbers).

1.4.6 Task *VI*: Evaluating the arsenic removal efficiency of developed nanoadsorbents through fixed bed reactors systems (1-D columns experiments)

Task VI highlights evaluation of the practical applicability of developed nanoparticles in arsenic removal in continuous mode, discussed in Chapter 6. BDST, Thomas, Yoon-Nelson and Adam-Bohart models were fitted to the dynamic experimental flow data obtained from fixed bed columns to analyse the breakthrough curve and determine the column characteristics. The fixed-bed reactor continuous flow system study provides a simple method for the determination of bed operation life span effectively at the laboratory scale. Further, the designing and fabrication of laboratory columns was undertaken based on the universally accepted methodology, for a better comparability and interpretation of arsenic removal data using different nanoadsorbents at a common platform.

1.4.7 Task *VII*: 3-D sand tank experimental model for *in-situ* employment of as-synthesized nanoparticles

Task VII delineated the efficacy assessment for *in-situ* deployment of BIO and BIO-DW nanoparticles representing Direct Injection mode of application (Chapter 6). To overcome the limitations of conventional *ex-situ* treatment technologies such as high operational cost and generation of toxic sludge, a laboratory scale model was developed to explore the role of various factors that could affect the *in-situ* injection of developed nanoparticles. The principal concept of this task included the assessment of distribution of nanoparticles after the injection into consolidated material through the injection ports having variable depths. Under constant head pressure, contaminated water was allowed to pass through the tank, and further the sequestration capability of material under these conditions were assessed by calculating the total volume of water treated.

1.5 Thesis organization

The thesis divides into seven chapters.

Chapter One presents an introduction, problem statement, research goal and objectives, strategic approaches along with the justification for research.

Chapter Two presents the literature review, global scenario of arsenic contamination, treatment technologies, discussing the earlier studies explored on arsenic removal employing nanoadsorbents in different modes, and their limitations along with the research gaps.

Chapter Three presents the synthesis of nanoadsorbents and cost estimation of their production, methodology of instrumentation, physiochemical characterization employing UV-Vis, XRD, Raman, XPS, FE-SEM, HR-TEM, BET, TGA/DTA, VSM, SQUID, FTIR and Zetasizer equipment.

Chapter Four deals with the batch studies involving optimization of arsenic removal process by RSM along with the modeling for removal kinetics and adsorption isotherms.

Chapter Five extends to the batch studies representing real world groundwater conditions, involving the optimization of arsenic removal process by Taguchi's design of experimental methodology and Surface complexation modeling (SCMs) for the understanding of adsorption behaviour.

Chapter Six deals with the modeling for the removal kinetics of arsenic under continuous flow employing columns (1-D) and Sand-tank (3-D) experiments.

Chapter Seven presents the conclusions along with the future research directions.



Literature review

2.1 Source of arsenic in subsurface environment

Arsenic from earth crust and bedrocks enriched with its ores, leaches moderately into groundwater [24]. The mineral iron arsenate (FeAsO_4) is considered to be a common source of arsenic in the subsurface environment. The compounds scorodite ($\text{FeAs}_4 \cdot 2\text{H}_2\text{O}$) and piteite [$\text{Fe}_x^{3+}(\text{AsO}_4)_y (\text{SO}_4)_z \cdot n\text{H}_2\text{O}$] are reported as direct and instantaneous source of arsenic in subterranean conditions [25]–[27]. Both of these are alteration products of mineral arsenopyrite (FeAsS) which constitutes a widespread source of arsenic in natural water [28].

2.2 Geochemical mechanisms of its release in groundwater

Arsenic mobilization in sub-surface environment and aquifer systems are controlled by two major factors viz. (1) adsorption and desorption, and (2) precipitation and dissolution of solid phase. The possible mechanisms that cause its release into groundwater are discussed below:

2.2.1 Reductive dissolution

Under reducing environment, the release of arsenic attached to iron has been considered as an important reason for the presence of elevated levels of arsenic in the sedimentary aquifer systems [29]. The generation of reducing conditions in sub-surface environment primarily depend on microbial activities in the sediments along with the abundance of organic matter. The major factors responsible for its mobilization in surrounding environment are diffusion of gases, sedimentation rate and microbial reactions. Nickson *et al.* [30] have described that the lowering of pH accelerates the dissolution of iron(oxy) hydroxides and subsequent release of associated arsenic through laboratory scale studies. In another study, the generation of highly reducing environment at near neutral pH has been suggested due to elevated concentration of carbonates and is considered to be the possible reason of its release into the aquifer media [31][32]. Recently, oxidation of organics along with microbial triggered reductive processes have been reported to be crucial in the mobilization of arsenic in alluvial aquifers of Terai Region, Nepal [33]. However, high

concentrations of Fe, Mn, HCO_3^- ions, NH_4^+ ions, CH_4 gas, and an absence of oxidized species such as NO_3^- and SO_4^{2-} ions are the indicators of strongly reducing conditions [34]. Moreover, the microbial mechanisms of arsenic release require the presence of abundant of organic matter in sub-surface environment.

2.2.2 Alkali desorption

Arsenic attachment in the subterranean environment onto the surface of iron oxides is an example of adsorption, and its detachment occurs through desorption. Its adsorption and release in the aquifer systems mainly occur through solid-phase precipitation and solid-phase dissolution respectively. In alluvium plains, arsenic is present as FeAsS (arsenopyrite) along with its transformed phases such as FeAsO_4 (ferric arsenate) and FeAsO_3 (ferric arsenite) [35]. It has been reported that the presence of an oxidizing agent, most commonly atmospheric oxygen (as O_2), controls the oxidation rate of arsenic containing sulphide minerals [36][37]. Thus, increment in the discharge rate of groundwater makes the arsenic bearing sulphide mineral exposed to oxygen which causes their oxidation and further release of arsenic to aquifer system.

2.2.3 Geothermal trigger

The elevated levels of arsenic have been reported in the hot springs on Qinghai-Tibet plateau that caused thorough leaching of rocks under high temperature conditions [38]. The generation of these conditions occurred due to either circulation of groundwater (deep and rapid) or shallow volcanism. Incidentally, the rivers and groundwater of Chile have also been reported with severe arsenic pollution caused due to seepage triggered by geothermal forces from the mountain, Andes located hundreds of kilometres from the point of groundwater abstraction areas [39].

2.3 Arsenic speciation and its aqueous chemistry

Being thermodynamically unstable, the percent distribution of dominant inorganic arsenic species (As^{III} and As^{V}) varies in natural water. The dominant inorganic species with common valance states of 0, +3 and +5 are present in the aquifer systems. The major controlling factors for its speciation in groundwater are: the pH and redox potential (E_h) [40][41]. In highly oxidizing environment (E_h : 600 to 1200 mV), HAsO_4^{2-} and H_2AsO_4^- are dominant arsenic species in the pH range of 2.0-6.5 and 6.5-11.5, respectively. However, the weaker oxidizing environment (E_h : 0 to

600 mV) and anaerobic environment (E_h : 0 to -800 mV) favours the presence of uncharged $H_3AsO_3^0$ species in natural water [34][42]. Figure 2.1, represents the distribution of arsenic species in the aqueous solution under different pH and E_h conditions is shown below:

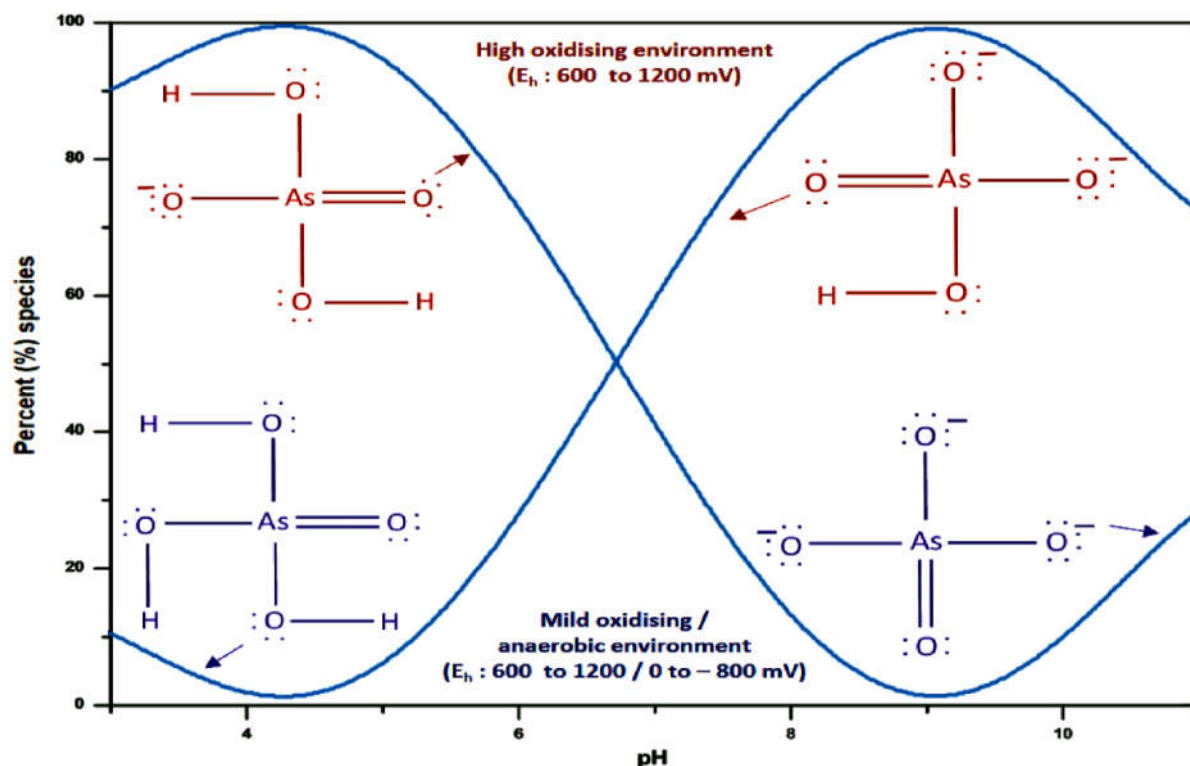


Figure 2.1. Pictorial representation of different arsenic species produced under varied pH and E_h conditions [43].

2.4 Global scenario of arsenic contamination in groundwater

Both developed and developing countries are under a potential threat of problems related to arsenic contaminated groundwater. The countries such as Argentina [44], Bangladesh [45], Brazil [46], Canada [47], Cambodia [48], Chile [49], Ghana [50], Hungary [51], Mexico [52], Pakistan [53][48], Republic of China, Taiwan, United States of America and Vietnam [48] are affected with arsenic contaminated groundwater. In India, the states of Assam [54], Bihar [55], Chhattisgarh [56], [57], Jharkhand [58], Punjab [59], Manipur [60], Uttar Pradesh [61] and West Bengal [62] are reported to have arsenic in groundwater with the concentration exceeding the permissible limit set for drinking water.

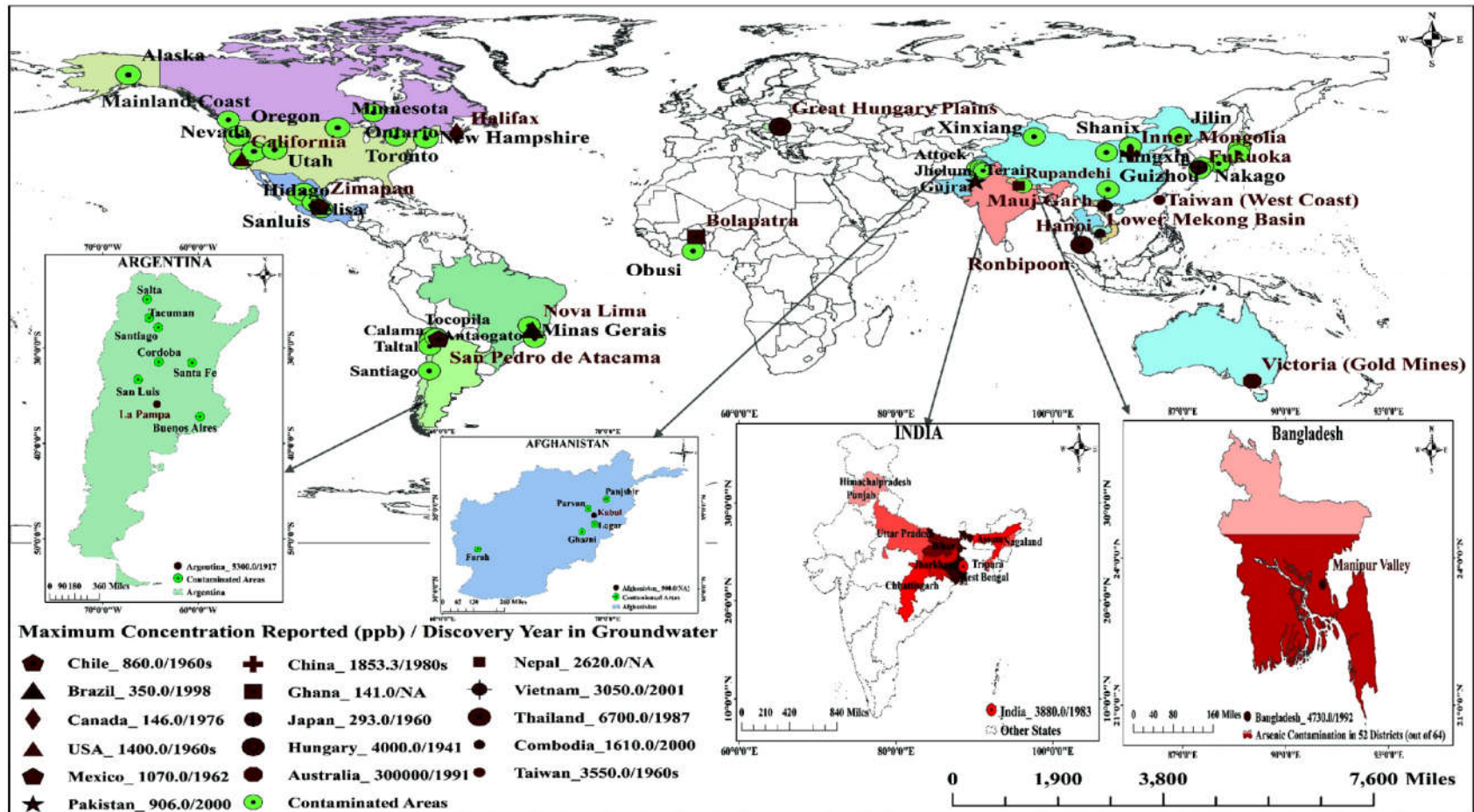


Figure 2.2. Global map of location of different arsenic contaminated groundwater highlighting their respective maximum arsenic concentration in $\mu\text{g L}^{-1}$ along with year of discovery in groundwater [63]–[67].

Figure 2.2 represents the arsenic contamination scenario in groundwater worldwide [44], [48], [63]–[66], [68]–[75] (the data set for several locations were gathered from the published literature which was plotted using ArcGIS, version 10.2.2). The map highlights the arsenic contaminated areas, its year of detection in groundwater along with the maximum concentration reported in the respective countries. It may be interesting to note that one of the first countries to report the arsenic contamination in the groundwater in the beginning of 20th century (1917), was Argentina [44], whereas, in India, its potential health hazards were reported as late as in early 1990s.

A close examination of Fig. 2.2 reveals that maximum concentration of arsenic with the value of 300000 $\mu\text{g L}^{-1}$ has been reported in the gold mining region of Victoria, Australia [69], whereas, the regions of Manipur valley in Bangladesh (4730 $\mu\text{g L}^{-1}$), red river deltaic regions in Vietnam (3050 $\mu\text{g L}^{-1}$), West Bengal in India (3900 $\mu\text{g L}^{-1}$) and loess aquifers of La Pampa Argentina (5300 $\mu\text{g L}^{-1}$) have also been reported with an alarming contamination [76].

2.5 Employed technologies for its removal in groundwater

Several technologies have been developed so far to remove the arsenic from groundwater. However, the most common removal methods which have been widely explored include: oxidation and adsorption [77][78][79][80], chemical precipitation/sedimentation and filtration [81] [82], use of ion exchange resins [83] and membrane technology including reverse osmosis [84]. Recently, the *in-situ* arsenic removal technology using Permeable Reactive Barriers (PRBs) has drawn considerable attention among the research communities and is being practised in few countries. All these methods have been discussed briefly below:

2.5.1 Coagulation/ Flocculation

It involves the mixing of chemicals such as salts of iron (ferric chloride), aluminium (alum) and manganese (manganese sulphate) into water to settle-down the arsenic through precipitation, co-precipitation or combination of both these processes. Afterward, the arsenic is separated from the solution by filtration as it gets adsorbed onto the solid matrix [85]. In general, this approach removes As^{III} as compared to As^{V} , and ferric chloride has been reported to be more efficient than alum. The effectiveness of this method depends on the pH, concentration of arsenic, arsenic speciation and presence of competing ions in the water. However, it requires pre-treatment process to oxidize As^{III} to As^{V} using chlorine or permanganate ions since it causes partial removal of As^{III} from aqueous

solution [86]. Nowadays, solar and microbial oxidation have also been commonly utilized to convert As^{III} to As^V [20].

Although, utilization of ferric chloride has been considered as a useful coagulant to arsenic removal but its characteristics in aqueous phase limit its application for the treatment of arsenic contaminated groundwater effectively. It forms amorphous hydrous ferric oxide (HFO) during hydrolysis which makes it difficult to separate from the treated water. Its separation has been reported to be accomplished through rapid sand filters or micro-filters and sedimentation. However, these types of filtration techniques are economically viable for centralized large scale water treatment systems, but are not suitable for smaller rural areas.

2.5.2 Ion-exchange resins

It is a physio-chemical process involving exchange of ions between solid phase and resin (solid) phase of similar charge. The exchanged ions are held electrostatically on the surface of solid phase with ions of similar charge in a solution. The ion exchange media is usually packed into a column and then water containing arsenic is allowed to pass for removing the desired contaminant. The columns can be regenerated with the brine solution for preparation of next cycle of removal [87].

2.5.3 Membrane processes

In this technique, a semi-permeable membrane has been utilized to separate the arsenic from contaminated water. This membrane acts as a physical barrier to some ions depending on their physio-chemical characteristics. The driving force responsible for the movement of ions across the membrane is the generation of potential difference between the two sides of membrane. The process involved for the arsenic removal depends on the mechanisms of filtration, adsorption of arsenic bearing compounds and electric repulsion [88]. The removal rate of arsenic through this process is affected by shape, size and chemical characteristics of contaminant species. Several membranes have been developed so far for the removal of arsenic, which can be broadly classified into two categories such as high pressure membrane (75-250 psi) and low pressure membranes (10-30 psi). Low pressure membrane includes micro-filtration (MF) and ultra-filtration (UF), whereas, high pressure membrane includes nanofiltration (NF) and reverse osmosis (RO).

2.5.4 Oxidation and adsorption

Oxidation followed by adsorption is one of the conventional methods to treat arsenic contaminated water. Mostly, As^{III} is oxidised to As^{V} using several oxidants, such as chlorine, potassium permanganate, ozone and hydrogen peroxide. Typically, adsorption involves passing of contaminated water through a packed media to which arsenic get attached *via* physical or chemical bonds. The common adsorbents that have been reportedly employed in the field include granular ferric hydroxides, activated alumina, iron coated sand and activated carbon with surface modifications [89], [90].

2.5.5 Relevance of adsorption technology

The above mentioned removal methods have been reported to have the disadvantages in terms of generating highly toxic waste that causes its easy mobilization in the living ecosystems. Arsenic removal through coagulation/flocculation requires addition of chemicals and thereafter removal in the form of precipitates after the completion of process. This serves as one of the drawbacks of this technology. Also, there are the possibilities of generation of secondary pollutants in treated water, which may cause diseases related to these pollutants. Moreover, the technologies such as ion-exchange and membrane processes have limitations in terms of their higher energy consumption, higher costs and complex removal mechanisms.

Among the above mentioned removal methods, arsenic removal by adsorption has still gained considerable attention even considering its limitation in handling toxic waste after the exhaustion of adsorbed material. It is widely acceptable technology as on today due to its easy operation, less maintenance cost, and cost effectiveness [91]. Generally, the formation of two types of surface complexes have been considered responsible between adsorbate and adsorbent. These are represented such as monolayer and multilayer adsorption and shown in Figure 2.3. The literature is also replete in providing several reviews highlighting a number of adsorbents for arsenic removal in groundwater, which involve the use of naturally originated, synthetic adsorbent materials and low cost materials [78][92][93][94]–[100]. In recent years, a number of nano-adsorbents such as nZVI alone [101] supported on clay, tea waste, polyaniline and starch [102][103][104]; oxides of iron [105][106][107]; titania as anatase [108][109]; cerium^{IV} oxide [110][111]; copper [112][113]; polymer based adsorbents [114][115] including the sulphides of iron [116] and zinc [117] have been explored for arsenic removal.

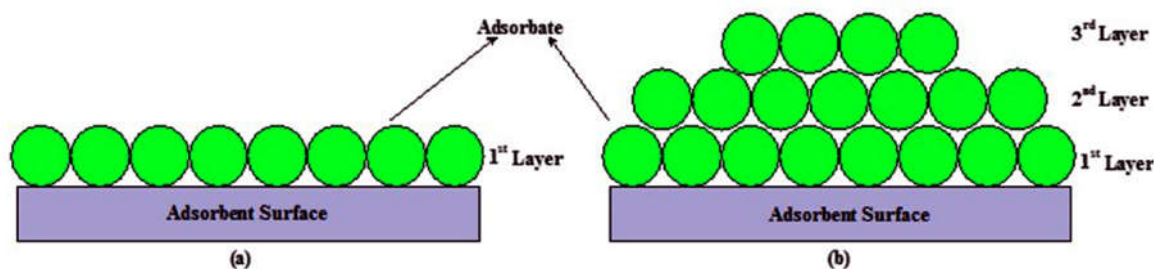


Figure 2.3. Overview of molecular models depicting molecular models (a) Monolayer adsorption (b) Multilayer adsorption [118].

However, the development cost of nanoadsorbents is a research concern to make their usage feasible in real world application because of their requirement in large quantities. Efforts are being made across the globe to develop more efficient, economic and environmental friendly adsorbents.

2.6 *Ex-situ* mode of remediation technique

Several authors have reported that the above-surface (pump-and-treat) treatment of As contaminated groundwater using a variety of processes such as chemical precipitation, adsorption, ion-exchange and filtration [119].

2.6.1 Adoption of technology at rural scale

In order to fulfil the requirement of arsenic free drinking water for densely populated countries such as India and Bangladesh, adoption of the technology at rural scale in a convenient, economic and effective manner is a challenging task among the scientific communities. Several conventional technologies with modifications have been reported to be accomplished in rural and remote areas to provide safe drinking water [120][121]. These technologies have been generally classified as: household treatment systems or community based treatment systems. A brief description of these technologies is presented below:

Aeration, boiling of water, sand filters, ceramic filters and oxidation using solar light are among the typical methods of household treatment systems, where contaminated water is treated from a single source and utilized for livestock's purposes such as cooking and drinking [122][123]. Whereas, in community based treatment systems, many households invest money as a society and make a single treatment unit. The advanced and costly methods for the treatment of arsenic contaminated groundwater are not affordable to most of the populations in the world [124]–[126].

Therefore, the focus of this research also describes the development of arsenic remediation materials by utilizing industry waste as precursor material, which might present a sustainable approach to upgrade the existing arsenic removal units by providing indigenously generated nanoadsorbents.

2.6.1.1 Domestic or household treatment systems

This type of technology was developed to provide arsenic free water to the poor people. Many developing countries are unable to afford centralized treatment methods for arsenic remediation; therefore, different types of economic treatments have been developed. Among these, the Bucket Treatment Units (BTU), Sono-filters and Bio-sand filter are quite common.

Bucket treatment unit is based on the arsenic removal processes such as coagulation, co-precipitation and adsorption. It consists of two buckets placed one above another. From the top, the arsenic contaminated water is poured along with the mixing of alum (as a flocculant) and potassium permanganate (as an oxidizing agent). This mixture is allowed to settle after stirring for a couple of minutes. Then, the settled water is passed to lower bucket through the pipe attached to lower end of upper bucket [127], [128]. The arsenic free water is collected from the lower part of the bucket after passing through sand filter. The obtained aluminium-arsenic complex can be removed by filtration process at the end of remediation process.

Sono-filters is an another simpler household technique which involves the process of oxidation, precipitation, adsorption and filtration during removal of arsenic [129], [130]. It consists of top and middle pots as reactors along with lower one as storage pot for treated water. The layers of polyester cloth, coarse sand, iron chips; and polyester cloth, fine sand, charcoal are placed as removal material medium in top and middle pot of the filter system respectively. This approach has been reported to be quite efficient for arsenic removal in the pH range of groundwater which involves surface complexation reactions mechanisms.

Arsenic bio-sand filter (ABF) is among the one of most effective and economical technology adopted for arsenic removal to provide drinking water in rural areas [131]. It consists of two layers such as pathogen removal unit (PRU) and ATU (ARU) representing lower part and upper part of filter system, respectively. These parts are equipped with iron nails, polyester cloth, metal diffuser box and fine sand, coarse sand, gravels as components of ARU and PRU, respectively.

This filter works on the principal of arsenic removal through adsorption onto iron hydroxides and slow sand filtration mechanism [132]. The formation of iron hydroxide particles responsible for arsenic adsorption is produced after the oxidation of iron nails in the presence of air. Then, arsenic

loaded water is allowed to pass through underlined sand filter to acquire potable water. Further, the PRU unit is considered to remove the pathogens by steps such as mechanical trapping (occurs due to entrapment of pathogens along with sediments in the space between the consolidated material), adsorption (attachment of pathogens to sediments and each other), predation (consumption due to already existing microbes in bio-films layer) and natural death due to scarcity of food.

2.6.1.2 Community based treatment systems

In rural areas, many people consume water from common tube-wells and hand-pumps. To provide safe drinking water, arsenic treatment unit (ATU) is generally attached to water source which is operated with an intermittent flow of water. Generally, the conventional treatment is done through the processes such as mixing of chemicals, flocculation, sedimentation and filtration [133], [134]. In the first stage, sodium hypochlorite and alum are added to the arsenic infested water for the oxidation and coagulation, respectively. In the second stage, the mixing of these chemicals leads to the formation of flocks containing arsenic, which is followed by sedimentation and filtration to get arsenic free water. Nowadays, this mode of conventional treatment has been occasionally modified by utilizing the nanoscale based absorbents as remediation material.

2.7 *In-situ* mode of remediation technique

2.7.1 Technology advantages

Sub-surface remediation of contaminant of organic volatile pollutants has been considered an environmental friendly approach in terms of its attenuation and release to the atmosphere [135], [136]. Similarly, the treatment of arsenic contaminated groundwater in subterranean environment (below surface) is a logical choice in respect to reduce the chance of its mobilization in living environment. *In-situ* treatment has been considered more environmental friendly, cost-effective and reliable as compared to *ex-situ* mode of treatment [137]. Developing a better understanding about *in-situ* remediation methods and further improvement appears to be more rational and relevant choice now rather than to improve the already developed conventional techniques. Some recent methods explored for the removal of arsenic in sub-surface environment are discussed further.

2.7.2 Methods of treatment

2.7.2.1 Permeable reactive barriers (PRBs)

In early 1990s, permeable reactive barriers (PRB's) made use of zero valent iron, iron work slags materials. An overview is shown in the Figure 2.4. Initially, ZVI has been applied in permeable reactive barrier (PRB's) system for the remediation of groundwater [138]. In this approach, multiple functional barriers were employed for the remediation of arsenic from groundwater [139]. The system was widely explored for the remediation of both As^{III} and As^V due to its easy availability and environmental friendly characteristics.

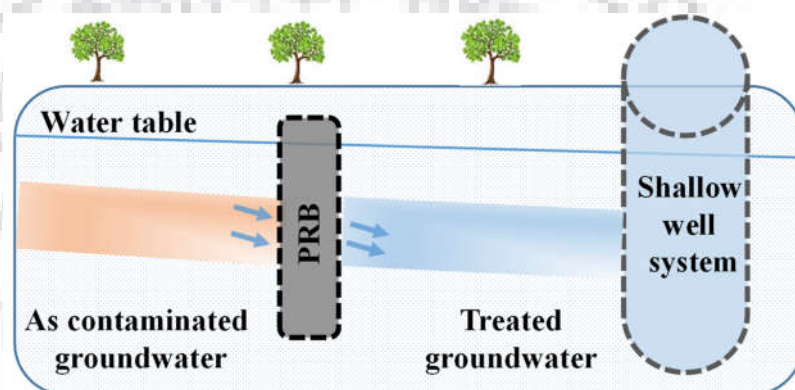


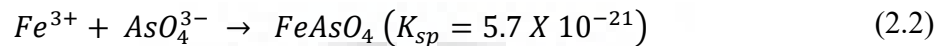
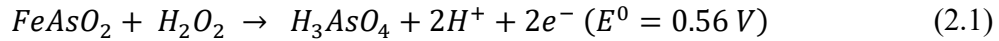
Figure 2.4. An illustration of PRB based technique representing remediation of arsenic in shallow groundwater system [140], [141].

In recent years, the nanoscale zero valent iron (nZVI) has been explored in PRB system and is considered as an extension of conventional ZVI technology [139], [142]. In subsurface environment, nZVI has proved as one of the most popular adsorbent for the removal of dominant arsenic species as compared to micrometre size iron [22].

2.7.2.2 *In-situ* chemical treatment

Generally, it involves the direct injection of oxidants to the sub-surface such as $KMnO_4$ or oxygen which promotes the oxidation of As^{III} to As^V , and then the co-precipitation of As^V from iron oxides. In this process, the chemical oxidant is injected in an aquifer upstream of the contaminated site and a closed loop can be generated by pumping of water in the downstream site to utilize it for reinjection. The reaction between injected chemical and the contaminant inhibits the mobilization of arsenic in aquifer systems. The most efficient chemicals injected into aquifer are hydrogen peroxide and ferric chloride [143]. Both of these chemicals have to be injected sequentially because

the oxidation by hydrogen peroxide is a rapid process. The oxidation and precipitation reactions included in this process are:



Where, E^0 is standard electrode potential and K_{sp} is solubility product constant. Ipsen *et al.* [144] have utilized this technology for the remediation of a contaminated site in Tacoma, Washington, USA, where contamination of arsenic in groundwater was caused by sodium arsenite.

2.7.3 Concern associated to technology

Although, Permeable reactive barriers (PRBs) have been proved to offer a promising technology as compared to the conventional mode of treatment methods for arsenic removal, but there are still significant limitations which occur due to geochemical and physical characteristics of contaminated sites [145]. The major limitation is the lack of information on the long-term effectiveness of large-scale remediation systems. Therefore, it has not been yet approved by USEPA till now.

The PRB based treatment requires to study the effects of aging of the reagent, decrease in permeability due to precipitation, microbiological growth and accumulation of gas and evaluating the long term performance which cannot be predicted in short-term laboratory experiments [146][147]. Also, the literature has not been updated about the possible issues which may take place during the elimination process of system media after its exhaustion. Further, the injection of the dissolved phase of remediation materials (iron salts) in aquifer systems may cause the generation of secondary pollutants due to their possible chemical reactions with other ions. The possibility of recontamination due to dissolution of the compounds is also a concern in this application [101].

2.7.4 Scope for future studies

The installation of PRBs requires the process of excavation for the remediation of arsenic, which is viable to treat the shallow aquifers systems (such as wells) effectively, where the source of

arsenic is well defined. Figure 2.5 presents a pictorial representation demonstrating an approach of nanomaterial injection in deep aquifer systems displaying a distributed source of arsenic.

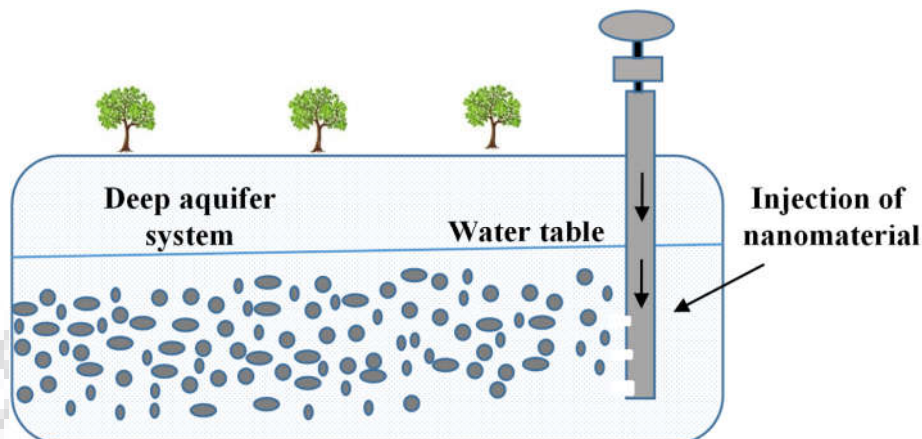


Figure 2.5. An overview of injection based technique representing remediation of arsenic in deep aquifer system [148].

Future research could be useful in exploring the utilization of colloidal or sub-colloidal iron or iron nanoparticles for injection as substitutes for using iron salts [149]. In this method, the injection of nanomaterials creates a reactive which further sequester the arsenic through different removal [150]. It also requires in depth analysis of fate and transport of nanomaterials in porous media as well as possibilities of secondary pollution. Moreover, injection of materials may be done through exiting deep wells or abandoned wells, in which the reactive material may be introduced.

2.8 Metallic nanoadsorbents for arsenic removal

The literature demonstrates the development of several types of metal based inorganic nanomaterials, which have been investigated for arsenic removal from an aqueous solution. Broadly, these inorganic nanomaterials can be categorized into different groups such as iron, titanium, aluminium, zirconium and cerium, zinc and copper. A brief description explaining their structural behaviour and stability characteristics are discussed in brief below:

2.8.1 Ti, Al, Zr, Ce, Zn and Cu based nanomaterials

Anatase, brookite and rutile are common polymorphs of titanium dioxide which have been reported to be explored for arsenic. These have been considered as significant nanomaterials for the environmental applications due to their non-corrosive, non-toxic and chemically stable properties

[151]. The anatase and brookite are metastable phases and their conversion to rutile at high temperature has been extensively reported. Considering the adsorption capabilities, their efficiency has been observed to depend on the surface structure, crystallinity, particle size and the surface energy [152]. Among these, high removal efficiency of their amorphous form has been reported, which is ascribed due to their large surface area and disordered structure. Moreover, its amorphous is capable to oxidize the arsenite, possibly due to the presence of surface or adsorbed O_2 and high surface hydroxyl groups, and the mechanism is shown in Figure 2.6.

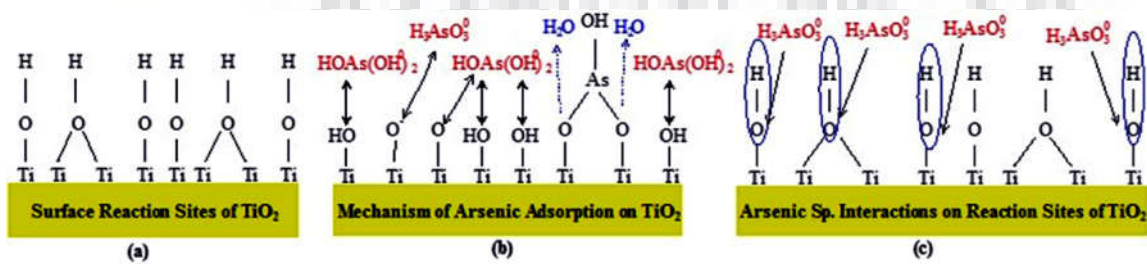


Figure 2.6. Schematic showing mechanism adsorption of arsenic by nanoscale titanium oxides [108].

Alumina is an important adsorbent as it acquires excellent physical and textural properties comparable to those of other transitional metal oxides [153]. It has been found in several industrial wastes such as blast furnace slag, coal combustion ash and water works sludge. The nanostructures of these nanoparticles reported to have poorer adsorption capacity for the arsenic removal compared to those of iron(oxy) hydroxides and TiO₂ nanoparticles [78][154].

Nanoscale zirconia and ceria based nanomaterials have demonstrated an adequate affinity for As^V due to which it has been explored for arsenic treatment [155] [156]. These have been considered as suitable adsorbents for field scale applications due to their stable characteristic features [45]. Various polymorphs of zirconium oxides have been reported in the literature exhibiting monoclinic (*P2₁/c*), tetragonal (*P4₂/nmc*) and cubic (*Fm₃m*) These exist in equilibrium at different temperatures as shown in Figure 2.7 (a-c). The noticeable change during the transformations among the polymorphs is demonstrated in Figure 2.7(d). Further, a major group of metallic nanoparticles needs a pre-treatment step for the oxidation of As^{III} to As^V and/or post pH adjustment of treated water during the removal process using adsorption [157][158]. Therefore, it is advantageous to develop the adsorbents having potential for As^{III} removal effectively without pre-oxidation step and post adjustment of pH in the treated solution [159]. These nanoparticles have been reported to qualify in this respect.

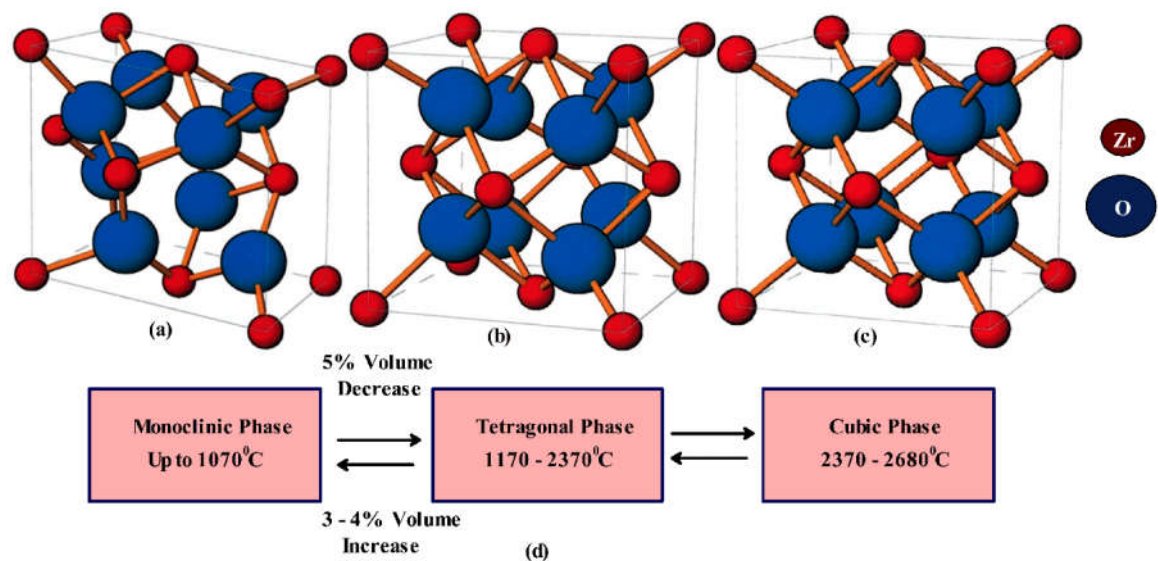


Figure 2.7. Picture representing crystal structure phases of zirconium oxides nanoparticles (a) monoclinic (b) tetragonal (c) cubic [160].

The polymorphs of metallic zinc nanoparticles such as ZnO and ZnS have been explored for the removal of arsenic. The structural stability of ZnS at nanoscale is sensitive to natural environmental conditions due to their ability to adsorb water and aggregation characteristics [161]. However, ZnO nanoparticles are slightly stable in comparison to ZnS nanoparticles, having capability to receive several structural conformations by forming nanowires [162] and nanobelts [163]. Copper oxide(s) are other class of nanomaterials which do not require pre-treatment and post pH adjustments during adsorption. It has two types of polymorphs: Cu^I oxide and Cu^{II} oxide. Lastly, the bulk Cu₂O is known to get oxidised into CuO at ambient conditions, however, nanostructured Cu₂O has been observed to be fairly stable [164].

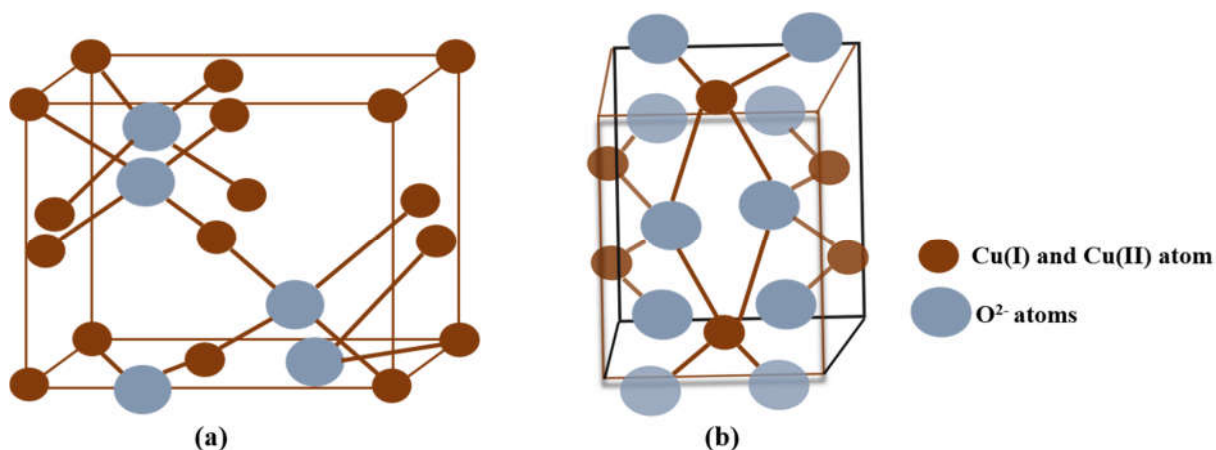


Figure 2.8. Picture representing crystal structures phases of (a) Cu^I (b) Cu^{II} oxides nanoparticle [165].

2.8.2 Fe based nanoparticles

Among the several polymorphs of iron, the nanoscale zero-valent (nZVI), iron(oxy) hydroxides (α -FeOOH and β -FeOOH) and iron^{II,III} oxides (magnetite) nanostructures are discussed in this section.

2.8.2.1 Nanoscale zero valent iron (nZVI)

It is a widely explored phase among the iron based nanomaterials utilized for arsenic removal through both *ex-situ* and *in-situ* treatment processes. As compared to bulk, its nanosize does not only enhance the surface area [166], but the high intrinsic activity of these nanoparticles deliver the high density of reactive sites to the contaminant for electrostatic interactions [167], [168]. These nanoparticles are composed of Fe⁰ atoms as a nucleus and outer layer of mixed phase of iron oxide(s) [169]. Various environmental factors such as oxygen content, pH, pE and concentration of trace elements present in natural water have been reported to affect the structural configuration and variations in the outer layer thickness of these nanoparticles [169], [170]. Such a core-shell formation delivers a series of removal mechanisms by forming outer and inner sphere complexes, after the significant interactions between arsenic species and outer surface functional moieties. [170]–[172]. Generally, the arsenic removal mechanism of bare nZVI involves the precipitation, co-precipitation, oxidation and reduction reactions as have been suggested by a number of authors earlier [169], [170], [173], and is shown in Figure 2.9.

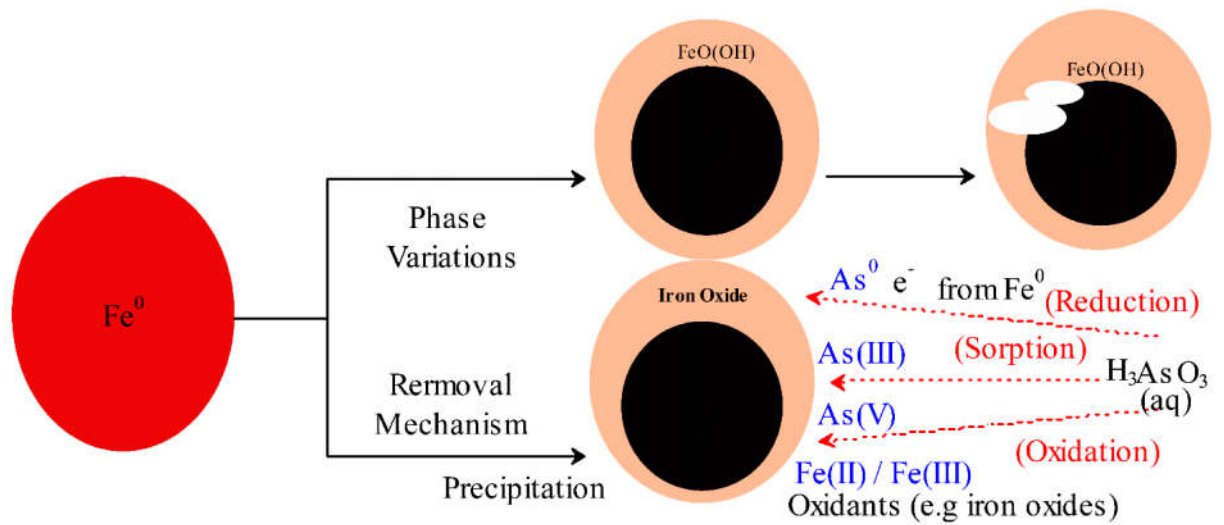


Figure 2.9. Schematic showing redox reaction of arsenic on nZVI [173].

2.8.2.2 Di-valent iron nanostructures

The common nanostructured phases of divalent iron such as: FeO (wustite) and FeS (mackinawite, troilite) are reported in the literature. The wustite have a defect rock salt structure ($Fm3m$), ordered iron vacancies and nonstoichiometric phase (as shown in Figure 2.10 a), which exhibit the substantial stability above $560\text{ }^\circ\text{C}$ [174][175][176]. Below temperature $560\text{ }^\circ\text{C}$, it is unstable and prone to decompose into hematite ($\alpha\text{-Fe}_2\text{O}_3$) and magnetite (Fe_3O_4) after oxidation [176][177][178][179]. It has been revealed that the phase transformation occurs due to the chelation of iron with oxygen atoms to satisfy the octahedral coordination (crystal field stabilization). But, its nano hybrid structures have been found to be stable under ambient conditions, unlike their bulk counterpart [174], [180]. Moreover, due to unstable structure of bare wustite, it has not been explored widely, specifically, for the removal of arsenic from the natural water.

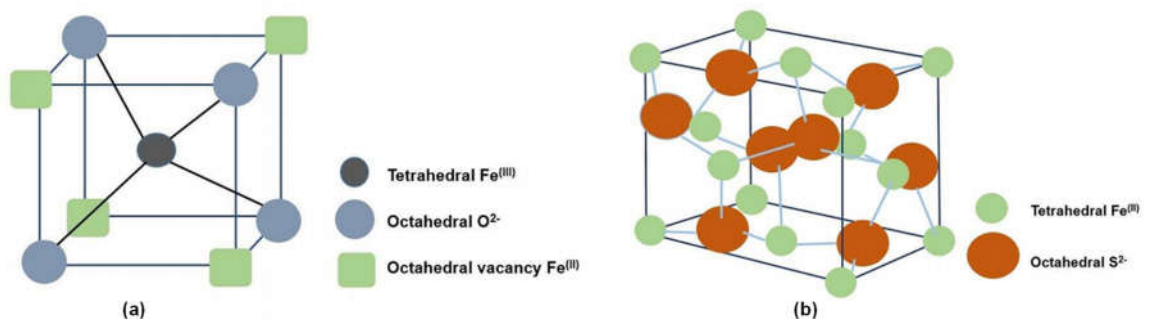


Figure 2.10. Crystal structure of divalent iron^{II} compounds a. Wustite b. Mackinawite [181].

The polymorphs of iron^{II} sulphide such as troilite, mackinawite and metastable iron sulphide have been reported in the literature. Their crystallites have hexagonal ($P6_2c$), tetragonal ($P4_nmm$) and cubic ($F4_3m$) structures, respectively. The nanostructured troilite has been considered to be stable in comparison to mackinawite, which transforms into greigite after oxidation under natural environmental conditions. Few authors have explored the mackinawite phase by incorporation it into the sand for arsenic removal. These phases have been found effective in the removal of As^{III} under anoxic conditions. However, nanostructured divalent iron polymorphs have not been widely reviewed for the removal of arsenic due to their unstable nature.

2.8.2.3 Iron^{II,III} oxides nanostructured phases

Magnetite is a predominant constituent of the subsurface environment [182]. Its crystal structure exhibits an inverse spinel structure with a unit cell of 8 Fe^{II} cations, 16 Fe^{III} cations and 32 O²⁻ anions. The unit cell $[(Fe_8^{3+})_{tet} (Fe_8^{3+}Fe_8^{2+})_{oct} O_{32}]$ contains half of the Fe^{III} ions coordinated tetrahedrally, the remaining half and Fe^{II} ions are octahedrally coordinated. (Figure 2.11). It is unstable in aerobic environment due to the presence of reduced form of iron and oxidizes to maghemite [183]. This phase has been found to be more efficient for the arsenic removal as compared to extensively explored bare zero valent iron nanoparticles [184].

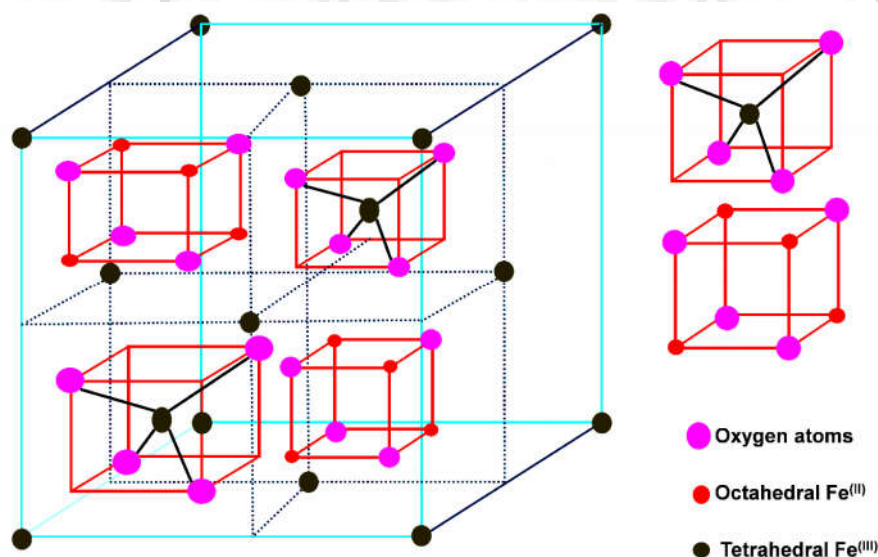


Figure 2.11. Crystal structure of magnetite nanoparticles [185].

Its nanoparticles are reported to have fairly high magnetization value of 30-50 emu g⁻¹ [186]. This characteristic makes it easy to harvest and separate by applying low intensity magnetic field after the completion of adsorption process, as is also desirable for large scale water decontamination treatment processes [187][188]. An illustration explaining the mechanism of arsenic removal under aerobic and anaerobic conditions are shown in Figure 2.12. The literature has been reported with different polymorphs of iron oxy (hydroxides) having different types of properties. Its nanostructured phases have been reported to have affinity for the removal of contaminants such as cations (heavy metals), anions, oxyanions and organic [189]. But, the phases such as goethite (α -FeOOH) [190][191], akaganeite (β -FeOOH) [192], lepidocrocite (γ -FeOOH) [193] and δ -FeOOH [194] have been explored for the remediation of arsenic. These may bind anions through both covalent and hydrogen bond [195][196]. Since, iron oxides phases have hydroxyl group through which remediation has been explored.

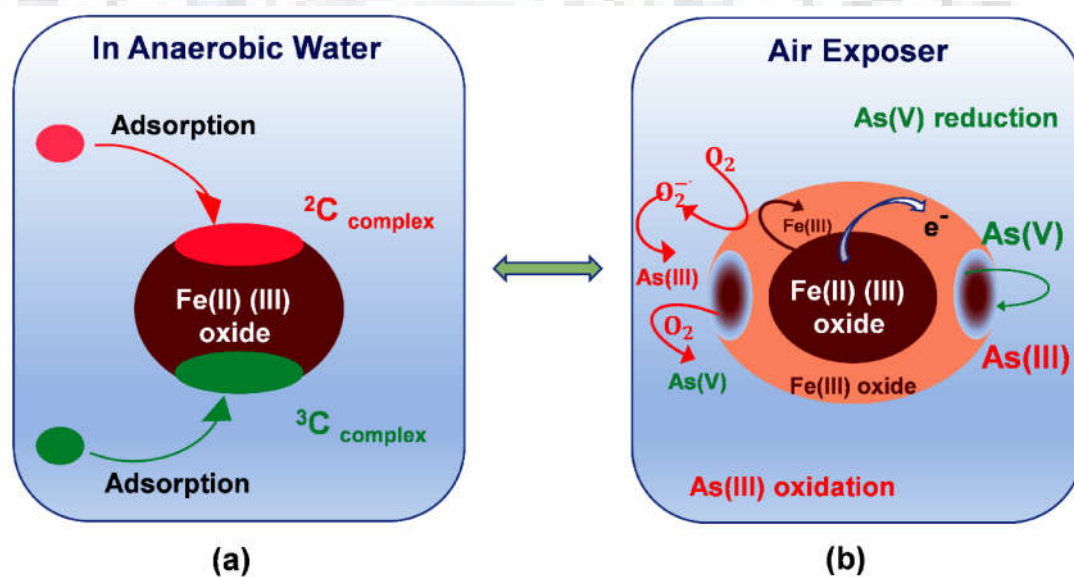


Figure 2.12. Schematic showing the proposed redox reactions on the surface of magnetite nanoparticles during adsorption under (a) anoxic (b) oxic environment [197], [198].

2.8.2.4 Iron(oxy)hydroxides nanostructured phases

γ -FeOOH is a predominant and highly reactive phase which occurs as ore deposits, sediments and terrestrial soil [199][200]. It has hexagonal closed-packed structure with Fe^(III) in the octahedral interstices and surrounded by O²⁻ along with formation of zig-zag chains of OH⁻ between the oxygen planes [201]. However, its orthorhombic structure (space group, *Pn/ma*) has been

reported to have the edge sharing linkage between double chain octahedra in which three OH⁻ and three O²⁻ are present across each Fe ion. The vacant sites are located between the Fe occupied double chain rows, and considered as false tunnel like structures [202].

β -FeOOH is known as akaganeite and occurs in the soil as natural component, geothermal brines and as a corrosion product of steel and iron bearing meteorites [202]. It has been found isostructural with hollandite Ba(Mn⁴⁺₆Mn³⁺₂)O₁₆ and its unit cell has been reported with monoclinic (space group, *I2m*) [203]. This phase is less dense due to the body-centred array arrangement of anions in comparison to the *hcp* (hexagonal close packing) or (*ccp*) cubic close packing structures of iron oxides/hydroxides. However, disparity of the agreement related to its space group among scientific communities has been discussed by Gracia [204]. Its basic structure has double chains of Fe^(III)[O,OH] (edge-shared) octahedra [205], and the compensation of charge occurs through the substitution of cations into octahedral sites.

The nanostructured β -FeOOH has been considered as having a true tunnel like structure along with the single row of anions missing in the unit cell [206]. The presence of tunnels like formation has been considered to be responsible for its efficient adsorption capabilities, providing large surface area and reactive sites. It is reported that these nanostructures have not been extensively employed as an adsorbent for arsenic removal under varied experimental conditions of pH and real water conditions; and need systematic investigations. Further the γ -FeOOH and δ -FeOOH have not been reportedly investigated for arsenic removal.

2.8.2.5 Iron^{III} oxides nanostructured phases

The nanostructured iron oxides containing iron in trivalent state such as: hematite (α -Fe₂O₃), beta phase (β -Fe₂O₃), maghemite (γ -Fe₂O₃) have been investigated for various environmental applications [207][208][209][210]. The adsorption data recorded on these polymorphs used for the removal of As^{III} and As^V have been summarised in Table 2.1, and each individual phase is discussed below in brief.

Hematite (α -Fe₂O₃) is a common, thermodynamically stable and reactive environmental sorbent which plays an important role in contaminant removal from groundwater aquifers and soils [211]. It has a distorted hexagonal closest packed structure (space group *R3c*) with iron occupying 2/3rd of octahedral holes. The nanoparticulate structure has been found thermodynamically metastable under ambient environment due to its high surface energy or surface enthalpy [212]. It has been revealed

that the anion substituted protohematite phase is formed when O^{2-} is partly replaced by OH^- , which is accompanied by the creation of Fe^{III} vacancies to provide charge balance. Furthermore, it has been demonstrated that the disparity in the hydroxylated surfaces of metal oxides are likely to be a crucial factor for influencing the different environmental reactivity [213][214]. The two hydroxyl moieties such as: singly $[(OH)_3-Fe-Fe-R]$ and doubly $[(OH)_3-Fe-H_3O_3-R]$ coordinated hydroxyls with iron have been reported for $\alpha-Fe_2O_3$ [215]. However, the double coordinated surface hydroxyls has been reported to be particularly stable and unreactive [216]. Further, Trainor *et al.* [215] has demonstrated that the singly and triple coordinated hydroxyls are more reactive towards cationic species due to their efficient proton lability.

Beta phase ($\beta-Fe_2O_3$) is rare with scarce abundance in nature and only stable at nanoscale dimension [217][218]. It shows bixbyite type body-centered, cubic crystal structure (space group $Ia\bar{3}$), two non-equivalent sites occupied by Fe^{III} ions with no vacant position remaining [217][219][220]. The preparation of its monophasic phase is quite difficult [218] and might be a responsible factor, due to which it has not been investigated for the removal of arsenic.

Maghemite ($\gamma-Fe_2O_3$) is the second most stable polymorph of iron oxides. In bulk, it is metastable relative to $\alpha-Fe_2O_3$, but the nanostructured $\gamma-Fe_2O_3$ has been found to be more stable than hematite, peculiarly under dry environment [221]. It exhibits the cubic crystal structure (space group $Fd\bar{3}m$) with each cell contains 32 O^{2-} ions, $21^{(1/3)}$ Fe^{III} ions and $2^{(1/3)}$ vacancies. Crespo *et al.* [222] has reported that the cationic vacancies are located in the octahedral sites, however, their degree of ordering is a concern of investigation from past few decades. Somogyvari *et al.* [223] and Jorgensen *et al.* [224] have reported its transformation from cubic crystal structure into spinel tetragonal structure which results in complete ordered arrangements of iron atoms.

2.9 Maghemite nanoparticles

2.9.1 Bare and functionalized nanostructures

Different methods have been used for its synthesis such as physical and sol-gel [225], chemical [226][227][228][229][230], DF and IDF [231], and hydrothermal [232][233]. Some of the important studies are tabulated in Table 2.1. Yang *et al.* [233] have demonstrated the impregnation of non-aggregated $\gamma-Fe_2O_3$ nanoparticles using hydrothermal method into the pores of macroporous siliceous foam (MOSF) of large dimension (~ 100 nm) and high volume. The porous foam was synthesized using supra-assembly approach which involved the utilization of non-ionic block

polymers. The implantation of non-aggregated nanoparticles has been attributed to the homogenous distribution of trinuclear iron^{III} complex as a precursor material on the walls of MOSF.

Recently, the synthesis of bichar impregnated maghemite nanoparticles using corn straw employing thermal pyrolysis method has been reported by He [234]. But, these nanostructures exhibited poor adsorption capacity 6.8 for As^V. It has been considered that this may be due to the inappropriate dispersion of precursor material (FeCl₃·6H₂O) into fine pore structures of corn straw.

Among discussed methods, the surface area of these nanoparticles are observed to follow the order: IDF > mechanochemical > chemical > sol-gel > DF. The γ -Fe₂O₃@MOSF (macroporous siliceous foam) nanocomposites have been synthesized by loading different percent amount of γ -Fe₂O₃. A significant reduction in the pore volume (1.57 to 0.49 cm³ g⁻¹) and surface area (250 - 155 m² g⁻¹) has been observed by the incorporation of γ -Fe₂O₃ nanoparticles from 11.8 to 34.8 wt % in the MOSF. This nanocomposite has been observed to have the maximum adsorption capacity (mg g⁻¹) 320 and 248 for As^{III} and As^V respectively, achieved within a short contact time (10 min). These data revealed that the adsorption capacity is largely contributed by the effective dispersion of nanoparticles in the macropores without blocking the open pore network of the silica matrix. However, the adsorption capacity () of its monodispersed bare γ -Fe₂O₃ nanostructures has been observed as 108 mg g⁻¹ for the removal of As^V by Martina [227]. For the concentration ratio of Fe/As (20:1), the removal efficiency of 100 % has been observed for both As^{III} and As^V. The possible mechanisms of arsenic removal in engineered magnetite are shown in Figure 2.13. Tuttijarvi *et al.* [225] have examined the adsorption capacity (mg g⁻¹) of As^V using various samples of γ -Fe₂O₃, synthesized mechano-chemically from the bulk samples and by sol-gel methods. Further, these have been compared with the commercial available samples having particle size of 3.8, 12.1 and 18.4 nm, respectively. For these samples, they have observed the adsorption capacity (mg g⁻¹) as 50, 25 and 16.7, which showed a direct correlation with the particle size. The highest adsorption capacity has been demonstrated by the smallest size particles obtained by mechano-chemical method.

Recently, a bifunctional nanocomposites demonstrating the photocatalytic ability of anatase for oxidation of As^{III} and their utilization for adsorption characteristic has been examined by Yu *et al.* [229]. The anatase phase was found not to be incorporated into the crystal structure of maghemite nanoparticles.

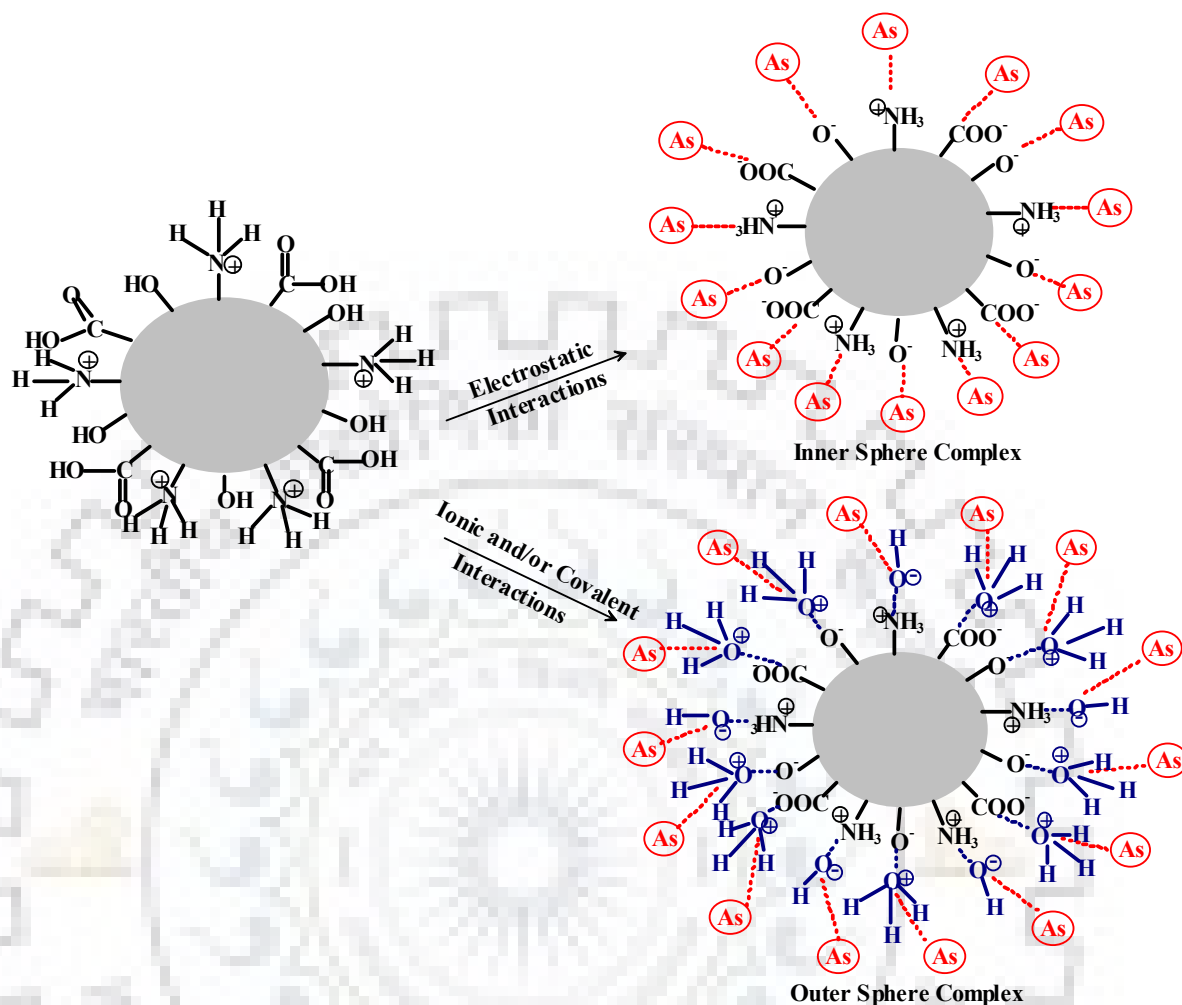


Figure 2.13. The schematic represents the occurrence of possible electronic interactions and type of adsorption on the surface of engineered nanoadsorbents [235].

2.9.2 Scope of development

The stable characteristics of maghemite nanoparticles in a wide range of environmental conditions is expected to be extremely helpful during field scale applications. Also, this phase has not been reported to be widely explored for arsenic removal till date. The presence of cationic vacancies in their crystal structure helps in providing efficient interactions between the nanoparticles and arsenic species. This phase is considered as an efficient adsorbent due to its large surface area and rapid separation after adsorption from the aqueous solution under an external magnetic field. Therefore, further studies might be conducted for synthesizing its nanohybrids using bio-templates and organics to support them on the different matrices so as to overcome its limitation of dispersion and stability in the aqueous medium.

In this regard, a novel and techno-economic approach is being explored for the synthesis of maghemite nanohybrids by the incorporation of raw distillery waste as one of a precursor material, as, over the decades, the cost-effective generation of nanoadsorbents on one hand as well as management of distillery waste on the other have been a concern among the scientific communities. Employing distillery waste also takes care of the issue of stable and bulk production of nanoparticles for their usage in pilot scale remediation applications, considering distillery as one of the most widespread industries in India and in many other countries.

The raw waste of distillery industries is rich in organic components such as: oligosaccharides and polysaccharides (starch, cellulose, hemicellulose and lignin). Under strong alkaline conditions, these have capabilities to form reducing sugars with different compositions. The utilization of industrial waste as a precursor material for the synthesis of nanohybrids led to the encapsulation of functional groups on the iron nanoparticles surface having different characteristics.



Table 2.1. Comparison of experimental protocols and arsenic remediation attributes of maghemite nanoadsorbents.

Nanopowder Composition	Primary Materials	Synthesis Method	Removal Species	Temp. / pH	Particle Size (nm) / Surface Area (m ² g ⁻¹)	Reaction Kinetics, Adsorption Isotherm	Removal Method	Initial conc./ Range (ppm)	Dose (g/L)	Adsorp. Capacity (mg g ⁻¹)	Adsorp. / Desorp. Effi. (%)	Reference
γ -Fe ₂ O ₃ / Silica	Fe(NO ₃) ₃ .9 H ₂ O, TMOS	Chemical	+5,+3	25 / 6-10	2-12 / 155	Pseudo 2 nd order,	Batch	(+3) 0.1-560, (+5) 0.1-600	1	(+3) 320 (+5) 248	(+3)88 (+5)98 /ND	[233]
Ultrafine Mg _{0.27} Fe _{2.5} O ₄	FeCl ₂ and MgCl ₂	Solvo-Thermal	+5,+3	25 / 7	3.7 / 438.2	Pseudo 2 nd order, Langmuir	Batch	0.1	0.02	(+3) 127 (+5) 83	100/ 90	[236]
Ultrafine γ -Fe ₂ O ₃	FeCl ₂ .4H ₂ O FeCl ₃ .6H ₂ O	Chemical	+5	25 / 5-7.6	4 / 100	Freundlich	Batch	100	0.3-2.15	64-108	33-100/ ND	[227]
α -Fe ₂ O ₃ / Rutile@ Graphene	Fe(NO ₃) ₃ .9H ₂ O C ₁₂ H ₂₈ O ₄ Ti	Chemical	+5,+3	RT/ 6-7	20-45/ 275.23	Langmuir	Batch	3-80	0.2	(+3)99.5 (+5)77.7	ND/ ~89	[237]
γ -Fe ₂ O ₃	FeCl ₂ .4H ₂ O, FeCl ₃ .6H ₂ O	Chemical	+5,+3	30 / 3-11	7-12 / 168.73	Pseudo 2 nd order, Langmuir	Batch	100	ND	(+3) 67 (+5) 95	ND / 40	[226]
Ultrafine α -Fe ₂ O ₃	FeCl ₃ .6H ₂ O	Solvo-thermal	+3	25 / 7	4-5 / 162	Langmuir, Freundlich	Batch	0.115	0.04	95	98.3/85	[238]
Mesoporous γ -Fe ₂ O ₃	FeSO ₄ PFR HMTA	Hydro-thermal	+5	RT	35.7/ 3.6	Langmuir	Batch	1-80	0.1	73.2	ND	[232]
γ -Fe ₂ O ₃ -TiO ₂ / ceramic	TiO ₂ and Fe ₂ O ₃ powders	Chemical	+5,+3	RT/ 7± 0.5	2-3 mm/ 62.8	Pseudo 2 nd order,	Langmuir Freundlich	5-50	2	(+3) 67.02 (+5) 95.37	>90/ ND	[230]
α -Fe ₂ O ₃	FeCl ₃ (anhy.)	Chemical	+5	RT	5.5/ 18	Langmuir DR model	Batch	2-30	0.5-2	38.48	ND	[239]
α -Fe ₂ O ₃ / Activated Carbon	FeCl ₃ .6H ₂ O	Micro-wave	+5	25 / 7	55-60 / 135	Pseudo 2 nd order, Langmuir, Freundlich, SIPS	Batch	0.5-20	0.75	27.78	99.9/ ND	[240]
γ -Fe ₂ O ₃ -TiO ₂	FeCl ₃ .6H ₂ O FeCl ₂ .4H ₂ O TiCl ₄	Chemical	+3	RT/ 7± 0.1	25-35/ 153.9	ND	Batch	50	0.5	26.52	~ 98/~ 83	[229]

2.10 Gaps pertaining to laboratory scale studies

2.10.1 Fabrication of columns

The adsorption data employing laboratory columns have provided a base for the application of nanoadsorbents at pilot and full scale remediation projects [241], [242]. In most of the studies, the laboratory columns have been reported to be conventionally designed which are unambiguously based on the batch removal experiments [243]. In the reviewed literature, the ratio of $d_{\text{column}}/d_{\text{particles}}$ (d-diameter) has been used for the laboratory scale column experiments, which depends on the ignorance of wall effect on the mass transfer [244].

Further, suitable binder is necessary, when the nanoadsorbents have to be used as packing materials because the loss of particles might occurs under the non-uniformity of flow [245]. At the pilot scale in the household treatment units of arsenic, the nanoadsorbents have been allowed to mix with easily available porous materials like soil particles. However, the pursuance of an absolute methodology for the development of laboratory columns is a need among the research community for the better comparability and interpretation of arsenic removal data at a common platform. Therefore, for designing of laboratory columns, the factors which need to be considered are height of reactive zone and column with constant porosity and their correlation with the required mass of adsorbents as established by Noubactep [246]. The mathematical equation to calculate the height of reactive zone is shown below:

$$h_{rz} = \frac{4V_{rz}}{\pi D^2} = \frac{4V_{solid}}{C\pi D^2} \quad (2.3)$$

Where, D , C , h_{rz} , V_{rz} and V_{solid} represents internal diameter of the column, packing density of the nanoadsorbents, height of reactive zone, volume of reactive zone and volume of solids (for the usage of two types of nanoadsorbents), respectively. The h_{rz} is the fraction of L (length of column) and length of column should be more than the magnitude of height of reactive zone ($L > h_{rz}$).

2.10.2 Studies representing real world conditions

Generally, the water resources are sensitive to physical, chemical and thermal variations. There are several ions in groundwater which might affect arsenic removal during adsorption processes. The batch experiments are not feasible using actual groundwater at laboratory scale due

to a large volume requirement of samples and fluctuating water quality issues. In order to evaluate the arsenic removal potential of different nanoadsorbents, using the groundwater concentration representing the real world conditions is the most appropriate approach. Therefore, proper calculation of the required quantity of ingredients for the synthesis of artificial water is a necessity [209]. Lin *et al.* [226] have investigated the effects of Cl^- , SO_4^{2-} , NO_3^- and PO_4^{3-} ions on arsenic removal using $\gamma\text{-Fe}_2\text{O}_3$ nanoparticles. To the best of my knowledge, studies evaluating the adsorption capacity of $\gamma\text{-Fe}_2\text{O}_3$ nanoparticles for the As^{V} in the groundwater compositions representing the real world are still not reported in the literature.

2.10.3 Cost evaluation of nanomaterials production

In developing a cost-effective arsenic treatment system, it is required to examine the production cost of different nanoadsorbents during laboratory scale studies. Needless to say, the chemical (co-precipitation) approach of synthesis has been reported to be a common mode of generation of nanoadsorbents at laboratory scale. In the absence of a clear cut methodology demonstrating the cost based evaluation of nanoadsorbents, an approach for calculating the production cost of nanoadsorbents using chemical approach of synthesis has been discussed in this study.

2.11 Summary and scope of research

The literature reveals that the continuous efforts are being made by scientific communities for providing the safe drinking water to the people from arsenic contaminated groundwater. Its removal through adsorption has been considered as a reliable and convenient technology. Around the world, most of the people are receiving the arsenic free water for drinking and cooking purposes using the household treatment set-up and centralized treatment systems based on the adsorption technology. In the beginning of 21st century, several conventional adsorbents (sand, ZVI, alumina, iron chips etc.) have been reported to be utilized for its remediation which were subsequently improved employing different types of nanoadsorbents. Recently, the nanotechnology based remediation systems employing nanoadsorbents have proved to be significant in terms of resource recovery and efficiency.

Among developed nanoadsorbents, iron based nanoparticles have been investigated widely due to their easy availability, bio-friendly characteristics, intrinsic affinity and selectivity towards

arsenic. But, the nanoscale zero-valent iron (nZVI) has been studied extensively both at laboratory and pilot scale level. However, these nanoparticles are thermodynamically unstable and prone to oxidize under natural environment conditions into iron (II)/(III) oxides, which increases the possibilities of its recontamination. Its unstable nature thus limits the applicability of their nanoparticles at large scale effectively. The maghemite ($\gamma\text{-Fe}_2\text{O}_3$) nanoparticles have not been extensively explored for arsenic removal, which is considered as the foremost stable phase (at nanoscale) among the different polymorphs of iron oxide(s). Further, performing the experiments in the appropriately designed columns to evaluate the removal efficacy for representative ground water samples is necessary before attempting the field scale applications of developed nanoparticles.



Maghemite nanoparticles and their engineered nanostructures: Synthesis and characterization

3.1 Chapter abstract

Among different iron^{III} oxide based nanosystems, γ -Fe₂O₃ (maghemite) NPs have not been investigated extensively for arsenic removal. It is the second most stable (in bulk) and foremost stable (at nanoscale) phase among the polymorphs of iron oxide(s). Its cubic crystal structure in each cell exhibits 32 O²⁻ ions, 21^(1/3) Fe^{III} ions and 2^(1/3) vacancies.

In the present work, engineered nanostructures of iron^{III} oxide have been synthesized by using the industry waste as a precursor material for coating of γ -Fe₂O₃ NPs (BIO), which produced γ -Fe₂O₃ nanohybrids (BIO-DW). The phase identification in as-synthesized nanostructures is evidently revealed by XRD, Raman and XPS techniques. The modified nanostructures have been observed with the characteristics of enhanced surface area and increased stability in colloidal solution. The variation in surface morphologies has been investigated through FESEM and TEM analysis. VSM and SQUID techniques have been explored to examine the magnetic characteristics. TGA analysis has revealed the presence of organics onto the surface of nanostructured BIO-DW. Further, the possible interactions among γ -Fe₂O₃ NPs and different organic moieties in the BIO-DW nanohybrids have been demonstrated by FTIR.

The average particle sizes (nm) of iron oxide NPs in BIO and BIO-DW have been estimated to be 19.3 ± 3.0 and 16.7 ± 4.1 , respectively. The decrease in the particle size for BIO-DW nanohybrids is also associated with an increase in its surface area ($97.39 \text{ m}^2 \text{ g}^{-1}$) as compared to BIO ($59.80 \text{ m}^2 \text{ g}^{-1}$) NPs. FESEM and HRTEM analysis has demonstrated the formation of agglomerates in BIO NPs. However, their dispersion gets significantly increased in BIO-DW nanohybrids. The BIO-DW indicates a superparamagnetic behavior with a insignificant decrease in saturation magnetization (emu g^{-1}) of 66.9 in comparison to those observed for BIO (72.1). at room temperature. At near neutral pH condition, an increase in the zeta (ζ) potential value for BIO-DW (-34.8 mV) has been

observed as compared to that of BIO (-24.9 mV), clearly indicating an increased stability for nanohybrids.

3.2 Materials and reagents

The salts of ferric chloride hexahydrate ($\text{FeCl}_3 \cdot 6\text{H}_2\text{O}$, M.W. = 270.3 g mol^{-1}) and ferrous sulphate heptahydrate ($\text{FeSO}_4 \cdot 7\text{H}_2\text{O}$, M.W. = $278.01 \text{ g mol}^{-1}$) of analytical reagent grade have been procured from Thermo Fisher Scientific enterprises (Waltham, Massachusetts, USA). Their aqueous solutions at different molar concentrations have been used as a source of Fe^{3+} and Fe^{2+} ions for the synthesis of NPs. Ammonium hydroxide (NH_4OH , 28 % w/w), perchloric acid (HClO_4 , 37 % w/w), hydrochloric acid (HCl , 37 % w/w) and sodium hydroxide (NaOH , ≥ 97 %) pellets of analytical reagent (AR) grade have been purchased from the Sigma-Aldrich enterprises (Missouri, USA). The required solutions of desired normality/concentration have been prepared using deionized water (Millipore, electrical conductivity, $18.2 \text{ m}\Omega\text{-cm}$ at room temperature).

3.3 Instrumentation

The concentration of iron in NPs has been determined on Inductively Coupled Plasma Spectrometry ELAN DRC-e (ICP-MS; ELAN DRC-e) purchased from Perkin Elmer. The UV-spectra(s) have been examined by using double beam UV-visible spectrophotometer(s) (Agilent, Cary 100, Monochromator: Czerny-Turner 0.278 m; and Shimadzu 1601BC) equipped with the set-up for temperature control. Bruker X-ray diffractometer is used to record the diffraction patterns in powdered samples (Model: D8-Advance, Source: 2.2 kW Cu anode). Raman spectra(s) have been measured on an inVia Renishaw spectrometer (Laser: Argon ion; Resolution: $\pm 1 \text{ cm}^{-1}$; Wavelength: 514 nm). It is equipped with a confocal microscope having a resolution of $2.5 \mu\text{m}$ which is coupled with CCD detector. The XPS surveys have been put through on a PHI 5000 Vary Probe II, which is equipped with a monochromatic radiation source of $\text{Al K}\alpha$ 945. (Model: ULVAC PHI Inc., Japan). The Brunauer-Emmett-Teller (BET) surface area is measured using Autosorb-iQ and High Speed Automated Surface Area Analyzer (NOVA 2200e) procured from Quantachrome Instruments, USA. The morphological measurements have been explored using FESEM (Model: Carl Zeiss Ultra Plus) equipped with In-Lens Detector for surface structure analysis and HR-TEM (Model: FEI Tecnai G² 20 S-Twin, Electron source: LaB_6 or W emitter) purchased from FEI Electron Optics International BV enterprises, Netherlands. Thermo-gravimetric (TG) and Differential Thermal

Analysis (DTA) have been performed on a SII TG/DTA 6300 (EXSTAR, Seiko). It has a temperature control ranging from ambient to 1500 °C with heating rates ranging from 0.01-100 °C min⁻¹. VSM and SQUID analyses have been carried on VSM, PAR 155 and MPMS XL Evercool SQUID, obtained from Quantum design Inc. (San Diego, USA) respectively. Infrared (IR) spectra have been recorded using an Agilent Cary 630 FTIR equipped with a sample interface of Diamond ATR. The surface charge of these NPs (ζ -potential) has been measured on a Malvern Zetasizer Nano ZS90 (Light source: He-Ne laser 633 nm, Measurement range: 0.3 nm – 100 μ). The as-synthesized samples of NPs have been dried in a vacuum oven (Model: LVO 2030) purchased from Daihan Lab. Tech. India Pvt. Ltd. (Gurugram, New Delhi), equipped with the temperature and vacuum control in the range of 5 - 250 \pm 1 °C and 10 - 760 mm Hg, respectively.

3.4 Methodology and operating conditions

3.4.1 Chemical co-precipitation mode of NPs synthesis

This is a widely employed mode of generation of NPs due to its easy operation and less complexities. Generally, the synthesis of metal oxide NPs involves the mixing of relevant metal salts solution(s) further followed up to the addition of precipitating reagent in aqueous medium. It requires metal cations as soluble salts (e.g. chlorides, sulphates and nitrates), which are co-precipitated from an aqueous medium, generally by using oxalates, citrates, carbonates and hydroxides. In the present study, an industry waste has been utilized for the functionalization of NPs. This raw waste from the distillery industry is rich in organic components, such as oligosaccharides and polysaccharides (starch, cellulose, hemicellulose and lignin) [247] leading to the encapsulation of organic moieties containing different functionalities onto the surface of iron oxide NPs [248].

3.4.2 Analysis employing Inductively coupled plasma-mass spectrometry (ICP-MS)

ICP-MS is equipped with quadrupole mass spectrometry Q-MS, which allow the instrument to analyze the samples with high accuracy. The samples have been digested in HCl (2 mg/100ml) and, thereafter, filtered through Whatman TM⁴² cellulose filter prior to the analysis of iron ions using ICP-MS. The standards solutions of iron in the range of 0.5-3.0 have been used for the calibration purposes. The minimum detection limit of the instrument is 0.01 μ g L⁻¹.

3.4.3 Evaluation for the cost of nanomaterials production

The chemical (co-precipitation) approach of synthesis has been reported to be a popular mode of nanoadsorbents generation at laboratory scale [235], [248]. A functional equation covering the maximum possible steps involving in nanoadsorbents production is presented below in equation 3.1:

$$F = L_F \cdot \sum_{\substack{P, RM=n \\ P, RM=1 \\ e=1}}^{e=n} S_{NPS} + \sum_{e=1}^{e=n} H_{NPS} + \sum_{e=1}^{e=n} H_E + \sum C_{OHS} \quad (3.1)$$

Where, F is total cost involved in nanomaterial production (\$), S_{NPS} is cost for the synthesis of nanoparticles (\$), L_F - representing the loss-coefficient occur at different steps involving from extraction to storage of nanoparticles precipitates, H_{NPS} is handling cost for produced nanoparticles (\$), H_E is equipment handling cost (\$), C_{OHS} is cost related to occupational health and safety measures (\$), P is total amount of nanoparticles precipitates, e and R_M are representing cost of electricity and manpower, respectively (\$).

Further, the development of nanoparticles requires several kind of precursor materials which has been classified as primary and secondary materials in present methodology. The capital and facility cost involved in synthesis process is presented in equation 3.2 below:

$$S_{NPS} = \sum_{Pi=1}^{Pi=n} P_{MS} + \sum_{P=1}^{P=n} P_{SS} + T_C \quad (3.2)$$

Where, P_{MS} and P_{SS} are cost representing for the primary and secondary precursor materials, respectively (\$). P_i is a variable highlighting material generation from unit mass to variable n . T_C is representing the facility cost for tableware's and storage of nanomaterial (\$).

After the production of nanoadsorbents, adoption of significant handling procedures and storage are also crucial steps to conserve the stability material which also involves the capital and facility cost. Therefore, it is advantageous to develop the nanoadsorbents which are stable in wide range of environmental variables. This in further light led to decrease in the production cost of nanomaterial. The cost related to handling, storage and occupational health for nanomaterials production is present below as equation 3.3 below:

$$H_{NPS} = \sum_{e=1}^{e=n} C_S + S_R \text{ and } C_{OHS} = \sum_{Pi=1}^{Pi=n} T_w + E_S \quad (3.3)$$

Where, C_S is representing capital cost of equipment handling for produced nanoadsorbents, S_R is representing the facility cost of storage for produced nanoadsorbents, T_w is cost of treatment for secondary pollution generated during synthesis process (\$) and E_S is the facility cost (\$) to meet the standards for precautions involved in MSDS (Material safety Data Sheet). The equation can be customized in several ways to get the optimized values of cost during the technology transfer.

3.4.4 Analysis employing UV-visible spectrophotometer

It deals in the measurement of absorbed photons corresponding to different transitions which is a characteristic feature of specific molecule [249]. A well dispersed solution of NPs has been prepared through sonication (0.10 g L^{-1}) to record the absorption spectra. The spectrophotometer consists of two lamps as a light source: tungsten filament-halogen lamp (350-900 nm) and deuterium arc lamp (185-350 nm). It is equipped with R928 photomultiplier tube (185-900 nm) and silicon photodiode used as a detector, respectively. the photometric and wavelength accuracy of the systems are $1; \pm 0.5 \text{ nm}$ and $\pm 0.008; \pm 0.004$ absorbance, respectively.

3.4.5 Analysis employing X-ray diffractometer (XRD)

A fine powder of sample has been prepared using agate pestle and mortar, for performing XRD measurement [250] and thereafter compacted in aluminium rack (hollowed) to record the diffraction patterns at 40 kV and 40 mA flux. The angular range and scanning speed has been kept at of $5^\circ - 90^\circ (2\theta)$ and $0.01^\circ \text{ min}^{-1}$, respectively. Further, the XRD data has been smoothed with the subtraction of $K\alpha_2$ stripping followed by the background corrections. The observed XRD data has been compared with the joint committee for powder diffraction standards (JCPDS) database for the identification of the phase using PAN analytical X'pert high score software procured from PAN analytical B.V. Almelo, Netherlands. Using Scherrer's formula, the average particle size of as-synthesized nanostructures has been calculated by applying equation as shown below:

$$L = \frac{K\lambda}{\beta \cos\theta} \quad (3.4)$$

Where, L is demonstrating the size of crystallite (Å), λ denotes the Cu K α wavelength (0.15418 nm), K is a dimensionless factor indicating the crystallite shape factor (0.9), β is the full width at half maxima (FWHM) obtained after correcting band broadening and θ is Bragg's diffraction angle.

3.4.6 Analysis employing Raman spectrometer

Raman measurements have been performed on a Renishaw inVia Raman spectrometer equipped with an argon ion 514 nm laser as an excitation source. It has a resolution of $\pm 1 \text{ cm}^{-1}$. It is equipped with Leica confocal microscope having computer controlled XYZ meter stage; objective lenses of 5x, 10x, 50x, 100x magnification; a resolution of 2.5 μm . During analysis, the solid samples have been applied on the glass. The spectra have been recorded in the wave number range of 100-1200 cm^{-1} at 0.5 mW laser power with 30 s exposure time in order to avoid any kind of damage to sample(s).

3.4.7 Analysis employing X-ray photoelectron microscopy (XPS)

It deals in the analysis of chemical composition of the materials surfaces upto certain depth in nanometer scale range [251]. During measurements, the surface of nanomaterial has been irradiated with a source of X-ray under high vacuum conditions. Afterwards, the characteristics of the emitted electrons (with respect to kinetic energy) has been detected by an electrostatic analyzer. The emitted electrons in this technique are mentioned as photoelectrons. To irradiate the sample(s) of nanomaterials, a monochromatic source of X-ray (Al K α : 8.34 Å) has been utilized. The spectra(s) have been recorded at an electron take-off angle of 90°. The sample(s) been employed onto the carbon tape during analyses. Further, the values of binding energy (eV) and orbital splitting have been matched with database as suggested by the NIST (National Institute of Standards and Technology).

3.4.8 Analysis employing Field emission scanning electron microscopy (FE-SEM)

This technique is used for the evaluation of surface morphologies [252]. It offers a wide depth of field analysis; i.e. relatively large portion of the specimen can be kept in focus at the same time.

The electron beam interacts with the near surface region of the sample. As the electrons penetrate the specimen surface, they are scattered from a range of depths, some of which escape from the surface. Electrons which escape from near the surface are known as secondary electrons, and are created through inelastic collisions whereas electrons scattered back from deeper levels are known as backscattered electrons, which are generated through multiple elastic collisions.

During measurements for 3-D imaging, a gold sputtering of powdered sample is performed under vacuum condition, primarily to increase the conductivity of sample. Using the voltage of 15 kV, the images have been recorded by In-Lens detector at a magnification of 110 and 200 K along with resolution of 7.6, 7.9 nm, respectively.

3.4.9 Analysis employing Transmission electron microscopy (TEM)

TEM imaging is examined by depositing the sample on carbon coated copper TEM grid having the mesh size of 200 μm . Firstly, a known amount (10 mg/100 ml) of sample is sonicated in water for 5 min at room temperature. The sample loaded on the grid is applied by dipping it into the dilute colloidal solution of NPs and is dried at room temperature for further analysis. The high resolution 3-D images are recorded by applying accelerating voltage of 200 keV and beam current of 1 nA.

3.4.10 Brunauer, Emmett and Teller (BET) surface area

BET is an extensively employed method for the determination of surface area of nanomaterials. It utilizes low temperature sorption of inert gas(es) onto the surface of particles [253]. It accounts microscopic irregularities of the external surface, including internal porosity of NPs unlike other geometrical surface area measurements. Nitrogen is commonly used for samples exhibiting surface areas $> 2 \text{ m}^2 \text{ g}^{-1}$. During analysis, ~ 200 mg of powdered sample is degassed under high vacuum in order to remove all the possible contaminants. The BET data has been analyzed using NovaWin software.

3.4.11 Thermo-gravimetric analysis (TGA/DTA)

This technique measures the variation in mass of a sample with respect to temperature under the controlled atmosphere [254], [255]. This variation occurs after the loss of water and vapour emission of the material. Further, the differential thermal analysis measures the difference in

temperature between a sample and a reference as a function of time/temperature, when allowed to undergo temperature scanning under controlled atmosphere. For this, the samples have been applied to undergo the temperature scanning under the controlled atmosphere. In this study, TG/TGA analysis of the powdered samples of as-synthesized nanomaterials have been carried out in the temperature range of 25-1400 °C and at a heating rate of 10 °C min⁻¹ in the nitrogen atmosphere. Similar, this analysis has also been performed in the temperature range of 25-600 °C for industry waste and at a heating rate of 5 °C min⁻¹ in the nitrogen atmosphere.

3.4.12 Analysis employing Vibrating sample magnetometer (VSM)

Magnetic behaviour of the as-synthesized nanomaterials has been recorded on VSM, PAR 155 at 300 K. The applied external magnetic field has been varied upto 1 Tesla. The sensitivity range of the instrument is 0.00001-10000 e.m.u for 10 mg of sample. These measurements have been performed mCFMS-3 cryogenic free mini VSM systems with a pulse cryocooler from 4-300 K upto 3T with a ramp rate of 1 T min⁻¹. Afterward, the data has been analyzed in origin Pro 8 software.

3.4.13 Analysis employing Superconducting quantum interface device (SQUID)

The magnetic measurements for all samples are carried out on MPMS XL supercool SQUID, obtained from Quantum design, Inc. The sensitivity of SQUID is 10⁻⁹ e.m.u and has temperature range and maximum field of 1.9 - 400 K and ±7 T, respectively. Further, the M-H loops have also been recorded at 5, 100 and 300 K and the magnetic field increased gradually in steps upto ±0.5 T (0.05 T min⁻¹) in gradient mode, ±0.5 T upto 1.5 T (0.01 T min⁻¹). The data have been processed using MPMS multiVu Window based software.

3.4.14 Analysis employing Fourier transform infrared (FTIR) spectrophotometer

The IR spectra(s) have been recorded on a FTIR spectrophotometer in the mid IR range (4000-400 cm⁻¹) in KBr medium having resolution of 0.1 cm⁻¹. The appropriate amounts of the prepared sample(s) are being inserted into the sample chamber, thereafter, the FTIR peaks have been recorded using transmission mode of the instrument. A total of 64 scans have been collected for a single sample run at a resolution of 1 cm⁻¹.

3.4.15 Analysis employing Zetasizer

The electrophoretic measurements are performed by dispersing the NPs in the water through sonication at room temperature. For this, several sets of colloidal solutions have been prepared in the pH range of 2 to 10. The pH has been adjusted using dilute solutions of perchloric acid and liquid ammonia. Then, the zeta potential of these solutions have been measured using folded type capillary cell (disposable) at a measurement position of 2 mm by average runs of 20 for each sample.

3.5 Synthesis of maghemite nanostructures and their nanohybrids

The γ -Fe₂O₃ NPs have been synthesized using a previously reported co-precipitation method [209] with a slight modification. For this, the solution(s) containing Fe²⁺ (ferrous) and Fe³⁺ (ferric) salts have been allowed to reflux above the room temperature. For the synthesis of bare nanostructures, the salts of FeSO₄·7H₂O and FeCl₃ (anhydrous) with an amount of 4.2 g and 3.7 g have been dissolved in ultra-pure water (100 mL), respectively. Then 10 mL of NH₄OH added to the solution. The produced magnetic precipitates have been isolated from the alkaline solution using laboratory magnets followed by washing several times with distilled water to remove all the non-magnetic and soluble products. The collected powder thus obtained has been dried in anaerobic environment (vacuum oven). Further, the powder sample(s) has been subjected to characterization and adsorption experiments.

3.6 Results and discussion

3.6.1 Determination of iron content in as-synthesized nanomaterials

The percentage of iron content has been determined in the both as-synthesized BIO NPs and BIO-DW nanohybrids, after digesting 2 mg of nanopowder in hydrochloric acid. Its percentage in these nanosystems has been calculated to be 68.2 % and 38.7 %, respectively. In this study, the removal capacity of arsenic has been presented as mg g⁻¹ of iron content for both of BIO NPs and BIO-DW nanohybrids.

3.6.2 Cost estimation of as-synthesized nanomaterials

The cost of development of as-synthesized BIO and BIO-DW nanosystems has been evaluated by using the previously mentioned Equation 3.1. Although, the production of

nanomaterials includes both capital and consumables cost, but, in the present study, their cost of synthesis has been calculated by considering the consumable cost only. However, this methodology can be extrapolated in calculating the synthesis cost by maximizing the production amount of nanomaterials as well as optimum utilization of the non-consumable facilities. At lab scale, the maximum possible process parameters utilized for the synthesis of BIO and BIO-DW nanomaterials are mentioned in the Table 3.1 below:

Table 3.1. Analysis of cost in the production of as-synthesized BIO NPs and BIO-DW nanohybrids.

Consumable for synthesis	Actual cost (\$)	Cost per unit (\$)	Utilized resources during synthesis	Total cost of the utilized resources (\$)
(Sigma Aldrich) FeCl ₃ .8H ₂ O	45.7	0.091	3.7 g	0.34
F-2877- 500g (Sigma Aldrich)				
FeSO ₄ .7H ₂ O	102.9	0.103	4.2 g	0.43
215422- 1000g (Sigma Aldrich)				
NH ₄ OH	62.1	0.025	10 ml	0.25
221228-2.5 L-A				
Electricity	0.2	0.03	0.15 unit	0.03
Manpower	357.2	1.49	1 nos.	1.49
Total cost				2.54

In regard to the lab scale cost analysis considering the consumables of precursor materials, the Equation 3.1 is reduced to following equation 3.5:

$$F = L_F \cdot \sum_{\substack{P, RM = n \\ P, RM = 1 \\ e=1}}^{e=n} S_{NPS} \quad (3.5)$$

For unit production, the above relation is further modified to equation 3.6 as mentioned below: -

$$F = L_F \cdot \sum_{\substack{P, RM = 1 \\ e=1}} S_{NPS} \quad (3.6)$$

where, L_F is the coefficient related to loss function for the produced nanopowder. This factor mainly leads to determine the loss of nanopowder in the process of collection of material after vacuum drying during scratching from the petri-dish. Its value has been calculated by dividing the weight of nanopowder produced after drying to that of actual weight of nanopowder collected after scratching process ($L_F = \text{wt. of nanopowder produced after drying} / \text{actual wt. of nanopowder collected}$). Its value has been determined to be 1.27 and 0.86 for BIO NPs and BIO-DW nanohybrids, respectively. The factors P , R_M and e are representing the weight of the nanopowder, manpower and electricity, respectively. The details of all the components along with the unit cost are presented in Table 1.

By using the above-mentioned amount of precursor materials, the 2.96 ± 0.16 g and 3.87 ± 0.11 g of nanopowder has been obtained for BIO NPs and BIO-DW nanohybrids, respectively. Thus, the cost (\$) for unit mass production of these as-synthesized nanomaterials has been calculated to be 0.86 and 0.66, respectively. However, the cost of commercial available bare nanopowder has been reported to be \$7.75 (Sigma-Aldrich: 544884), which is overmuch as compared to those examined in present study.

3.6.3 UV-Vis spectra

Figure 3.1, is displaying the electronic absorption spectra of as-synthesized BIO and BIO-DW nanosystems. It has been recorded in the wavelength range of 200-800 nm. The spectrum due to BIO NPs exhibits an outset of absorption above ~ 650 nm and depicts the two broad band(s) peaking at 364 nm and 383 nm along with a shoulder at 485 nm. Whereas, BIO-DW nanohybrids displays two broad peak(s) at 364 nm and 372 nm along with a shoulder at 476 nm. A well-defined

band in the range of 360–390 nm with maxima near around 372 nm for the γ -Fe₂O₃ NPs has been also suggested by Maiti [256].

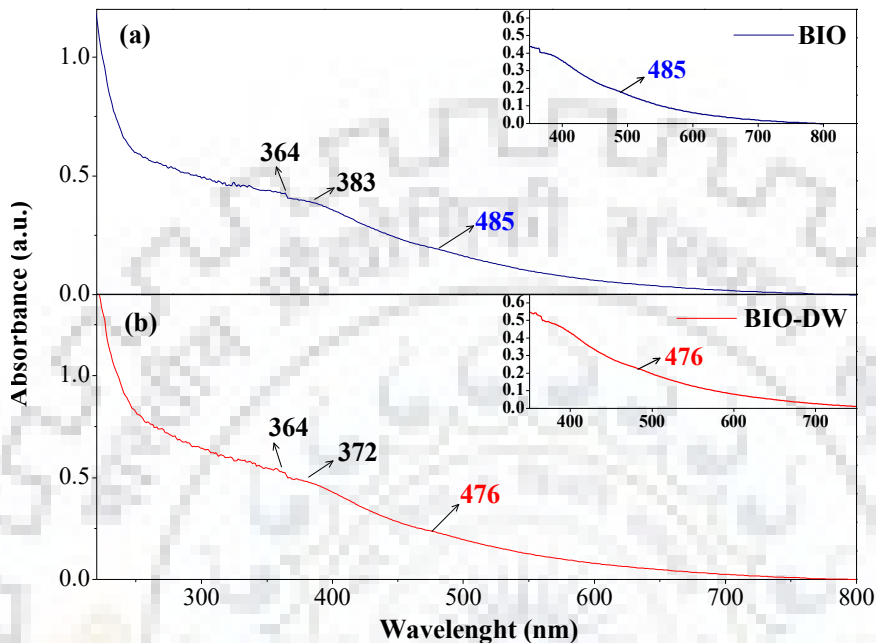


Figure 3.1. UV-visible absorption spectra of as-synthesized (a) BIO NPs and (b) BIO-DW nano hybrids. Inset: depicting the absorption spectrum in larger wavelength.

A comparison of the absorption spectra indicates that BIO-DW exhibit a decrease in its absorbance associated with a slight blue shift of absorption peak from 383 nm to 372 nm in the presence of distillery waste. Besides, the absorption observed around 485 nm for bare γ -Fe₂O₃ NPs [210], also shows a blue shift to 476 nm. The coating of organics from distillery waste onto the γ -Fe₂O₃ NPs has exhibited the hypsochromic shift associated with a small increase in the intensity of absorbance for the entire wavelength range under investigation. Thus, it is suggesting to cause a decrease in the size of iron oxide cluster(s) in BIO-DW nano hybrids.

3.6.4 XRD diffraction patterns

Figure 3.2 describes the XRD patterns of the as-synthesized nanostructures of BIO and BIO-DW NPs. The diffraction patterns for BIO NPs have been found to match with the reflections due to planes (111), (220), (311), (400), (422), (511) and (440) [210]. These diffraction patterns are comparable to the cubic structure of γ -Fe₂O₃ NPs as suggested by Joint Committee on Powder

Diffraction Standards (JCPDS file no. 39-1346). The addition of distillery waste during the synthesis of BIO-DW nanohybrids results in the disappearance of two peak(s) corresponding to the plane (111) and (422) as compared to that of BIO NPs. These observations are depicting that the crystallinity of γ -Fe₂O₃ phase remains conserved even after the functionalization of BIO NPs.

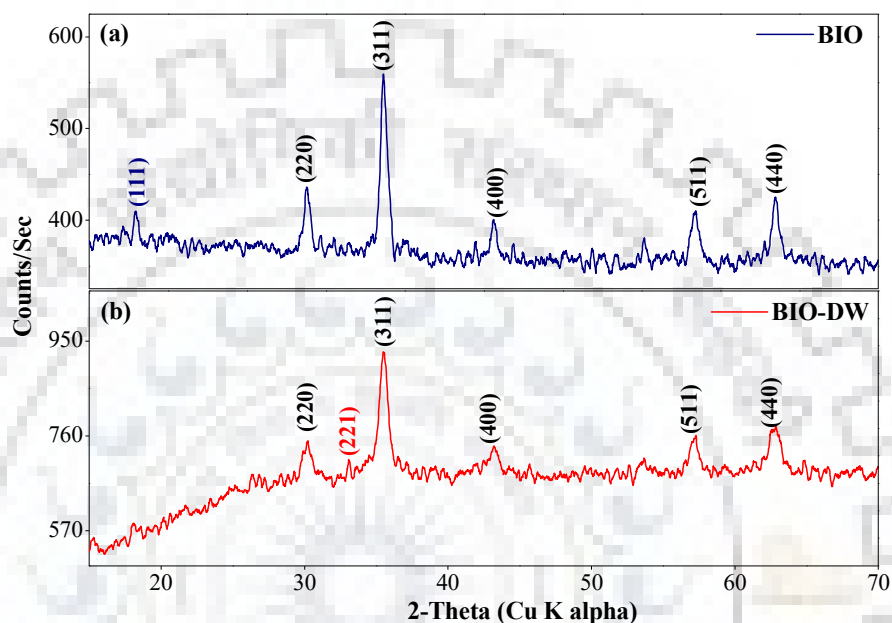


Figure 3.2. XRD diffraction patterns of as-synthesized (a) BIO NPs and (b) BIO-DW nanohybrids.

Further, the patterns of X-ray diffraction alone cannot be used to evaluate the phase determination of γ -Fe₂O₃ NPs, as the diffraction patterns from XRD for maghemite (γ -Fe₂O₃) and magnetite (Fe₃O₄) are virtually identical [257]. Therefore, the exact phase for concerned iron^{III} oxide has been further confirmed through Raman and XPS analyses.

Using Scherrer's formula, the average particle sizes of iron oxide in as-synthesized BIO NPs and BIO-DW nanohybrids have been calculated to be 19.3 ± 3.0 nm and 16.7 ± 4.1 nm, respectively. These values are presented in Table 3.2 and 3.3. This partial decrease in the average particle size has been found in line with observation revealed from the electronic absorption data (Figure 3.1).

3.6.5 Raman spectroscopy

The Raman spectra of BIO and BIO-DW nanosystems have been recorded to confirm the γ -Fe₂O₃ phase (Figure 3.3). The Raman bands (cm⁻¹) for both of these samples have been observed at 366, 499, 676, 706 (for BIO) and 366, 492, 665, 718 (for BIO-DW). A slight shift of bands in BIO-

DW nanohybrids indicates that the coating of organics has possibly influenced the absorption. But in both the cases, these bands are fairly different than those matched with previously recorded bands due to maghemite phase [210][258]. In a comparison of spectra of BIO and BIO-DW nanosystems, a considerable decrease in the intensity of bands is observed which might have occurred due to the coating of organics onto BIO NPs.

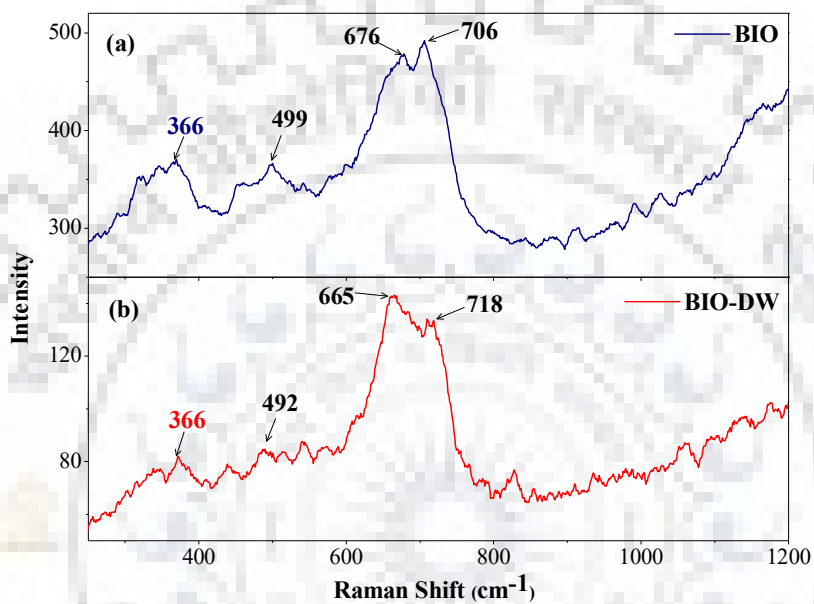


Figure. 3.3. Raman spectra of as-synthesized (a) BIO NPs and (b) BIO-DW nanohybrids.

Table 3.2. Crystallite size obtained from Scherrer's formula for BIO NPs.

Peak (h k l)	Peak intensity minima (y1)	Peak intensity maxima (y2)	$y1 + \frac{(y2 - y1)}{2}$	2θ High/degree	2θ Low/degree	FWHM	Peak maxima (2θ)/degree	Peak maxima (θ)/radian	d value/ Å	Crystallite size (nm)
111	373.75	410.55	392.15	18.43	18.01	0.00733	18.24	0.159174	191.7128	19.17
220	368.02	436.72	402.37	30.45	29.98	0.008203	30.153	0.263134	175.1856	17.52
311	355.92	559.57	457.75	35.8	35.3	0.008727	35.567	0.31038	166.9919	16.70
400	356.41	401.6	379.01	43.4	42.99	0.007156	43.127	0.376354	208.5099	20.85
422	345.12	380.94	363.03	53.92	53.52	0.006981	53.589	0.467652	222.5779	22.26
511	352.64	411.53	382.09	57.46	56.95	0.008901	57.206	0.499216	177.5533	17.76
440	359.35	426.25	392.8	63.06	62.61	0.007854	62.804	0.548068	207.0034	20.70

Table 3.3. Crystallite size obtained from Scherrer's formula for BIO-DW nanohybrids.

Peak (h k l)	Peak intensity minima (y1)	Peak intensity maxima (y2)	$y1 + \frac{(y2 - y1)}{2}$	2θ High/degree	2θ Low/degree	FWHM	Peak Maxima (2θ)/degree	Peak maxima (θ)/radian	d value/ Å	Crystallite size (nm)
220	670.46	749.99	710.23	30.46	29.95	0.008901	30.24	0.263911	161.495	16.15
311	675.75	927.69	801.72	35.85	35.19	0.011519	35.511	0.309892	126.482	12.65
400	352.48	400.57	376.53	43.35	42.94	0.007156	43.21	0.377078	208.555	20.87
511	682.70	760.28	721.49	57.45	56.91	0.009425	57.29	0.499949	167.766	16.78
440	694.38	778.91	736.65	63.13	62.59	0.009425	62.86	0.548557	172.543	17.25

3.6.6 XPS spectroscopy

In order to further confirm the γ - Fe_2O_3 phase in the as-synthesized samples (BIO and BIO-DW), surface analysis of these nanosystems has been performed using XPS analysis (Figure 3.4 and 3.5). The survey scans for the spectrum have been recorded in the binding energy range of 0–800 eV. Both BIO and BIO-DW nanosystems exhibit the peak(s) due to elements such as Fe, O and C (Figure 3.4). The scan due to each of these elements have also been recorded and is subjected to baseline correction. The deconvolution of peak(s) due to Fe (2p) and O (1s) has been executed using Gaussian software (Figure 3.5).

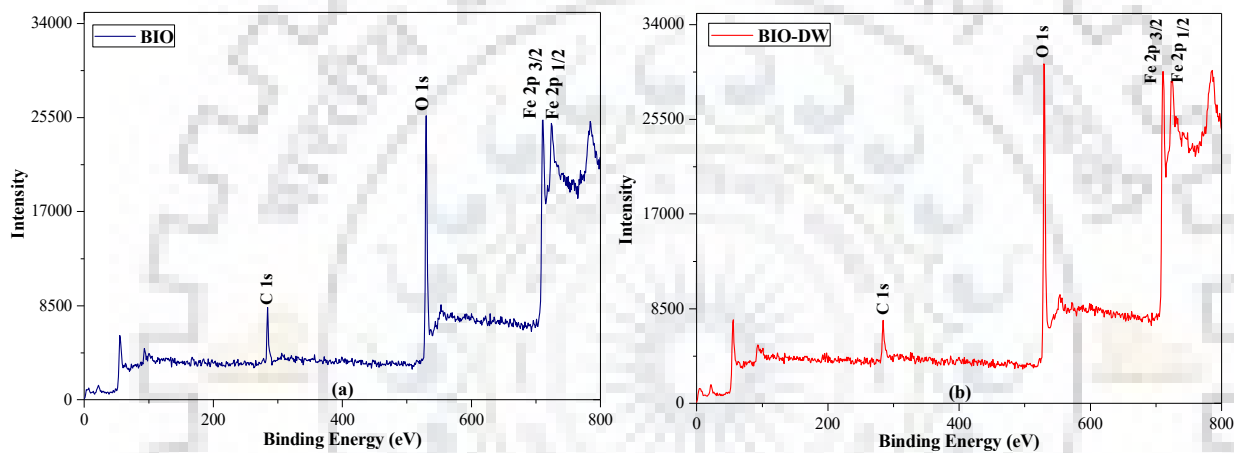


Figure 3.4. Spectra of XPS representing survey scan for (a) BIO NPs and (b) BIO-DW nanohybrids.

In BIO and BIO-DW nanosystems, the panels exhibit a peak doublet with the binding energy (eV) of 710.5, 724.2 eV and 710.43 and 723.9, respectively. These are known to occur due to elemental spins of $\text{Fe } 2p^{3/2}$ and $\text{Fe } 2p^{1/2}$ [210][259]. Also, a peculiar spin-orbit separation of 13.7 eV and 13.5 eV along with satellite peak(s) at 718.4 and 718.6 eV has been observed for BIO and BIO-DW nanosystems, respectively. The appearance of these charge transfer satellite peaks indicates that the iron is present as +3 oxidation state in both the samples [260]. This interpretation also differentiates the γ - Fe_2O_3 phase to that of Fe_3O_4 phase. The absence of this characteristic peak is due to the presence of mixed oxidation state (+2 and +3) of iron in magnetite phase

The spectrum due to O1s show the two bands centered at 529.5, 530.7 and 529.33, 530.53 eV for BIO and BIO-DW nanosystems respectively [261]–[263]. These intense bands at 529.5 and 529.33 eV have been attributed to lattice oxygen, whereas, the shoulder bands at 530.7 and 530.53 eV are assigned to anionic species in γ - Fe_2O_3 phase. A shift in the binding energy and peak(s)

intensities in comparison to that of BIO NPs might have arisen due to the attachment of organic moieties during the functionalization in BIO-DW nanohybrids.

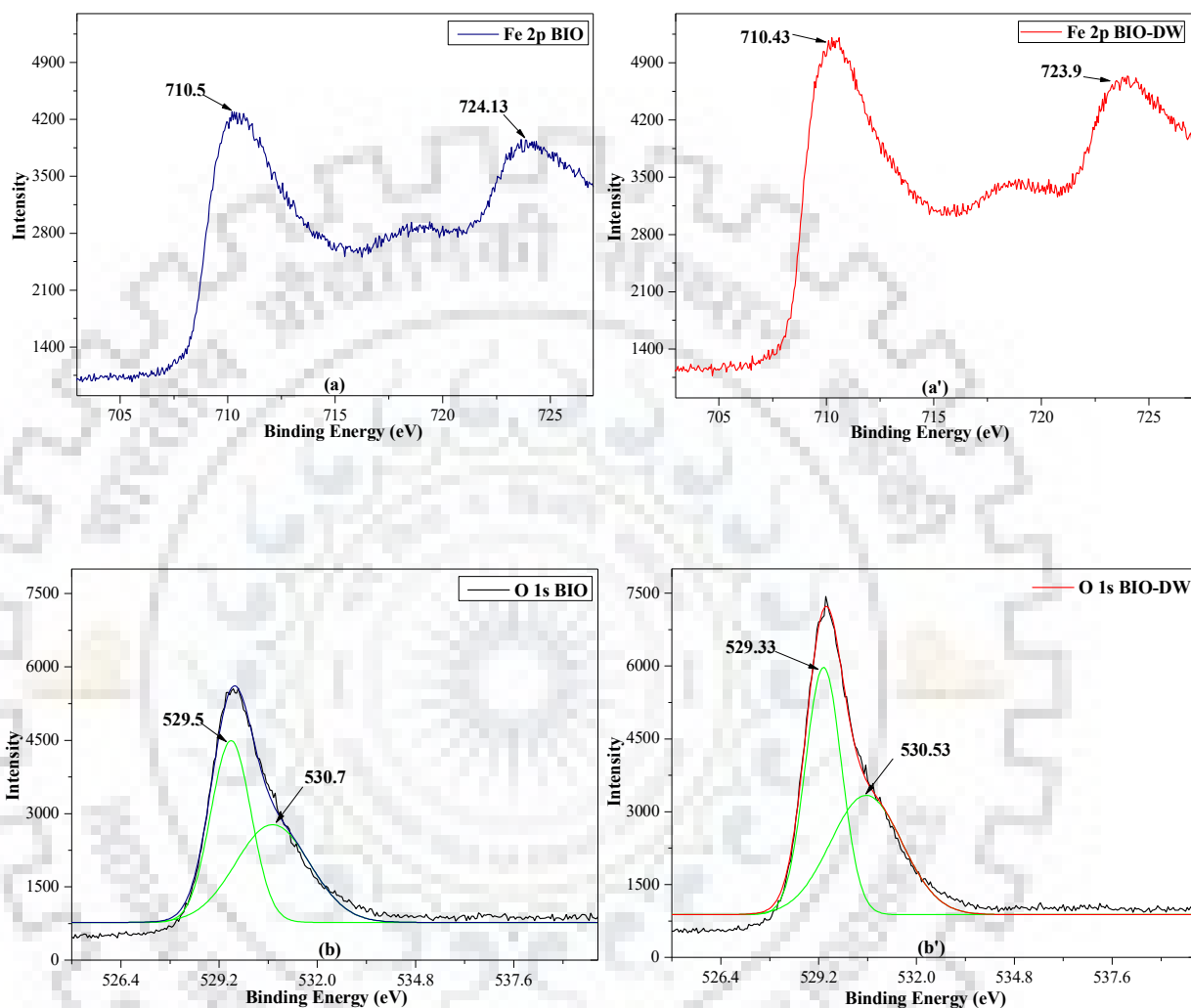


Figure 3.5. XPS spectra of BIO NPs (a-b) and BIO-DW nanohybrids (a'-b'): narrow scan of Fe2p (a and a'); O1s (b and b').

3.6.7 Field Emission Scanning Electron Microscopy (FESEM)

FE-SEM images of BIO NPs and BIO-DW nanohybrids are presented in Figure 3.6. Both the images are showing the clusters consisting of NPs. However, the average size of the NPs is reduced significantly and determined to be about 52 nm and 19 nm, respectively. It is indicated that the coating of organic moieties onto these BIO NPs results in the reduction of size of NPs clusters. Moreover, this analysis demonstrates that the formation of agglomerates in these samples occurs due to the strong magnetic interactions among NPs [264].

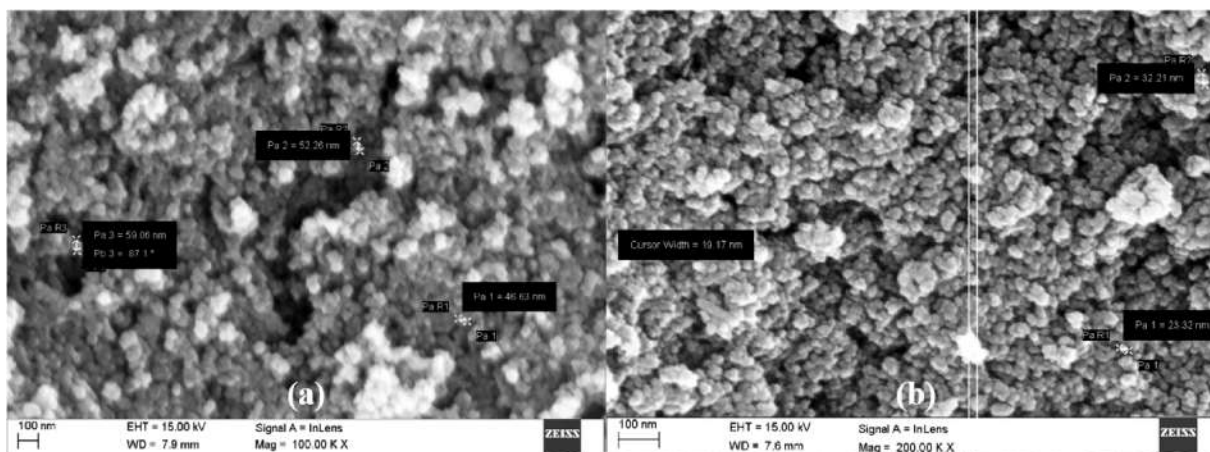


Figure 3.6. FE-SEM images of BIO NPs and BIO-DW nanohybrids (100 nm scale).

3.6.8 Transmission Electron Microscopy (TEM)

The TEM micrographs of BIO NPs and BIO-DW nanohybrids are shown in Figure 3.7. A close examination of these images clearly depict a decrease in particles size in BIO-DW nanohybrids as compared to those of BIO NPs. The average particle sizes using different HRTEM images have been determined to be 18.1 ± 0.27 and 15.8 ± 0.19 for BIO and BIO-DW nanosystems, respectively. These observations show fairly good agreement with the analyzed particle size using XRD data.

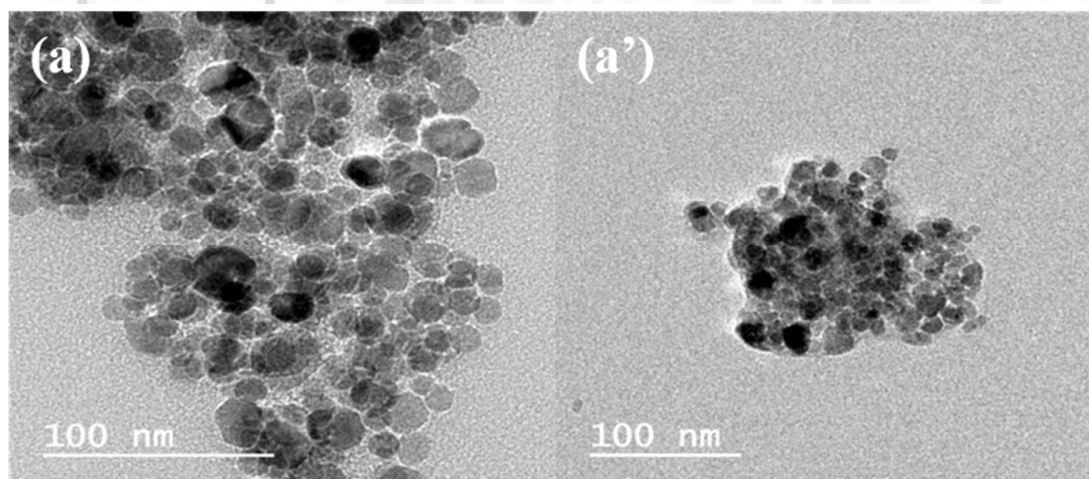


Figure 3.7. TEM images of (a) BIO NPs and (a') BIO-DW nanohybrids (100 nm scale).

3.6.9 Brunauer–Emmett–Teller (BET) surface area

The surface area of as-synthesized nanomaterials is determined by performing BET measurements. It has been found to be $59.80 \text{ m}^2 \text{ g}^{-1}$ and $97.39 \text{ m}^2 \text{ g}^{-1}$ for BIO NPs and BIO-DW nanohybrids, respectively. The utilization of distillery waste as one of the precursor material results in an increase in the surface area indicating that the size of NPs gets decreased in BIO-DW nanohybrids. This reduction in the particle size has also been confirmed using XRD, FESEM and HRTEM analyses.

3.6.10 Thermo-gravimetric (TG) analysis

The thermo-gravimetric (TG) experiments have been performed in order to analyse the thermal stability of as-synthesized nanomaterials (BIO and BIO-DW) and distillery waste. These are examined in the temperature range of 25-1350 °C and 25-600 °C, respectively (Figure 3.8 and 3.9). For both BIO and BIO-DW nanosystems, the TGA curves vary significantly in a similar manner upto about of 100 °C. This loss is possibly attributed due to the adsorbed water/moisture in this temperature range.

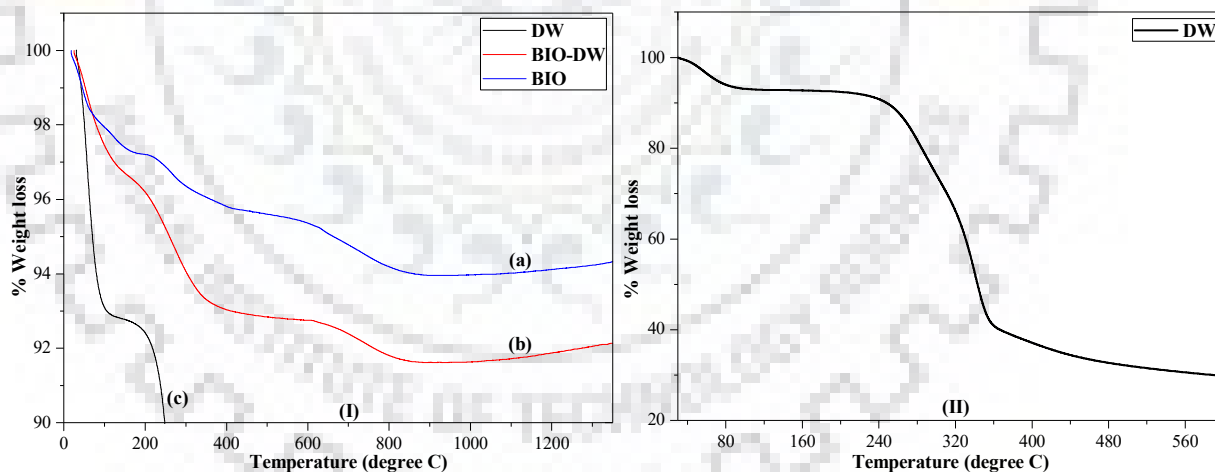


Figure 3.8. Thermo-gravimetric plots in Panel I. BIO NPs (a) BIO-DW nanohybrids; Panel II. TGA plots of Distillery waste depicting in the entire recorded temperature range.

In BIO-DW nanohybrids, a weight loss % of 5.18 has been observed beyond the temperature range of $>100 \text{ }^\circ\text{C}$ [210]. It has apparently occurred due to degradation of organic functionalities attached to these nanostructures [254]. A comparison of their TGA curves clearly indicate that the

thermal stability of BIO-DW nanohybrids is lower as compared to those of BIO NPs. Further, this study has also confirmed the attachment of organics onto the surface of functionalized nanostructures.

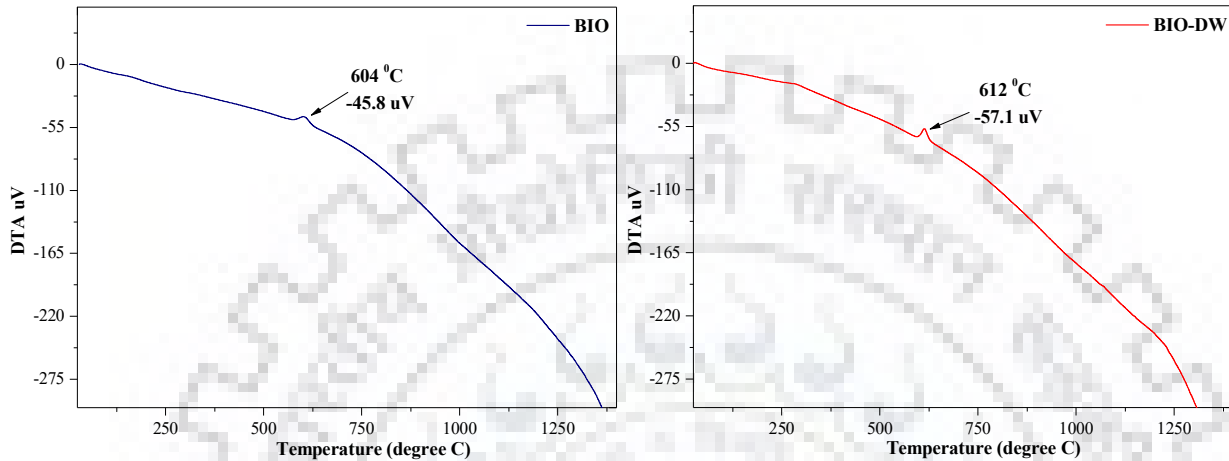


Figure 3.9. DTA curves of as-synthesized nanomaterials (a) BIO NPs and (b) BIO-DW nanohybrids.

3.6.11 Vibrating sample magnetometer (VSM) analysis

The hysteresis loops of BIO NPs and BIO-DW nanohybrids at room temperature are shown in Figure 3.10 (a-b), along with their magnified image Figure 3.10 (a'-b'), respectively. The saturation magnetization of BIO NPs and BIO-DW nanohybrids have been depicted to be 72.1 and 66.9 emu g⁻¹, respectively. Both of these nanosystems are having significant value of magnetic moment which make their extraction from the treatment systems easy even by applying simple magnets. These observations are found to be matched significantly with those observed by several authors previously [209][265].

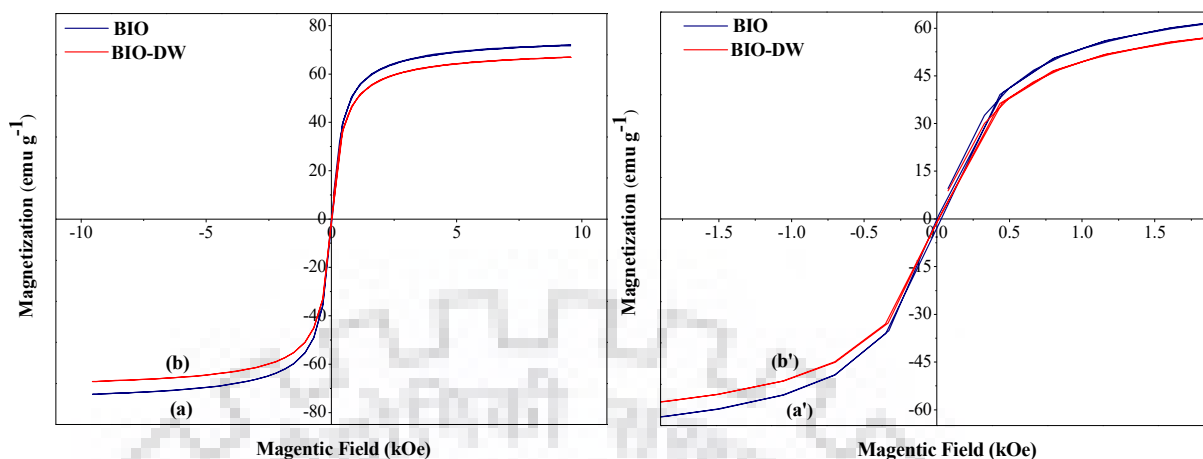


Figure 3.10. M-H curves of BIO NPs and BIO-DW nano hybrids recorded in the different magnetic field range A. -10 to +10 kO_e (a and b) B. -2 to +2 kO_e (a' and b') at ambient temperature.

3.6.12 SQUID analysis (M-H curve)

The magnetic behaviour of as-synthesized BIO NPs and BIO-DW nano hybrids has been examined by recording their M-H curves at three different temperatures (K): 300, 150 and 5 at an interval of 0.02 T of applied field (Figure 3.11 and 3.12). The M-H curves at 300 K for both BIO and BIO-DW nanosystems exhibit reversible hysteresis loop with a fairly high magnetization value and very low value of magnetic remanence and coercivity. A very similar magnetic behaviour for both of these nanosystems has been observed at 150 K (Table 3.4). Generally, the magnetic materials in nanometer size range show superparamagnetic behaviour having coercivity value below 150 O_e [266]. It suggests that both of these samples have high magnetization and exhibit superparamagnetic behaviour. A slight lower value (Table 3.4) of BIO-DW is understood to have arisen due to the coating of organics from the industry waste.

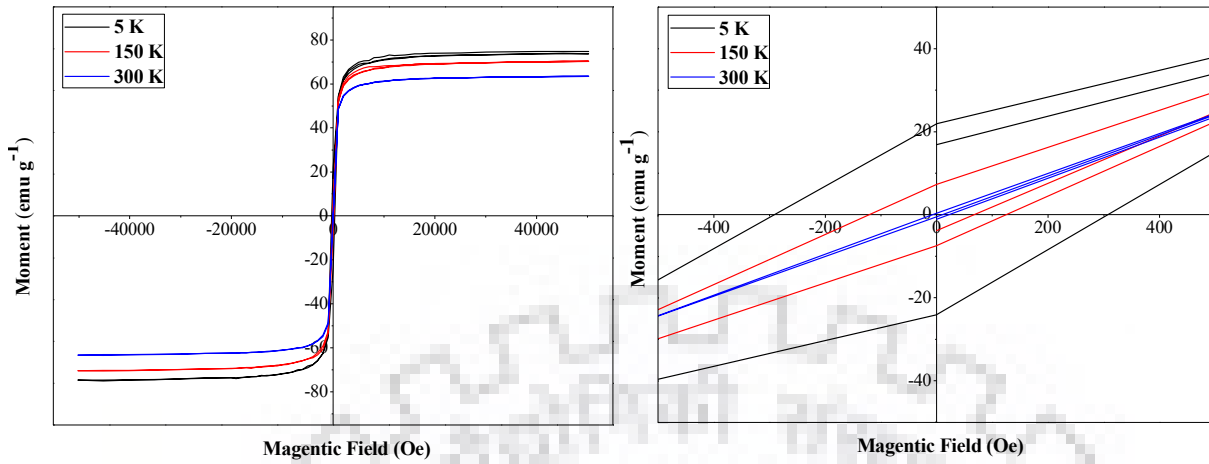


Figure 3.11. M-H curves of BIO NPs at 5K, 150 K and 300 K.

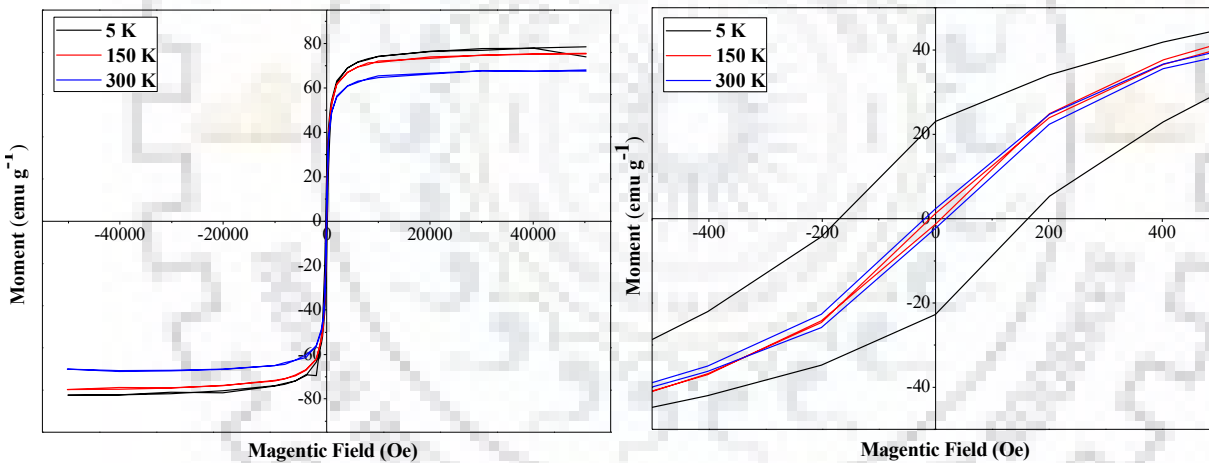


Figure 3.12. M-H curves of BIO-DW nanohybrids at 5K, 150 K and 300 K.

The M-H curves at 5 K for both BIO and BIO-DW nanosystems exhibit irreversible hysteresis loop with a fairly high magnetization having relatively higher M_r (20.9; 22.9) and H_c (305.1; 164.2) compared to those recorded at 300 and 150 K. It indicates that at 5 K, these samples have ferromagnetic nature. It may be attributed to the surface anisotropy of these samples at low temperature.

Table 3.4. Details of M-H curve for BIO NPs and BIO-DW nanohybrids at temperature (K) 300, 150 and 5.

Sample	Saturation magnetization (M_s) (emu g^{-1})	Remanence (M_r) (emu g^{-1})	Coercivity (H_c) (O_e)
300 K			
BIO	63.8	0.34	8.5
BIO-DW	67.4	0.99	9.5
150 K			
BIO	69.5	7.0	126.4
BIO-DW	75.7	2.4	19.8
5 K			
BIO	74.4	20.9	305.1
BIO-DW	77.9	22.9	164.2

3.6.13 Zero-field-cooled (ZFC) and Field-cooled (FC) measurements

Figure 3.13 shows the temperature dependence of magnetization under FC (field-cooled) and ZFC (zero-field-cooled) conditions. It has been recorded at an external field of $800 O_e$ under the varied temperature range from 5-300 K for both of the as-synthesized BIO and BIO-DW nanosystems.

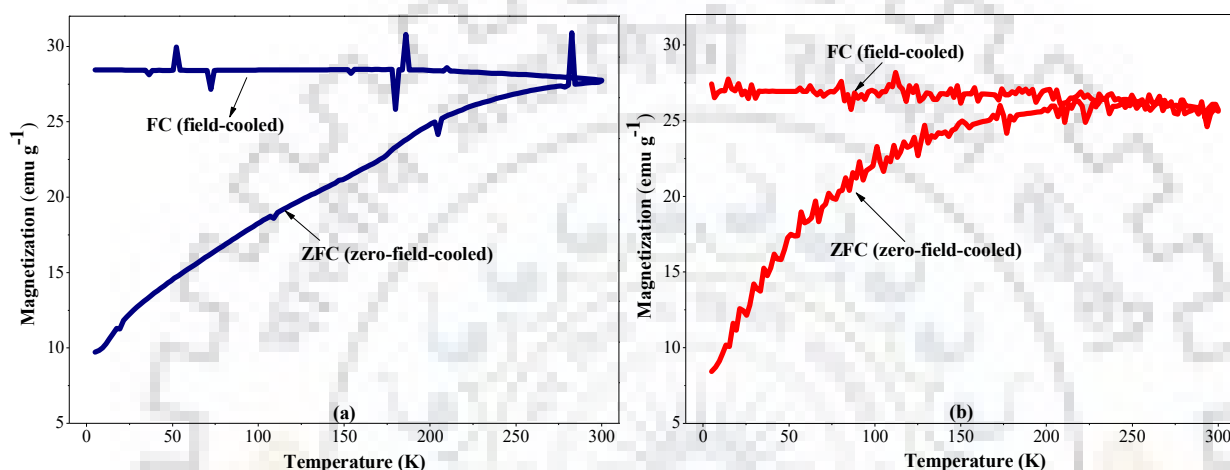


Figure 3.13. Temperature dependence of the magnetization for ZFC (zero-field-cooled) and FC (field-cooled) for (a) BIO NPs and (b) BIO-DW nanohybrids in a range of 5 to 300 K at applied field $H= 800 O_e$.

3.6.14 FTIR spectra

The FTIR spectra of industry waste, bare maghemite NPs and their functionalized nanostructures have been recorded in the wavenumber range of $400-4000 \text{ cm}^{-1}$. The details of their vibrational bands have been presented in Table 3.5. Whereas, the respective spectra(s) are shown in Figure 3.14.

The vibrational bands (cm^{-1}) for assigned functional groups(s) observed for distillery waste include: [861 (C-O-C), 928 (Symm. SO_4^{2-}), 1039 (C=S and CC alicyclic, aliphatic chain vibrations), 1119 and 1196 (C=S, CC alicyclic, aliphatic chain vibrations and SO_4^{2-} (asym.)), 1271, 1315 and 1400 (CH_2 and CH_3 (asym.)), 1570 (C=C, C- NO_2 (asym.)), N=N aliphatic), 1766 (C=C and C=O), 2976 (CH stretch) and 3194 (OH stretch)]. Whereas, the vibrational bands for BIO NPs include: [430, 532, 622, 687 (Fe-O stretch), 807 (SO_4^{2-}), 891, 977 (Symm. SO_4^{2-}), 1050, 1109 (=S, CC alicyclic, aliphatic chain vibrations and SO_4^{2-} (asym.)), 1622 (NH stretch), 3275 (OH stretch)]. Further, the vibrational bands for BIO-DW nanohybrids are including groups such as: [431, 532,

690 (Fe-O stretch), 818 (C-O-C), 974 (Symm. SO_4^{2-}), 1039 (C=S and CC alicyclic, aliphatic chain vibrations), 1119 (C=S, CC alicyclic, aliphatic chain vibrations and SO_4^{2-} (asym.)), 1413 (CH_2 and CH_3 (asym.)), 1590 (C=C, C- NO_2 (asym.)), 1840, 3283 (OH stretch)]. For BIO and BIO-DW nanosystems, these bands are fairly matched with those reported for bare $\gamma\text{-Fe}_2\text{O}_3$ NPs in the literature. The presence of these functional groups suggest the possible organics as observed earlier [209], [210].

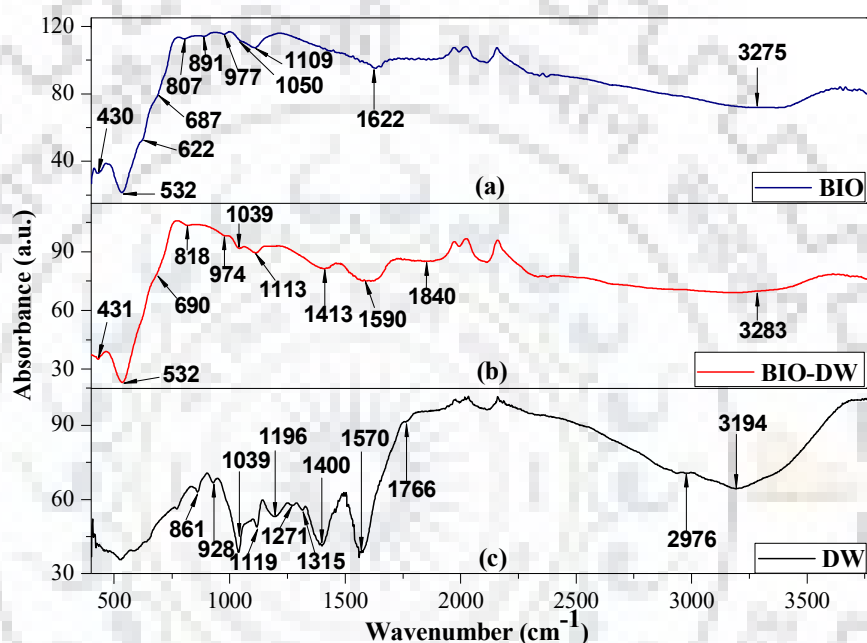


Figure 3.14. FTIR spectra of as-synthesized NPs (a) BIO (b) BIO-DW (c) DW (distillery waste).

An examination of IR-spectra in Figure 3.14 shows that the functionalization of BIO NPs using industry waste results in a change in the vibrational frequencies due to $-\text{OH}$, C=C/ C=O, CH_2/CH_3 (asym.), C=S/ CC alicyclic/ aliphatic chain vibrations/ SO_4^{2-} (asym.), symm. SO_4^{2-} and C-O-C upon reacting with the different molecules present in waste, and get shifted from 3194, 1766, 1400, 1119, 928, 861 to 3283, 1840, 1413, 1113, 974 and 818 cm^{-1} , respectively. Moreover, the skeletal vibration(s) 2976, 1570, 1315, 1271, 1196 cm^{-1} have completely vanished. The results depict that distillery waste interacts with BIO NPs not only through organic groups such as amines ($-\text{NH}_2$) and hydroxyls ($-\text{OH}$), but also some other groups such as carbonyl ($-\text{C}=\text{O}$) and azo ($\text{N}=\text{N}$) along with alkene and alkynes to a certain extent.

Table 3.5. FTIR data (cm^{-1}) of BIO NPs, BIO-DW nanohybrids and distillery waste.

Group/Moiety	Vibrational frequency (cm^{-1})		
	BIO	Distillery Waste (viscous pH-12.5)	BIO-DW
OH stretch	3275	-	3283
	-	3194	-
CH stretch	-	2976	-
NH stretch	1622	-	Disappeared
C=C and C=O	-	1766	1840
C=C, C-NO ₂ (asym.)	-	-	1590
C=C, C-NO ₂ (asym.), N=N aliphatic	-	1570	-
CH ₂ and CH ₃ (asym.)	-	1400	1413
	-	1315	-
	-	1271	-
C=S, CC alicyclic, aliphatic chain vibrations and SO ₄ ²⁻ (asym.)	1109	1196	-
	-	1119	1113
	1050	-	-
C=S and CC alicyclic, aliphatic chain vibrations	-	1039	1039
Symm. SO ₄ ²⁻	977	928	974
	891	-	-
SO ₄ ²⁻	807	-	Disappeared
C-O-C	-	861	818
FeO peaks	687	-	691
	622	-	-
	532	-	532
	430	-	431

3.6.15 Zeta-potential measurements

The surface modification and stability behaviour of the as-synthesized BIO NPs and BIO-DW nano hybrids have been confirmed through zeta (ζ) potential measurements (Figure 3.15). These calculations are measured in the colloidal aqueous solution for both of NPs in a wide pH range of (2.0 - 10.0), adjusted using acetic acid and/or NaOH.

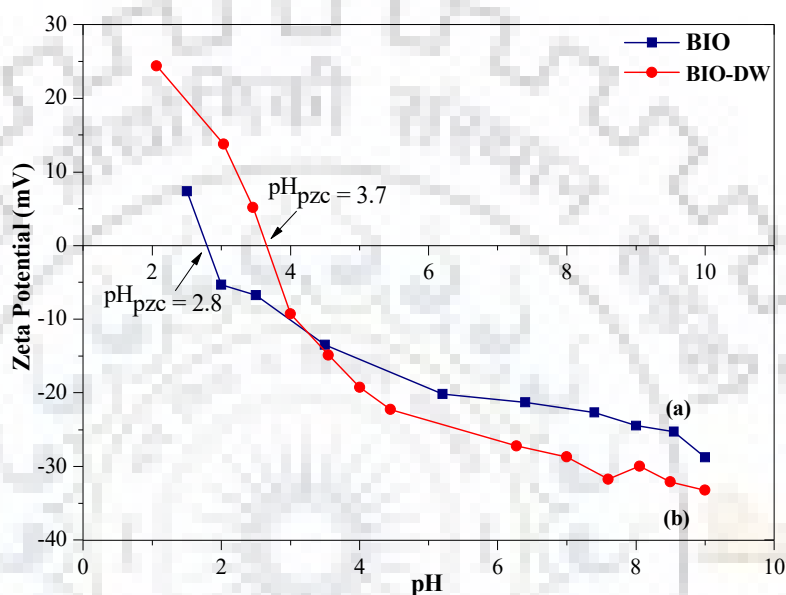


Figure 3.15. Zeta (ζ) potential measurements of as-synthesized (a) BIO NPs and (b) BIO-DW nano hybrids.

The values of zeta-potential have got transformed from 9.5 mV to -29.6 mV and 24.9 mV to -34.8 mV with an increase in pH 2 to 10, respectively. The data reveal that colloidal stability of functionalized nanostructures (BIO-DW) increases as compared to those of BIO NPs. The pH_{pzc} of the bare $\gamma\text{-Fe}_2\text{O}_3$ NPs has been determined to be about 2.8, which are different from the values of 5.7, 6.1 and 7.5 as reported previously [225], [267]. After the binding of functional moieties in BIO-DW nano hybrids, the pH_{pzc} has been found shifted to 3.7. This satisfies the binding of organic functionalities and also reveals that the BIO-DW nano hybrids are positively charged at $\text{pH} < 3.7$. However, both of these nanosystems are prone to have negatively charged surfaces in the pH range set for drinking water by WHO.



Batch experiments for arsenic removal and modelling of kinetics and adsorption isotherms

4.1 Chapter abstract

The literature reveals that the majority of metal oxide(s) based nanoadsorbents exhibit significant interactions with the oxyanions of As^{V} as compared to those of As^{III} . Therefore, investigations have been undertaken to explore the As^{V} removal utilizing BIO NPs and BIO-DW nanohybrids. Their adsorption potential has been evaluated in aqueous solution by designing various batch experiments.

The capabilities and behaviour of As^{V} removal have been evaluated through fractional factorial design of experiments, kinetic and isotherm models by utilizing both the as-synthesized NPs. Firstly, an optimized value of contact time has been calculated along with simultaneously maximizing the adsorption capacity and minimizing the dose amount under near neutral pH conditions at 15 °C by employing Response Surface Methodology (RSM). For this purpose, variation of the following parameters in the stated ranges have been taken into consideration keeping a fixed concentration of As^{V} at 4.0 mg L⁻¹; pH (7-9), temperature (10-30 °C), adsorbent dose (0.25-0.45 g L⁻¹) and contact time (2-314 min). Then, the appropriate kinetic and isotherm models have been investigated for analysing the nature of the adsorption process. These include Pseudo-first-order, pseudo-second-order, intra-particle diffusion, Elovich and Freundlich, Langmuir, Tempkin and Dubinin models respectively. Further, the possibilities of secondary pollution have also been examined by analysing the concentration of iron and organics in the supernatant.

Lesser contact time to achieve an optimum value of removal has been observed by BIO-DW (151 min) nanohybrids as compared by BIO (272 min) NPs suggesting a relatively faster adsorption of As^{V} onto BIO-DW nanohybrids. A good correlation coefficient (R^2) of > 0.99 for pseudo-second-order kinetics has indicated that the removal occurred largely through chemisorption. Fitting of adsorption data in Webber and Morris equation has indicated removal process to be complex involving both boundary layer and intra-particle-diffusion mechanisms.

A fairly good fit of adsorption data in Elovich model has demonstrated the involvement of heterogeneous surfaces during the interactions of As^{V} oxyanions and surface moieties. In order to examine the possibility of adsorption of As^{V} on the used NPs, the kinetic data have also been analyzed by employing Tempkin model, which displayed a moderately good association at low dose concentration of 0.30 g L^{-1} of adsorbent suggesting partial involvement of physisorption in the removal process. Further, the Langmuir capacity ($\text{mg g}^{-1}\text{-Fe}$) for As^{V} removal has been calculated to be 129.86 and 166.67 for BIO NPs and BIO-DW nano hybrids respectively. Both the nanosystems have not shown any signs of secondary pollution due to iron after removal of As^{V} in the near neutral pH conditions.

4.2 Materials and instrumentation

Arsenic working solution(s) have been prepared using sodium arsenate, dibasic heptahydrate ($\text{Na}_2\text{HAsO}_4 \cdot 7\text{H}_2\text{O}$, M.W. = $312.01 \text{ g mol}^{-1}$) salt, purchased from Merck enterprises. The ICP-MS grade (Merck) standard solution of As^{V} has been used for the calibration. All other required salts and reagents have been procured/prepared as mentioned in the chapter 3 (Section 3.2).

The arsenic concentration in all the samples has been measured using Microwave-Plasma Atomic Emission Spectroscopy 4100 (MP-AES) of Agilent Technologies (California, USA). The orbital shaking incubator (Model: CIS - 24 Plus from M/S REMI laboratories, India) has been used to carry out the batch experiments in the temperature and shaking speed range of $5 - 60 \pm 0.5 \text{ }^\circ\text{C}$ and 20 - 250 RPM, respectively.

4.3 Methodology

4.3.1 Experimental design, model fitting and statistical analysis

In the present work, we have optimized the contact time required for As^{V} removal using BIO and BIO-DW nanosystems along with simultaneously maximizing the adsorption capacity and minimizing the amount of dose under near neutral pH conditions. Generally, the response surface methodology (RSM) is a widely used statistical approach for the design of experiments among the research communities [268], [269]. This methodology greatly helps in reducing the number of experiments, thus minimizing the experimental cost and consumption of time [270].

This study utilizes the CCD (central composite design) to use RSM for optimization procedure. To validate the results of removal capacity, adsorption experiments have been conducted employing

the optimized process variables values derived from RSM prediction. Further, the removal kinetics and adsorption isotherm experiments have also been carried out using the optimized conditions obtained from RSM.

4.3.2 Predictive Modeling Using Response Surface Methodology

In the determination of linear and quadratic models, a statistical experimental approach based on central composite design (CCD) has been utilized. This design includes a combination of cubic, star and centre which represent a set of two level full factorial design, additional axial points and centre points for the experimental region respectively [120][271]. The repetition of center points is indicated as the step of improvement for experimental precision.

The reproducibility and experimental error of data have been used in determination through the center points, represented with code (0). The codes (-1, +1) have been used for independent variables. Among these, low level values have been coded as -1, and +1 for high level values. The relationship between the five independent variables of four process variables have been approximated by mathematical empirical (2nd order polynomial multiple regression) equations, as shown below in 4.1:

$$y = \beta_0 + \sum_{i=1}^n \beta_i x_i + \sum_{i=1}^n \beta_{ii} x_i^2 + \sum_{i < j}^n \beta_{ij} x_i x_j + \varepsilon \quad (4.1)$$

Where, the predicted response (y) of the experimental design is correlated to the set of regression coefficient (β), the intercept (constant, β_0), linear coefficient ($\beta_i - \beta_n$), interaction coefficient ($\beta_{ii} - \beta_{nn}$) and quadratic coefficient ($\beta_{ij} - \beta_{in}$); n is denoting the variables number; ε refers to the experimental error which has been assumed to be randomly distributed about the mean value near to zero. The Design-Expert software, (Stat-Ease Inc., 7.0) has been used for regression, ANOVA, desirability coefficient and for the graphical analyses of corresponding data.

This study has investigated the interactive effects and relative significance of input process variables such as pH, temperature, adsorbent dose and contact time on the removal capabilities of as-synthesized nanomaterials employing RSM with CCD. A set of 30 experimental runs have been performed as indicated by design expert software, comprising 16 (factorial), 8 (axial) and 6

(replicate) experiments at the central (0) point. Equation 4.2 has been employed for arriving at this design of experiments:

$$N = 2^n + 2n + n_c = 2^4 + (2 \times 4) + 6 = 30 \quad (4.2)$$

Where, N and n are referring to the total number of required experiments and numeric factors, respectively, n_c denotes the number of replicates at the central point. These experiments have been performed for the different range values of pH, temperature ($^{\circ}\text{C}$), adsorbent dose (g L^{-1}) and contact time (min) for both BIO NPs and BIO-DW nanohybrids at the As^{V} concentration of 4.0 mg L^{-1} and shaking speed of 250 rpm. The details of process parameters are mentioned in Table 4.1.

Table 4.1. Range of experimental input variables for As^{V} (initial concentration- 4 mg L^{-1}) removal using BIO NPs and BIO-DW nanohybrids at shaking speed of 250 rpm.

Parameters	Levels			Star point $\alpha = 2.0$	
	Low (-1)	Central (0)	High (+1)	- α	+ α
(A ₁) pH	5.5	7.0	8.5	4	10
(A ₂) Temperature ($^{\circ}\text{C}$)	15	20	25	10	30
(A ₃) Dose (g L^{-1})	0.30	0.35	0.40	0.25	0.45
(A ₄) Shaking Time (min)	80	158	236	2	314

4.3.3 Desirability Function

The CCD, utilizes the Derringer's desirability function in determining the optimal conditions by describing the desirability function (D_F). For each response (d_i), this methodology develops a function (D) after the transformation of experimental response (U_i) and predicted response (\hat{U}_i). This function creates an optimum value by maximizing the selection of effective variables by considering the interaction among them [272]. In the first step, a desirability function (df_i) between the range of 0 to 1 is formed after the conversion of response (U). Its value equal to zero represents that the response is undesirable or having minimum applicability [273], whereas, its unit value indicates the desirable or absolute response. In second step, each desirability value is then combined using

geometrical mean, which gives the overall desirability D for an experimental run. Its equation can be described as mentioned below:

$$D_f = \left\{ d_{f_1}^{v_1} \times d_{f_2}^{v_2} \times d_{f_3}^{v_3} \dots \dots d_{f_n}^{v_n} \right\}^{1/n}; 0 \leq v_i \leq 1 (i = 1, 2, 3 \dots, n) \quad (4.3)$$

Where, d_{f_i} to d_{f_n} are demonstrating the desirability of the response ($i = 1, 2, 3, \dots, n$) and V_i is highlighting the importance of responses. It can be presented as below:

$$\sum_{i=1}^n v_i = 1 \quad (4.4)$$

The desirability function for each characteristic involves the computation utilizing the following equations:

$$d_{f_i} = \left[\frac{U - \alpha}{\beta - \alpha} \right]^{w_i}; \alpha \leq U \leq \beta \quad (4.5)$$

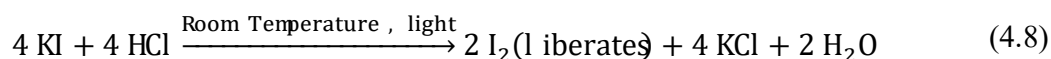
$$d_{f_i} = 1, \quad U > \beta \quad (4.6)$$

$$d_{f_i} = 0, \quad U < \alpha \quad (4.7)$$

Where, α and β indicate the low and high values for the experimental response; and W_i denotes the weight value.

4.3.4 Determination of arsenic concentration

To prepare the samples for arsenic determination using Inductively Coupled Plasma Spectrometry (ICP-MS), the samples were treated with potassium iodide (KI, 1.5 g / 100 ml) and hydrochloric acid (HCl, 1 ml / 100 ml) at least one hour prior to the analysis. For calibration, the arsenate stock standard solution was diluted with a solution containing KI and HCl having the percentage ratio of 15:10 to prepare the concentrations. The reaction between potassium iodide and hydrochloric acid generates iodine gas which reduces As^V to As^{III} . The reaction is mentioned below:



The vapour generation apparatus was used to aspirate the sample through a standard nebulizer to microwave magnetically excited nitrogen plasma at flow uptake of 1.4 ml min⁻¹. The emission lines were recorded at two identical wavelengths of 193.695 nm and 234.984 nm during the measurements.

The acid digested samples were filtered through WhatmanTM 42 cellulose, before the analysis of heavy metals using ICP-MS equipped with quadrupole mass spectrometry Q-MS technique, which allowed the instrument to analyse the samples with high accuracy [274]. The detection limit for all heavy metals were in µg L⁻¹ range.

4.3.5 Calculation of arsenic removal capacity

The adsorption capabilities of BIO NPs and BIO-DW nanohybrids have been determined by using the material balance in an adsorption system. It mainly measures the adsorbate which gets disappeared from the solution. The As^V removal capacity (mg g⁻¹ of Fe) values have been calculated using the following equation:

$$\text{Removal cap acity}(q_e) = \frac{(C_0 - C_f) V}{W} \quad (4.9)$$

Where C_0 and C_f are demonstrating the initial and final concentration (mg L⁻¹) of As^V in the aqueous solution, respectively; W refers to the nanoadsorbent mass in grams; V is denoting the volume of the solution in litres.

4.3.6 Kinetic models

In literature, different mathematical models have been proposed by several authors to examine the removal kinetics of adsorption data. Generally, these adsorption models are classified on the basis of chemical reactivity and diffusion mechanisms which have been explored for analysing the kinetics of the adsorption process(s) for contaminant removal. Among different kinetic models, the mechanism of adsorption process can be explained using first-order-kinetics, second-order-kinetics, intra-particle diffusion and Elovich models. These experiments have been performed for a varied adsorbent dose ranging from 0.15-0.45 g L⁻¹ and As^V concentration of 4 mg L⁻¹ at the optimized

contact time, as calculated by RSM for both BIO and BIO-BW NPs. The details of the explored models have been discussed further.

4.3.6.1 Pseudo-first-order model

It has been considered as the foremost model which explained the relation between rate of adsorption and adsorption capability of an adsorbent [275]. Lagergren (1898) has described the kinetics of liquid-solid phase adsorption in the form of first-order rate equation. It has been presented in equation form as follows:

$$\frac{dq_t}{dt} = k_1(q_e - q_t) \quad (4.10)$$

Where, q_t demonstrates the adsorption capacity (mg g^{-1}) at time t ; k_1 denotes the pseudo-first-order rate constant (time^{-1}) and q_e indicates the adsorption capacity (mg g^{-1}) at equilibrium. The equation has been transformed after integrating [276] the above equation by applying the boundary conditions (i.e. $t = t$; $q_e = q_t$), and the resulting equation is presented below:

$$\log(q_e - q_t) = \log q_e - k_1 t \quad (4.11)$$

The linearized form of the above equation is given as below:

$$q_t = q_e(1 - e^{-k_1 t}) \quad (4.12)$$

The linear plot between $\log(q_e - q_t)$ vs. t give the value of k_1 , which can be determined from the slope of the plot. The Lagergren's first-order rate equation has also been considered as pseudo-first-order because of its demonstration to calculate the adsorption capacity from solution concentration.

4.3.6.2 Pseudo-second-order model

It is based on the characteristic that the removal of contaminants from aqueous solution involves the interactions through sharing or the exchange of electrons among the adsorbate and

functionalities of the adsorbent [276]. It has been described by Ho and McKay (1995), who assumed that the removal capabilities are directly related to available number active sites onto the adsorbent surface [277]. The expression for pseudo-second-order rate is given as below:

$$\frac{dq_t}{dt} = k_2(q_e - q_t)^2 \quad (4.13)$$

Where, q_t demonstrates the adsorption capacity (mg g^{-1}) at time t ; k_2 denotes the pseudo-second-order rate constant for sorption ($\text{g mg}^{-1}\text{min}^{-1}$) and q_e indicates the adsorption capacity (mg g^{-1}) at equilibrium. The equation has been transformed after integrating the above equation by applying the boundary conditions (i.e. $t = t$; $q_e = q_i$), and the equation is presented below:

$$\frac{1}{(q_e - q_t)} = \frac{1}{q_e} + k_2 t \quad (4.14)$$

This reaction represents the integrated rate law for pseudo-second-order kinetics. The linearized form of the above equation is given as below:

$$\frac{t}{q_t} = \frac{1}{k_2 q_e^2} + \frac{1}{q_e} t \quad (4.15)$$

The rate constant (k_2) can be obtained from a plot of t/q_t against t .

4.3.6.3 Intra-particle diffusion

Generally, the adsorbate species are transported onto the solid phase from bulk solution via an intra-particle diffusion process. It has been related with the rate-limiting steps in most of the adsorption processes. Weber and Morris have described that the adsorption process occurs through different steps as the adsorbate approaches the adsorbent in aqueous solution [278]. The process has been explained by the following equation:

$$q_t = k_{\text{Dif}} t^{1/2} + C \quad (4.16)$$

Where, C indicates the intercept; k_{dif} ($\text{g mg}^{-1} \text{min}^{-1/2}$) represents the intra-particle diffusion rate constant which can be calculated from the slope of the regression line.

4.3.6.4 Elovich kinetic model

This model is useful in describing the adsorption of contaminant ions onto highly heterogeneous adsorbents [279]. It is represented by the following equation:

$$q_t = \frac{1}{\beta} \log(\alpha\beta) + \frac{1}{\beta} \log t \quad (4.17)$$

Where, q_t is a linear function of $\log(t)$; β and α demonstrate the Elovich constants and their values can be obtained from the slope and intercept, respectively.

4.3.7 Isotherm models

Adsorption isotherms are valuable tools for the evaluation and explanation of experimental adsorption data. The maximal adsorption capacity can be derived from the adsorption isotherm, and has also been used to compare the efficiency of different adsorbents. Adsorption can be divided into two main groups: physisorption and chemisorption.

Physisorption occurs due to the interaction of adsorbate through the residual forces onto the surface of adsorbent. These are known as van der Waal forces, dipole and induced dipole interactions. These attractions are long-range and weak, and the adsorbate retains its identity during the adsorption. Typical values of the enthalpy are about 20 kJ mol^{-1} . Because of the involvement of low energy, these types of interactions are not led to the formation of a chemical bond. Further, the interaction between ligands and a metal ion is also considered as physisorption. A ligand is described as a molecule (a functional group) or an ion that forms a complex with a metal ion. Chelating ligands are formed symmetrically around the metal ion via multiply bound ligands, such that the metal ion occupies the central position.

Chemisorption generally involves covalent bonding. It is much stronger than that of the Van der Waal interactions. The enthalpy of chemisorption is thus much higher as compared to those of

physical adsorption. It has been reported to be in the range of 20-200 kJ mol⁻¹. In evaluating the adsorption data in the present study, following adsorption models have been explored.

4.3.7.1 Freundlich adsorption isotherm

It is a common and widely explored isotherm model which describes the adsorption characteristics of the heterogeneous surface [280]. It is represented as:

$$Q_e = K_f C_e^{1/n} \quad (4.18)$$

Where K_f denotes the Freundlich isotherm constant (mg g⁻¹); n refers to intensity of adsorption; C_e demonstrates the concentration (mg L⁻¹) of adsorbate at equilibrium; Q_e indicates the adsorbed (mg g⁻¹) amount of adsorbate at equilibrium. The linearized form of the above equation is given below:

$$\log Q_e = \log K_f + \frac{1}{n} \log C_e \quad (4.19)$$

The K_f is a constant and indicates the adsorption capabilities; $1/n$ refers to a function which demonstrates the strength of adsorption process. It represents the adsorption process to be normal and cooperative for values of < 1 and > 1 , respectively. Whereas, value of n equal to 1 indicates that the partition between the two phases is concentration independent.

4.3.7.2 Langmuir adsorption isotherm

This model represents the equilibrium distribution of contaminant ions between the solid and liquid phases. During the adsorption process, it quantitatively describes the formation of monolayer onto the surface of adsorbent which is having finite number of adsorption sites [279]. Thereafter, no adsorption takes place. It also assumes a uniform distribution of energies during adsorption and an absence of migration of adsorbate into the surface planes. It is represented by the following equation:

$$q_e = \frac{Q_0 K_L C_e}{1 + K_L C_e} \quad (4.20)$$

Further, Langmuir adsorption parameters are calculated by transforming the above equation into linear form, as mentioned below:

$$\frac{1}{q_e} = \frac{1}{Q_0} + \frac{1}{Q_0 K_L C_e} \quad (4.21)$$

Where, C_e demonstrates the concentration (mg L^{-1}) of adsorbate at equilibrium; q_e denotes the amount of contaminant adsorbed (mg g^{-1}) onto the adsorbent at equilibrium; Q_0 refers to the maximum monolayer capacity or Langmuir capacity (mg g^{-1}); K_L (L mg^{-1}) indicates the Langmuir isotherm constant. After the Langmuir plot between $1/q_e$ vs. $1/C_e$, the values of q_{max} and K_L are determined from the slope and intercept. The dimensionless constant, which is a necessary characteristic of the Langmuir isotherm and expressed as equilibrium parameter (R_L), is calculated from the following equation:

$$R_L = \frac{1}{1 + (1 + K_L C_0)} \quad (4.22)$$

Where, C_0 indicates the adsorbate initial concentration; K_L represents the constant highlighting the energy of adsorption. The value of R_L explains the nature of adsorption. Its value > 1 and $0 < R_L < 1$ demonstrate the adsorption process to be unfavourable and favourable, respectively. However, the R_L value equal to 1 represents the adsorption process as irreversible [281].

4.3.7.3 Tempkin adsorption isotherm

In this model, it has been assumed that a linear decrease in the heat of adsorption occurs as the adsorbate occupies the surface of adsorbent [282]. It is applicable to all the molecules present in aqueous solution. Further, this adsorption of molecules has been characterized through uniform distribution of binding energy. This isotherm is described by the following equation:

$$q_e = \frac{RT}{b} \ln K_T + \frac{RT}{b} \ln C_e \quad (4.23)$$

Where, K_T denotes the equilibrium binding constant ($L \text{ mol}^{-1}$), which corresponds to the maximum binding energy; R represents the gas constant ($8.314 \text{ J K}^{-1}\text{mol}^{-1}$); b denotes the heat of adsorption and T is the temperature (K). The straight line plot between q_e vs. $\log_n(C_e)$ gives slope and intercept as RT/b and $(RT \ln KT)/b$ respectively.

4.3.7.4 Dubinin-Radushkevich adsorption isotherm

Generally, this model is applicable in exploring the adsorption mechanism onto the heterogeneous surface of adsorbents [283]. It describes the Gaussian energy distribution of adsorbate in adsorption process. However, this model has been reported to fit often for high solute as well as intermediate range of concentrations. This isotherm is described by the equation mentioned below:

$$q_e = (q_s) \exp(-K_{ad} \varepsilon^2) \quad (4.24)$$

The linearized form of the above equation is given as:

$$\log q_e = \log(q_s) - (K_{ad} \varepsilon^2) \quad (4.25)$$

Where, q_e demonstrates the amount (mg g^{-1}) of contaminant onto adsorbent; q_s refers to the theoretical value of saturation capacity of contaminant; K_{ad} demonstrates the isotherm constant of the model (Dubinin-Radushkevich); “ ε ” indicates the polyani potential. This approach usually distinguishes the adsorption behaviour as physisorption and chemisorption. Therefore, the apparent energy (E) for the adsorption process is calculated as mentioned in the equation below:

$$E = \left[\frac{1}{\sqrt{2B_{DR}}} \right] \quad (4.26)$$

The value of polyani potential has been calculated by applying the following equation:

$$\varepsilon = RT \ln \left[1 + \frac{1}{C_e} \right] \quad (4.27)$$

Where, R is representing the gas constant ($8.314 \text{ J K}^{-1} \text{ mol}^{-1}$); T is the temperature (K) and C_e demonstrates the concentration (mg L^{-1}) of adsorbate at equilibrium. The slope and intercept of the linear plot between $\log q_e$ vs ε^2 (polyani potential) determine the value of B_{DR} and K_{ad} , respectively.

4.4 Results and discussion

4.4.1 Response surface modelling and ANOVA analysis

A number of experiments have been performed to evaluate the removal capacity under the effect of various variables in specific operational ranges viz. pH (4-10), temperature ($10\text{-}30 \text{ }^\circ\text{C}$), dose concentration ($0.25\text{-}0.45 \text{ g L}^{-1}$) and contact time (2-314 min). The details of these experiments have been summarized in Table 4.2.

Linear, interactive and quadratic models have further been fitted to the experimental data and ANOVA (Analysis of variance) used to analyse the outcomes from RSM and experimental response models [284] in order to arrive at the optimal values of operating variables.

4.4.2 Optimization of arsenic removal

In order to optimize the operational variables (pH, temperature and time of mixing), experiments had been designed by varying these parameters for both BIO and BIO-DW nanosystems. The graphical representation of the data and analysis from RSM have been compared in the form of RS plots to understand the effects of different process parameters on As^{V} removal. The comparative RSM plots as a function of different variables for both BIO NPs and BIO-DW nanohybrids are shown in Figures (a-f) and Figures (a'-f').

4.4.2.1 Effect of process variables

The effects of variables have been discussed below on the basis of interpreting the response surface plots:

BIO nanoparticles

An examination of Figure a shows that a variation in pH from 5.5 to 8.5 by keeping rest of the conditions identical, i.e. dose (0.35 g L^{-1}) and contact time (158 min), results in a decrease in the extend of adsorption of As^{V} . This trend is observed for the examined temperature range ($10\text{-}30 \text{ }^{\circ}\text{C}$). However, this decrease in the removal capacity is slightly higher at $25 \text{ }^{\circ}\text{C}$. In the graph shown in Fig. b, a variation in the dose from $0.25\text{-}0.45 \text{ g L}^{-1}$ exhibits the maximum adsorption for the adsorbent amount of 0.36 g L^{-1} at a temperature of $20 \text{ }^{\circ}\text{C}$ and contact time of 158 min. Further, a variation in the contact time from 2-314 min at a temperature of $20 \text{ }^{\circ}\text{C}$ and dose of 0.35 g L^{-1} indicates the minimum and maximum removal capacity at about 80 min and 238 min, respectively (Fig. c).

In Fig. d, it is observed that a decrease in dose concentration (g L^{-1}) from 0.40 to 0.30 enhances the removal capacity in the whole range of studied temperature ($10\text{-}30 \text{ }^{\circ}\text{C}$). However, the removal capacity is found to be slightly higher at a lower dose of 0.30 g L^{-1} . In another plot (Fig. e), the simultaneous variation of time and temperature at a pH 7 and adsorbent dose of 0.35 g L^{-1} , shows less adsorption capability at a lower temperature and high contact time. The highest capacity is obtained at a temperature and time $25 \text{ }^{\circ}\text{C}$ and 236 min, respectively. Similar patterns i.e. the maximum adsorption for low adsorbent dose and time of mixing at 236 min have been observed by simultaneously varying time and dose while keeping pH and temperature constant to those concluded other observations (Fig. f).

BIO-DW nanoparticles

All the observations are quite similar to those analyzed for BIO NPs except for the variation in pH and time in BIO-DW nanohybrids. The removal capacity at pH increases from 5.5-8.5 at $25 \text{ }^{\circ}\text{C}$. High removal capacity is observed at the lower temperatures as compared to BIO NPs, whereas, at higher temperatures, the trend is quite similar to that BIO NPs. Moreover, these variations are sharper as compared to those observed for BIO NPs.

These observations clearly suggest that BIO NPs provide additional adsorption sites, which enhance the adsorption capacity at high temperature and pH conditions. Apparently, the functional groups available on the surface undergo increase in covalent interactions with the As^{V} oxyanions involving groups such as $-\text{NH}_2$, $-\text{OH}$, $-\text{C}=\text{O}$ and $\text{N}=\text{N}$, alkene and alkynes to a certain extent [285][286], [287].

4.4.2.2 Statistical analysis and fitting of second-order polynomial equation

ANOVA results of As^V removal for BIO NPs and BIO-DW nanohybrids are given in Table 4.3 and 4.4 respectively. Based on ANOVA, all the variables appear to demonstrate second-order effects, yielding a quadratic model for As^V removal for both BIO and BIO-DW nanosystems. Values of “Prob > F” less than 0.0001 indicated the model display high statistical significance. The large P-value (> 0.05) suggests lack of fit indicating that the F-statistics was insignificant for both the nanoparticles. These observations imply that there is a significant model correlation between experimental variables and response.

For BIO nanoparticles, ANOVA response for As^V removal obtained from response surface quadratic model (Table 4.3) shows that model term A, C and D are highly significant, whereas, BC and BD are significant terms. A high value of R² of 0.9800 (98 %) confirms a satisfactory fit of the quadratic model to experimental data. The quadratic equation in terms of the coded factors for response on As^V removal of BIO NPs is as follows:

$$\begin{aligned} \text{As}^{\text{V}} \text{ Removal}_{\text{BIO}} &= 12.13 - 1.09(A_1) + 0.09(A_2) - 0.96(A_3) + 0.44(A_4) \\ &+ 0.46(A_1^2) + 0.52(A_2^2) + 0.32(A_3^2) + 0.18(A_4^2) - 0.24(A_1A_2) \\ &+ 0.08(A_1A_3) + 0.04(A_1A_4) - 0.03(A_2A_3) + 0.12(A_2A_4) \\ &- 0.11(A_3A_4) \end{aligned} \quad (4.28)$$

For BIO-DW nanohybrids, the model terms A, C, D and B² are highly significant, whereas, B, AB, CD, A² and C² are significant terms (Table 4.4). A value of R² of 0.9715 (97.15 %), being close to unity, represents excellent fit. The quadratic equation in terms of the coded factors for response on As^V removal of BIO-DW nanoparticles is given below:

$$\begin{aligned} \text{As}^{\text{V}} \text{ Removal}_{\text{BIO-DW}} &= 18.55 - 1.14(A_1) + 0.40(A_2) - 1.93(A_3) + 0.75(A_4) \\ &+ 0.50(A_1^2) + 0.65(A_2^2) + 0.57(A_3^2) - 0.17(A_4^2) + 0.76(A_1A_2) \\ &- 0.25(A_1A_3) - 0.017(A_1A_4) + 0.013(A_2A_3) + 0.064(A_2A_4) \\ &- 0.11(A_2A_4) \end{aligned} \quad (4.29)$$

Where, A, B, C and D are representing the process variables such as pH, temperature (°C), nanoadsorbent dose (g L⁻¹) and contact time (min), respectively.

Table 4.2. Experimental inputs and response of BIO NPs and BIO-DW nanohybrids at As^V concentration 4 mg L⁻¹ and 250 rpm.

Factor					Removal capacity (mg g ⁻¹ -Fe)	
Runs	A ₁	A ₂	A ₃	A ₄	BIO	BIO-DW
1.	5.5	25	0.40	236	13.95	19.57
2.	10.0	20	0.35	158	11.39	17.01
3.	5.5	15	0.40	236	13.11	20.22
4.	8.5	25	0.40	236	11.43	18.34
5.	7.0	20	0.35	158	11.98	18.67
6.	8.5	15	0.30	80	12.84	19.31
7.	5.5	25	0.30	80	15.05	21.80
8.	5.5	15	0.40	80	12.62	19.33
9.	7.0	10	0.35	158	13.98	19.93
10.	5.5	25	0.40	80	13.28	18.65
11.	7.0	20	0.35	314	12.56	19.12
12.	8.5	25	0.40	80	10.87	18.11
13.	5.5	25	0.30	236	16.02	23.14
14.	8.5	15	0.40	80	11.51	15.82
15.	4.0	20	0.35	158	16.50	23.41
16.	7.0	20	0.35	158	11.88	18.64
17.	7.0	20	0.35	2	10.16	15.93
18.	7.0	20	0.35	158	12.65	17.91
19.	7.0	20	0.35	158	12.13	18.62
20.	7.0	20	0.35	158	12.21	18.93
21.	8.5	25	0.30	236	13.91	24.14
22.	7.0	20	0.45	158	11.32	16.85
23.	7.0	20	0.35	158	11.92	18.53
24.	8.5	15	0.30	236	13.47	21.55
25.	7.0	20	0.25	158	15.39	24.17
26.	5.5	15	0.30	236	15.25	24.73
27.	5.5	15	0.30	80	14.74	21.98
28.	8.5	25	0.30	80	12.24	21.38
29.	7.0	30	0.35	158	14.37	21.74
30.	8.5	15	0.40	236	11.86	16.21

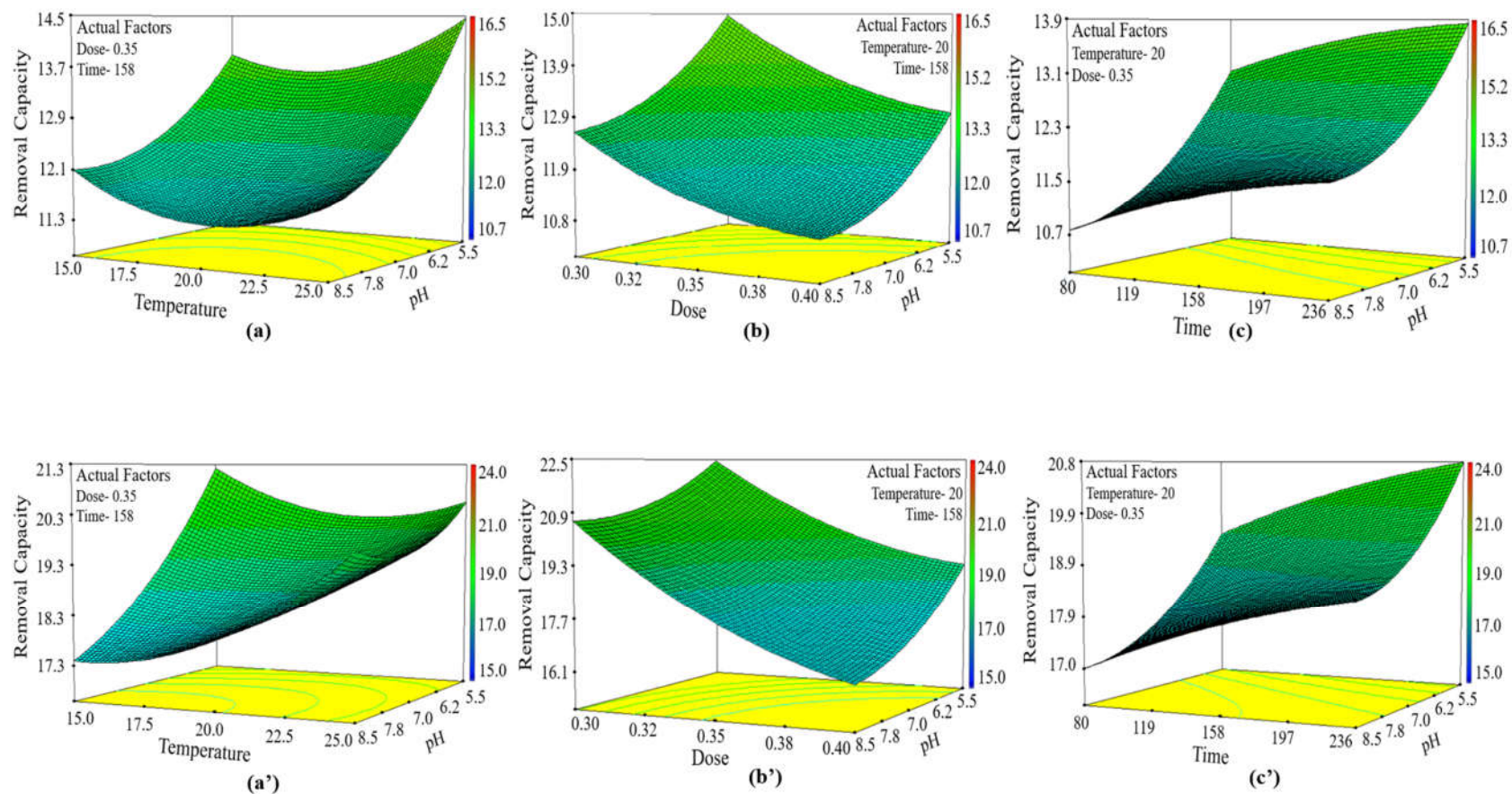


Figure 4.1. Response surface plots showing the effect of different input variables on removal capabilities of As^V using BIO NPs (a-c) and BIO-DW (a'-c') nanohybrids.

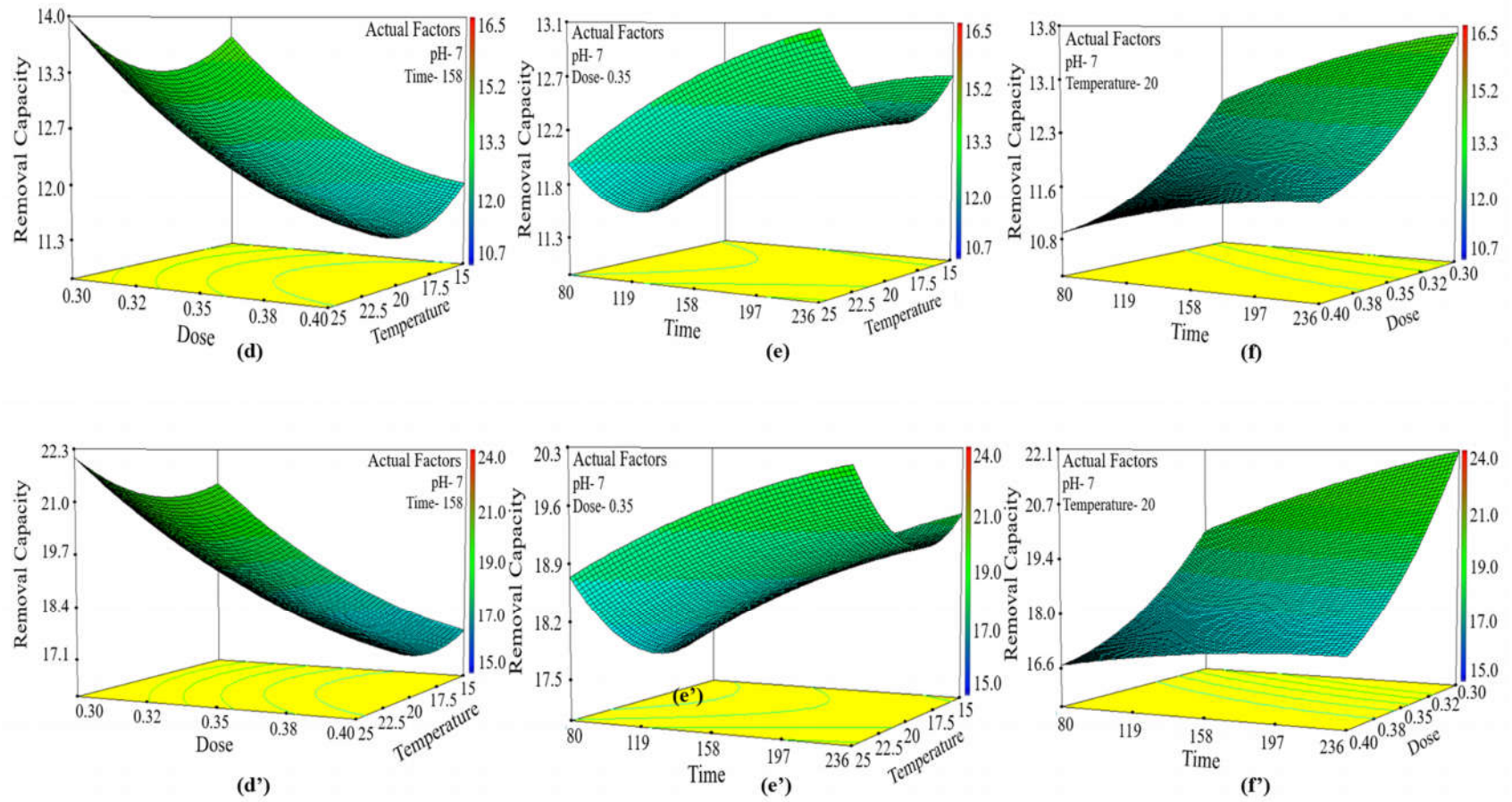


Figure 4.2. Response surface plots showing the effect of different input variables on removal capabilities of As^V using BIO NPs (a-c) and BIO-DW (a'-c') nanohybrids.

Table 4.3. ANOVA for Response surface quadratic model for As^V removal using BIO NPs.

Response source	Sum of Squares	DF	Mean Square	F-value	P > F	Remark
Model	72.66	14	5.19	52.38	< 0.0001	Highly significant
A- pH	28.41	1	28.41	286.68	< 0.0001	Highly significant
B- Temperature	0.19	1	0.19	1.91	0.1336	
C- Dose	22.10	1	22.10	223.03	< 0.0001	Highly significant
D- Contact time	4.73	1	4.73	47.70	< 0.0001	-do-
AB	0.91	1	0.91	9.16	< 0.0001	-do-
AC	0.11	1	0.11	1.08	< 0.0001	-do-
AD	0.020	1	0.020	0.20	< 0.0001	-do-
BC	0.015	1	0.015	0.15	0.0118	Significant
BD	0.22	1	0.22	2.25	0.0034	Significant
CD	0.18	1	0.18	1.84	0.2508	
A ²	5.87	1	5.87	59.24	0.6108	
B ²	7.42	1	7.42	74.88	0.6614	
C ²	2.72	1	2.72	27.49	0.1053	
D ²	0.93	1	0.93	9.34	0.1397	
Residual	1.49	15	0.099			
Lack of fit	1.08	10	0.11	1.33	0.3963	Not Significant
Pure error	0.41	5	0.081			
Cor. total	74.15	29				

Table 4.4. ANOVA for Response surface quadratic model for As^V removal using BIO-DW nanohybrids.

Response source	Sum of Square	DF	Mean Square	F-value	P > F	Remarks
Model	176.68	14	12.62	37.75	< 0.0001	Highly significant
A- pH	31.19	1	31.19	85.89	< 0.0001	Highly significant
B- Temperature	3.84	1	3.84	10.57	0.0054	Significant
C- Dose	89.78	1	89.78	247.24	< 0.0001	Highly significant
D- Contact time	13.35	1	13.35	36.76	< 0.0001	Highly significant
AB	9.27	1	9.27	25.53	0.0001	Significant
AC	1.01	1	1.01	2.78	0.1161	
AD	0.005	1	0.005	0.013	0.9091	
BC	0.003	1	0.003	0.007	0.9350	
BD	0.065	1	0.065	0.18	0.6782	
CD	2.77	1	2.77	7.63	0.0145	Significant
A ²	6.80	1	6.80	18.73	0.0006	Significant
B ²	11.74	1	11.74	32.32	< 0.0001	Highly significant
C ²	9.0	1	9.0	24.79	0.0002	Significant
D ²	0.82	1	0.82	2.27	0.1527	
Residual	5.45	15	0.36			
Lack of fit	4.87	10	0.49	4.18	0.0639	Not Significant
Pure error	0.58	5	0.12			
Cor. total	182.13	29				

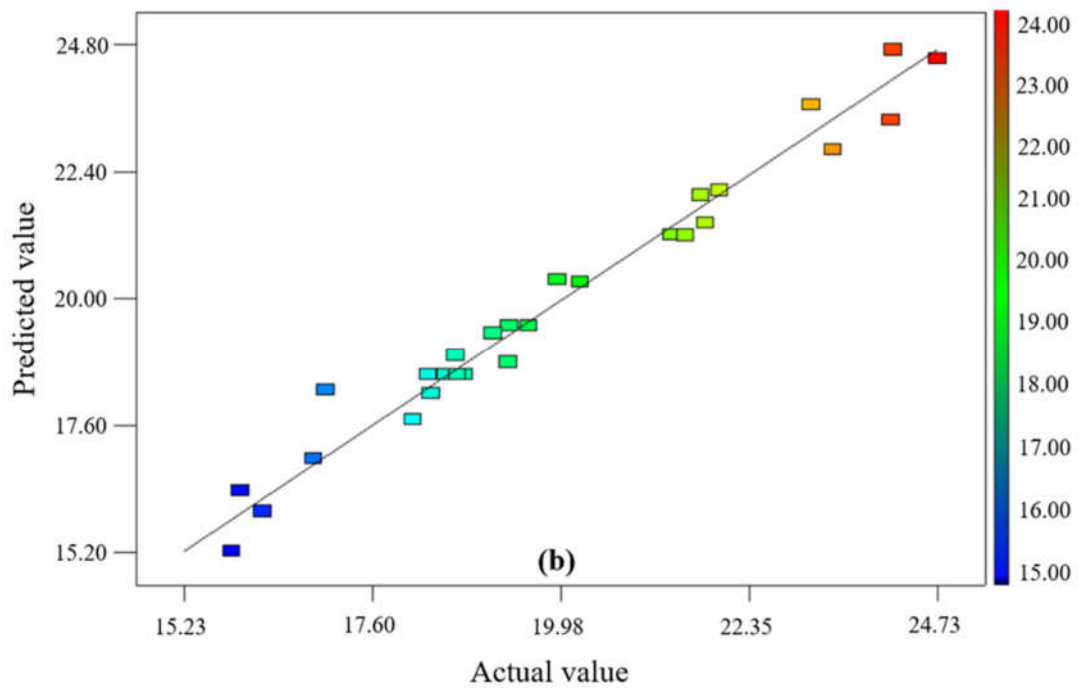
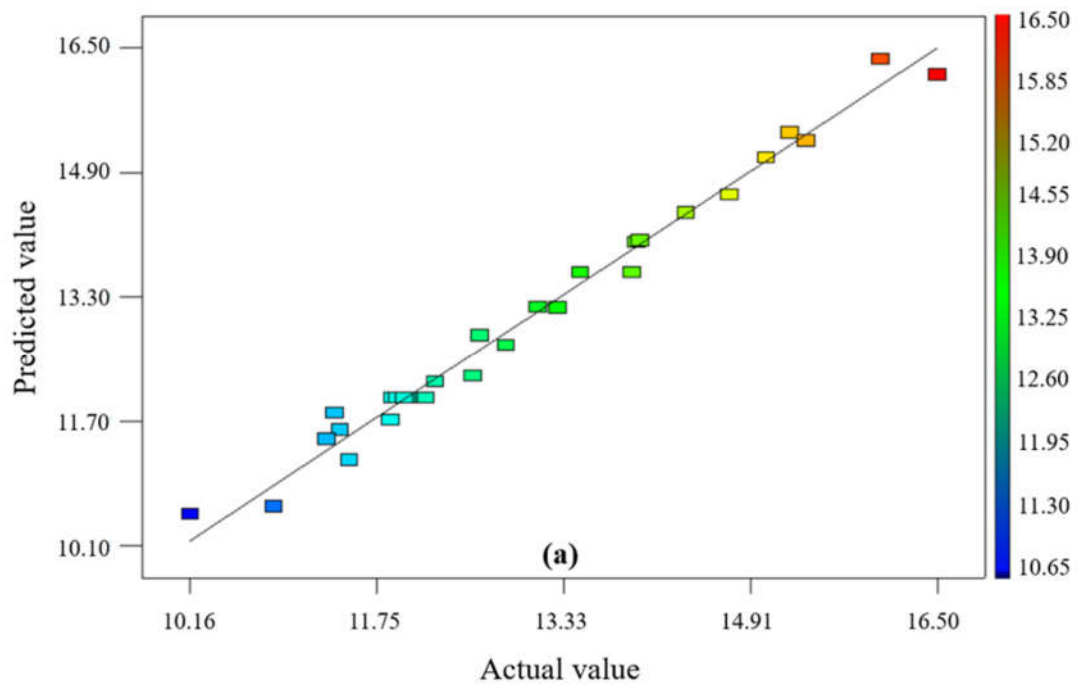


Figure 4.3. Correlation of actual and predicted values of As^V removal capacity for BIO NPs (R^2 - 0.9800) and BIO-DW nanohybrids (R^2 - 0.9701).

4.4.2.3 Multiple response optimization

In the numerical optimization, a desired value of experimental inputs has been provided for each variable. The experimental variables have been optimized for the contact time by maximizing the removal capacity of As^{V} for the groundwater conditions representing the real world (i.e. pH 7.0 and Temperature $15\text{ }^{\circ}\text{C}$) and minimizing the requirement of dose concentration (0.25 g L^{-1}) for both BIO NPs and BIO-DW nanohybrids. The results in Figure 4.4 and 4.5 illustrate the ranges of the variables obtained from the model (their exact values are shown by the circles) for both BIO NPs and BIO-DW nanohybrids, respectively. The lower horizontal lines depict the optimized values for contact time and their respective removal capacity.

At desirability 0.983, the optimized value of contact time has been predicted to be 272 min to achieve the maximum removal capacity ($16.1\text{ mg g}^{-1}\text{-Fe}$) of As^{V} using BIO NPs. Similarly, at desirability 0.983, the optimized value of contact time has been predicted to be 151 min to achieve the maximum removal capacity ($24.83\text{ mg g}^{-1}\text{-Fe}$) of As^{V} using BIO-DW nanohybrids. Thus, for BIO-DW nanohybrids, an increase in the extend of As^{V} removal efficiency together with a decrease in the contact time depicts their strong and quick affinity towards the arsenic oxyanions as compared to those of BIO NPs.

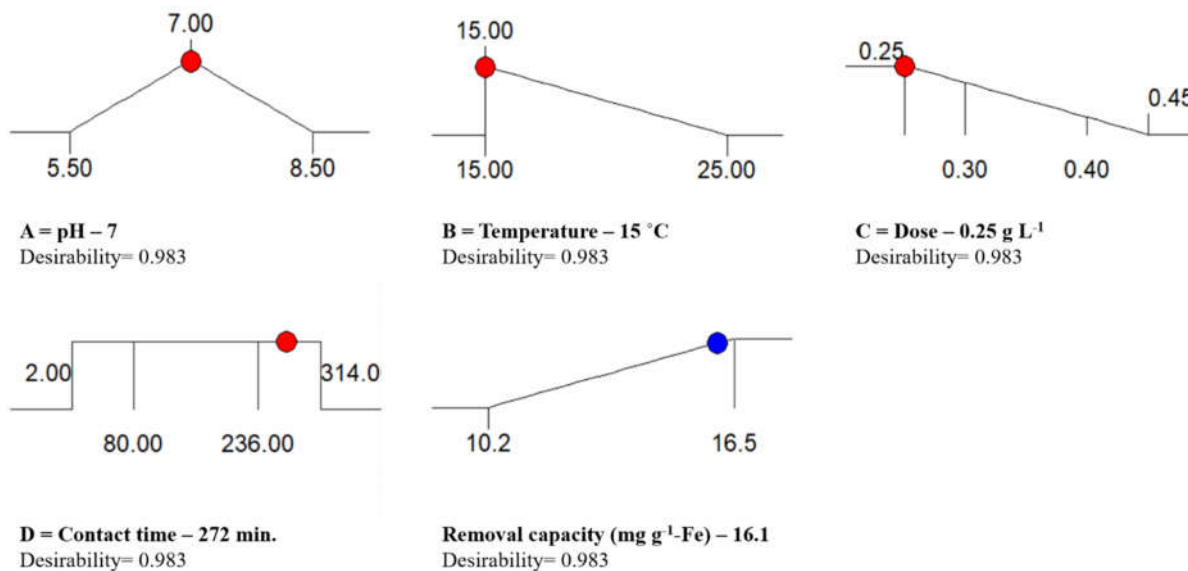


Figure 4.4. Optimization process representing the predicted values and desirability function for the removal capacity of As^{V} using BIO NPs.

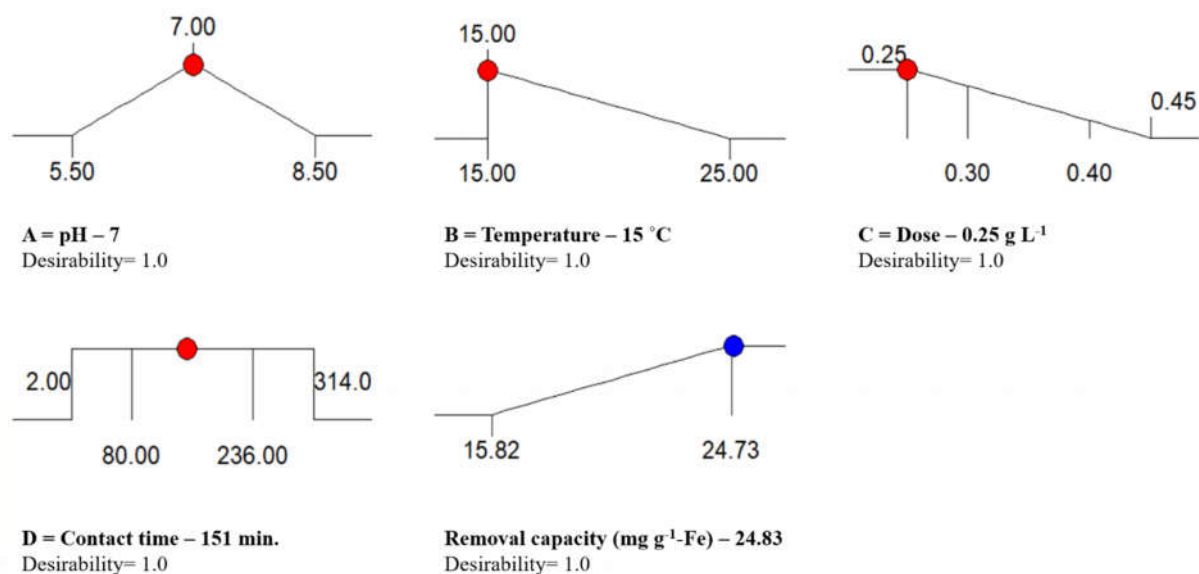


Figure 4.5. Optimization process representing the predicted values and desirability function for the removal capacity of As^V using BIO-DW nanohybrids.

Further, the model prediction has been validated by conducting the confirmation experiments and demonstrating the results at desired optimal conditions for both BIO NPs and BIO-DW nanohybrids. Three runs have been performed for each of optimal conditions using as-synthesized nanoparticles. In these experiments, the average value of the As^V removal capacity (mg g⁻¹-Fe) has been determined to be 15.2 ± 0.35 and 22.9 ± 1.04 for BIO NPs and BIO-DW nanohybrids, respectively. The outcomes are in significant agreement with the predicted response. Less than 7 % error for each response demonstrates the reliability of the optimization process using CCD.

4.4.3 Analysis of As^V removal employing different kinetic models

The behaviour of As^V removal for both of as-synthesized nanomaterials have been explored by fitting the adsorption data into different kinetic models. For this, As^V (4 mg L⁻¹) removal has been studied by varying the amount of adsorbent dose ranging from 0.15 – 0.45 g L⁻¹ at the shaking speed of 250 rpm. For the optimized contact time for BIO NPs and BIO-DW nanohybrids, the kinetic data for the removal of As^V has been recorded at various time intervals (Figure 4.6 to 4.8). These data have been fitted in different kinetic models and are discussed below:

First-order-kinetic model

For first-order-kinetics, the results have indicated that the q_e (calculated) values are not in good agreement with the q_e (experimental) values for all the dose concentrations of BIO NPs and BIO-DW nanohybrids (Table 4.5), and exhibited poor correlation at lower dose values ($< 0.40 \text{ g L}^{-1}$). Relatively better correlation (> 0.95) has been observed at higher dose concentrations (0.40 and 0.45 g L^{-1}) for BIO NPs only. It indicates that the adsorption on BIO NPs follows first-order-kinetic model for the dose beyond 0.35 g L^{-1} , which would have occurred due the greater degree of freedom (DoF) for As^{V} distribution onto the surface of adsorbent [288][289]. However, no such trend is observed for BIO-DW nanohybrids which might be due the presence of different types of surface functionalities available on their surface. The graphical representation is showed in the Figure 4.6 below:

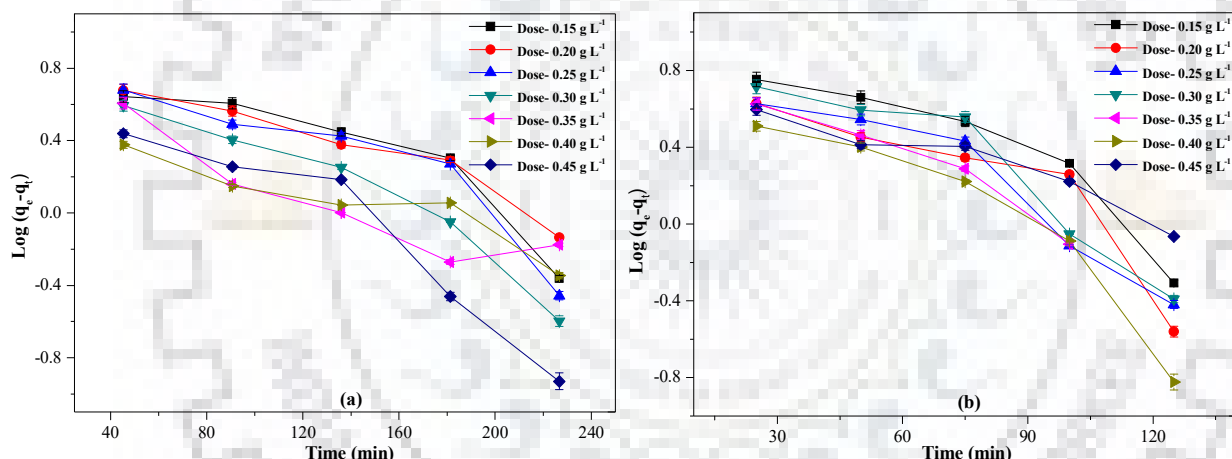


Figure 4.6. Graphical representation of First-order kinetic for As^{V} adsorption onto (a) BIO NPs. and (b) BIO-DW nanohybrids.

Second-order-kinetic-model

The results obtained after fitting the second-order Lagergren's model to the adsorption data are presented in Figure 4.6 and 4.7, and the different kinetic parameters obtained are summarized in Table 4.5. The theoretical value of removal capacity q_e (calculated) matches fairly well with the q_e (experimental) values for both BIO NPs and BIO-DW nanohybrids, suggesting that the second order Lagergren's model is significantly followed. It shows a very good correlation (> 0.99) for As^{V} adsorption in the entire range of the adsorbent dose investigated. This analysis reveals that the As^{V}

removal depends on the number of active sites present on these nanosystems, which primarily occurs through chemisorption [104], [290], [291].

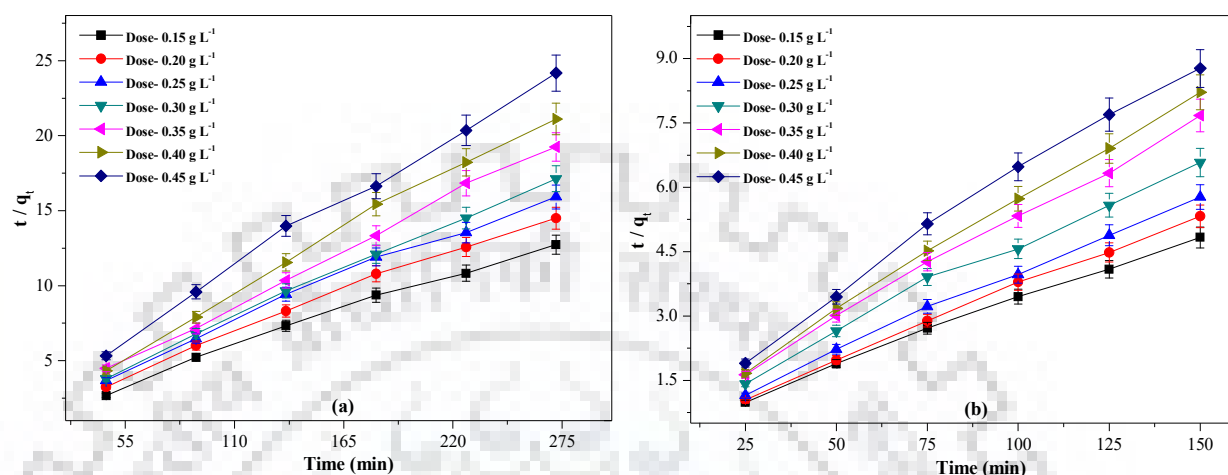


Figure 4.7. Graphical representation of Pseudo-second-order kinetic for As^V adsorption onto (a) BIO NPs. and (b) BIO-DW nanohybrids.

Intra-particle-diffusion model

The fitting of the above model on the adsorption data has exhibited fairly good correlation for both BIO NPs and BIO-DW nanohybrids (Figure 4.8 and Table 4.5). The applicability of the intra-particle diffusion model implies that the adsorption process of the As^V onto both BIO NPs and BIO-DW nanohybrids follows a complex process involving both boundary layer and intra-particle diffusion [292][293]. The graphical representation is showed in the Figure 4.8.

For BIO NPs, the constant C is found to increase from 17.667 to 32.434 with an increase in the adsorbent dose from 0.15-0.45 g L⁻¹. Similarly, the value of C is found to increase from 15.412 to 34.403 for BIO-DW nanohybrids. A change in C value has been attributed to an increase in the thickness of the boundary layer which decreases the possibility of external mass transfer and subsequently prominently increases the amount of internal mass transfer. Whereas, relatively larger C values for both of these nanosystems indicate the greater effect of the boundary layer. Fairly high values of R² may confirm that the rate-limiting step is the intra-particle diffusion process for both of as-synthesized nanosystems [294].

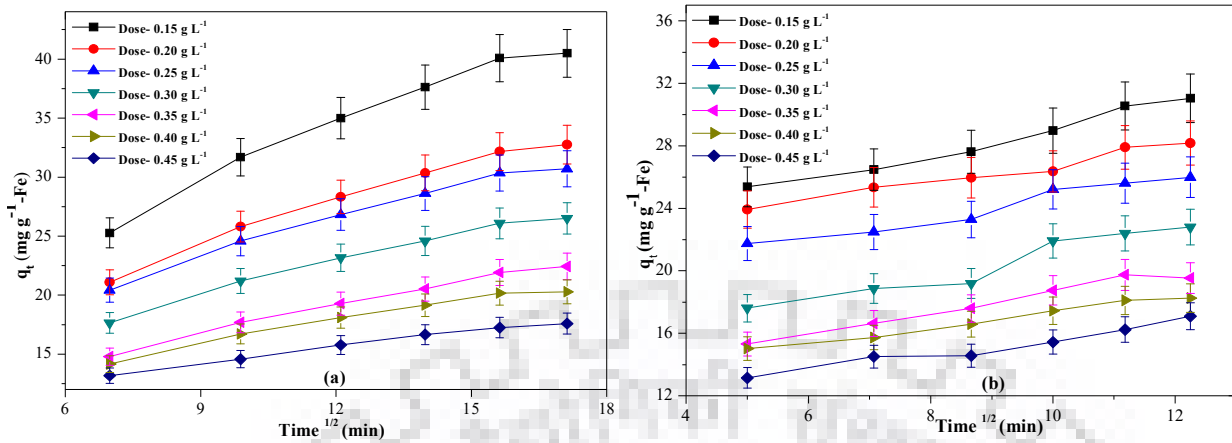


Figure 4.8. Graphical representation of Intra-particle-diffusion kinetic for As^{V} adsorption onto (a) BIO NPs. and (b) BIO-DW nanohybrids.

Elovich-kinetic-model

A fairly good correlation of this model has been observed for both as-synthesized nanosystems (Figure 4.8). However, the fit is found to be a little better for BIO NPs (R^2 - 0.88 to 0.99) as compared to BIO-DW nanohybrids (R^2 - 0.89 to 0.96). The adsorption data following Elovich equation with a fairly high value of R^2 suggests heterogeneity in both the systems [292], which possibly arises due to the singlet ($\equiv \text{FeOH}^{-0.5}$) and triplet ($\equiv \text{Fe}_3\text{O}^{-0.5}$) coordinated sites [274], [295]. The presence of organic moieties in BIO-DW nanohybrids could also have contributed to the heterogeneous adsorption of As^{V} for this nanosystem. This aspect has been further explored in the next chapter.

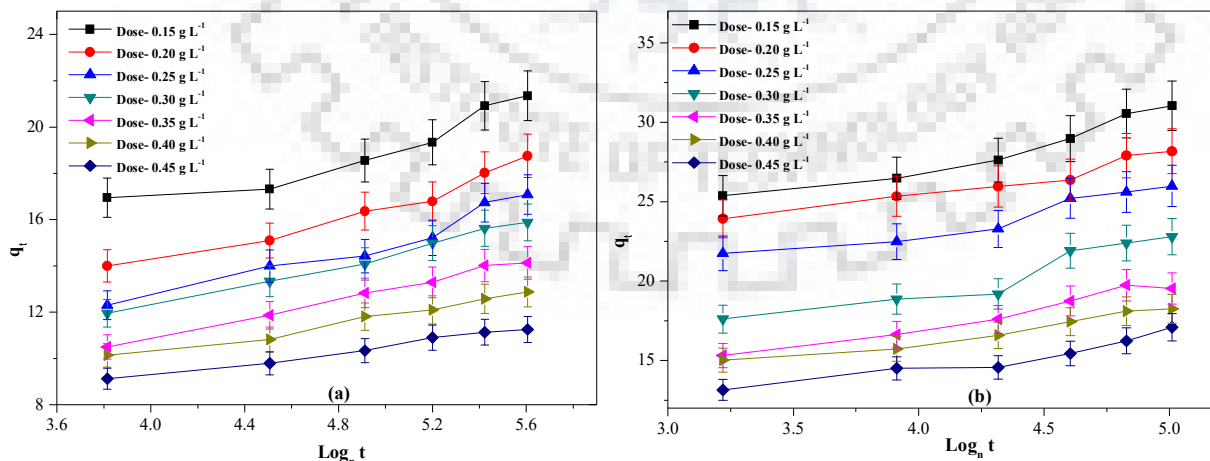


Figure 4.9. Graphical representation of Elovich model for As^{V} adsorption onto (a) BIO NPs. and (b) BIO-DW nanohybrids.

Table 4.5. Kinetic parameters obtained during the removal of As^V by as-synthesized BIO NPs and BIO-DW nanohybrids under different experimental conditions.

Model		1 st -Order-kinetics			2 nd -Order-kinetics			Intraparticle diffusion			Elovich			
Parameter	Dose (g L ⁻¹)	K_1	q_e (calc.)	R^2	K_2	q_e (calc.)	R^2	K_{diff}	C	R^2	β	α	R^2	q_e (exp.)
BIO	0.15	0.0051	10.60	0.80	0.0017	22.94	0.99	1.933	24.713	0.95	2.573	6.436	0.88	21.35
	0.20	0.0042	8.39	0.92	0.0023	19.31	1.00	2.029	21.333	0.99	2.613	3.672	0.95	18.75
	0.25	0.0055	10.70	0.81	0.0017	18.69	0.99	1.993	17.667	0.97	2.626	2.066	0.95	17.08
	0.30	0.0063	9.36	0.93	0.0027	17.18	1.00	2.409	22.335	0.99	2.246	3.282	0.99	15.88
	0.35	0.0076	10.74	0.88	0.0026	15.36	1.00	2.579	20.798	0.98	2.086	2.523	0.99	14.14
	0.40	0.0051	5.36	0.96	0.0035	13.72	1.00	3.285	26.455	0.99	1.536	4.160	0.97	12.88
	0.45	0.0069	5.68	0.95	0.0048	11.95	1.00	4.277	32.434	0.98	1.260	4.259	0.99	11.25
BIO-DW	0.15	0.0099	13.51	0.85	0.0028	32.89	1.00	1.179	24.398	0.98	3.280	14.190	0.93	31.05
	0.20	0.0103	9.94	0.78	0.0053	28.74	1.00	1.653	34.403	0.98	2.342	16.174	0.94	28.18
	0.25	0.0110	10.96	0.91	0.0038	27.47	1.00	1.470	26.328	0.95	2.568	12.975	0.91	25.99
	0.30	0.0114	13.87	0.88	0.0056	22.80	0.99	1.942	15.412	0.93	3.110	7.095	0.89	24.81
	0.35	0.0073	6.32	0.88	0.0038	21.19	1.00	1.520	18.224	0.97	2.585	6.778	0.97	19.54
	0.40	0.0126	9.78	0.87	0.0051	19.37	1.00	1.940	23.777	0.99	1.906	8.621	0.95	18.26
	0.45	0.0060	5.86	0.92	0.0042	18.05	0.99	7.878	19.462	0.96	2.023	6.4413	0.92	17.10

4.4.4 Isotherm modeling using Langmuir, Freundlich, Tempkin and Dubinin-Radushkevich adsorption models

In the present work, the As^V adsorption has been studied in the concentration range of 5-125 mg L⁻¹ employing both the BIO NPs and BIO-DW nanohybrids in the dose range of 0.30 and 0.40 g L⁻¹. These experiments have been performed at temperature and shaking speed of 15 °C and 250 rpm, respectively. All the samples have been allowed to react for 272 min and 151 min for BIO and BIO-DW nanohybrids, respectively. The observed adsorption isotherm and their respective data are presented in Table 4.6 to 4.8. The graphical representation of these isotherm models are shown in Figures 4.10 to 4.18. The obtained value of removal capacity (mg g⁻¹-Fe) against the different concentration of As^V for both of these nanosystems are plotted and shown in Figure 4.10.

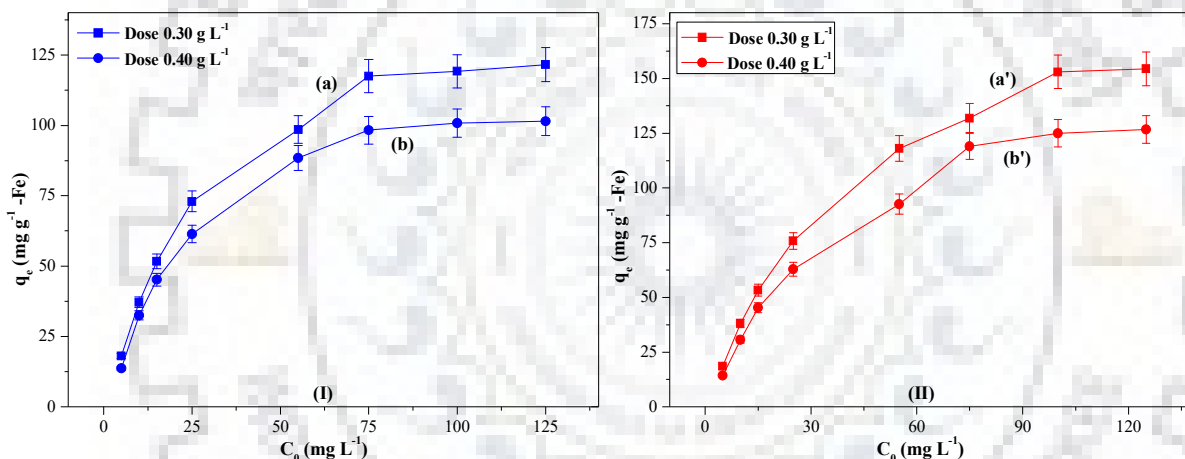


Figure 4.10. Plots of adsorption isotherms; (I) BIO NPs and (II) BIO-DW nanohybrids at dose concentration of 0.30 g L⁻¹ (a-a') and 0.40 g L⁻¹ (b-b').

Freundlich

Figure 4.11 and 4.12 show the plots obtained after fitting the Freundlich model to the adsorption data. The poor correlation coefficient has been observed for both of BIO and BIO-DW nanosystems, indicating the lower efficiency of model in explaining the adsorption behaviour. A fairly good correlation for BIO-DW nanohybrids is demonstrating that the adsorption process involves the heterogeneous surface. This statement has also justified the outcomes which are observed previously. The value of constant $1/n$ has been found less than 1 for both of these nanosystems, indicating the uniform adsorption behaviour onto their surfaces. However, this adsorption data is fitted to Langmuir model further.

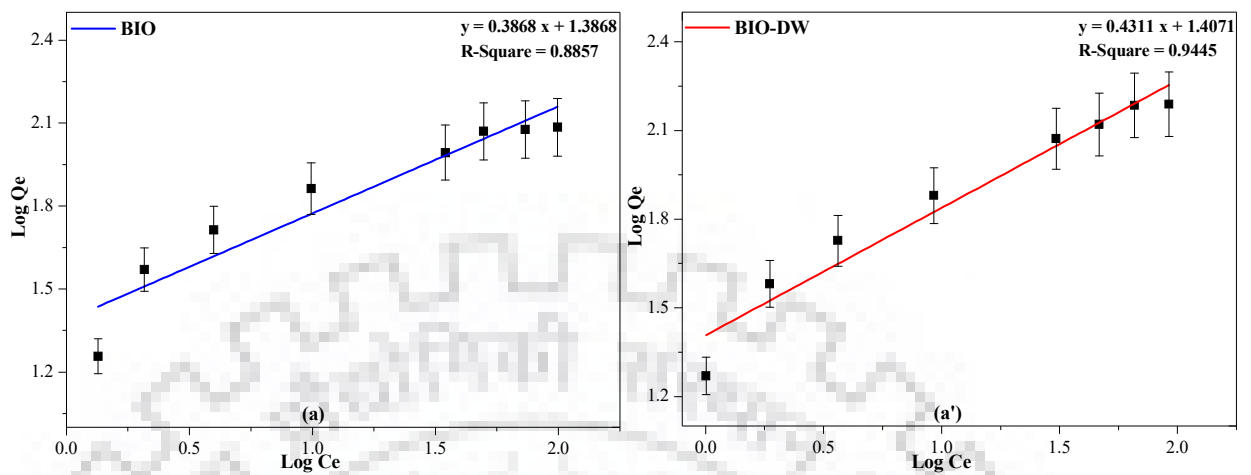


Figure 4.11. Graphical representation of Freundlich adsorption isotherms of As^{V} removal onto (a) BIO and (a') BIO-DW nanoparticles (Adsorbent dose- 0.30 g L^{-1}).

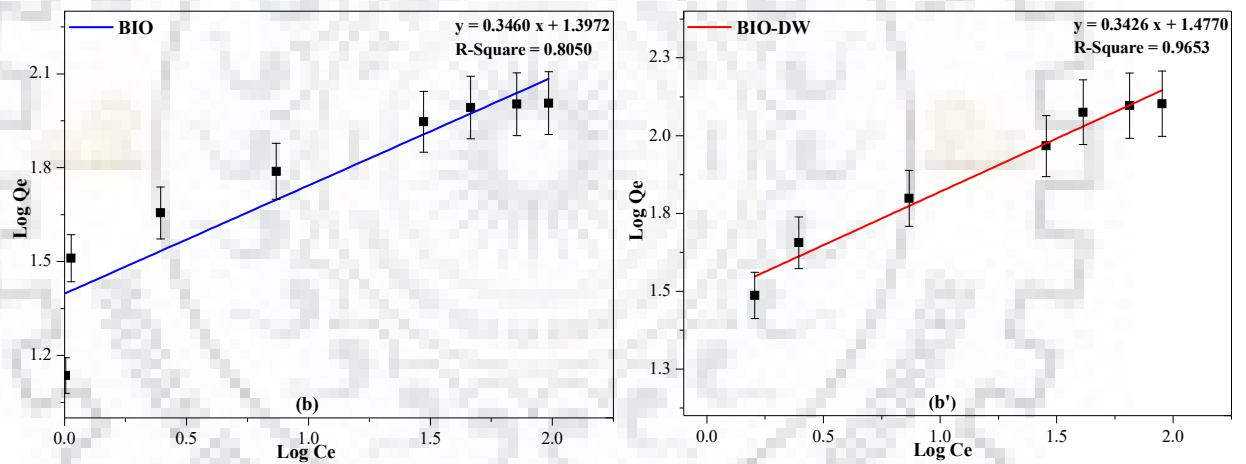


Figure 4.12. Graphical representation of Freundlich adsorption isotherms of As^{V} removal onto (a) BIO NPs and (a') BIO-DW nanohybrids (Adsorbent dose- 0.40 g L^{-1}).

Langmuir

Figure 4.13 and 4.14 show the graphical representation of Langmuir model fitted to the adsorption data. A significant correlation with coefficient values in the range of 0.9972-0.9984 and 0.9922-0.9927 has been observed for both BIO and BIO-DW nanosystems, respectively. The value of R_L has been found to vary from 0.034 to 0.371 for BIO NPs and 0.054 to 0.393 for BIO nanohybrids. It implies the adsorption process to be favourable for both of these nanosystems. The

range of maximum monolayer capacities have been examined to be 106.38-129.87 and 136.99-166.67, respectively.

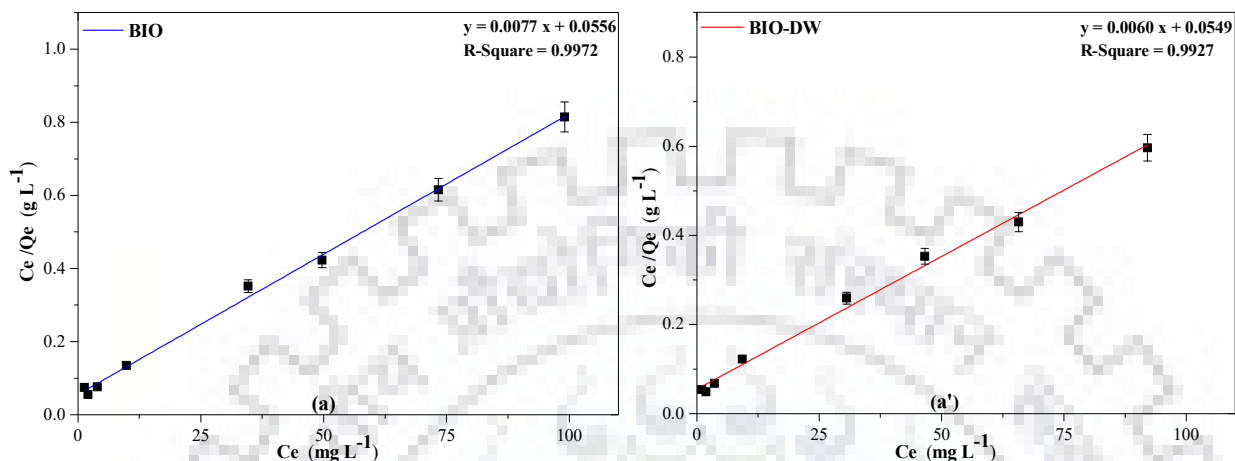


Figure 4.3. Graphical representation of Langmuir adsorption isotherms of As^V removal onto (a) BIO and (a') BIO-DW nanoparticles (Adsorbent dose- 0.30 g L⁻¹).

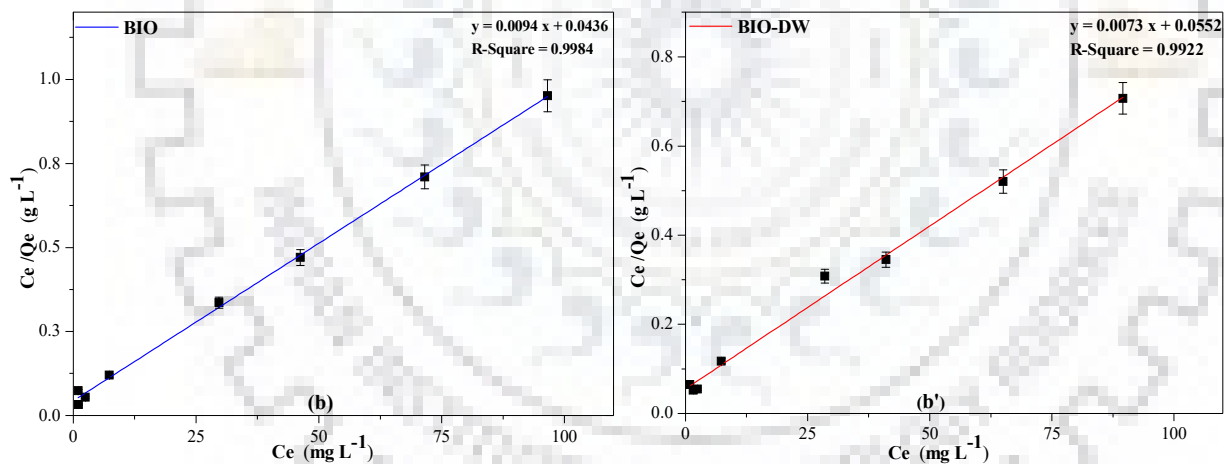


Figure 4.4. Graphical representation of Langmuir adsorption isotherms of As^V removal onto (b) BIO and (b') BIO-DW nanoparticles (Adsorbent dose- 0.40 g L⁻¹).

The results show the applicability of Langmuir model for interpreting the experimental data over all the concentration range investigated. The obtained R_L values for As^V removal, which are observed between 0.052 and 0.393, suggest favourable adsorption of the target contaminant onto the as-synthesized BIO and BIO-DW nanosystems.

Temkin

The values of correlation coefficients (R^2) obtained from the model are comparable to those obtained from the Langmuir and Freundlich isotherm equations. It explains the applicability of the Temkin model to the adsorption of As^V onto the BIO and BIO-DW nanoparticles (Figure 4.15 and 4.16). The R^2 values with the range of 0.9660-0.9881 and 0.9732-0.9896 have been observed for BIO and BIO-DW nanoparticles, respectively.

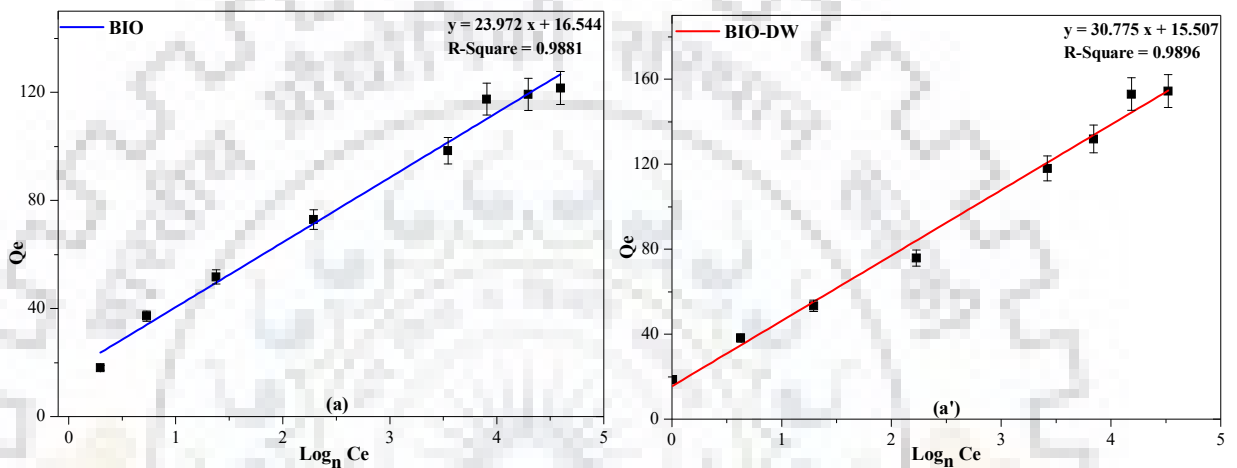


Figure 4.5. Graphical representation of Temkin adsorption isotherms of As^V removal onto (a) BIO and (a') BIO-DW nanoparticles (Adsorbent dose- 0.30 g L^{-1}).

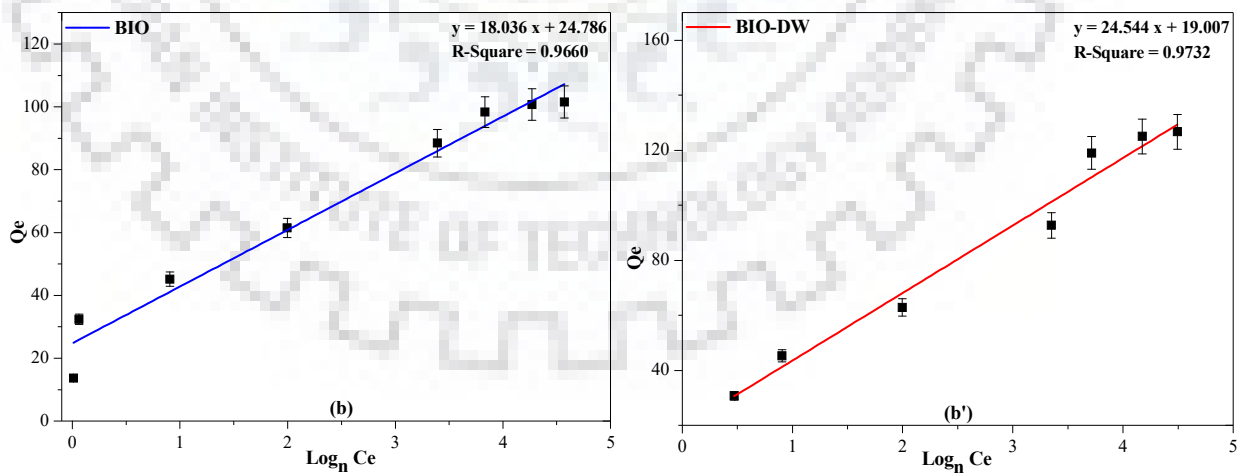


Figure 4.6. Graphical representation of Temkin adsorption isotherms of As^V removal onto (a) BIO and (a') BIO-DW nanoparticles (Adsorbent dose- 0.40 g L^{-1}).

The values of constant B (heat of sorption) in the range of 18.036-23.972 KJ mol⁻¹ and 25.544-30.775 for BIO and BIO-DW nanoparticles respectively indicates the potential of physical adsorption process. An increase (%) in the heat of sorption in the range of 29.39-22.11 for BIO-DW nanoparticles has been observed, indicating that the developed functionalized nanostructures of maghemite strongly favour the physical adsorption in comparison to that of BIO NPs.

The values of the Temkin constants (B, J mol⁻¹) and correlation coefficients (R²) are lower than the Langmuir values. The Temkin isotherm represents a significant fit than the Freundlich isotherm to the experimental data. However, the Langmuir isotherm provides the best fit with the experimental data for both BIO and BIO-DW nanosystems. Therefore, it appears justified that the occurrence of more abundant adsorption of the As^V onto developed nanoparticles takes place through a monolayer sorption on a surface which is homogenous in sorption affinity.

Dubinin-Radushkevich

To calculate the mean free energy values of sorption, Dubinin-Radushkevich (D-R) isotherm model has been applied on the adsorption data. The lower R² values of 0.8549-0.8890 and 0.7910-0.8698 have been observed over the whole range of adsorbent dose (0.30-0.40 g L⁻¹) for BIO and BI-DW nanoparticles respectively. It indicates the non-suitability of the model.

Further, the values of free energy E (KJ mol⁻¹) of sorption estimates the behaviour of adsorption process for As^V onto the nanoparticles. Its value > 400 KJ mol⁻¹ for both of as-synthesized BIO NPs and BIO-DW nanohybrids indicates that the adsorption is probably chemically controlled onto their surfaces.

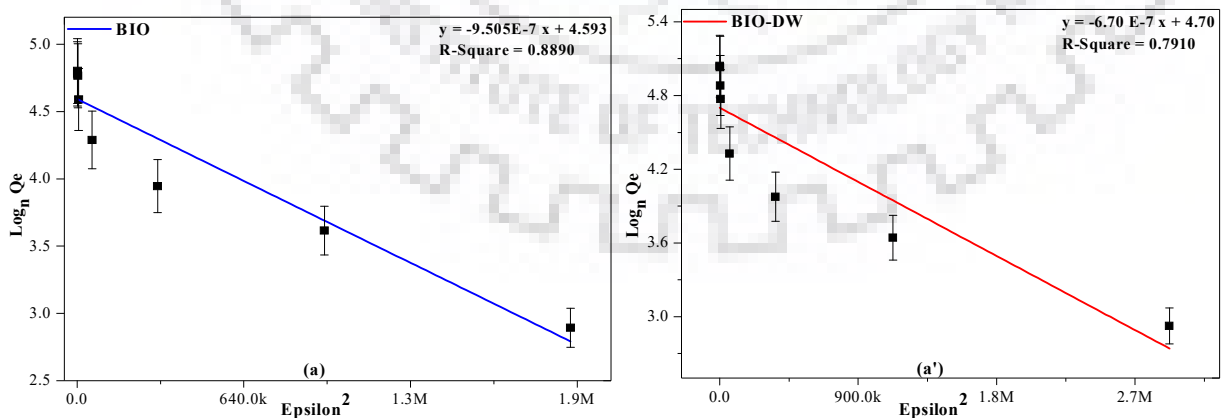


Figure 4.17. Graphical representation of Dubinin-Radushkevich adsorption isotherms of As^V removal onto (a) BIO and (a') BIO-DW nanoparticles (Adsorbent dose- 0.30 g L⁻¹).

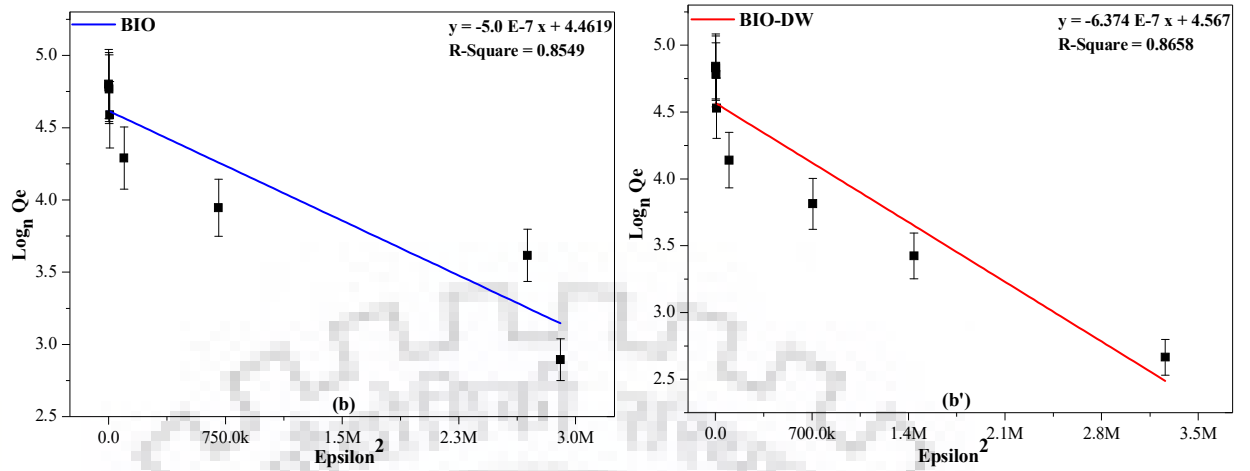


Figure 4.18. Graphical representation of Dubinin-Radushkevich adsorption isotherms of As^V removal onto (a) BIO and (a') BIO-DW nanoparticles (Adsorbent dose- 0.40 g L⁻¹).

Table 4.6. Parameters for plotting Langmuir, Freundlich, Tempkin and Dubinin-Radushkevich adsorption isotherms of As^V removal onto BIO nanoparticles (Dose- 0.30 g L⁻¹) and (Dose- 0.40 g L⁻¹).

<i>Sl. No.</i>	C_0	C_e	$1/C_e$	$\text{Log } C_e$	$\text{Log}_n C_e$	Q_e	$1/Q_e$	$\text{Log } Q_e$	$\text{Log}_n Q_e$	C_e/Q_e	ε^2
1.	5	1.7	0.889	0.051	0.118	18.1	0.055	1.257	2.894	0.062	1.90 x 10 ⁶
2.	10	2.1	0.482	0.317	0.730	37.2	0.027	1.570	3.616	0.056	9.49 x 10 ⁵
3.	15	4.0	0.252	0.599	1.380	51.7	0.019	1.714	3.946	0.077	3.01 x 10 ⁵
4.	25	9.9	0.101	0.995	2.290	73.0	0.014	1.863	4.289	0.135	5.71 x 10 ⁴
5.	55	34.7	0.029	1.540	3.545	98.5	0.010	1.993	4.589	0.352	4.97 x 10 ³
6.	75	49.7	0.020	1.696	3.906	117.5	0.009	2.070	4.766	0.423	2.44 x 10 ³
7.	100	73.4	0.014	1.865	4.295	119.2	0.008	2.076	4.781	0.615	1.13 x 10 ³
8.	125	99.1	0.010	1.996	4.596	121.6	0.008	2.085	4.801	0.815	6.19 x 10 ²

Table 4.7. Parameters for plotting Langmuir, Freundlich, Tempkin and Dubinin-Radushkevich adsorption isotherms of As^V removal onto BIO nanoparticles (Dose- 0.40 g L⁻¹).

<i>Sl. No.</i>	C_0	C_e	$1/C_e$	$\text{Log } C_e$	$\text{Log}_n C_e$	Q_e	$1/Q_e$	$\text{Log } Q_e$	$\text{Log}_n Q_e$	C_e/Q_e	ε^2
1.	5	1.7	0.989	0.005	0.011	13.7	0.073	1.136	2.615	0.074	2.90 x 10 ⁶
2.	10	1.1	0.939	0.027	0.063	32.5	0.031	1.511	3.479	0.033	2.69 x 10 ⁶
3.	15	2.5	0.404	0.394	0.906	45.2	0.022	1.655	3.811	0.055	7.10 x 10 ⁵
4.	25	7.4	0.136	0.868	1.998	61.4	0.016	1.788	4.118	0.120	9.93 x 10 ⁴
5.	55	29.7	0.034	1.473	3.391	88.4	0.011	1.947	4.482	0.336	6.73 x 10 ³
6.	75	46.3	0.022	1.665	3.834	98.3	0.010	1.993	4.588	0.470	2.81 x 10 ³
7.	100	71.6	0.014	1.855	4.270	100.8	0.010	2.003	4.613	0.710	1.18 x 10 ³
8.	125	96.6	0.010	1.985	4.571	101.5	0.010	2.007	4.620	0.951	6.52 x 10 ²

Table 4.8. Parameters for plotting Langmuir, Freundlich, Tempkin and Dubinin-Radushkevich adsorption isotherms of As^V removal onto BIO-DW nanoparticles (Dose- 0.30 g L⁻¹) and (Dose- 0.40 g L⁻¹).

Sl. No.	C_0	C_e	$1/C_e$	$\text{Log } C_e$	$\text{Log}_n C_e$	Q_e	$1/Q_e$	$\text{Log } Q_e$	$\text{Log}_n Q_e$	C_e/Q_e	ε^2
1.	5	1.3	0.994	0.003	0.006	18.621	0.054	1.270	2.924	0.054	2.92 x 10 ⁶
2.	10	1.9	0.535	0.272	0.626	38.147	0.026	1.581	3.641	0.049	1.23 x 10 ⁶
3.	15	3.6	0.275	0.561	1.291	53.326	0.019	1.727	3.976	0.068	3.63 x 10 ⁵
4.	25	9.3	0.108	0.967	2.227	75.821	0.013	1.880	4.328	0.122	6.44 x 10 ⁴
5.	55	30.6	0.033	1.486	3.421	118.037	0.008	2.072	4.771	0.259	6.35 x 10 ³
6.	75	46.6	0.021	1.668	3.842	131.904	0.008	2.120	4.882	0.353	2.77 x 10 ³
7.	100	65.8	0.015	1.818	4.187	153.026	0.007	2.185	5.031	0.430	1.40 x 10 ³
8.	125	92.1	0.011	1.964	4.522	154.406	0.006	2.189	5.040	0.596	7.17 x 10 ²

Table 4.9. Parameters for plotting Langmuir, Freundlich, Tempkin and Dubinin-Radushkevich adsorption isotherms of As^V removal onto BIO-DW nanohybrids (Dose- 0.40 g L⁻¹).

Sl. No.	C_0	C_e	$1/C_e$	$\text{Log } C_e$	$\text{Log}_n C_e$	Q_e	$1/Q_e$	$\text{Log } Q_e$	$\text{Log}_n Q_e$	C_e/Q_e	ε^2
1.	5	1.1	1.073	0.042	0.095	14.359	0.070	1.157	2.664	0.065	3.26 x 10 ⁶
2.	10	1.6	0.623	0.205	0.473	30.681	0.033	1.487	3.424	0.052	1.44 x 10 ⁶
3.	15	2.5	0.404	0.394	0.906	45.301	0.022	1.656	3.813	0.055	7.07 x 10 ⁵
4.	25	7.4	0.136	0.868	1.998	62.863	0.016	1.798	4.141	0.117	9.93 x 10 ⁴
5.	55	28.6	0.035	1.456	3.352	92.671	0.011	1.967	4.529	0.308	7.28 x 10 ³
6.	75	41.1	0.024	1.613	3.715	118.977	0.008	2.075	4.779	0.345	3.56 x 10 ³
7.	100	65.1	0.015	1.813	4.175	124.991	0.008	2.097	4.828	0.520	1.43 x 10 ³
8.	125	89.6	0.011	1.952	4.495	126.687	0.008	2.103	4.842	0.707	7.57 x 10 ²

Table 4.10. Isotherm constant parameters and correlation coefficients calculated for the adsorption of As^V onto BIO and BIO-DW nanoparticles.

Isotherms	Parameters	BIO NPs		BIO-DW nanohybrids	
		0.30 g L ⁻¹	0.40 g L ⁻¹	0.30 g L ⁻¹	0.40 g L ⁻¹
Freundlich	<i>n</i>	2.59	2.89	2.32	2.92
	<i>1/n</i>	0.387	0.346	0.431	0.343
	<i>K_F</i> (mg g ⁻¹ -Fe)	24.37	24.96	25.53	30.00
	<i>R</i> ²	0.89	0.83	0.95	0.97
Langmuir	<i>Q_{max}</i> (mg g ⁻¹ -	129.87	106.38	166.67	136.99
	<i>K_L</i> (L mg ⁻¹)	0.139	0.216	0.109	0.132
	<i>R_L</i>	0.052-0.371	0.034-0.325	0.064-0.393	0.054-0.376
	<i>R</i> ²	1.00	1.00	0.99	0.99
Tempkin	<i>B</i> (J mol ⁻¹)	23.972	18.036	30.775	24.544
	<i>b_T</i>	99.88	132.76	77.80	97.56
	<i>K_T</i> (L mg ⁻¹)	1.994	3.96	1.662	2.169
	<i>R</i> ²	0.99	0.97	0.99	0.97
DR-Model	<i>Q_s</i> (mg g ⁻¹ -Fe)	98.79	86.66	109.54	96.25
	<i>K_{ad}</i> (mol ² KJ ⁻²)	1.0 x 10 ⁻⁶	5 x 10 ⁻⁷	7 x 10 ⁻⁷	6 x 10 ⁻⁷
	<i>E</i> (KJ mol ⁻¹)	7.0 x 10 ²	1.0 x 10 ³	8.4 x 10 ²	9.1 x 10 ²
	<i>R</i> ²	0.89	0.86	0.79	0.87

4.5 Leaching test for the determination of secondary pollution

Figure 4.19 demonstrates the possibility of leaching of iron into the treated aqueous solution during the removal process of As^V. For both BIO NPs and BIO-DW nanohybrids, several experiments have been performed for the pH and As^V concentration range of 7-9 and 5-125 mg L⁻¹, respectively. All the samples were filtered through Whatman™ 42 cellulose, prior to the analysis of iron. Increase in the concentration of arsenic leads to an increase in the addition of iron in the aqueous solution. This can understand by an interaction of the organic functionalities bound to iron start interacting with As^V. Thereby, causing the leaching of iron^{III} from BIO-DW nanohybrids.

At high concentration of As^V, it possibly starts interacting with the ligand/template through its functionalities, removing iron from the functional groups attached from the industry waste. Moreover, these examinations reveal that both the as-synthesized nanosystems have significant

potential in As^V removal for the groundwater representing real world conditions without causing any appreciable leaching of iron.

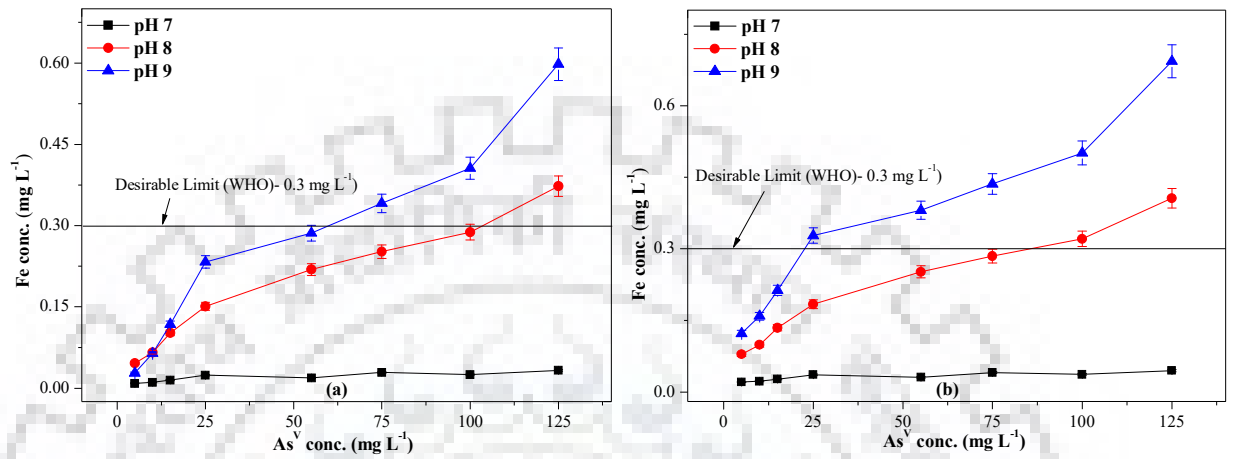


Figure 4.19. Graphical representation showing the possibility of secondary pollution occurring at higher pH through leaching of Fe³⁺ ions during As^V removal (a) BIO NPs and (b) BIO-DW nanohybrids.



Multi-variate statistical design for arsenic removal: Taguchi's design of experimental methodology

5.1 Chapter abstract

The present chapter investigates the As^V removal capabilities of as-synthesized BIO NPs and BIO-DW nanohybrids under the conditions representing the real world. Artificial water has been formulated representing the elemental concentrations equivalent to that of groundwater samples collected from the district Ballia, Uttar-Pradesh, India. The arsenic concentration in the samples has been found to be beyond the standard limit of drinking water as suggested WHO ($> 10 \mu\text{g L}^{-1}$).

This study utilizes a computational analysis involving the formulation array and square matrix for the synthesis of artificial water for batch studies. A Taguchi's L₂₇ (3¹³) orthogonal array has been used for the design of experiments. For the optimisation of removal capacity, the following range of parameters have been explored: As^V concentration (55 - 200 $\mu\text{g L}^{-1}$), TDS (436 - 1591 mg L^{-1}), shaking speed (100 - 240 rpm), temperature (10 - 30 °C), pH (7 - 9), dose (0.05 - 0.15 g L^{-1}) and contact time (2 - 104 min). A geochemical code using Visual MINTEQ has been employed to examine the behaviour of As^V removal as a function pH using charge distribution multisite complexation (CD-MUSIC) and 2pK-Three plane model (TPM) models. Then, the ANN model has been trained to evaluate the Taguchi's response using MATLAB neural network tool.

A significant agreement between the actual groundwater and artificial formulated water (AFW) with the correlation coefficient (R^2) > 0.99 has been observed. At the optimized conditions, the adsorption capacity ($\mu\text{g g}^{-1}\text{-Fe}$) has been found to be 4.8 and 7.0, respectively. This low value of adsorption capacity reveals the significant effects of competing ions on the As^V removal using for both of as-synthesized nanomaterials. An analysis through surface complexation models (SCMs) suggested that the singlet ($\text{FeOH}^{-0.5}$) and triplet ($\text{Fe}_3\text{O}^{-0.5}$) specie(s) contribute larger to the As^V absorption by forming different complexes. Additionally, the FeO^- species has also been observed to influence the adsorption behaviour in case of BIO-DW nanohybrids under near neutral pH conditions. A significant agreement between the outcomes of Taguchi's model and ANN predicted

values has been observed with the mean square error (MSE) 0.0174 and 0.0126, respectively. It indicates the significance of both of these tools in explaining the adsorption behaviour.

5.2 Materials and instrumentation

The standard solution for Na^+ , K^+ , F^- , Cl^- , NO_3^- , Ca^{2+} , Mg^{2+} , Mn^{2+} , Cu^{2+} , Pb^{2+} , Cd^{2+} , Zn^{2+} , SO_4^{2-} , PO_4^{3-} , Fe^{3+} , and SiO_4^{3-} ions are procured from Merck manufactures (Massachusetts, USA) and utilized for the calibration purposes. Their salts (Table 5.3) of analytical grade (ACS) containing these ions has been purchased and used for the formulation of artificial water. Besides these, the chemical and reagents mentioned in Chapter 3 and Chapter 4 have been used for the same.

The physical characterization such as pH, electrical conductivity (EC) and total dissolved solids (TDS) are performed using HACH (Model: HQ40D Multi/2 channels) portable multi-meter purchased from Colorado, USA. The concentration of cations (Ca^{2+} , Mg^{2+} , Na^+ , K^+) and anions (F^- , Cl^- , SO_4^{2-} , NO_3^-) have been analysed using Ion chromatogram (Metrohm, 819-IC-Detector) by employing ion-exchange columns Metrosep-C2-250 and Metrosep-A-Supp-5, respectively. The determination of sulphate and phosphate ions concentration are analysed colorimetric technique. The concentrations of heavy metals and metalloid arsenic have been determined using ICP-MS and MP-AES instruments, and their details are mentioned in previous chapters.

5.3 Methodology

5.3.1 Study area, sample collection and their preparation

The arsenic removal characteristics of as-synthesized BIO NPs and BIO-DW nanohybrids are evaluated for real world water. For this, two groundwater samples (Near Lohapatti and Kanspur road) have been collected from arsenic affected area(s) of district Ballia, Uttar-Pradesh, India (shown in Figure 5.1) and designated as location I and location II in the present study. These are representing as shallow (Mark II hand-pumps, depth 30 - 33 m) and deep (Bore-well, depth 66 - 75 m) aquifer systems, respectively.

The trapped water in the shaft of hand-pump and bore-well has been driven out by pumping for 10-15 minutes prior to samples collection. Three set of samples from each location were collected in pre-washed polyethylene bottles of 500 ml capacity. One set of the collected is utilized for the determination of cations and anions, containing no preservatives. The remaining two samples have been preserved (1 ml in 500 ml) with nitric acid and hydrochloric acid for the determination of heavy

metals like iron, manganese, copper, lead, cadmium, zinc and metalloid (arsenic), respectively. All the samples were stored at the temperature of $\leq 4\text{ }^{\circ}\text{C}$ using ice/cold packs or refrigerator [296]. The parameters such as pH, electrical conductivity and total dissolved solids have been examined on the sampling sites.

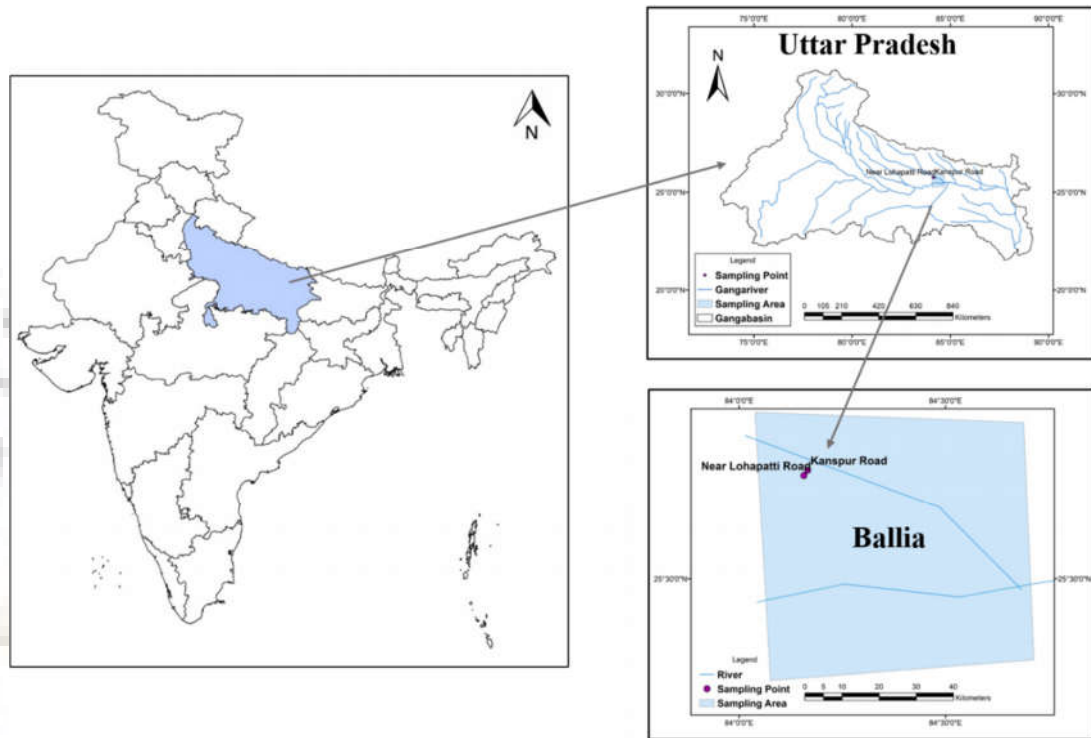


Figure. 5.1. Map showing location of the groundwater sampling points.

5.3.2 Artificial water formulation (AWF)

The batch experiments are not feasible using actual groundwater at laboratory scale due to the large volume of sample requirement and fluctuating water quality issues [297]. The literature requires to investigate a methodology deals in the formulation of water at workplace accurately and conveniently. The utilization of synthetic water for batch studies having the concentrations actual representing the real world conditions is an innovative perspective. In this study, the artificial water containing majority of the ionic elements equivalent to those present in the collected groundwater samples (location I and II) have been formulated [297], [298]. These are further used for performing batch adsorption experiments for As^{V} removal. The details are given below in Tables 5.1 and 5.2.

Table 5.1. Elements contributed in the formulation of artificial water.

Elements	Atomic wt.	Concentration		Molarity		ZnSO ₄	NaCl	CaCl ₂	MgCl ₂	NaHCO ₃	Na ₂ SO ₄	NaF	MnSO ₄	K ₂ SO ₄	Na ₂ PO ₄	KNO ₃	Na ₂ SiO ₃	Charge	
		Location I	Location II	Location I	Location II														
Chloride	35.45	132	435	3.72 x 10 ⁻³	1.23 x 10 ⁻²	0	1	2	2	0	0	0	0	0	0	0	0	0	-1
Sodium	22.98	33	169	1.44 x 10 ⁻³	7.35 x 10 ⁻³	0	1	0	0	1	2	1	0	0	3	0	2	1	
Bicarbonate	61.02	27	115	4.43 x 10 ⁻⁴	1.88 x 10 ⁻³	0	0	0	0	1	0	0	0	0	0	0	0	-1	
Potassium	39.10	15	95	3.84 x 10 ⁻⁴	2.43 x 10 ⁻³	0	0	0	0	0	0	0	0	2	0	1	0	1	
Fluoride	18.99	1.5	3	7.90 x 10 ⁻⁵	1.58 x 10 ⁻⁴	0	0	0	0	0	1	0	0	0	0	0	0	-1	
Nitrate	62.00	20	140	3.22 x 10 ⁻⁴	2.26 x 10 ⁻³	0	0	0	0	0	0	0	0	0	0	1	0	-1	
Calcium	40.08	29	185	7.24 x 10 ⁻⁴	4.62 x 10 ⁻³	0	0	1	0	0	0	0	0	0	0	0	0	2	
Zinc	65.38	2	4	3.06 x 10 ⁻⁵	6.12 x 10 ⁻⁵	1	0	0	0	0	0	0	0	0	0	0	0	2	
Magnesium	24.31	27	33	1.11 x 10 ⁻³	1.36 x 10 ⁻³	0	0	0	1	0	0	0	0	0	0	0	0	2	
Sulphate	96.06	30	220	3.12 x 10 ⁻⁴	2.29 x 10 ⁻³	1	0	0	0	1	0	1	1	0	0	0	0	-2	
Silicates	96.03	18	42	1.87 x 10 ⁻⁴	4.37 x 10 ⁻⁴	0	0	0	0	0	0	0	0	0	0	0	1	-2	
Manganese	54.94	2	3	3.64 x 10 ⁻⁵	5.46 x 10 ⁻⁵	0	0	0	0	0	0	1	0	0	0	0	0	2	
Phosphates	35.45	0.91	2	9.59 x 10 ⁻⁶	2.11 x 10 ⁻⁵	0	0	0	0	0	0	0	0	0	1	0	0	-3	

Table 5.2. Comparison of ionic concentration between actual groundwater and artificial formulated water.

Element	Location I				Location II			
	Actual groundwater conc. (mg L ⁻¹)	Calculated values from matrix	Artificial water conc. (mg L ⁻¹)	Diff. (%)	Actual groundwater conc. (mg L ⁻¹)	Calculated values from matrix	Artificial water conc. (mg L ⁻¹)	Diff. (%)
TDS (gravimetric)	435.9	-	411.5	5.6	1590.6	-	1405.7	11.6
TDS (calculated by ions)	337.4	261.4	310.6	7.9	1446	1171.1	1321.5	8.6
Chloride	132	67.1	112.0	15.2	435	222.7	346	20.5
Sodium	33	23.1	28.0	15.2	169	111.2	141	16.6
Bicarbonate	27	27.0	28.0	-3.7	115	114.8	113	1.7
Potassium	15	13.8	13.3	11.3	95	91.6	93	2.1
Fluoride	1.5	1.5	1.5	1.3	3	2.94	3.16	-5.3
Nitrate	20	20.0	21.2	-6.0	140	139.8	139	0.7
Calcium	29	28.9	26.4	9.0	185	185.3	181.5	1.9
Zinc	2	1.9	1.9	5.0	4	4.43	4.1	-2.5
Magnesium	27	27.0	24.5	9.3	33	33.2	32.4	1.8
Sulphate	30	30.1	32.4	-8.0	220	219.4	221.1	-0.5
Silicates	18	18.1	18.6	-3.3	42	41.4	42.3	-0.7
Manganese	2	1.9	1.9	7.5	3	3.4	3.2	-6.7
Phosphates	0.91	1.1	1.0	-6.6	2	1.06	1.75	12.5
Arsenate*	55	-	57.0	-3.6	200	-	201	-0.5

*The arsenate concentration representing the unit of (µg L⁻¹). The large difference (%) for calcium and magnesium ions concentration is contribute to high hygroscopic nature of their salts. Similar, the higher variation for sodium ions is due to ignorance of sodium arsenate salts during matrix calculations.

This study is utilized a computational analysis for calculating the required quantity of available salt compounds for the synthesis of artificial water [209]. During the first step of formulation array, a square matrix has been designed between the different elemental atoms and the charge associated with these ion(s) contributing to groundwater composition, shown in Table 5.1. Then, a multiplication of inverse matrix with the targeted values of concentration(s) has been applied for calculating the amount of required compounds, in achieving the desired concentration of ion(s). element. This formulation array is customized by varying the types of compounds containing common ions and arrangement of array in order to obtain the appropriate results. Further, the compound containing As^V specie has been ignored during matrix array calculations due to its large concentration difference as compared to other ion(s). Additionally, an inorganic salt (sodium arsenate) is added prior to the adsorption studies in the synthetic water.

Table 5.3. Final amount of salts taken for artificial water formulation.

Compounds	Molecular weight	% contribution of each salt		Amount required (mg)	
		Location I	Location II	Location I	Location II
ZnSO ₄ . 7H ₂ O	287.54	1.64	1.06	8.4094	19.4786
NaCl (anhy.)	58.45	0.70	0.94	3.5765	17.2316
CaCl ₂ . 2H ₂ O	147	20.74	37.13	106.1647	679.4825
MgCl ₂ . 6H ₂ O	203.3	44.05	15.15	225.5227	277.3068
NaHCO ₃ . (anhy.)	84.01	7.27	8.64	37.2290	158.0520
Na ₂ SO ₄ (anhy.)	142.04	6.09	16.03	31.1764	293.4096
NaF (anhy.)	41.99	0.65	0.35	3.3450	6.4957
MnSO ₄ . 6H ₂ O	169.06	1.16	0.57	5.9271	10.3408
K ₂ SO ₄ (anhy.)	174.26	1.02	0.85	5.2023	15.5235
Na ₃ PO ₄ . 12H ₂ O	380.12	0.86	0.23	4.4103	4.2673
KNO ₃ (anhy.)	101.1	6.38	12.46	32.6809	227.9586
Na ₂ SiO ₃ . 9H ₂ O	284.2	10.48	6.69	53.6529	122.4339

5.3.3 Analysis for different elemental ions

The methods related to water samples collection, mode of their preservation and sample preparation for different analysis have been carried out through standards procedure(s) [299], [300]. The analysis for the total hardness, total alkalinity and bicarbonate ions are performed using the titrimetric methods, followed by standard operating procedures of APHA (American Protection

Health Agency). For the determination of phosphate and silicate ions, the filtered sample(s) are analysed through spectrophotometric techniques. Stannous chloride method is used to determine the concentration of phosphate ions, and the developed colour measured in a path length of 1 cm at wavelength of 690 nm. It determines the reactive phosphorous in the sample which largely involves the orthophosphates. The minimum detection limit of the method is $0.01 \text{ PO}_4^{3-}\text{-P mg L}^{-1}$. The common aqueous phases of silica present in groundwater are H_4SiO_4 and H_3SiO_4^- . Their concentration(s) are measured using molybdosilicate method, involving the colorimetric detection at 410 nm for light path length of 1 cm. The minimum detection limit is $0.04 \text{ SiO}_2 \text{ mg L}^{-1}$. The concentration(s) of remaining the cations and anions are determined by employing ion chromatography technique.

Further, for the analysis of heavy metal(s) and arsenic, the samples have been digested with nitric acid and further allowed to filtered through Whatman™ 42 cellulose filter prior to the analysis on ICEP-MS and MP-AES, respectively. The detection limit for these ions are in $\mu\text{g L}^{-1}$ range.

5.3.4 Taguchi's design of experimental methodology

It is an effective statistical tool in developing a suitable experimental approach for laboratory investigations at optimized parametric levels by selecting minimum number of experiments [301]. It depends on modeling of experiments classifying the engineering aspects for cost-effectiveness of process along with to overcome drawbacks related to conventional removal techniques [302], [303]. It helps to identify the different levels of design and process parameters that exhibiting better performance for the removal of contaminant. The orthogonal arrays (OA's), S: N analysis and variance were expressed as significant tools to analyse the outcomes of parameter design [304]. To prevent the effect of uncontrollable components (noise factors), the levels that causes minimum variations to system performance were selected as optimized conditions for the process parameters. The Taguchi's approach, as adopted in present study, comprises four phases such as planning of parameters, experimental investigations, analyses and validation along with various steps.

Each phase includes individual objectives which are associated sequentially to establish an optimization process. In this method, the design of experiments (DoE's) involves the organization

of several number of experimental variables as suggested by orthogonal array so that to reduce the experimental errors by enhancing the efficiency and reproducibility of laboratory experiments.

Design of experiment (Step 1)

The first step in Stage I includes the selection of different factors to be optimized through laboratory scale batch experiments which affect the removal of As^V from aqueous solution using BIO NPs and BIO-DW nanohybrids. The literature is widely reviewed in explaining the role of experimental variables affecting removal capabilities of As^V onto the surface of iron^(III) metallic oxides nanoadsorbents [236], [305], [306]. It is therefore, the primary factors such as temperature, pH, dose and contact time have considered for parametric design in the present investigation. The studies evaluating removal capacity of arsenic for real world water conditions using nanoadsorbents is a prerequisite of literature [233]. During preliminary experiments, factors such as total dissolved solids (TDS) and shaking speed are found to be crucial, affecting the removal capabilities of as-synthesized nanomaterials. For systematic approach, these parameters have also explored for the evaluation of removal characteristics. Goswami *et al.* [112] have examined the effect of shaking speed in removal of arsenic using copper oxide nanoparticles. Based on the several analyses, seven process parameters are selected for the present experimental design. The details of these parameters along with their designation and assigned levels are given in Table 5.4. Although, As^V removal is analysed to be simultaneously affected by all the mentioned variables. Therefore, three two-parameter interactions (A. B, A. C, B. C) have also been examined for the inter-parametric investigations.

Table 5.4. Process parameters for As^V adsorption study in a multicomponent system onto BIO NPs and BIO-DW nanohybrids using Taguchi's design of orthogonal array (OAs).

	Parameters	level 1	level 2	level 3
A	Arsenate concentration ($\mu\text{g L}^{-1}$)	55	128	200
B	TDS (mg L^{-1})	436	1014	1591
C	Shaking speed (rpm)	100	170	240
D	Temperature ($^{\circ}\text{C}$)	10	20	30
E	pH (pH unit)	7	8	9
F	Dose (g L^{-1})	0.05	0.10	0.15
G	Contact time (min)	2	53	104

Orthogonal array (OA) and assignment of parameters

The second approach of stage I includes to design the matrix of experiments which define the procedure for data analysis. An appropriate orthogonal array was selected for the controlling parameters suitable for present study. Several orthogonal arrays have been proposed by Taguchi in selecting the experimental design based on number of parameters and for the interaction to be explored. In selecting a suitable OA, the design must satisfy the following pre-requisite:

$$\text{total DOF required for experiment} \leq \text{total DOF of OA}$$

where OA and DOF represent orthogonal array and degree of freedom. The selected parameters have significant effects on the removal of As^V which are crucial and need to be investigated at different level along with their inter-parametric interaction. Therefore, the process parameters were categorised into a three levels which were explained the high order of polynomial behaviour.

In this study, the calculated degree of freedom is 26 [= no. of parameters (7) x {no. of levels (3) – 1} + {no. of two-PI (3) x no. of PI (2) x no. of columns assigned for each PI (2)}]. Hence, a standard three level OA of L₂₇ (3¹³) was selected for further studies. The details of L₂₇ array highlighting parameters and interactions for both of BIO NPs and BIO-DW nanohybrids are shown in Table 5.5 and 5.6.

Batch removal experiments (Step 2)

Batch adsorption studies have been explored for the removal of As^V using BIO NPs and BIO-DW nanohybrids for the selected 27 experimental trails, having seven process factors with three levels (Table 5.4). The obtained results from individual set in terms of total amount of As^V adsorbed (q_e , $\mu\text{g g}^{-1}$) onto the surface of BIO NPs and BIO-DW nanohybrids, shown in Table 5.5 and 5.6. For reproducible results, each set of experimental trails are performed in the replicates of three times, designated as R₁, R₂ and R₃.

In each experimental trail, 100 mL of aqueous solution containing different As^V concentration (levels) are taken in 200 mL glass stoppered conical flask containing specific dose (mg/100 mL) of BIO NPs and BIO-DW nanohybrids. The formulated water for representing the ionic concentration to those for location I and II have been divided into three sets of solutions having pH 7, 8 and 9. The pH has been adjusted using NaOH (0.001 N) and per-chloric acid (0.001 N) without any adjustment of pH during the sorption process. Then, the batch experiments are performed for different process parameters as suggested Taguchi's orthogonal array. Finally, the

samples are filtered after the appropriate contact time of sorption process and filtrate(s) have been analysed for the determination of residual concentration of As^V ions.

The removal capacity ($\mu\text{g mg}^{-1}$) of As^V from the aqueous solution is calculated by using the following equation 5.1:

$$\text{Removal capacity } (Q_e) = \frac{(C_0 - C_f) V}{W} \quad (5.1)$$

where C_0 and C_f are the initial and final concentration ($\mu\text{g L}^{-1}$) of As^V, respectively, V is the volume (in litre) of solution under investigation and W is the adsorbent dose (mg). The sum of removal capacity for different replication (i.e. $R_1 - R_3$) is represented by q_e .

Evaluation of outputs and performance assessment (Step 3)

The explored experimental data is organized with higher-is-better quality characteristics (i) to identify the optimum removal conditions (ii) along with the potential of individual factor affecting the adsorption process and (iii) the estimation of performance (Q_e) under optimized conditions. This methodology defines the loss - function as quantity which is directly related to the deviation from the attributes of nominal quality. Taguchi identified a quadratic relationship to be practical viable function which depend on the Taylor Expansion Series as expressed below in equation 5.2:

$$L_{(y)} = k (y - m_T)^2 \quad (5.2)$$

Where L , k , y and m are denoting the loss in removal capacity, proportionality constant (depend on the magnitude of characteristic and removal capacity unit), experimental value calculated for individual trial and target value, respectively. However, Taguchi modify the loss function into a statistical tool known as signal-to-noise (S: N) ratio which is discussed further.

Signal to noise ratio (S: N ratio)

This attribute of the methodology combines the two characteristics of a distribution into a single metric. It unites the average levels of the quality characteristics along with the variance to around of average. The large value of S: N ratio signify that the signal is higher as compared to

random effects of noise component. This depicts the optimum value of removal characteristics for BIO NPs and BIO-DW nanohybrids. Among three types of S: N ratio responses (smaller-is-better, nominal-the-best, larger-is-better), larger-is-better characteristic is used in this study [307] which integrate various repetition (minimum two are required) into one value and its equation is given below as 5.3:

$$(S:N)_{LB} = -10 \log \frac{\sum_{i=3}^n 1/(q_i)^2}{N} \quad (5.3)$$

where ' q_i ' is the value of experimental outcome (adsorption capacity) in an observation ' i ' and ' N ' represents the replication number of experiments. However, Taguchi had suggested several number of methods for the analysis of S: N data [308]. Among those, plotting of response curves (average value), ANOVA for raw and S: N data have been examined in the present investigation.

In these factors, the curve plot at individual level indicates a trend which is a pictorial representation showing the effect of process parameter(s) on response. The S: N ratio is considered as an experimental response and generally used to measure the variations among a trail. Further, the ANOVA test has been conducted for the calculated values of adsorption capacity (q_e) and S: N ratio. It identifies the significant parameters such as mean and variance.

Prediction of mean

After the optimization of experimental conditions, the average value of response (μ) at the optimized conditions have been predicted for As^V removal using both BIO NPs and BIO-DW nanohybrids. This has been calculated by considering significant parameters, identified during ANOVA analysis. For example, the parameters total dissolved solids (B) and shaking speed (C) were found to be significant at the levels of B₃ and C₂ respectively, thereafter, the mean of response can be estimated as suggested by Taguchi's, using the following equation 5.4:

$$\mu_{\text{BIO and BIO-DW}} = (\bar{T} + (\bar{B}_3 - \bar{T}) + (\bar{C}_2 - \bar{T})) = \bar{B}_3 + \bar{C}_2 - \bar{T} \quad (5.4)$$

where \bar{T} is representing the overall mean of identified response; \bar{B}_3 and \bar{C}_2 are indicating the response mean value at third and second level for parameter B and C, respectively; μ is the only value which estimate the average of the results derived from the experiments.

Table 5.5. Taguchi's orthogonal array (OA) $L_{27}(3^{13})$ for experimental runs assignment along with three interactions levels (2^{nd} order) and calculation of adsorption capacity (Q_e) values for As^{V} in multicomponent ionic systems using BIO nanoparticles.

Runs	Trials													Calculated Q_e ($\mu\text{g mg}^{-1}\text{-Fe}$)			S: N ratio (dB)
	1, A	2, B	3, A. B	4, A. B	5, C	6, A. C	7, A. C	8, B. C	9, D	10, E	11, B. C	12, F	13, G	R ₁	R ₂	R ₃	
1.	1	1	1	1	1	1	1	1	1	1	1	1	1	1.21	1.22	1.23	1.75
2.	1	1	1	1	2	2	2	2	2	2	2	2	2	0.45	0.46	0.45	-6.89
3.	1	1	1	1	3	3	3	3	3	3	3	3	3	0.38	0.35	0.44	-8.31
4.	1	2	2	2	1	1	1	2	2	2	3	3	3	0.18	0.17	0.19	-14.89
5.	1	2	2	2	2	2	2	3	3	3	1	1	1	0.74	0.79	0.85	-2.03
6.	1	2	2	2	3	3	3	1	1	1	2	2	2	0.69	0.63	0.69	-3.49
7.	1	3	3	3	1	1	1	3	3	3	2	2	2	0.28	0.26	0.29	-11.09
8.	1	3	3	3	2	2	2	1	1	1	3	3	3	0.38	0.38	0.40	-8.26
9.	1	3	3	3	3	3	3	2	2	2	1	1	1	0.59	0.57	0.59	-4.71
10.	2	1	2	3	1	2	3	1	2	3	1	2	3	1.07	1.04	1.11	0.62
11.	2	1	2	3	2	3	1	2	3	1	2	3	1	0.62	0.58	0.64	-4.25
12.	2	1	2	3	3	1	2	3	1	2	3	1	2	4.01	3.79	4.00	11.88
13.	2	2	3	1	1	2	3	2	3	1	3	1	2	0.59	0.55	0.57	-4.86
14.	2	2	3	1	2	3	1	3	1	2	1	2	3	2.03	2.01	2.05	6.15
15.	2	2	3	1	3	1	2	1	2	3	2	3	1	0.61	0.64	0.63	-4.04
16.	2	3	1	2	1	2	3	3	1	2	2	3	1	0.52	0.40	0.49	-6.70
17.	2	3	1	2	2	3	1	1	2	3	3	1	2	1.12	1.13	1.15	1.09
18.	2	3	1	2	3	1	2	2	3	1	1	2	3	0.84	0.93	0.80	-1.40
19.	3	1	3	2	1	3	2	1	3	2	1	3	2	1.38	1.40	1.43	2.94
20.	3	1	3	2	2	1	3	2	1	3	2	1	3	5.93	5.52	6.12	15.33
21.	3	1	3	2	3	2	1	3	2	1	3	2	1	1.38	1.36	1.41	2.83
22.	3	2	1	3	1	3	2	2	1	3	3	2	1	3.08	2.93	3.03	9.57
23.	3	2	1	3	2	1	3	3	2	1	1	3	2	0.99	1.06	0.96	0.02
24.	3	2	1	3	3	2	1	1	3	2	2	1	3	0.37	0.30	0.33	-9.70
25.	3	3	2	1	1	3	2	3	2	1	2	1	3	1.46	1.74	1.52	3.87
26.	3	3	2	1	2	1	3	1	3	2	3	2	1	1.61	1.36	1.48	3.38
27.	3	3	2	1	3	2	1	2	1	3	1	3	2	2.10	2.03	2.33	6.62
Total														34.64	33.62	35.20	
Mean															1.28		

Table 5.6. Taguchi's orthogonal array (OA) $L_{27}(3^{13})$ for experimental runs assignment along with three interactions levels (2nd order) and calculation of adsorption capacity (Q_e) values for As^V in multicomponent ionic systems using BIO-DW nanoparticles.

Runs	Trials													Calculated Q_e ($\mu\text{g mg}^{-1}\text{-Fe}$)			S: N ratio (dB)
	1, A	2, B	3, A. B	4, A. B	5, C	6, A. C	7, A. C	8, B. C	9, D	10, E	11, B. C	12, F	13, G	R ₁	R ₂	R ₃	
1.	1	1	1	1	1	1	1	1	1	1	1	1	1	2.53	2.52	2.52	8.05
2.	1	1	1	1	2	2	2	2	2	2	2	2	2	0.80	0.79	0.79	-2.03
3.	1	1	1	1	3	3	3	3	3	3	3	3	3	0.70	0.71	0.72	-2.99
4.	1	2	2	2	1	1	1	2	2	2	3	3	3	0.45	0.46	0.46	-6.81
5.	1	2	2	2	2	2	2	3	3	3	1	1	1	1.60	1.60	1.61	4.09
6.	1	2	2	2	3	3	3	1	1	1	2	2	2	1.15	1.16	1.15	1.22
7.	1	3	3	3	1	1	1	3	3	3	2	2	2	0.43	0.42	0.42	-7.53
8.	1	3	3	3	2	2	2	1	1	1	3	3	3	0.92	0.91	0.91	-0.78
9.	1	3	3	3	3	3	3	2	2	2	1	1	1	1.22	1.22	1.21	1.72
10.	2	1	2	3	1	2	3	1	2	3	1	2	3	1.06	1.05	1.05	0.43
11.	2	1	2	3	2	3	1	2	3	1	2	3	1	1.13	1.13	1.14	1.10
12.	2	1	2	3	3	1	2	3	1	2	3	1	2	6.33	6.33	6.32	16.02
13.	2	2	3	1	1	2	3	2	3	1	3	1	2	8.82	8.82	8.81	18.91
14.	2	2	3	1	2	3	1	3	1	2	1	2	3	3.53	3.52	3.53	10.95
15.	2	2	3	1	3	1	2	1	2	3	2	3	1	0.82	0.83	0.83	-1.65
16.	2	3	1	2	1	2	3	3	1	2	2	3	1	1.29	1.30	1.30	2.24
17.	2	3	1	2	2	3	1	1	2	3	3	1	2	1.65	1.66	1.65	4.36
18.	2	3	1	2	3	1	2	2	3	1	1	2	3	0.43	0.41	0.41	-7.58
19.	3	1	3	2	1	3	2	1	3	2	1	3	2	0.14	0.16	0.14	-16.66
20.	3	1	3	2	2	1	3	2	1	3	2	1	3	12.08	12.06	12.05	21.63
21.	3	1	3	2	3	2	1	3	2	1	3	2	1	2.62	2.62	2.63	8.37
22.	3	2	1	3	1	3	2	2	1	3	3	2	1	5.07	5.08	5.08	14.11
23.	3	2	1	3	2	1	3	3	2	1	1	3	2	2.18	2.19	2.19	6.79
24.	3	2	1	3	3	2	1	1	3	2	2	1	3	2.64	2.63	2.63	8.41
25.	3	3	2	1	1	3	2	3	2	1	2	1	3	2.95	2.97	2.97	9.43
26.	3	3	2	1	2	1	3	1	3	2	3	2	1	2.16	2.15	2.15	6.66
27.	3	3	2	1	3	2	1	2	1	3	1	3	2	3.80	3.79	3.79	11.58
Total														68.47	68.47	68.45	
Mean																	2.54

Determination of confidential interval

Taguchi has suggested two different types of confidence intervals (CI) in regard for the estimation of mean at optimum experimental conditions which are discussed below:

(i). The *CI* lie across the estimated the average value of a treatment conditions used in a conformation experiment to verify predictions. It is designated as CI_{CE} (confidence interval for a group of sample). It is a representation of small group of samples considered for a specific condition.

(ii). The *CI* lie across the estimated average value of a particular treatment condition predicted from the experimental runs. It is designated as CI_{POP} (confidence interval for whole experimental outcomes). It is representing the entire population is under specified conditions as whole.

Due to smaller sample size in CI_{CE} as compared to CI_{POP} in the conformation experiments, CI_{CE} must be moderately larger value. The expression for the calculation of *CI* are mentioned below in equations 5.5 and 5.6:

$$CI_{CE} = \sqrt{F_{\alpha}(1, f_e) V_e \left[\frac{1}{n_{effective}} + \frac{1}{R} \right]} \quad (5.5)$$

$$CI_{POP} = \sqrt{\frac{F_{\alpha}(1, f_e) V_e}{n_{effective}}} \quad (5.6)$$

Where, $F_{\alpha}(1, f_e)$ is representing the *F*-ratio at a *CI* of $(1 - \alpha)$ corresponding to the $DOF=1$ and a DOF with an error of f_e ; V_e is an error variance calculated in ANOVA and $n_{effective}$ is expressed as equation 5.7:

$$n_{effective} = \frac{N}{1 + [total\ DOF\ accounted\ in\ the\ estimation\ of\ mean\ response]} \quad (5.7)$$

Where ' N ' is denoting the total number of experimental outcomes and ' R ' represents the sample size included in the conformation experiments.

Conformation experiments (Stage 4)

This is a crucial step for the verification of experimental outcomes. It includes an evaluation of predicted removal capacity at optimized conditions. The assignment of insignificant parameters can be selected on the basis of economic priorities. The conformation experiments have been carried out at optimized conditions for As^V removal using both BIO NPs and BIO-DW nanohybrids. Moreover, the average value of these experimental outcomes have been compared with those of expected average value, based on the investigation of parameters and levels tested.

5.3.5 Artificial neural network (ANN) for predictive modeling

Arsenic removal using nanoparticles require a robust methodology for predictive analysis. This tool has a capability to explore input and output parameters effectively in complex conditions. Also, few authors have explored the predictive modeling for the arsenic removal onto different adsorbents using ANN [309], [310]. The topology network architecture for this study is illustrated in Figure 5.2 below:

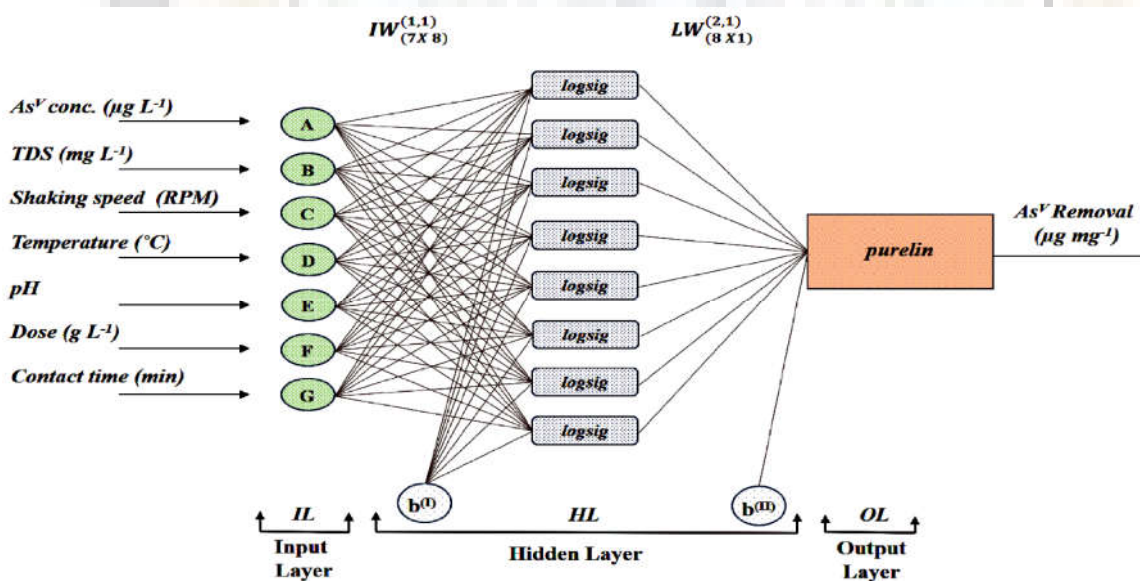


Figure 5.2. Architecture of ANN model for the prediction of removal efficiency of As^V using BIO NPs and BIO-DW nanohybrids.

In present study, the training of ANN model for Taguchi's data has been evaluated using MATLAB neural network tool. An approximation algorithm based on feed-forward back propagation has been applied, which includes the mean square error representing the accuracy

index. Three layered architecture of back propagation neural network (BPNN) represented as IL-HL-OL, where, IL is input nodes (equal to number of variables in the model), HL is hidden nodes (optimized using runs), OL is output nodes (based on numbers).

5.4 Results and Discussion

5.4.1 Physicochemical characterization of collected groundwater samples

The physicochemical characterization of collected groundwater samples has been performed for the several elements (Table 5.7). Among those, the phosphate, silicates, sodium, potassium, fluoride, chloride, calcium, magnesium, sulphate, nitrate, iron, manganese, zinc and arsenic ions have been taken into consideration in the formulation of artificial water.

The arsenic concentration in both of these samples are determined beyond the concentration limit as suggested by WHO for drinking water ($> 10 \mu\text{g L}^{-1}$). Moreover, the validation of formulated water in terms of accuracy has also been performed by analysing the concentration of different ions. A comparison between the concentrations of ions present in actual groundwater and artificially formulated water along with their percent variations is given in Table 5.2. A significant agreement between the actual and formulated water with the correlation coefficient (R^2) values of 0.99 and 0.97 has been observed for the location I and location II, respectively.

Table 5.7. Percent distribution inorganic species (free or complex ions) possibly effecting the As^V adsorption.

Parameters	Unit	Method of test	DL*	PL*	Location I	Location II
pH	pH unit	pH probe	6.5-8.5	NR	7.45 ± 0.05	7.34 ± 0.05
Electrical conductivity	µS cm ⁻¹	EC probe	-	-	341 ± 6.0	1524 ± 7.4
Total Dissolved Solids	mg L ⁻¹	TDS probe	500	2000	435.9 ± 4	1590.6 ± 4.4
Total hardness	mg L ⁻¹	Titrimetric	300	600	160 ± 4	424 ± 4
Alkalinity	mg L ⁻¹	Titrimetric	200	600	86 ± 3	222 ± 3.6
Bicarbonate (as HCO ₃ ²⁻)	mg L ⁻¹	Titrimetric	-	-	26 ± 2	115.3 ± 1.5
Phosphate (as PO ₄ ²⁻)	mg L ⁻¹	Spectrophotometric	-	-	0.91 ± 0.04	2.02 ± 0.11
Silicates (as H ₄ SiO ₄)	mg L ⁻¹	Spectrophotometric	-	-	19.4 ± 1.6	42.4 ± 0.8
Sodium (as Na ⁺)	mg L ⁻¹	IC	-	-	32.4 ± 0.9	169.4 ± 1.0
Potassium (as K ⁺)	mg L ⁻¹	IC	-	-	15.3 ± 0.2	94.7 ± 0.97
Fluoride (as F ⁻)	mg L ⁻¹	IC	1.0	1.5	1.54 ± 0.05	3.04 ± 0.01
Chloride (as Cl ⁻)	mg L ⁻¹	IC	250	1000	132.4 ± 1.0	435.2 ± 1.2
Calcium (as Ca ²⁺)	mg L ⁻¹	IC	75	200	28.9 ± 0.4	185.1 ± 0.6
Magnesium (as Mg ²⁺)	mg L ⁻¹	IC	30	100	26.8 ± 1.0	32.4 ± 1.0
Sulphate (as SO ₄ ²⁻)	mg L ⁻¹	IC	200	400	30.4 ± 1.2	220.4 ± 1.5
Nitrate	mg L ⁻¹	IC	45	NR	20.0 ± 0.4	140.0 ± 1.1
Iron	mg L ⁻¹	ICP-MS	0.3	1.0	0.53 ± 0.02	0.37 ± 0.03
Manganese	mg L ⁻¹	ICP-MS	0.1	0.3	12 ± 0.07	3.03 ± 0.1
Copper	mg L ⁻¹	ICP-MS	0.05	1.5	ND	ND
Lead	mg L ⁻¹	ICP-MS	0.01	NR	ND	ND
Cadmium	mg L ⁻¹	ICP-MS	0.003	NR	ND	ND
Zinc	mg L ⁻¹	ICP-MS	5	15	2 ± 0.07	3.96 ± 0.27
Arsenic (as Total)	µg L ⁻¹	MP-AES	10	50	54 ± 2	200 ± 1

As per IS: 10500, NR, no relaxation; ND, not determined; *DL, desirable limit; *PL, permissible limit; IC, Ion chromatogram; ICP-MS, Inductively couple plasma mass spectroscopy; MP-AES, Microwave plasma atomic emission spectroscopy.

5.4.2 Effects of process parameters on As^V removal in multi-ionic system

Experimental runs have been executed for As^V removal using BIO NPs and BIO-DW nanohybrids under the specified conditions as suggested by Taguchi's L₂₇ OA (shown in Table 5.5 and 5.6). Three set of experiments are performed for each experimental run indicating different parametric conditions. The average values of the adsorption capacity (q_e) and S: N ratio have been calculated for individual parameter and parametric-interactions at three different levels (L₁, L₂, L₃), mentioned in Table 5.8 and 5.9. The notable interactions affecting the adsorption capacity are identified for different conditions at three levels for both of these BIO NPs and BIO-DW nanohybrids. These interactions are discussed in the following subheads:

5.4.2.1 Effects of shaking speed (C), temperature (D) and contact time (G)

The average value of Q_e and S: N ratio for each parameter for the assigned levels (L₁, L₂, L₃) have been determined for as-synthesized nanosystems. The increasing difference between the values of assigned levels indicate the growing influence of that experimental variable on the removal capacity. All the above listed parameters at each level have been demonstrated to bring notable effects on As^V adsorption. These effects have been discussed in details individually below:

BIO nanoparticles (NPs)

The formation of external boundary layer of adsorbing species on adsorbent and the distribution of remaining solute(s) in bulk are significant factors affecting the adsorption phenomena [311], [312]. The lower value of Q_e ($\mu\text{g mg}^{-1}\text{-Fe}$) at level L₁ (1.09) and L₃ (1.21) as compared to that of level L₂ (1.53) indicates that a variation in shaking speed is affecting the As^V removal significantly (Table 5.8). This decrease in the removal capacity can be attributed to the desorption of adsorbed As^V into the aqueous solution at the high shaking speed of (L₃) 240 rpm. This study revealed that the external diffusion is likely to be the rate limiting step in adsorption process [112]. Further, the lower value of adsorption capacity ensures that nanoparticles have not been completely and homogeneously suspended in the solution at the shaking speed of < 170 rpm.

An increase in the temperature from 10-30 °C, caused an increase in the adsorption at lower temperature (10 °C). This is suggested that the physical absorption is predominating. At 10 °C (L₁), the maximum value of Q_e ($1.5 \mu\text{g mg}^{-1}\text{-Fe}$) has been observed (Table 5.8). These observations are

quite opposite to those observed in previous chapter. It demonstrates that the presence of other ions (as specified in Table 5.1) influence the behaviour of As^V removal. Therefore, the surface complexation models have been explored to understand the possible causes of this shift in separate section (6.4.7). Further, the maximum value (1.41 $\mu\text{g mg}^{-1}\text{-Fe}$) of q_e is observed for larger contact time (L₃) indicating that As^V oxyanions and hydroxyl groups of nanoparticles are interacting with weak electrostatic interactions.

BIO-DW nanoparticles

For this nanosystem, a similar trend comparable to those of BIO-NPs is observed in As^V removal for the experimental variable of shaking speed (C). However, a different trend has been determined for the parameter(s) temperature (D) and contact time (G). The lower value of q_e ($\mu\text{g mg}^{-1}\text{-Fe}$) at the shaking speed level of L₁ (2.53) and L₃ (2.19) has been observed as compared to that of level L₂ (2.89).

An increase in the temperature from 10-30 °C, a complex effect of a variation in temperature has been noted. At (L₁) 10 °C, the maximum value of Q_e (4.07 $\mu\text{g mg}^{-1}\text{-Fe}$) indicates that removal process is followed the mechanism of primarily physisorption. Then, the removal is decreases to 1.53 $\mu\text{g mg}^{-1}\text{-Fe}$ at temperature of 20 °C and further increase to 2.0 $\mu\text{g mg}^{-1}\text{-Fe}$. But, this increase is also observed at higher temperature in a narrow window range, suggesting chemisorption also to be occurring simultaneously. These observations are the same to those examined in the previous chapter. Further, the maximum removal capacity (1.41 $\mu\text{g mg}^{-1}\text{-Fe}$) is achieved at the contact time (L₂) of 53 min indicating that the interactions between the As^V oxyanions surface functionalities are quicker in BIO-DW nanohybrids as compared to those of BIO NPs.

Table 5.8. Average and main effects of q_e values for BIO nanoparticles: Raw and S: N data.

Factor	Raw data, Average value			Main effects, Raw data		S: N data, Average value			Main effects, (S: N data)	
	L ₁	L ₂	L ₃	L ₂ -L ₁	L ₃ -L ₂	L ₁	L ₂	L ₃	L ₂ -L ₁	L ₃ -L ₂
A	0.6	1.3	2.0	0.7	0.8	-6.4	-0.2	3.9	6.3	4.0
B	1.8	1.0	1.0	-0.8	Nil	1.8	-2.6	-1.9	-4.4	0.7
C	1.1	1.5	1.2	0.4	-0.3	-2.1	0.5	-1.2	2.6	-1.7
D	2.2	0.9	0.8	-1.3	-0.2	3.7	-2.5	-3.9	-6.1	-1.5
E	0.9	1.2	1.7	0.3	0.5	-1.5	-2.1	0.9	-0.5	2.9
F	1.8	1.3	0.8	-0.5	-0.5	1.4	Nil	-4.1	-1.4	-4.1
G	1.1	1.3	1.4	0.2	0.1	-0.5	-0.4	-1.8	0.1	-1.4
A. B	2.2	2.8	2.7	0.7	-0.1	-2.5	-0.5	-2.4	2.0	-1.9
A. C	2.8	2.3	2.6	-0.5	0.3	-2.3	-2.5	-0.7	-0.2	1.9
B. C	2.2	2.8	2.7	0.6	-0.1	-0.6	-3.6	-1.2	-3.0	2.4

Table 5.9. Average and main effects of q_e values for BIO-DW nanohybrids: Raw and S: N data.

Factor	Raw data, Average value			Main effects, Raw data		S: N data, Average value			Main effects, (S: N data)	
	L ₁	L ₂	L ₃	L ₂ -L ₁	L ₃ -L ₂	L ₁	L ₂	L ₃	L ₂ -L ₁	L ₃ -L ₂
A	1.1	2.8	3.7	1.7	1.0	-0.6	5.0	7.8	5.5	2.8
B	3.0	2.9	1.7	-0.1	-1.3	3.8	6.2	2.2	2.5	-4.0
C	2.5	2.9	2.1	0.4	-0.7	2.5	5.9	3.9	3.4	-2.0
D	4.1	1.5	2.0	-2.5	0.5	9.5	2.3	0.5	-7.2	-1.8
E	2.5	2.1	3.0	-0.5	1.0	5.1	2.3	4.9	-2.8	2.6
F	4.4	1.9	1.3	-2.5	-0.6	10.3	2.7	-0.8	-7.6	-3.5
G	2.1	2.8	2.8	0.8	-0.1	5.0	3.6	3.6	-1.3	Nil
A. B	4.8	4.7	5.7	-0.2	1.1	10.0	6.1	8.4	-4.0	2.3
A. C	5.1	4.7	5.4	-0.4	0.6	8.2	7.4	8.9	-0.9	1.5
B. C	3.3	6.3	5.6	3.1	-0.7	3.3	10.0	11.7	6.2	2.2

5.4.2.2 Effects of arsenic initial concentration (A), TDS (B) and pH (E)

BIO nanoparticles (NPs)

An increase in the As^V initial concentration (A) from 55 to 200 $\mu\text{g L}^{-1}$, the maximum adsorption capacity (q_e) has been observed at level L₃. From level L₁ to L₃, the increase in competing ions concentration causes the high adsorption capacity (0.55 to 2.02 $\mu\text{g g}^{-1}\text{-Fe}$) which is due to a decrease in the hindrance for the uptake of As^V ions as mass-transfer operating force intensified.

An increase in the TDS (B) from 436 to 1591 mg L⁻¹, the maximum adsorption capacity (Q_e) has been observed at level L₁. A decrease in the value of Q_e (1.8 to 1.0) is identified with the increase in the TDS concentration (L₁ to L₃) and occurred due to the competition among As^V and other ions to occupy the vacant sites of nanoparticle surface. However, an insignificant variation in adsorption capacity from levels L₂ to L₃ is examined which might be due to the dominating effect of different competing ions leading to negligible adsorption of As^V beyond the TDS concentration of 1014 mg L⁻¹.

An increase in the pH (E) from 7 to 9, the maximum adsorption capacity (Q_e) has been observed at level L₃ (1.7 μg g⁻¹-Fe). It follows increasing trend for As^V removal. From level L₁ to L₃, the increase in the adsorption capacity from 0.9 to 1.7 μg g⁻¹-Fe is observed which might be due to the presence of charged species of As^V beyond the near neutral pH conditions.

As few authors have been reported the increase in removal capacity of nanoparticles in the presence of ions such as nitrate and bicarbonates [313]. Similar, observation have been observed for BIO-DW nanohybrids, but, the extend is larger as compared to those of BIO NPs.

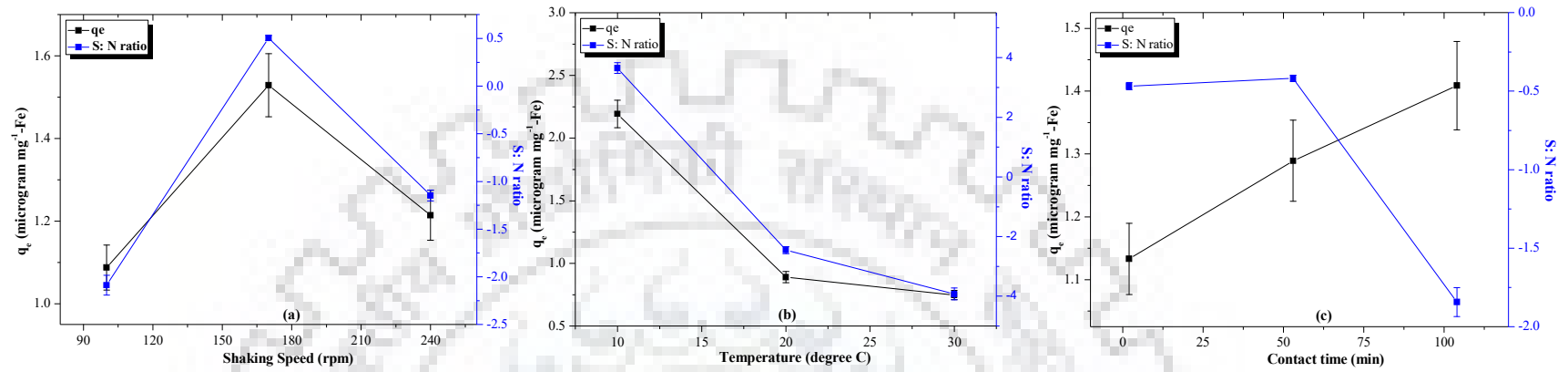


Figure 5.3. Effect of process parameters (a) shaking speed (b) temperature and (c) contact time on the removal capacity (q_e) and S: N ratio for multicomponent adsorption of As^V onto BIO NPs.

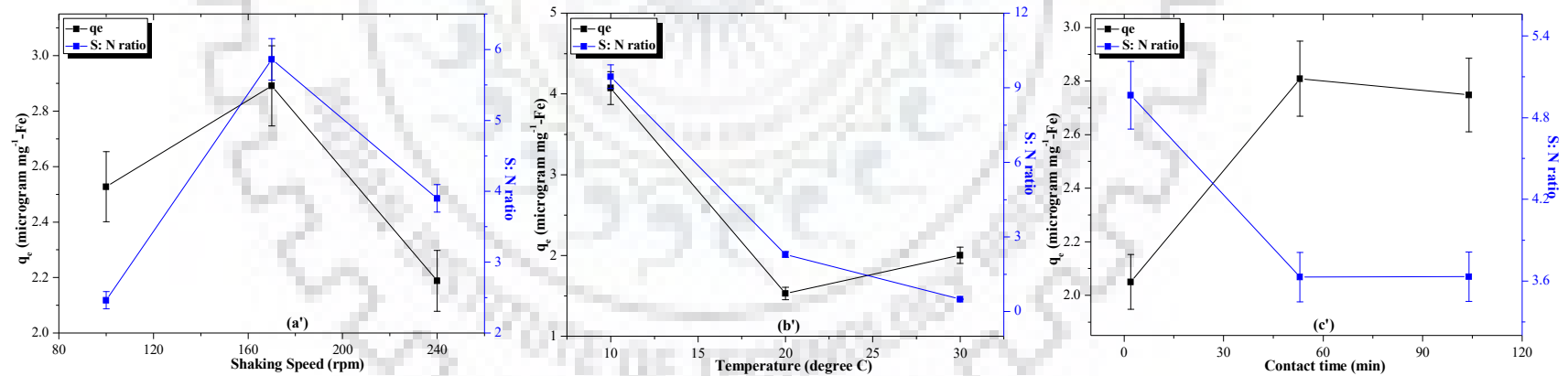


Figure 5.4. Effect of process parameters (a') shaking speed (b') temperature and (c') contact time on the removal capacity (q_e) and S: N ratio for multicomponent adsorption of As^V onto BIO-DW nanohybrids.

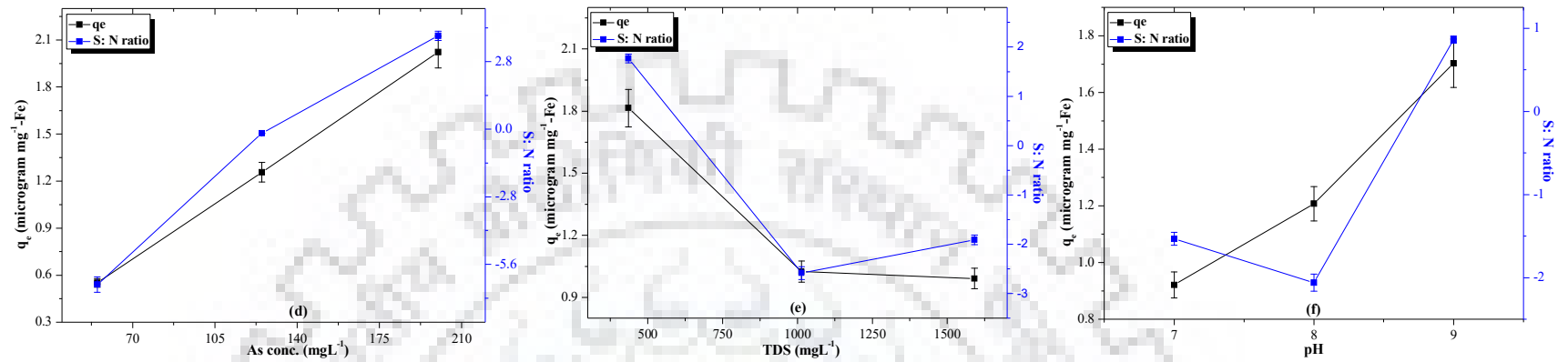


Figure 5.5. Effect of process parameters (d) As^V conc. (e) TDS and (f) pH on the removal capacity (q_e) and S: N ratio for multicomponent adsorption of As^V onto BIO NPs.

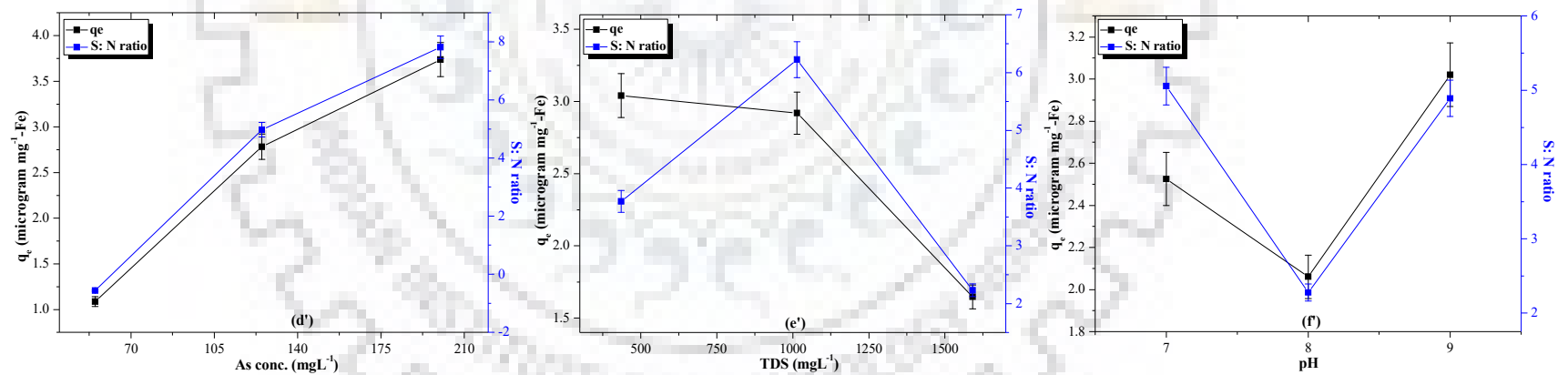


Figure 5.6. Effect of process parameters (d') As^V conc. (e') TDS and (f') pH on the removal capacity (q_e) and S: N ratio for multicomponent adsorption of As^V onto BIO-DW nanohybrids.

5.4.3 Analysis of inter-parametric interactions

Figure 5.7 (a – c) and Figure 5.8 (a' – c') are present the variations in the adsorption capacity as a function of initial concentration of As^{V} at each level of TDS ($L_1 - L_3$). At each level of TDS, an increase in the adsorption capacity has been observed to increase with an increase in the As^{V} concentration. This trend is similar to those examined earlier in the Figure 5.5 (a) and 5.6 (a'). However, in case of BIO-DW nanohybrids at high TDS (L_3), there is a hindrance in the uptake of As^{V} ions as compared to those of BIO NPs (Figure 5.8 c'). This is possibly because of the saturation is achieved in this case at relatively lower TDS. Further, a significant increase in the adsorption capacity has been observed for BIO-DW nanoparticles as compared to BIO NPs with an increase in TDS from L_2 to L_3 . It might be due to the secondary sites developed for As^{V} adsorption provided by the surface complexes produced with other ions.

Figure 5.9 (d – f) and Figure 5.10 (d' – f') are depicting the variations in the adsorption capacity as a function of initial concentration of As^{V} at each level of shaking speed ($L_1 - L_3$). At low concentration of As^{V} ($55 \mu\text{g L}^{-1}$), the shaking speed (L_1 to L_3) has not been examined to affect its removal using both BIO NPs and BIO-DW nanohybrids. Beyond the As^{V} concentration of $55 \mu\text{g L}^{-1}$, an antagonistic behaviour of its removal has been observed for both as-synthesized nanomaterials. A low removal capacity of As^{V} has been found at the shaking speed of 170 rpm (L_2) for BIO NPs and BIO-DW nanohybrids. This trend is different to that observed in the Figure 5.3 (a) and 5.4 (a').

In view of the above results, the combined effect of shaking speed along with TDS has been explored on the removal capacity of As^{V} for both of these nanomaterials. Figure 5.11 (g – i) and Figure 5.12 (g' – i') are demonstrating the effect of TDS (B) and shaking speed (L_1 to L_3) for BIO NPs and BIO-DW nanohybrids, as a function of total adsorption capacity. An insignificant variation in the removal capacity at low shaking speed for the whole range of TDS ($436 - 1591 \text{ mg L}^{-1}$) ensures that nanoparticles have not been homogeneously suspended in the solution at shaking speed of < 170 rpm, and external diffusion is likely to be the rate limiting step in adsorption process. These observations are similar to those examined previously. However, high removal capacity has been observed at high TDS and at a shaking speed of 170 rpm. The inter-parametric interactions studies are revealed that the removal of As^{V} is largely occurred through the formation of surface complexes onto both of BIO NPs and BIO-DW nanohybrids.

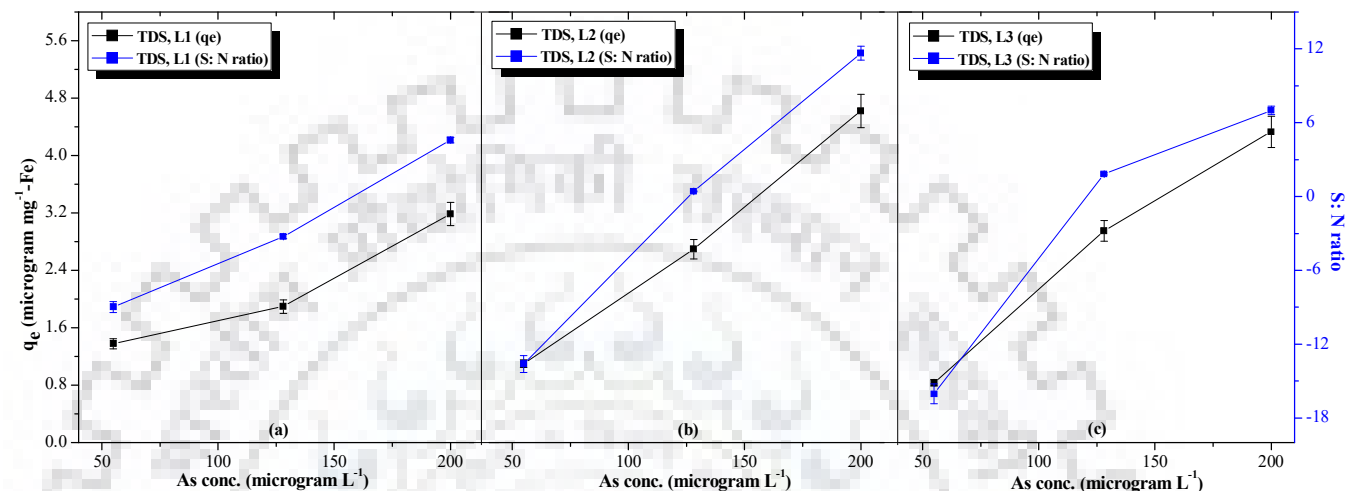


Figure 5.7. Interactions between parameters arsenic initial concentration (A) and TDS (B) at three levels on the removal capacity (q_e) and S: N ratio for multicomponent adsorption of As^V onto BIO NPs.

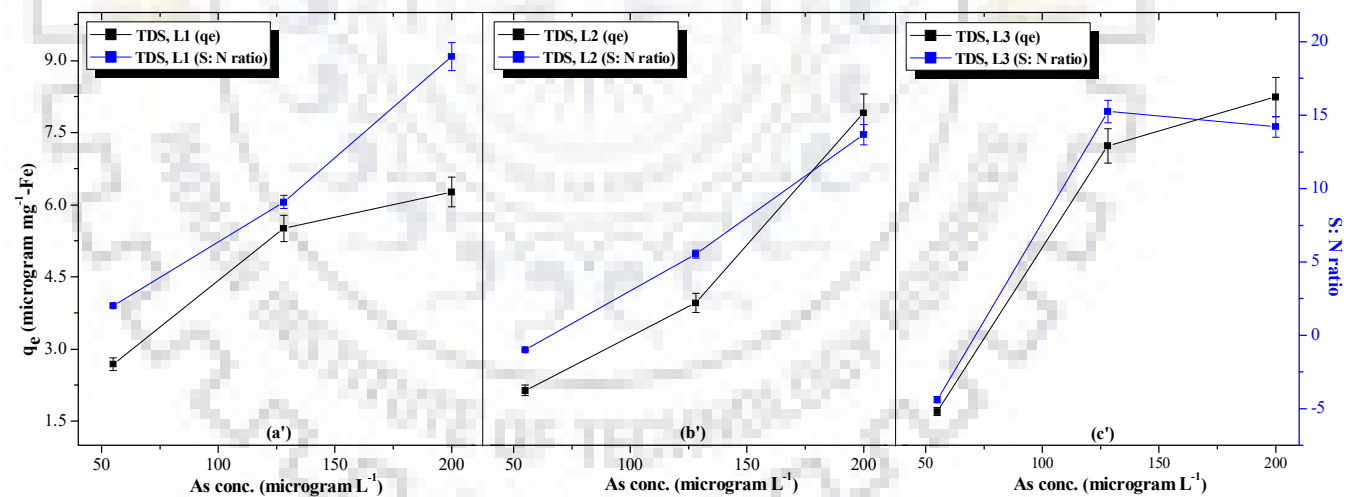


Figure 5.8. Interactions between parameters arsenic initial concentration (A) and TDS (B) at three levels on the removal capacity (q_e) and S: N ratio for multicomponent adsorption of As^V onto BIO-DW nanohybrids.

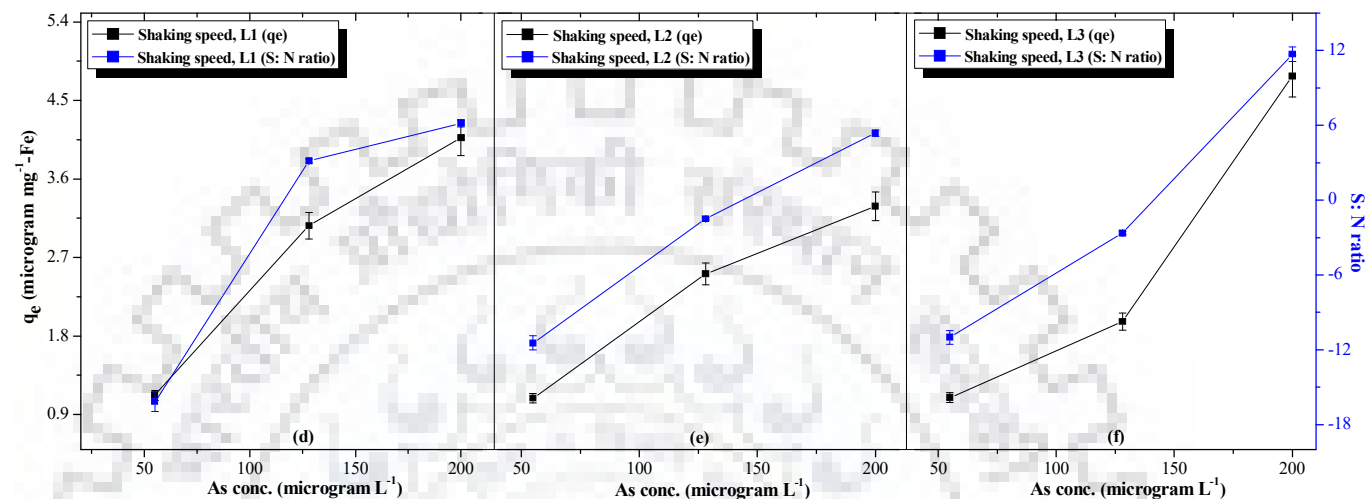


Figure 5.9. Interactions between parameters arsenic initial concentration (A) and shaking speed (C) at three levels on the removal capacity (q_e) and S: N ratio for multicomponent adsorption of As^{V} onto BIO NPs.

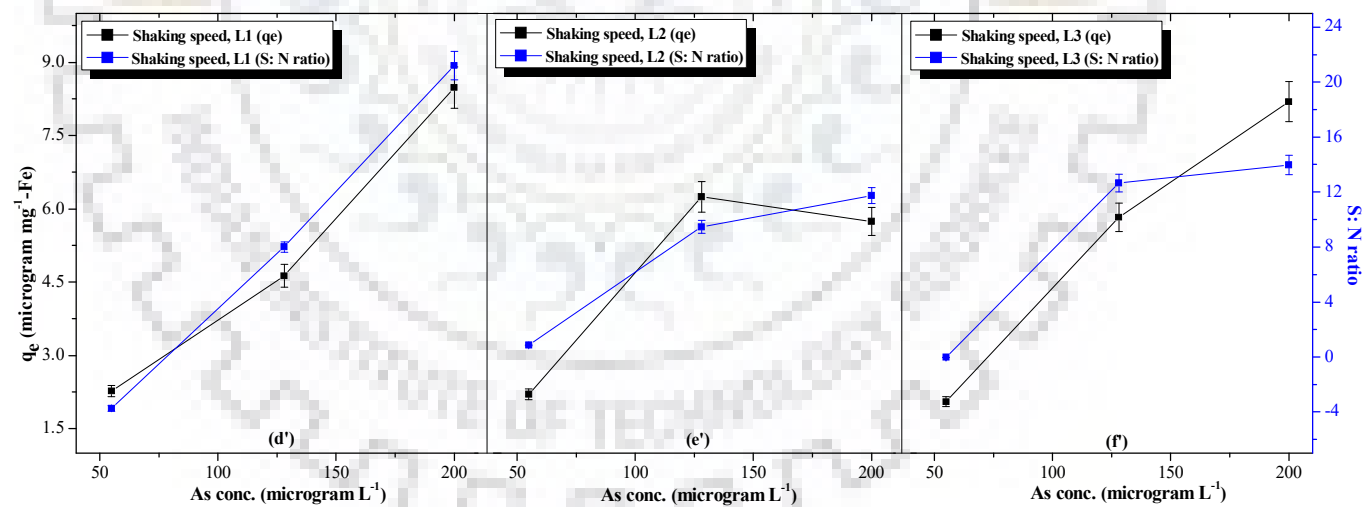


Figure 5.10. Interactions between parameters arsenic initial concentration (A) and shaking speed (C) at three levels on the removal capacity (q_e) and S: N ratio for multicomponent adsorption of As^{V} onto BIO-DW nanohybrids.

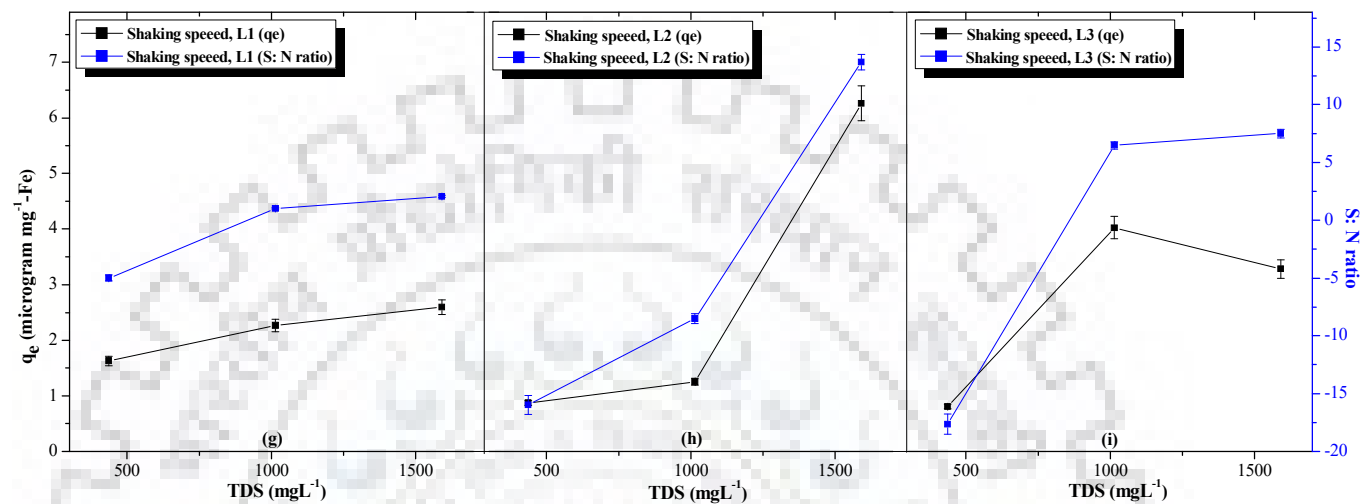


Figure 5.11. Interactions between parameters arsenic TDS (B) and shaking speed (C) at three levels on the removal capacity (q_e) and S: N ratio for multicomponent adsorption of As^V onto BIO NPs.

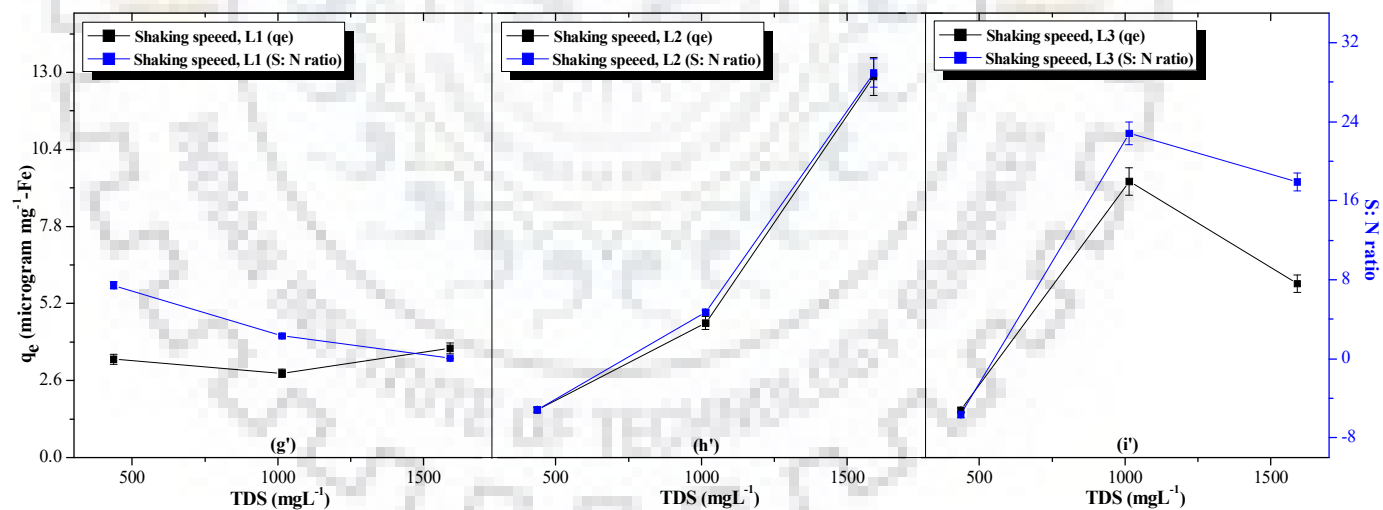


Figure 5.12. Interactions between parameters arsenic TDS (B) and shaking speed (C) at three levels on the removal capacity (q_e) and S: N ratio for multicomponent adsorption of As^V onto BIO-DW nanohybrids.

Table 5.10. ANOVA of Q_e and S: N ratio data for multi-ionic system in the adsorption of As^V using BIO-NPs.

Parameter	Raw Data					S : N Data				
	Sum of square	DOF ^a	Mean square	F value	% Contrib.	Sum of square	DOF ^a	Mean square	F value	% Contrib.
A	29.3	2	14.6	292.7	23.66	485.67	2	242.84	933.98	39.7
B	11.7	2	5.9	117.4	9.41	98.66	2	49.33	189.73	8.1
C	2.8	2	1.4	27.9	2.23	31	2	15.5	59.62	2.5
D	34.3	2	17.2	343.4	27.65	290.58	2	145.09	558.81	23.7
E	8.5	2	4.3	85.3	6.90	43.69	2	21.85	84.02	3.6
F	12.9	2	6.4	128.5	10.32	146.46	2	73.23	281.65	12.0
G	1.0	2	0.5	10.4	0.83	11.77	2	5.89	22.63	1.0
A x B	4.4	4	2.2	43.8	3.48	39.64	4	9.91	38.12	1.6
A x C	12.7	4	6.4	127.4	10.25	108.93	4	27.23	104.74	4.5
B x C	6.5	4	3.3	65	5.27	85.48	4	21.37	82.19	3.5
Residual	0.08	54	0.06			0.52	2	0.26		
Model	124.10	26	62.09			1341.08	24	612.69	2356.5	
Corr. Total	124.18	80	62.15			1341.60	26	612.43		

Table 5.11. ANOVA of Q_e and S: N ratio data for multi-ionic system in the adsorption of As^V using BIO-DW nanohybrids.

Parameter	Raw Data					S : N Data				
	Sum of square	DOF ^a	Mean square	F value	% Contrib.	Sum of square	DOF ^a	Mean square	F value	% Contrib.
A	97.2	2	48.6	4860.5	16.5	326.68	2	163.34	1256.5	16.6
B	32.2	2	16.1	1609.5	5.5	72.97	2	36.48	280.6	3.7
C	6.7	2	3.3	1859	1.1	52.38	2	26.19	201.5	2.7
D	98.9	2	49.4	333.5	16.8	403.95	2	201.97	1553.6	20.5
E	12.5	2	6.2	2342	2.1	43.72	2	21.86	168.2	2.2
F	149.6	2	74.8	4864.5	25.4	577.5	2	288.75	2221.2	29.3
G	9.6	2	4.8	4943	1.6	10.68	2	5.34	41.1	0.5
A x B	37.2	4	18.6	622.5	6.3	139.27	4	69.63	535.6	7.1
A x C	46.8	4	23.4	7478	8.0	140.71	4	70.36	541.2	7.1
B x C	97.3	4	48.6	480	16.6	204.45	4	102.22	786.3	10.4
Residual	0.03	54	0.01			0.13	2	0.02		
Model	587.82	26	293.92			1972.18	24	986.14		
Corr. Total	587.85	80	293.93			1972.31	26	986.16		

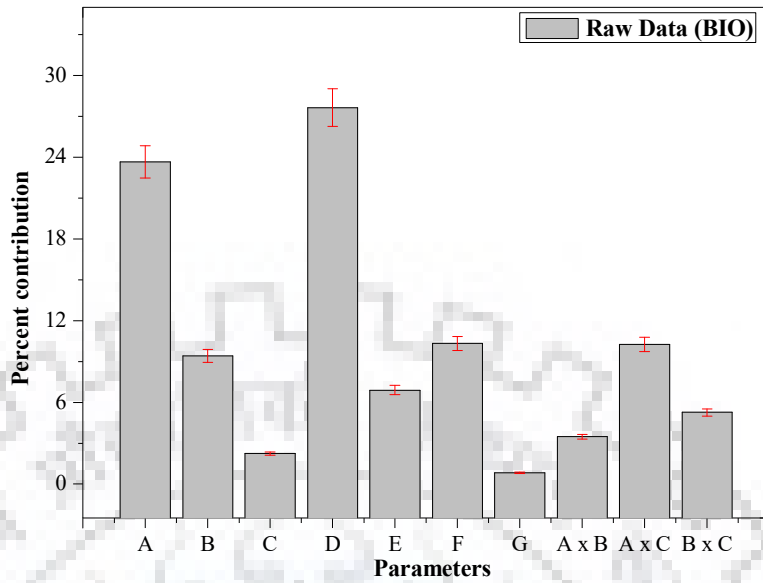


Figure 5.13. Percent contribution of various parameters for q_e for As^V adsorption in multi ionic system onto BIO NPs: parameter A, arsenate conc. ($\mu\text{g L}^{-1}$); parameter B, TDS (mg L^{-1}); parameter C, shaking speed (RPM); parameter D, temp. ($^{\circ}\text{C}$); parameter E, pH; parameter F, dose (g L^{-1}); parameter E, contact time (min).

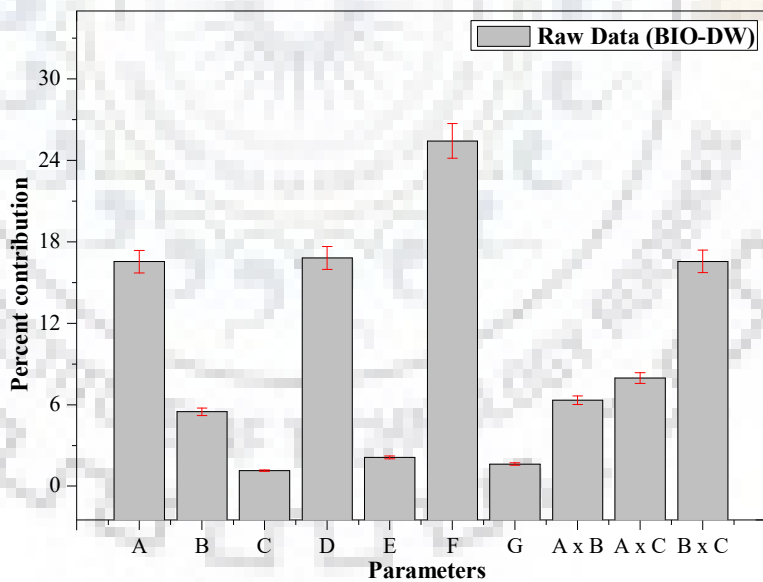


Figure 5.14. Percent contribution of various parameters for q_e for As^V adsorption in multi ionic system onto BIO NPs: parameter A, arsenate conc. ($\mu\text{g L}^{-1}$); parameter B, TDS (mg L^{-1}); parameter C, shaking speed (RPM); parameter D, temp. ($^{\circ}\text{C}$); parameter E, pH; parameter F, dose (g L^{-1}); parameter E, contact time (min).

5.4.4 Identification of optimal levels and estimation of optimum response characteristics

As the response is presented by larger-is-better type for quality characteristics, the maximum value of q_e has been considered optimal. Table 5.8 and 5.9, summarizes the optimal level for different parameters determined after the examination of response curve (Figure 5.3-5.6) for the average value of q_e and S: N ratio onto BIO NPs and BIO-DW nanohybrids. The intend of this study to remove the maximum amount of As^V in the presence of various ions representing the groundwater composition of location I and location II. Therefore, the first (L_1) and third (L_3) level of parameter A and B are taken into consideration for further calculations, respectively. However, the optimization for this experimental design has also been evaluated for As^V removal capacity has also been evaluated utilizing both of BIO NPs and BIO-DW nanohybrids. These studies are discussed individually for both of as-synthesized nanomaterials below:

BIO nanoparticles

In Table 5.12, the significant process parameters that affecting the As^V removal and their optimal levels using these NPs are including as: location I ($A_1, B_1, C_2, D_1, E_3, F_1, G_3$), location II ($A_3, B_3, C_2, D_1, E_3, F_1, G_3$) and experimental design ($A_3, B_1, C_2, D_1, E_3, F_1, G_3$). The average value of q_e for these parameters at optimal level (from Table) are given as:

first level of concentration of As^V ions (\bar{A}_1) = 0.6

third level of concentration of As^V ions (\bar{A}_3) = 2.0

first level of concentration of TDS (\bar{B}_1) = 1.8

second level of shaking speed (\bar{C}_2) = 1.5

first level of temperature (\bar{D}_1) = 2.2

third level of pH (\bar{E}_3) = 1.7

first level of dose concentration (\bar{F}_1) = 1.8

third level of contact time (\bar{G}_3) = 1.4

The overall mean for the total removal capacity ($\bar{T}_{BIO\ NP_s}$) is 1.28 (from Table 5.5). The predicted optimum values for removal capacity for location I, location II and experimental design has been calculated and mentioned as equation 5.8 5.9 and 5.10 below:

$$\mu_{Location\ I} = \bar{T}_{BIO\ NP_s} + (\bar{A}_1 - \bar{T}_{BIO\ NP_s}) + (\bar{B}_1 - \bar{T}_{BIO\ NP_s}) + (\bar{C}_2 - \bar{T}_{BIO\ NP_s}) + (\bar{D}_1 - \bar{T}_{BIO\ NP_s}) + (\bar{E}_3 - \bar{T}_{BIO\ NP_s}) + (\bar{F}_1 - \bar{T}_{BIO\ NP_s}) + (\bar{G}_3 - \bar{T}_{BIO\ NP_s}) = 3.2\ \mu g\ mg^{-1} \quad (5.8)$$

$$\mu_{Location\ II} = \bar{T}_{BIO\ NP_s} + (\bar{A}_3 - \bar{T}_{BIO\ NP_s}) + (\bar{B}_3 - \bar{T}_{BIO\ NP_s}) + (\bar{C}_2 - \bar{T}_{BIO\ NP_s}) + (\bar{D}_1 - \bar{T}_{BIO\ NP_s}) + (\bar{E}_3 - \bar{T}_{BIO\ NP_s}) + (\bar{F}_1 - \bar{T}_{BIO\ NP_s}) + (\bar{G}_3 - \bar{T}_{BIO\ NP_s}) = 3.8\ \mu g\ mg^{-1} \quad (5.9)$$

$$\mu_{q_{e,m\alpha}} = \bar{T}_{BIO\ NP_s} + (\bar{A}_3 - \bar{T}_{BIO\ NP_s}) + (\bar{B}_1 - \bar{T}_{BIO\ NP_s}) + (\bar{C}_2 - \bar{T}_{BIO\ NP_s}) + (\bar{D}_1 - \bar{T}_{BIO\ NP_s}) + (\bar{E}_3 - \bar{T}_{BIO\ NP_s}) + (\bar{F}_1 - \bar{T}_{BIO\ NP_s}) + (\bar{G}_3 - \bar{T}_{BIO\ NP_s}) = 4.6\ \mu g\ mg^{-1} \quad (5.10)$$

Further, the 95 % confidence interval for the mean of experimental run outcomes and three conformation experiments (CI_{CE} and CI_{POP}) is calculated by substituting the DOF error [$f_e = 54$ (80-26)], total number of results [$N = 81$ (27 x 3)] and the error variance [$V_e = 0.06$] (recalculated from Table 5.10) in equations 5.5 to 5.7:

$$n_{effective} = \frac{N}{1 + [total\ DOF\ accounted\ in\ the\ estimation\ of\ mean\ response]} = 3 \quad (5.11)$$

$F_{0.05}(1, 54) = 4.03$ (representing tabulated F-value)

$$CI_{CE} = \sqrt{F_{\alpha}(1, f_e)V_e \left[\frac{1}{n_{effective}} + \frac{1}{R} \right]} = \pm 0.5 \quad (5.12)$$

$$CI_{POP} = \sqrt{\frac{F_{\alpha}(1, f_e)V_e}{n_{effective}}} = \pm 0.3 \quad (5.13)$$

The details of the predicted ranges for the maximum removal capacity (q_e) of As^V at 95 % confidence intervals for location I, location II and experimental design onto BIO NPs are given in Table 5.12 below:

Table 5.12. Predicted optimal levels of parameters along with adsorption capacity (Q_e) values, confidence intervals, outcomes of conformation experiments and percent variation for location I, location II and experimental design (BIO NPs).

	Optimal levels of parameters	Predicted values	Confidence intervals (95 %)	Average ($\mu g\ mg^{-1}\text{-Fe}$)	% variation
Loc. I	$A_1, B_1, C_2, D_1, E_3, F_1, G_3$	3.2	$CI_{ICE}: 2.7 < \mu_{BIO\ NPs} < 3.7$	3.4 ± 0.04	5.9
Loc. II	$A_3, B_3, C_2, D_1, E_3, F_1, G_3$	3.8	$CI_{POP}: 2.9 < \mu_{BIO\ NPs} < 3.5$ $CI_{ICE}: 4.3 < \mu_{BIO\ NPs} < 3.3$	3.9 ± 0.09	2.6
$Q_{e,max}$	$A_3, B_1, C_2, D_1, E_3, F_1, G_3$	4.6	$CI_{POP}: 4.1 < \mu_{BIO\ NPs} < 3.5$ $CI_{ICE}: 5.1 < \mu_{BIO\ NPs} < 4.1$ $CI_{POP}: 4.9 < \mu_{BIO\ NPs} < 4.3$	4.8 ± 0.02	4.2

BIO-DW nanoparticles

In Table 5.13, the significant process parameters that affecting the As^V removal and their optimal levels using BIO-DW nanohybrids are including as: location I ($A_1, B_1, C_2, D_1, E_3, F_1, G_2$), location II ($A_3, B_3, C_2, D_1, E_3, F_1, G_2$) and experimental design ($A_3, B_1, C_2, D_1, E_3, F_1, G_2$). The average value of q_e for these parameters at optimal level (from Table) are given as:

first level of concentration of As^V ions (\bar{A}_1) = 1.1

third level of concentration of As^V ions (\bar{A}_3) = 3.8

first level of concentration of TDS (\bar{B}_1) = 3.0

third level of concentration of TDS (\bar{B}_3) = 1.7

second level of shaking speed (\bar{C}_2) = 2.9

first level of temperature (\bar{D}_1) = 4.1

third level of pH (\bar{E}_3) = 3.0

first level of dose concentration (\bar{F}_1) = 4.4

third level of contact time (\bar{G}_2) = 2.8

The overall mean for the total removal capacity (\bar{T}_{BIO-DW}) is 1.28 (from Table 5.6).

The predicted optimum values for removal capacity for location I, location II and experimental design has been calculated and mentioned as equation 5.11, 5.12 and 5.13 below:

$$\begin{aligned}\mu_{Location I} &= \bar{T}_{BIO-DW} + (\bar{A}_1 - \bar{T}_{BIO-DW}) + (\bar{B}_1 - \bar{T}_{BIO-DW}) + (\bar{C}_2 - \bar{T}_{BIO-DW}) \\ &+ (\bar{D}_1 - \bar{T}_{BIO-DW}) + (\bar{E}_3 - \bar{T}_{BIO-DW}) + (\bar{F}_1 - \bar{T}_{BIO-DW}) + (\bar{G}_3 - \bar{T}_{BIO-DW}) \quad (5.14) \\ &= 4.2 \mu g mg^{-1}\end{aligned}$$

$$\begin{aligned}\mu_{Location II} &= \bar{T}_{BIO-DW} + (\bar{A}_3 - \bar{T}_{BIO-DW}) + (\bar{B}_3 - \bar{T}_{BIO-DW}) + (\bar{C}_2 - \bar{T}_{BIO-DW}) \\ &+ (\bar{D}_1 - \bar{T}_{BIO-DW}) + (\bar{E}_3 - \bar{T}_{BIO-DW}) + (\bar{F}_1 - \bar{T}_{BIO-DW}) + (\bar{G}_3 - \bar{T}_{BIO-DW}) \quad (5.15) \\ &= 4.5 \mu g mg^{-1}\end{aligned}$$

$$\begin{aligned}\mu_{q_{e,max}} &= \bar{T}_{BIO-DW} + (\bar{A}_3 - \bar{T}_{BIO-DW}) + (\bar{B}_1 - \bar{T}_{BIO-DW}) + (\bar{C}_2 - \bar{T}_{BIO-DW}) + (\bar{D}_1 - \bar{T}_{BIO-DW}) \\ &+ (\bar{E}_3 - \bar{T}_{BIO-DW}) + (\bar{F}_1 - \bar{T}_{BIO-DW}) + (\bar{G}_3 - \bar{T}_{BIO-DW}) = 6.9 \mu g mg^{-1} \quad (5.16)\end{aligned}$$

Further, the 95 % confidence interval for the mean of experimental run outcomes and three conformation experiments (CI_{CE} and CI_{POP}) is calculated by substituting the DOF error and total number of results (mentioned in previous section). Whereas, the error variance has been observed to be $V_e = 0.01$ (recalculated from Table 5.11). These are further calculated using equations 5.5 to 5.7:

$$n_{effective} = \frac{N}{1 + [total\ DOF\ accounted\ in\ the\ estimation\ of\ mean\ response]} = 3 \quad (5.17)$$

$$CI_{CE} = \sqrt{F_{\alpha}(1, f_e)V_e \left[\frac{1}{n_{effective}} + \frac{1}{R} \right]} = \pm 0.2 \quad (5.18)$$

$$CI_{POP} = \sqrt{\frac{F_{\alpha}(1, f_e)V_e}{n_{effective}}} = \pm 0.1 \quad (5.19)$$

$F_{0.05}(1, 54) = 4.03$ (representing tabulated F-value)

The details of the predicted ranges for the maximum removal capacity (q_e) of As^V at 95 % confidence intervals for location I, location II and experimental design onto BIO-DW nanohybrids are given in Table 5.13 below:

Table 5.13. Predicted optimal levels of parameters along with adsorption capacity (Q_e) values, confidence intervals, outcomes of conformation experiments and percent variation for location I, location II and experimental design (BIO-DW nanohybrids).

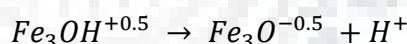
	Optimal levels of parameters	Predicted values ($\mu\text{g mg}^{-1}\text{-Fe}$)	Confidence intervals (95 %)	Average ($\mu\text{g mg}^{-1}\text{-Fe}$)	% variation
Loc. I	A ₁ , B ₁ , C ₂ , D ₁ , E ₃ , F ₁ , G ₂	4.2	CI _{CE} : $4.4 < \mu_{MNP_s} < 4.0$ CI _{POP} : $4.3 < \mu_{MNP_s} < 4.1$	4.3 ± 0.08	2.3
Loc. II	A ₃ , B ₃ , C ₂ , D ₁ , E ₃ , F ₁ , G ₂	4.5	CI _{CE} : $4.7 < \mu_{MNP_s} < 4.3$ CI _{POP} : $4.6 < \mu_{MNP_s} < 4.4$	4.6 ± 0.09	2.2
$Q_{e,max}$	A ₃ , B ₁ , C ₂ , D ₁ , E ₃ , F ₁ , G ₂	6.9	CI _{CE} : $7.1 < \mu_{MNP_s} < 6.7$ CI _{POP} : $7.0 < \mu_{MNP_s} < 6.8$	7.0 ± 0.08	1.4

5.4.5 Conformation experiments

The conformation experiments for the locations I, II and $Q_{e,max}$ (overall experimental design) in the removal of As^V onto BIO NPs and BIO-DW nanohybrids have been conducted in triplicate at selected optimal levels of experimental process parameters. Their average values are compared with those of predicted values, shown in Table 5.12 and 5.13. The values of q_e determined through conformation experiments are found within the 95 % confidential interval of CI_{CE} for both of as-synthesized nanomaterials. These optimal values are valid only within the range of designated process parameters. However, it is proposed to explore the removal capacity through additional conformation experiments during interpolation/exploitation.

5.4.6 Understanding of adsorption behaviour using surface complexation models (SCMs)

Surface complexation models (SCMs) have been explored to understand the result outcomes of Taguchi's batch experimental methodology. The geochemical code Visual MINTEQ is used for the calculation of adsorption equilibrium constant and modeling of As^V adsorption onto BIO NPs and BIO-DW nanohybrids [314]. As both of these as-synthesized nanomaterials are identified (Chapter 3) the presence of maghemite phase among the different polymorphs of iron^{III} oxide(s). Therefore, some of the characteristics related to this phase have been taken into account as described by previous authors in the present study. The charge distribution multi-sites complexation (CD-MUSIC) model [315] and 2pk-Three-Plane-Model (TPM) have been explored as a function of pH for both BIO NPs and BIO-DW nanohybrids. From the zeta-potential measurements, the surface moieties of both these nanoadsorbents have been observed to be negatively charged (Figure 3.15) in the pH range used for the present study. Therefore, the amphoteric ionization reactions for these nanomaterials possible under the used conditions could be the following:



For as-synthesized nanomaterials, the behaviour of different complexes formed from the above possible surface species with various ion(s) and their possible effects on the removal of As^V oxyanions have been discussed below individually:

BIO nanoparticles (NPs)

Generally, the hydroxyl moieties such as: single [(OH)₃-Fe-Fe-R] and double [(OH)₃-Fe-H₃O₃-R] coordinated hydroxyls have been reported for iron^{III} oxide(s) NPs [215] and the double coordinated surface hydroxyls has been previously demonstrated to be particularly stable and unreactive [216]. Trainor et al. [215] have shown that the singly and triple coordinated hydroxyls are more reactive towards cationic species due to their efficient proton lability. Therefore, the CD-MUSIC model along with 2pk-TPM has been explored for BIO NPs, which involves the reactivity

of singlet ($\text{FeOH}^{-0.5}$) and triplet ($\text{Fe}_3\text{O}^{-0.5}$) species of iron. This study provided the following parameters of surface complexation modelling has been summarized below in Table 5.14:

Table 5.14. Reactions and parameters of surface complexation modeling for BIO nanoparticles.

Surface species	$\equiv \text{FeOH}$	$\equiv \text{Fe}_3\text{O}$	Δ_{Z_0}	Δ_{Z_1}	Δ_{Z_2}	Log K	Ref.
$\equiv \text{FeOH}^{-0.5}$	1	0	0	0	0	0	[316]
$\equiv \text{Fe}_3\text{O}^{-0.5}$	0	1	0	0	0	0	[316]
$\equiv \text{FeOH}^{-0.5} - \text{Ca}^+$	1	0	0.32	1.68	0	3.17	[317][318]
$\equiv \text{FeOH}^{-0.5} - \text{CaCO}_3^-$	1	0	0.6	-1.6	0	15.55	[319]
$\equiv \text{FeOH}^{-0.5} - \text{CaHCO}_3$	1	0	0.6	-0.6	0	24.15	[319]
$\equiv \text{FeOH}^{-0.5} - \text{HNO}_3$	1	0	1.00	-	0	7.42	[320][318]
$\equiv \text{Fe}_3\text{O}^{-0.5} - \text{HNO}_3$	0	1	1.00	-	0	7.42	[318]
$2(\equiv \text{FeOH}^{-0.5}) - \text{AsO}_2\text{Ca}$	2	0	0.60	0.40	0	36.04	[321]
$2(\equiv \text{FeOH}^{-0.5}) - \text{AsO}_2\text{HCa}$	2	0	0.60	1.40	0	43.44	[321]
$2(\equiv \text{FeOH}^{-0.5}) - \text{Mg}^{2+}$	2	0	0.71	1.29	0	4.89	[295]
$2(\equiv \text{FeOH}^{-0.5}) - \text{PO}_2\text{Ca}$	2	0	0.60	0.40	0	38.57	[322]
$2(\equiv \text{FeOH}^{-0.5}) - \text{PO}_2\text{HCa}$	2	0	0.60	1.40	0	46.02	[322]
$2(\equiv \text{FeOH}^{-0.5}) - \text{PO}_2^-$	2	0	0.46	-	0	27.59	[321]
$2(\equiv \text{FeOH}^{-0.5}) - \text{POOH}$	2	0	0.63	-	0	32.89	[321]
$2(\equiv \text{FeOH}^{-0.5}) - \text{Si}(\text{OH})_2$	2	0	-0.29	-	0	5.85	[317][323]
$2(\equiv \text{FeOH}^{-0.5}) - \text{SiOHOSi}_3\text{O}_3(\text{OH})_9$	2	0	-0.29	-	0	13.98	[323]
$2(\equiv \text{FeOH}^{-0.5}) - \text{SiO}_2\text{HSi}_3\text{O}_{3+1}(\text{OH})_{9-1}$	2	0	-0.29	-	0	7.47	[323]
$2(\equiv \text{FeOH}^{-0.5}) - \text{ZnOH}$	2	0	0.50	0.50	0	-1.43	[324]
Modeling parameters							
Model Type	CD-MUSIC and 2-pk TPM						
Number of site types	2						
BIO NPs concentration (g L^{-1})	0.3						
Specific surface area ($\text{m}^2 \text{g}^{-1}$)	59.80						
Surface site density (sites nm^{-2})	51.13						
Inner capacitance (F m^{-2})	1.0						
Outer capacitance (F m^{-2})	0.2						
pH range	7 - 9						

The total (N_t) surface site concentrations (sites nm^{-2}) has been obtained from the adsorption isotherm data (Chapter 4) explored for As^{V} removal onto these nanoparticles. The equation for the calculation of surface sites is given as [325]:

$$N_t(\text{sites nm}^{-2}) = \frac{N C_s}{S C_{Ad.}} \quad (5.20)$$

Where, N_t (sites nm^{-2}) denotes the concentration of sites; N and C_s (mol L^{-1}) are the Avogadro number and concentration of As^{V} adsorbed at saturation point, respectively; S ($\text{m}^2 \text{g}^{-1}$) represents the surface area of nanoparticles and $C_{Ad.}$ (g L^{-1}) the dose of nanoparticles utilized.

Earlier in Figure 5.5 (f) the response curves depicted that an increase in the pH causes an increase in the removal capacity of As^{V} adsorption onto BIO NPs. Using geochemical code Visual MINTEQ, this trend is validated by the CD-MUSIC model along with to that of 2pK-TPM model (for both locations I and II) (Figure 5.13 a, b). It, therefore, evidently explains the involvement of singlet and triplet species of iron during the adsorption process. However, a reverse trend has been examined using 2pK-TPM model.

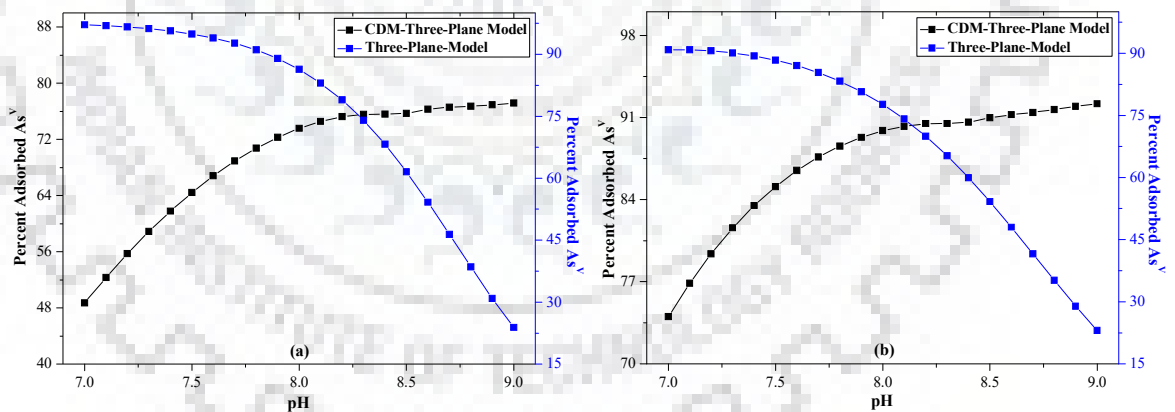


Figure 5.15. Representation of As^{V} adsorption behaviour onto BIO NPs using surface complexation models (a) location I and (b) location II.

BIO-DW nanohybrids

Earlier in Figure 5.5 (f) the response curve depicted an increase in the pH causes to decrease in the As^{V} adsorption onto these nanohybrids upto pH 8. A further increase in the pH causes to increase the adsorption capacity at pH 9. This behaviour of removal could be explained by 2pK-

TPM model till the pH 7, which involves deprotonated specie FeO^- in the removal process. The dominant complex between surface moiety and arsenic specie has been determined to be $=FeOHAsO_4^{3-}$ in the near neutral pH conditions. Above pH 7, the CD-MUSIC model along with that of 2pK-TPM has explained the removal behaviour for these nanohybrids, as also observed for BIO NPs. However, due to presence of several organic moieties onto the surface of these nanohybrids, it requires detailed investigations.

5.4.7 Predictive modeling of arsenic removal using multilayer concept of artificial neural network

Artificial neural network tool has been reported to be an appropriate tool for the prediction and estimation of adsorption properties due to its complex non-linear characteristics [309], [310], [326]. Neural network toolbox of MATLAB (version 2013a) is used to predict the adsorption behaviour of BIO NPs and BIO-DW NPs nanohybrids under batch study. A feed-forward back propagation neural network is explored to validate all the experimental results and the architecture contains one input layer (seven neurons), output layer (having one neuron) and hidden layer (including eight neurons). Table 5.15 and 5.16, shows the weights and biases related to the neural network after training for both of nanosystems.

For BIO nanoparticles, the network has been trained to get the minimum value mean square error (MSE: 0.0810) which is achieved after 309 iterations. details are shown in Table 5.15. The details of their weights and biases are mentioned in Table 5.15. Similarly, the minimum mean square error (MSE: 0.0158) for the results of outcomes obtained through Taguchi's methodology achieved after 150 iterations in case of BIO-DW nanohybrids. The details of their weights and biases are mentioned in Table 5.16.

Table 5.15. Optimal values of architecture weights and biases for ANN model using BIO NPs.

Input I to hidden layer I	$IW^{(1,1)}$	[3.6452	2.4041	1.3122	-0.7853	0.3063	-1.083	0.73908;
		0.91948	-0.5632	0.13657	0.69442	0.14616	0.22706	-0.26542;
		2.8757	-4.2484	-6.793	7.81	5.9914	-3.5516	1.5765;
		2.8282	-5.3899	-0.9429	-3.0861	-1.1793	1.6492	-4.6492;
		-0.9470	1.1106	0.5855	-4.243	0.93038	0.65776	1.6884;
		-1.4417	-2.3152	1.9083	-2.2759	-1.0128	-1.4177	-0.67739;
		0.33551	1.7197	0.68846	12.7681	-6.4251	-2.0039	-1.31;
Weight to layer	$LW^{(2,1)}$	[0.9357	-0.6390	0.64071	0.36988	-7.6781	0.8652	-7.8693]
Bias to layer I	$b^{(1)}$	[-2.1715;	-3.0639;	-7.6803;	-1.6847;	2.708;	-0.63665;	4.4477]
Bias to layer II	$b^{(2)}$	[-0.23964]						

Table 5.16. Optimal values of architecture weights and biases for ANN model using BIO-DW nanohybrids.

Input I to hidden layer I	$IW^{(1,1)}$	[1.923	0.39529	1.5262	-1.5243	0.83866	1.1302	0.83388;
		1.277	0.07763	-0.43379	0.3205	0.45953	0.85197	0.3184;
		-0.52626	1.1866	-0.38417	-0.5977	0.12041	-0.76983	-1.2079;
		1.6354	-0.3885	1.0929	-0.2904	-0.98819	1.5521	0.19288;
		-0.1002	1.5393	1.5474	0.236	0.20202	-0.02675	-0.33111;
		-1.9687	-0.0554	1.6085	-0.3764	0.60145	1.1441	1.5076;
		-0.7981	0.4979	0.8676	0.91157	-2.0979	0.9329	0.15184]
Weight to layer	$LW^{(2,1)}$	[3.5333	-1.0854	-0.58064	-2.2447	0.1071	1.18	1.2745]
Bias to layer I	$b^{(1)}$	[2.7025;	-2.2002;	-0.16844;	-1.4264;	0.88775;	-0.50907;	-1.4788]
Bias to layer II	$b^{(2)}$	[0.04916]						

Continuous flow reactive modeling using 1D columns and sand-tank experiments for arsenic removal

6.1 Chapter abstract

This chapter investigates the arsenic removal capabilities of as-synthesized BIO NPs and BIO-DW nanohybrids under the continuous mode of experiments. The 1-D columns and 3-D sand-tank setups have been fabricated for this purpose. During sand tank experiments, the removal of As^{III} species have been taken into the consideration.

Through columns studies, the effects of flow rate (4 -12 ml min⁻¹), bed height (14.6 – 58.4 cm), inlet concentration (0.055 – 4 mg L⁻¹) have been explored for the As^V removal employing BIO NPs and BIO-DW nanohybrids. The dynamic behaviour of these fixed column(s) has been analyzed through breakthrough curve analysis, Bohart-Adams model Thomas and Yoon Nelson model. Further, the sand tank model (dimensions X: 60; Y:50; Z0 cm) has been fabricated representing the direct injection (*in-situ*) mode of nanomaterials application. The COMSOL Multiphysics model has been explored to understand the behaviour of nanoparticles transport under homogenous and fully saturated conditions. The NaCl solution having the electrical conductivity of 5760 $\mu\text{S cm}^{-1}$ has been used for the tracer experiments. The simulations have been performed for the two injection points (x: 15 cm; Y: 20 cm; Z: 30 cm) and (x: 25 cm; Y: 40 cm; Z: 30 cm). The Indian standard (IS) sand having the particle size distribution in the range of 0.5 – 1 mm has been utilized as the experimental consolidated media during the column and sand experiments.

The adsorption capacity (mg g⁻¹ -Fe) has been found to be 203.5 and 345.1 for BIO NPs and BIO-DW nanohybrids. As the height of fixed bed increases from 14.6 cm to 58.4, the breakthrough point increases from 60 to 260 min and 165 to 455 for BIO NPs and BIO-DW nanohybrids, respectively. The outcomes of Adam-Bohart model examined that the overall system kinetics in the initial part of adsorption process has been dominated by an external mass. Although, the poor coefficient of determination reflects less applicability of this model. The good fit of the Thomas model to the experimental data indicates that the external and internal diffusions are not the

limiting steps for both of these nanosystems. The Yoon-Nelson model interpret that the driving force of mass transfer in the liquid film increases with an increase in the flow rate in case of both nanosystems. The retardation coefficient has been observed to be 0.0101 g m^{-3} and 0.0142 g m^{-3} for BIO NPs and BIO-DW nanohybrids, respectively. From the breakthrough data of As^{III} removal, it is estimated that the concentration of arsenic reached beyond the WHO permissible limit after 31 h.

6.2 Materials and equipment

Arsenic working solutions have been prepared using sodium arsenite (anhydrous) (Na_2HAsO_2 , M.W. = $129.91 \text{ g mol}^{-1}$) salt purchased from Merck enterprises. All other chemicals and reagents were utilized as mentioned earlier. The Indian standard (IS) clean sand 650 grade-II having the particle size distribution in the range of 0.5 – 1 mm has been employed as the consolidated media in the experiments. Peristaltic pumps (Model RH-P100VS-100-2H of Ravel Hitecks Pvt. Ltd. India) having dimensions (mm) of $115 \times 225 \times 280$ have been used having a roller cage driven pumping mechanism fitted with a stepper motor. The flow rate range of the pumps was $1 - 500 \text{ ml hr}^{-1}$.

6.3 Methodology

6.3.1 Mathematical equations for design of columns (1-D) for lab studies

A hypothetical cylindrical filter having an inner diameter D , a length L , and a reactive zone hrz is considered. The reactive zone is the fraction of L ($L > hrz$) containing the reactive material, possibly mixed with selected additives. The filter is filled with spherical particles (reactive materials and non-reactive additives) having a constant diameter d . Considering the granular material as composed of mono-dispersed spheres subjected to soft vibrations, the column compactness (or packing density) C ranges between 0.60 and 0.64 for a random close packing, but it is generally considered to be equal to 0.64 (limit value). It has been reported that the value of the compactness depends on various parameters as the distribution of particle size and their shape [327], [328]. The theoretical value of $C = 0.64$ is strictly valid for particles with spherical shape and similar sizes. It is assumed in this study that ratio of cylinder diameter ($D = 2R$) to particle diameter (d) = $2R/d$ is optimal for axial hydrodynamic dispersion [329], [330]. The volume of the reactive zone (V_{rz}), the volume of solid (V_{solid}), the volume of inter-granular pores (V_{pore}), the volume of individual solids (V_i) with the apparent specific weight i , and the thickness of the reactive zone (h_{rz}) are given below:

$$V_{rz} = \frac{\pi D^2 h_{rz}}{4} \quad (6.1)$$

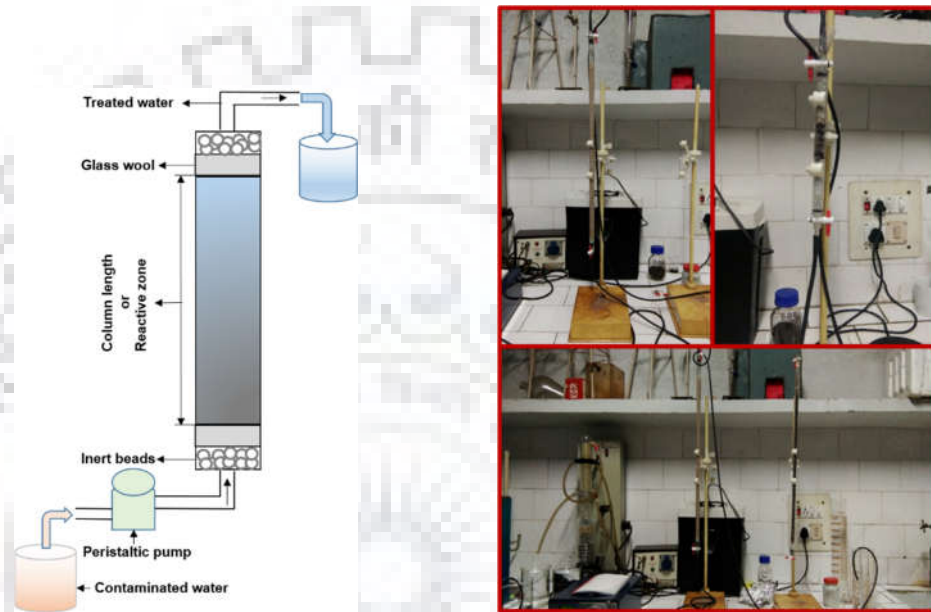


Figure 6.1. Schematic diagram of fixed column(s) utilized for breakthrough curve analysis using both BIO NPs and BIO-DW nanohybrids.

$$V_{rz} = V_{solid} + V_{pore} \quad (6.2)$$

$$V_{solid} = C V_{rz} \quad (6.3)$$

$$V_{pore} = (1 - C) V_{rz} \quad (6.4)$$

$$V_{solid} = \sum V_i = V_{solid\ 1} + V_{solid\ 2} \dots \dots V_{solid\ n} \quad (6.5)$$

$$V_i = \frac{m_i}{\rho_i} \quad (6.6)$$

$$h_{rz} = \frac{4V_{rz}}{\pi D^2} = \frac{4V_{solid}}{C\pi D^2} \quad (6.7)$$

Using these calculations, the columns with the length of 14.6, 29.2 and 58.4 with and internal diameter have demonstrated the constant porosity conditions. Therefore, the column having the dimensions greater than the calculated have been fabricated for laboratory investigations. During these experiments, then nanomaterials has been mixed along with the porous media for breakthrough curve in the fixed bed column(s).

6.3.2 Fabrication of sand-tank model for lab studies

Tracer and nanoparticle transport experiments have been conducted in a three-dimensional sand tank setup representing a subsurface system of variably saturated zone underlined with shallow unconfined aquifer. Figure 6.2 shows the schematic diagram of the 3-D sand tank setup used in the present study. The inlet and outlet ports of the tank setup have been connected with 1 cm thick water chamber attached with central chamber having sand mass, to ensure a uniform groundwater flow. These chambers are separated from the soil mass by a stainless steel mesh to prevent soil flow in the chambers.

The tank setup has been embedded with three rows of sampling ports spaced 10 cm apart vertically. The eleven injection ports are fixed at the top of the tank to the depth of 20 cm and 40 cm. The openings of sampling ports are attached with stainless steel needles of diameter 0.3 mm and which are located at 5 cm and 10 cm depth in the transverse direction. The middle row of sampling ports represents the surface sample ports. The tank is filled homogeneously with clean sand duly replaced with fresh sand for each new set of experiment. Filtration screens are fixed around the inlet and outlet valves to prevent the entrance of the sand particles in the connecting Viton tubes.

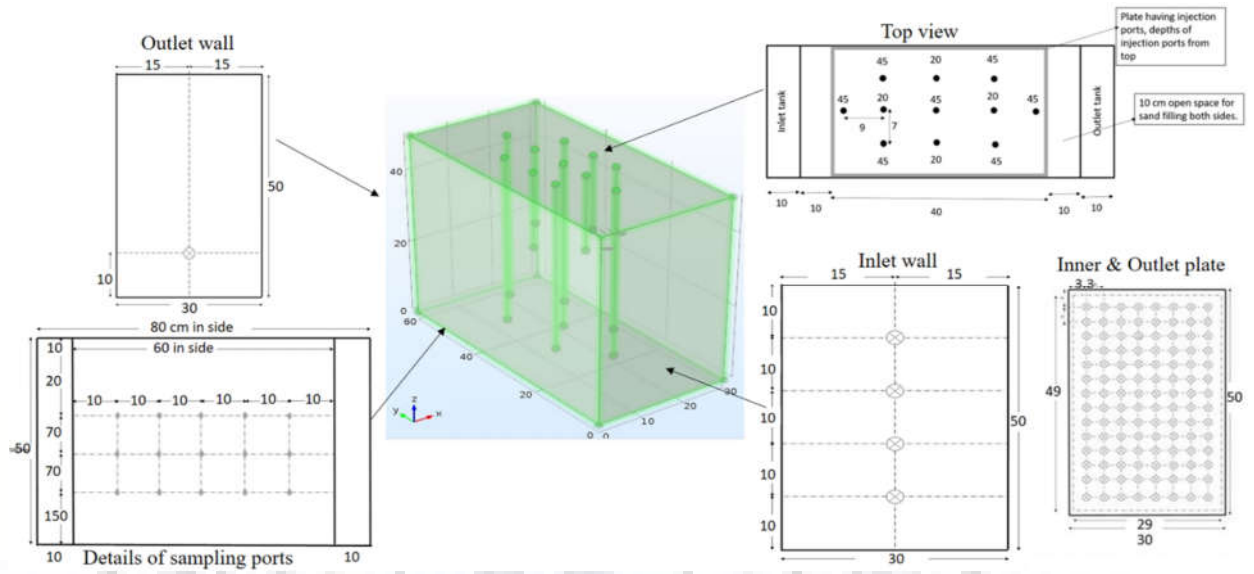


Figure 6.2. Details of the sand-tank set up used for the tracer and injection of nanoparticles.

6.3.3 Characteristics of consolidated material

The Indian standard (IS) clean sand 650 grade-II having less than 1 mm and greater than 0.5 mm particle distribution size has been used as the experimental porous media. The sand has been washed and dried at ambient conditions prior to the experimental analysis. The analytical sieve shaker (400 mm × 230 mm × 350 mm) of Retsch (Germany) series AS 200 having measuring range 20 μ m to 20 mm has been used in these studies. Mechanical sieve analysis has been performed to find the particle size distribution of the sand which is listed in along with other physical parameters in Table 6.1 below:

Table 6.1. Physical characteristics of sand used for laboratory experiments.

Sl. No.	Characteristics	Values	Reference
1.	Type of sand	Medium-Fine sand	Procured from TAMIM enterprises
2.	Grain size	0.5 – 1.0 mm	Determined
3.	Grain density	$2.33 \pm 0.2 \text{ g cm}^{-3}$	Calculated
4.	Bulk density	$1.55 \pm 0.09 \text{ g cm}^{-3}$	Determined
5.	Effective porosity	$0.34 \pm 0.03 \%$	Determined
6.	Particle size > 1 mm	$2.53 \pm 0.49 \%$	Calculated
7.	Particle size > 0.5 mm - 1 mm	$97.36 \pm 0.57 \%$	Calculated
8.	Particle size < 0.05 mm	$0.11 \pm 0.05 \%$	Calculated

6.3.4 Column (1-D) adsorption experiments

6.3.4.1 Analysis of breakthrough curve(s)

Breakthrough curves are obtained after fitting the modeling parameters to the experimental data, generated through column experiments. Generally, the breakthrough time and trend of the breakthrough curves explain the dynamic behaviour of the adsorption processes in column(s). These curves depict the loading behaviour of As^{V} in a fixed bed adsorber containing BIO NPs and BIO-DW nanohybrids. This analysis generally describes the normalized As^{V} concentration, and can be defined as a ratio of As^{V} concentration at outlet to that of inlet concentration (C_t/C_0), as a function of time for any reactive zone (h_{rz}) as well as different flow rate conditions. In this study, the time that has indicated the effluent concentration of As^{V} reach beyond $10 \mu\text{g L}^{-1}$ is considered as the breakthrough point (t_b). Similarly, its concentration reaches the arbitrary value i.e. $C_t/C_0 = 0.9$ in the effluent at time (t), represents the exhaustion time (t_s) of the fixed bed.

The total amount of As^V adsorbed onto as-synthesized nanomaterials up to the time 't' for a fixed bed height (h_{rz}) has been determined using following equation:

$$Q_t = F_v C_o \int_0^t \left(1 - \frac{C_t}{C_o}\right) dt \quad (6.8)$$

Where, C_o is the initial As^V feed solution concentration (mg L^{-1}); C_t indicates the As^V concentration at time t (mg L^{-1}) and f_v is the volumetric flow rate for feed solution (ml min^{-1}). The integration term has been evaluated by determining the area above the curve. The adsorbent bed capacity for As^V adsorption is calculated using the equation mentioned below:

$$ABAC \text{ or } q_t (\text{mg g}^{-1}) = \frac{Q_t}{m_a} \quad (6.9)$$

Where, m_a is the adsorbent mass (mg). The effluent volume ($v_{effec.}$) and total amount (m_{total}) of As^V entering the fixed bed have been determined using as follows:

$$V_{effec.} = F_v t_s \quad (6.10)$$

$$m_{total} = \frac{C_o F_v t_s}{1000} \quad (6.11)$$

Further, the total removal capability of As^V ions (performance of fixed bed) with respect to flow volume has also been calculated. It defines the ratio of total adsorbed As^V (Q_t) to that of total As^V (m_{total}) entering the fixed bed, and has been calculated using the following equation:

$$\eta (\%) = \frac{Q_t}{m_{total}} \times 100 \quad (6.12)$$

6.3.4.2 Adam-Bohart model

This model represents a relationship of concentration ratio (C_t/C_0) with time (t) in a continuous removal system. The establishment of equation depends on the surface reaction theory which describes the initial part of the breakthrough curve. It assumes that the equilibrium is not instantaneous and therefore, the concentration of As^V and the residual capacity of removal as-synthesized BIO NPs and BIO-DW nanohybrids are proportional to the rate of adsorption process. The linearized equation of the model can be written as:

$$\log_e \left(\frac{C_0}{C_t} \right) = K_{AB} C_0 t - \frac{K_{AB} N_0 h_{rz}}{V_0} \quad (6.13)$$

Where C_0 and C_t are inlet and outlet concentration of As(V) respectively, h_{rz} (cm) is the height of reactive zone, V_0 (cm min⁻¹) is the linear flow velocity determined as the ratio of flow rate F_{LV} and cross sectional area of reactive zone A_{rz} (cm⁻²), N_0 is the saturation concentration and K_{AB} is the mass transfer coefficient.

6.3.4.3 Thomas model

It is a common and extensively used model to examine the behaviour of removal process of contaminants in the fixed-bed columns. The data acquired from a bed in continuous mode experiments has been utilized to explore the maximum solid phase concentration of As^V adsorbed onto the surface of BIO NPs and BIO-DW nanohybrids. This model is based on the assumption that the removal process follows Langmuir kinetics along with no axial dispersion. Its derivation is based on the 2nd - order removal kinetic equations which leads to its limitations in understanding the absolute behaviour of the adsorbent [331]. Further, it considers that removal process does not primarily depends on the chemical reactions, but is also controlled by the mass transfer at the interface. Therefore, this inconsistency may lead to errors in explaining the removal process using model under specific environmental conditions. However, to understand the removal characteristic features of a nano-adsorbent, the exploration by considering the different aspects are necessary. Several authors have demonstrated the Thomas model to analyse the removal behaviour of

contaminant through fixed bed reactor [332], Fe-Mn nanocomposite [333], homoionic clinoptilolite [334], chemically modified rice straw [335], zirconium oxide-coated sand [336] and rice husk [337]. The linear form of the equation is expressed as:

$$\log \left[\frac{C_o}{C_t} - 1 \right] = \left[\frac{k_{T_h} q_{T_h}}{Q} - \frac{k_{T_h} C_o}{Q} V_{effec.} \right] \quad (6.14)$$

Where k_{T_h} , q_{T_h} , C_o , C_t are Thomas rate constant, maximum solid-phase concentration of contaminant (bed capacity), influent and effluent concentration respectively.

6.3.4.4 BDST model

The BDST is a simple model for predicting the relationship between bed height and service time in terms of process concentrations and adsorption parameters [338]. The original work on the BDST model has been reported to be carried out by Bohart and Adams [339] who proposed a relationship between bed height (H) and the time taken for the breakthrough to occur. The service time (t) is related to the process conditions and operating parameters as given below:

$$\log \left(\frac{C_o}{C_b} - 1 \right) = \log (e^{k_s N_s H F} - 1) - K_b C_o t_b \quad (6.15)$$

Where K_b is the rate constant in the BDST model ($L \text{ mg}^{-1} \text{ min}^{-1}$), t_b is the breakthrough time or service time (min), N_s is the bed adsorption capacity (mg L^{-1}), and n is the linear flow rate (cm min^{-1}). The values have been correlated with the process parameters and initial As^V feed concentration, solution flow rate, and the adsorption capacity.

6.3.4.5 Yoon-Nelson model

This is a simple model that describes the adsorption behaviour of fixed bed without the requirement of detailed data concerned to the adsorbent type as well as physical properties of adsorbent bed.

$$\frac{C_t}{C_o - C_t} = \exp (K_{YN}t - t_{0.5}K_{YN}) \quad (6.16)$$

where, K_{YN} is the rate constant (min^{-1}) and $t_{0.5}$ is the time required for 50 % adsorbate breakthrough (min). The values of parameters K_{YN} and $t_{0.5}$ for the adsorbate can be calculated from the plot of $\ln (C_t / (C_o - C_t))$ versus sampling time (t).

This model is applicable to a range of concentrations in the inlet contaminated water between the breakthrough and saturation time of bed depth [340]. It is independent of the parameters concerned with the physical properties of adsorbent column and type of the removal material [335]. The linearized equation of Yoon-Nelson model is represented below:

$$\log_n \left[\frac{C_t}{C_o} - C_t \right] = K_{YN}t - \tau_{0.5}K_{YN} \quad (6.17)$$

Where K_{YN} is the Yoon-Nelson constant (min^{-1}), $t_{0.5}$ is the time (min) required to achieve the 50 % breakthrough of bed depth and t is the breakthrough sampling time. The evaluation of the experimental data with respect to the initial concentrations of As^V for two different locations and bed height has enabled the analysis of Yoon-Nelson model parameters from the slope and intercept of the graph between $\log_n (C_t / C_o - C_t)$ against time (t). The above equation reveals that 50 % breakthrough (sampling) occurs at $t = \tau$. Thus the bed depth should be exhausted at $t = 2\tau$. Due to the symmetrical nature of breakthrough curve, the adsorption of As^V being adsorbed on maghemite nanoparticles in a fixed bed is the half of the total As^V entering bed depth within 2τ time period. Song et al [335] have demonstrated the following equation to determine the adsorption capacity of bed volume:

$$q_{yn} = \frac{q_{total}}{M} = \frac{(1/2)C_o \left(\frac{Q}{100} \right) 2\tau}{M} = \frac{C_o Q \tau}{1000 M} \quad (6.18)$$

This equation allows to calculate the adsorption capacity (q_{ym}) of the column as a function of reactive zone (h_{rz}), flow rate (Q), initial As(V) concentration, quantity of removal material (M) and 50% breakthrough time ($t_{0.5}$) using Yoon-Nelson model.

6.3.5 Sand-tank experiments

6.3.5.1 Sand packing

The sand has been first oversaturated and then allowed to flow into the experimental setup. A comb-like rectangular metallic sheet was used to remove air bubbles from sand layers. The water filled setup has been left overnight to make the sand packing stable before draining the excess water.

6.3.5.2 Preliminary experiments

Preliminary experiments have been conducted to characterize the flow and transport parameters. The saturated hydraulic conductivity (K) has been calculated to be $7.99 \times 10^{-5} \text{ m s}^{-1}$ using constant head permeameter method. From dispersivity flux, the longitudinal dispersivity (D_L) of media has been estimated from the breakthrough curves (BTCs) obtained during the tracer experiments under different flow rates. The vertical dispersivity has been considered 0.1 times of the obtained longitudinal dispersivity [341]. Time values corresponding to relative concentration ratios of tracer are used in calculating dispersion coefficient as mentioned in equation below:

$$D_{if} = 0.5 \left[\frac{t_{84\%} - t_{16\%}}{2t_{50\%}} \right] v \quad (6.19)$$

Where, $t_{84\%}$, $t_{50\%}$, and $t_{16\%}$ are indicating the time corresponding to 86 %, 50 % and 16 % for the relative concentration of tracer in BTCs and v is the volumetric flow rate.

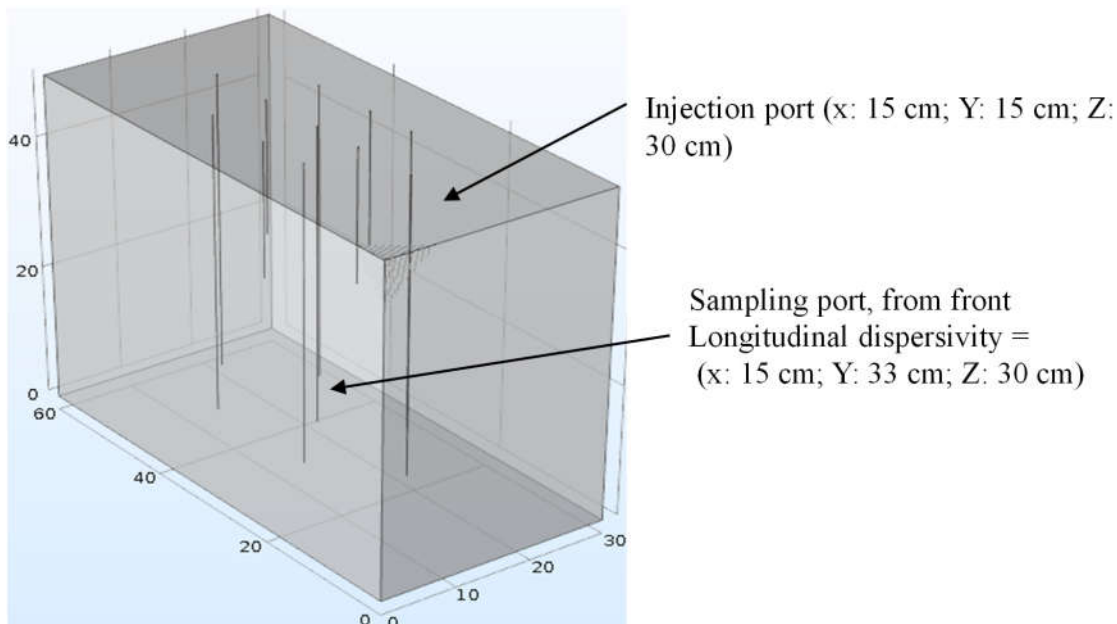


Figure 6.3. Picture showing the location of injection port and sampling ports considered during tracer experiments.

6.4 Results and discussion

6.4.1 Columns studies (1D)

6.4.1.1 Evaluation of fixed bed parameters for As^V adsorption

The study of nanoadsorbents under continuous flow conditions are essential towards scale-up of the contaminant remediation system for their applications in real world scenario. It can be achieved by performing column studies at different experimental conditions. Therefore, the effects of flow rate ($4 - 12 \text{ ml min}^{-1}$), bed height ($14.6 - 58.4 \text{ cm}$), inlet concentration ($0.055 - 4 \text{ mg L}^{-1}$) have been explored for the As^V removal employing as-synthesized BIO NPs and BIO-DW nano hybrids. These studies are discussed individually below:

Effect of volumetric flow rate (F_v)

Generally, the volumetric flow rate affects the efficiency of adsorbent in a fixed bed with respect to the service time in two ways. Its high rate of flow causes a decrease in the mass resistance of external film at the surface of nanoadsorbents. This mainly occurs due to the additional velocity shear which reduces the film thickness. Moreover, a decrease in the residence time of the feeding contaminated water at high flow rate affect the removal capacity of fixed bed column [342], [343].

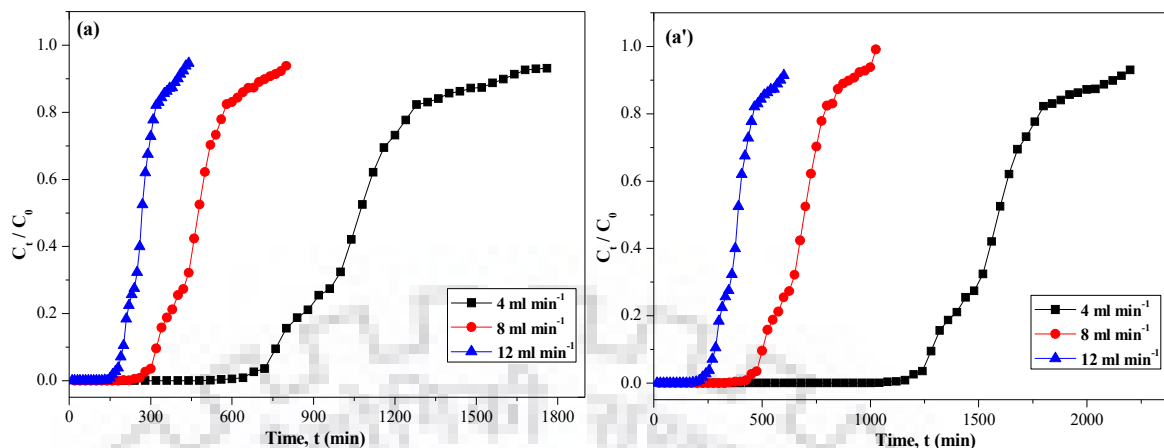


Figure 6.4. Breakthrough curves of As^{V} adsorption at different flow rate(s) (a) BIO NPs and (a') BIO-DW nanohybrids.

Figure 6.4 (a-a') depict the effect of volumetric flow rates on the As^{V} adsorption in a fixed bed column through experimental breakthrough curve(s) for BIO NPs and BIO-DW nanohybrids, which has been varied from 4 to 12 mL min^{-1} keeping the bed height and initial feed concentration constant with the values of 75.2 cm and 4.0 mg L^{-1} , respectively. In Table 6.2, the breakthrough point has been found to have occurred faster as the flow rate increased to 12 ml min^{-1} in case of both the nanosystems. At high flow rate of the feed solution, the As^{V} has shown less contact time for interacting with the nanoadsorbent before reaching the equilibrium and *vice versa*. This explains the steep behaviour of breakthrough curve as well as reduction in the adsorption capacity [344]. Further, the surface moieties of BIO NPs and BIO-DW nanohybrids get occupied instantaneously by As^{V} ions because of the increased mass transfer rate. Thus, it causes the saturation of fixed bed faster at high flow rate as compared to that of low flow rate. The obtained results in the present study have been found in good agreement with those observed earlier [335], [345].

Effect of height of reactive zone (h_{rz})

The accumulation of removal contaminant in a fixed bed adsorber is primarily depend on the amount of adsorbent present in remediation system. In order to explore this study, 1.2–1.7 g of nanoadsorbent(s) have been packed with the porous media of an approximate bed height ranging from 14.6–58.4 cm utilizing both of as-synthesized BIO NPs and BIO-DW nanohybrids. The effect of different bed heights has been studied at an initial concentration of As^{V} of 4.0 mg L^{-1} and a flow rate of 8.0 ml min^{-1} . The obtained breakthrough curves for different bed heights are shown in Figures below:

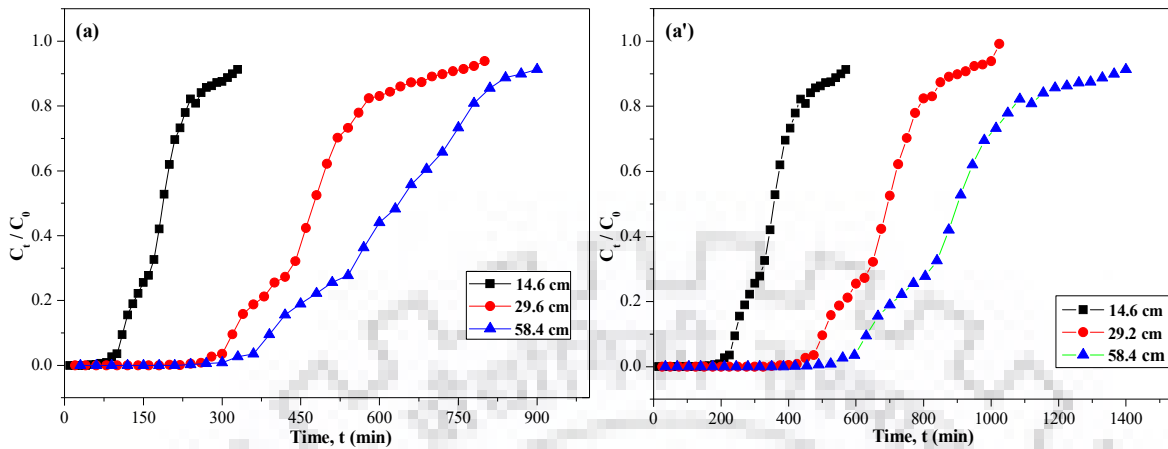


Figure 6.5. Breakthrough curve of As^{V} adsorption for different bed height(s) (a) BIO NPs and (a') BIO-DW nanohybrids.

This study reveals that the steepness of all the breakthrough curves is largely influenced by the bed height of fixed bed system while employing both of these nanosystems. A decrease in the slope of breakthrough curve(s) has been observed with an increase in the bed height due to a longer contact time. It has also resulted in the increase in the removal capacity and lower concentration of As^{V} in the treated water [344]. As the height of fixed bed increases from 14.6 cm to 58.4, the breakthrough point increases from 60 to 260 min and 165 to 455 min for BIO NPs (Table 6.2) and BIO-DW (Table 6.3) nanohybrids, respectively. It might be attributed to the increase in the effective surface area (larger fixed bed) with an increase in the adsorbent mass. This provides large number of active sites for the interaction with the As^{V} species during adsorption process. Further, an increase in the bed height leads to a longer mass transfer zone, which subsequently results in an extended breakthrough time. However, large height of fixed bed (H_{rz}) is not advised because the adsorber is prone to not get exhausted completely [335].

Effect of initial As^{V} feed solution concentration (C_0)

The mass transfer flux during the removal process is considered to depend on the factors such as area perpendicular to mass flux, mass-transfer coefficient and concentration gradient. Among these, the concentration of feed solution yields to a certain level of generating mass transfer driving force. The effect of initial As^{V} concentration along with the adsorption breakthrough curves for BIO NPs and BIO nanohybrids is presented in Figures below:

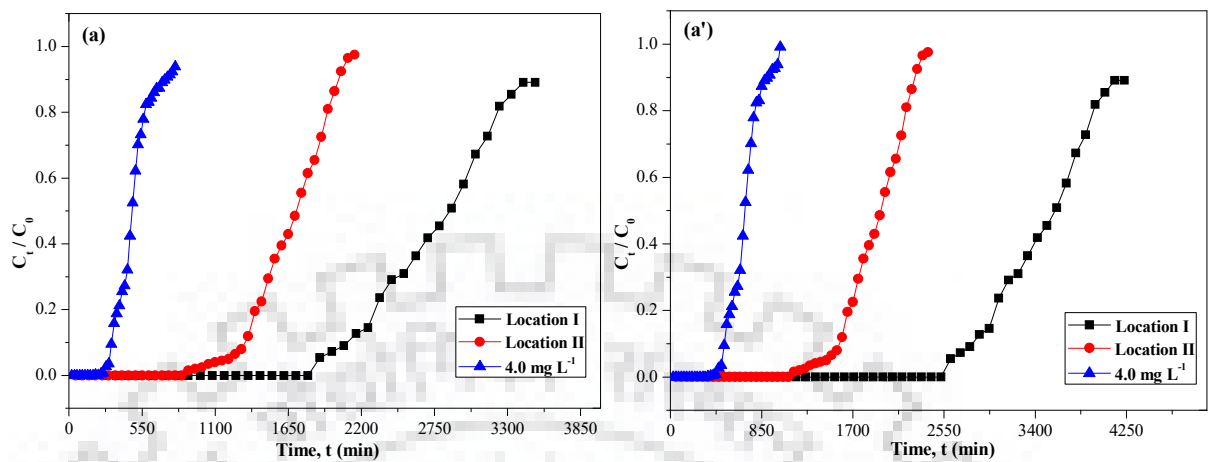


Figure 6.6. Breakthrough curve of As^{V} adsorption at different initial concentration(s) (a) BIO NPs and (a') BIO-DW nanohybrids.

In the present study, the initial As^{V} feed solution concentration has been varied from 0.055 to 4.0 mg L^{-1} with a fixed bed height of 29.2 cm and flow rate of 8.0 ml min^{-1} employing both of these nanosystems. It has been revealed that the breakthrough time (T_b) gets shortened with an increase in the initial As^{V} feed concentration employing both the as-synthesized nanosystems. It occurs due to an increased driving force for As^{V} oxyanions to overcome the mass transfer resistance. This causes the binding sites to be easily available along with the quick adsorption at high feed concentration of As^{V} [346], [347]. Conversely, a low feed concentration causes a slow transport of As^{V} ions from the film layer to the surface of adsorbent due to the lower concentration gradient. It implies a decreased diffusion coefficient and mass transfer driving force during the adsorption process [348].

6.4.1.2 Empty bed contact time (EBCT) and usage rate of adsorbent (U_r)

The EBCT (or bed service time) is the time during which an adsorbent is in contact with the feed solution containing As^{V} ions. It is a significant parameter for designing of a continuous adsorbing system. This parameter affects the volume to breakthrough as well as the shape of breakthrough curve. It has been calculated for the different experimental conditions using following equation [349]:

$$EBCT (min) = \frac{V_b}{F_v} = \frac{A_b h_{rz}}{F_v} \quad (6.20)$$

Where, V_b is the volume of the fixed bed (L); A_b is indicating the cross sectional area of fixed bed (cm^2); h_{rz} and F_v are the height of reactive zone (cm) and volumetric flow rate ($ml\ min^{-1}$), respectively.

Further, the performance of fixed bed employing BIO NPs and BIO-DW nanohybrids have been evaluated through usage rate of nanoadsorbent(s). It can be denoted as U_r ($g\ L^{-1}$). Generally, it is expressed as the weight of adsorbent saturated per liter of the adsorbate solution treated. It has been calculated using the following equation [350], [351]:

$$U_r = \frac{m_a}{V_s} \quad (6.21)$$

Where, m_a is the mass of nanoadsorbent (g); V_s is the volume of the treated feed solution at breakthrough point (L).

In the present study, the time after which the As^V concentration in the treated water reaches the limit as set by WHO for drinking water ($> 10\ \mu g\ L^{-1}$), has been considered as breakthrough point. The experiments have been performed for the concentration range of 0.055 to $4.0\ mg\ L^{-1}$ for As^V employing BIO NPs and BIO-DW nanohybrids. The value of EBCT and U_r have been determined using the breakthrough curve data examined at various fixed bed height and volumetric flow rates. Their details are given in the Table 6.3 and 6.4. A comparison of these observations indicate that the usage rate of nanoadsorbent(s) decreases with the increase in EBCT. It tends to decrease from 0.59 to $0.24\ g\ L^{-1}$ as the usage rate of adsorbent increases from 47.1 to $752.9\ min$ in case of BIO NPs. Similarly, it tends to decrease from 0.27 to $0.16\ g\ L^{-1}$ in case of BIO-DW nanohybrids.

These observations reveal that the rate of occupying the reactive sites onto nanoadsorbents by As^V oxyanions decreases with time at a high EBCT, which also causes to reach the breakthrough time slowly. Additionally, it has also been predicted that the diffusion process is less effective at lower EBCT, resulting in lower adsorption of As^V . It requires more time by the adsorbent to interact with the As^V ions effectively [352]–[354].

6.4.1.3 Breakthrough model analysis

The behaviour of fixed bed reactor has been described through the concept of breakthrough curve(s) employing BIO NPs and BIO-DW nano hybrids. These curves deliver the understanding related to the operation and dynamic response of the removal process in columns experiments. For an effective design of adsorption column, it is required to analyze the breakthrough curves appropriately [355]. Several mathematical models have been proposed to describe the contaminant(s) removal onto different nano adsorbents for efficacy assessment in their application in real world. The dynamic behaviour of these fixed column(s) has been analyzed through Bohart-Adams model, Bed Depth Service Time (BDST), Thomas and Yoon Nelson model in the present study. These are discussed in details below:

Bohart-Adam model

Figures 6.7 to 6.9 show the fitting of Adam-Bohart model to the breakthrough curve data at different experimental variables for BIO NPs and BIO-DW nano hybrids. The time range in the present study has been considered from the beginning to the end of the breakthrough curve. A linear relationship has been determined for the breakthrough time (at time concentration crossing to beyond $10 \mu\text{g L}^{-1}$). The mass transfer coefficient and experimental uptake capacity along with K_{AB} and N_0 and other statistical parameters are shown in Table 6.4 and 6.5 for BIO NPs and BIO-DW nano hybrids respectively. It has been observed that N_0 increased with an increase of As^{V} concentration employing both of these nanosystems. This increase is 68.7 to 200.4 and 121.7 to 403.9 for BIO NPs and BIO-DW nano hybrids, respectively.

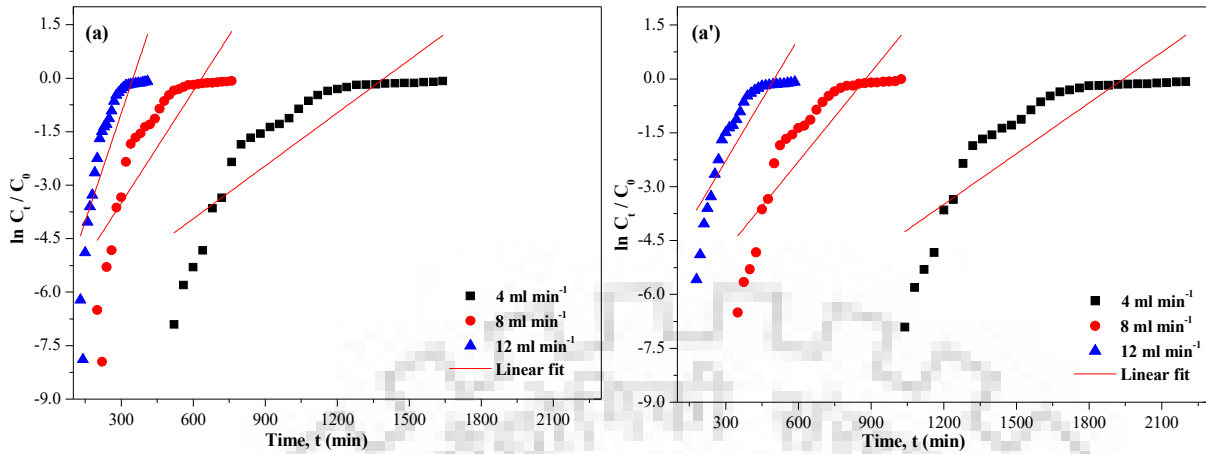


Figure 6.7. Linear plot of Adam-Bohart model with experimental data at different flow rate(s) for (a) BIO NPs and (a') BIO-DW nanohybrids [$C_0 = 4.0 \text{ mg L}^{-1}$; $h_{rz} = 29.2 \text{ cm}$].

An increase in flow rate causes to decrease the adsorption capacity (N_0) of nanoadsorbents indicating more saturation of adsorption sites. It has been decreased from 486.5 to 382.8 and 1184.0 to 196.7 for BIO NPs and BIO-DW nanohybrids respectively. This shows that the overall system kinetics in the initial part of adsorption process has been dominated by an external mass transfer [356]. Although, this model provides a simple and comprehensive approach for evaluating breakthrough data, but, it should be noted that its validity is limited to the range of conditions explored. Moreover, the poor coefficient of determination reflects less applicability of this model too.

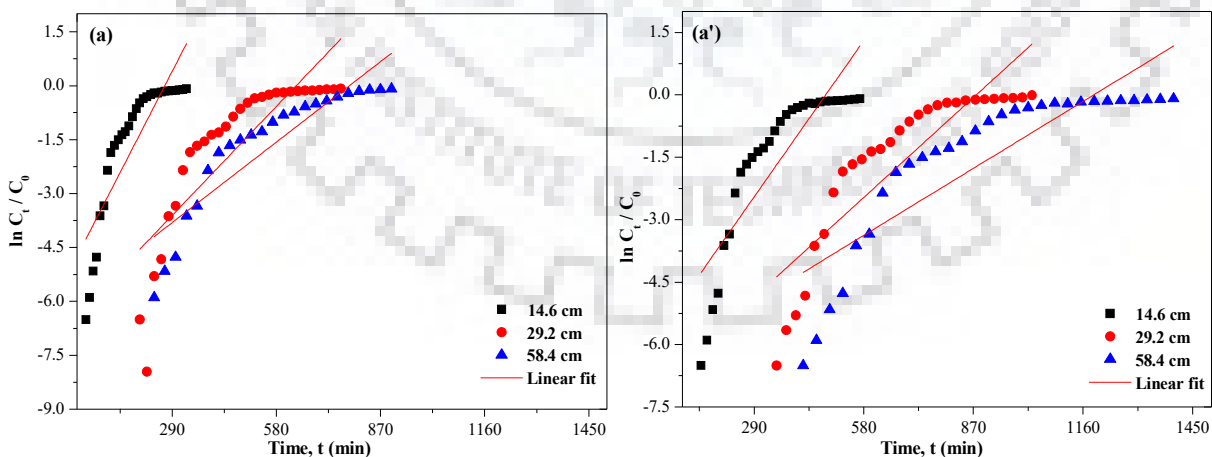


Figure 6.8. Linear plot obtained at different flow rate for; Adam-Bohart model with experimental data at different fixed bed height(s) for (a) BIO NPs and (a') BIO-DW nanohybrids [$C_0 = 4.0 \text{ mg L}^{-1}$; $F_v = 8.0 \text{ ml min}^{-1}$].

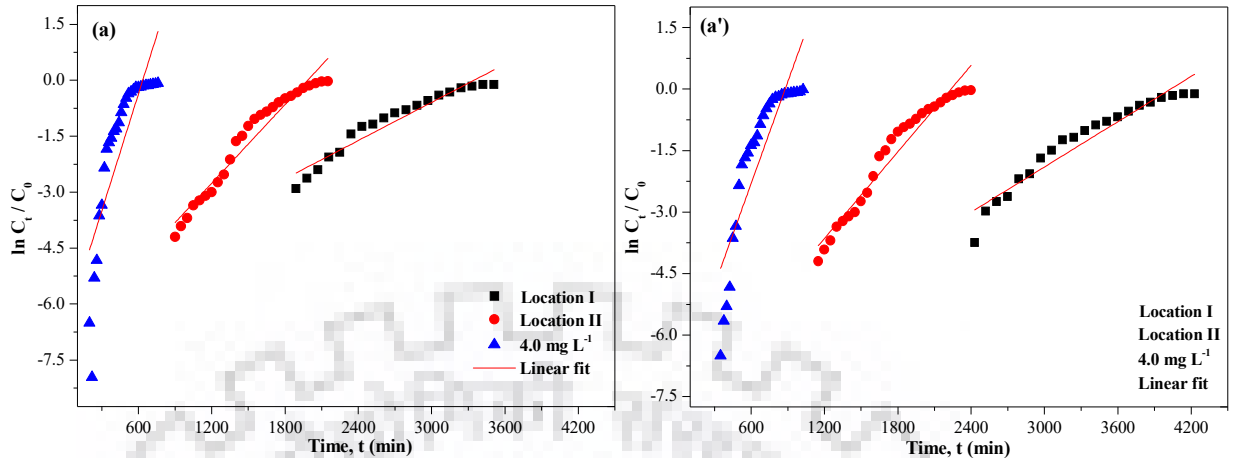


Figure 6.9. Linear plot of Adam-Bohart model with experimental data at different As^{V} initial concentrations(s) for (a) BIO NPs and (a') BIO-DW nanohybrids [$F_v = 8.0 \text{ ml min}^{-1}$; $h_{\text{rz}} = 29.2 \text{ cm}$].

Thomas model

Figures 6.10 to 6.12 show the fitting of Thomas model to the breakthrough curve data at different experimental variables for BIO NPs and BIO-DW nanohybrids. The relative constants and coefficient for the Thomas model have been calculated as given in Tables 6.4 and 6.5. For both nanosystems, the values of the initial adsorption capacity, q_0 increases with increasing initial feed concentrations. The values of coefficient of determination (R^2) and other statistical parameters demonstrate a good fit of the experimental data to the Thomas model. The predicted and experimental uptake capacity along with K_{TH} , q_0 , and other statistical parameters are given in Tables 6.3 and 6.4. As the flow rate are increased (4 to 12 ml min^{-1}), the K_{TH} value get increased, whereas the value of q_0 showed a reverse trend. These observations indicate that at a lower concentration, the mass transfer is slower, and enhances the adsorption capacity [357].

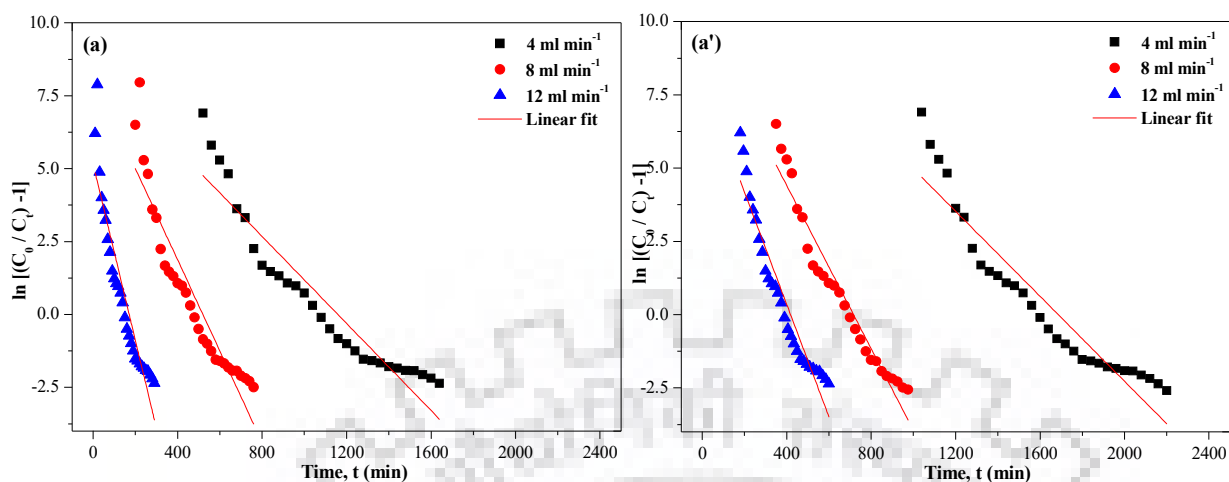


Figure 6.10. Linear plot of Thomas model with experimental data at different flow rate(s) for (a) BIO NPs and (a') BIO-DW nano hybrids [$C_0 = 4.0 \text{ mg L}^{-1}$; $h_{rz} = 29.2 \text{ cm}$].

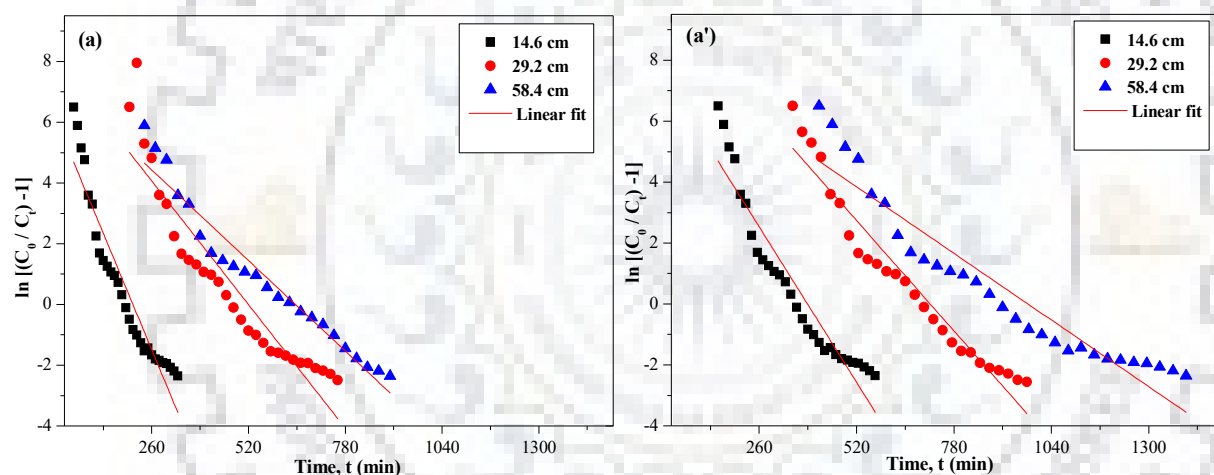


Figure 6.11. Linear plot of Thomas model with experimental data at different fixed bed height(s) for (a) BIO NPs and (a') BIO-DW nano hybrids [$C_0 = 4.0 \text{ mg L}^{-1}$; $F_v = 8.0 \text{ ml min}^{-1}$].

Further, it has also been observed that with an increase in the bed height (14.6 to 58.4 cm), the K_{TH} value is decreased in case of both BIO NPs and BIO-DW nano hybrids. Thus, the lower flow rate, the higher feed concentration and the higher bed height would increase the adsorption of As^V onto both types of fixed bed(s) employed with nano adsorbents. The good fit of the Thomas model to the experimental data indicates that the external and internal diffusions are not the limiting steps [358].

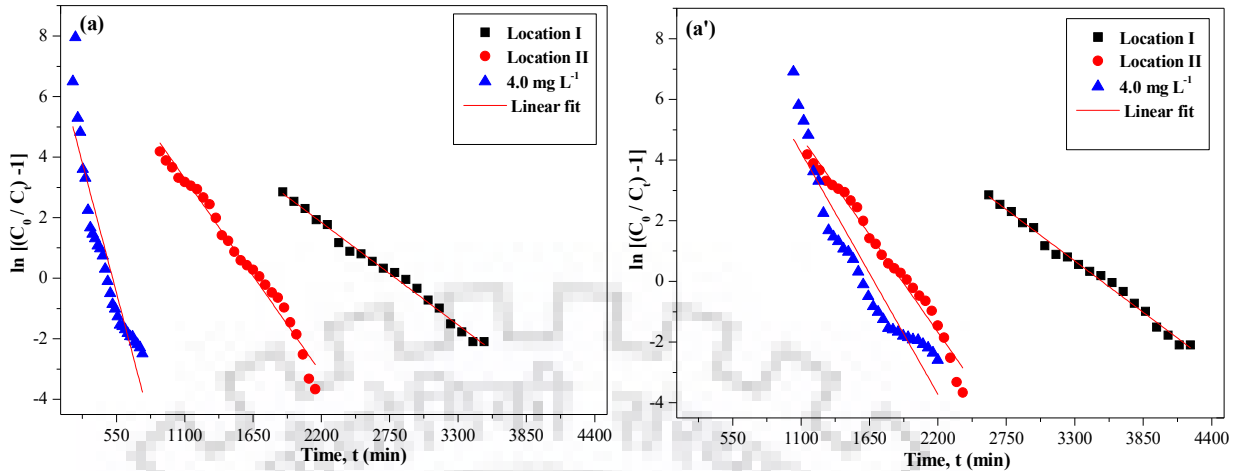


Figure 6.12. Linear plot of Thomas model with experimental data at different As^V initial concentrations(s) for (a) BIO NPs and (a') BIO-DW nanohybrids [$F_v = 8.0 \text{ ml min}^{-1}$; $h_{rz} = 29.2 \text{ cm}$].

Yoon-Nelson model

Figures 6.13 to 6.15 show the fitting of Yoon-Nelson model to the breakthrough curve data at different experimental variables for BIO NPs and BIO-DW nanohybrids. The relative constants and coefficient for the Yoon-Nelson model have been calculated and given in Tables 6.4 and 6.5. The good coefficient of determination values confirms the applicability of the Yoon Nelson model to the system examined.

The proportionality constant (K_{YN}), gets slightly increased with the flow rate showing that the mass transport resistance decreases for both of these nanosystems. However, the extent of increase is more in case of BIO NPs as compared to that of BIO-DW nanohybrids. It indicates that the removal capacity of As^V using BIO NPs is largely influenced by the mass transport forces. These observations are similar to those in batch experiments presented in previous chapters. The time required to reach 50 % of the retention, $t_{0.5}$, significantly decreases with the increase of initial As^V feed concentration and flow rate because of faster saturation of the fixed bed [359]. The mass transport resistance is proportional to the axial dispersion and thickness of the liquid film on the particle surface [32]. In the present study, the flow rates (4 to 12 ml min^{-1}) are small enough and their effect on the increase of axial dispersion is negligible, which is confirmed by the increase of the K_{YN} constant. Therefore, it might be assumed that the driving force of mass transfer in the liquid film increases with an increase in the flow rate in case of both nanosystems. Several similar results

have been observed in the literature, in which the dependency of K_{YN} with respect to different experimental conditions was explained [360], [361].

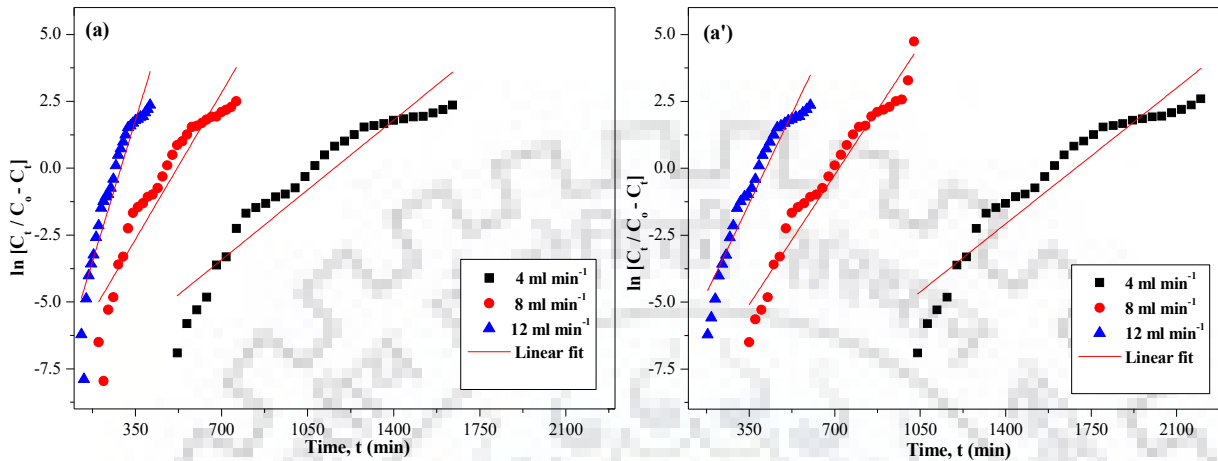


Figure 6.13. Linear plot of Yoon-Nelson model with experimental data at different flow rate(s) for (a) BIO NPs and (a') BIO-DW nanohybrids [$C_0 = 4.0 \text{ mg L}^{-1}$; $h_{TZ} = 29.2 \text{ cm}$].

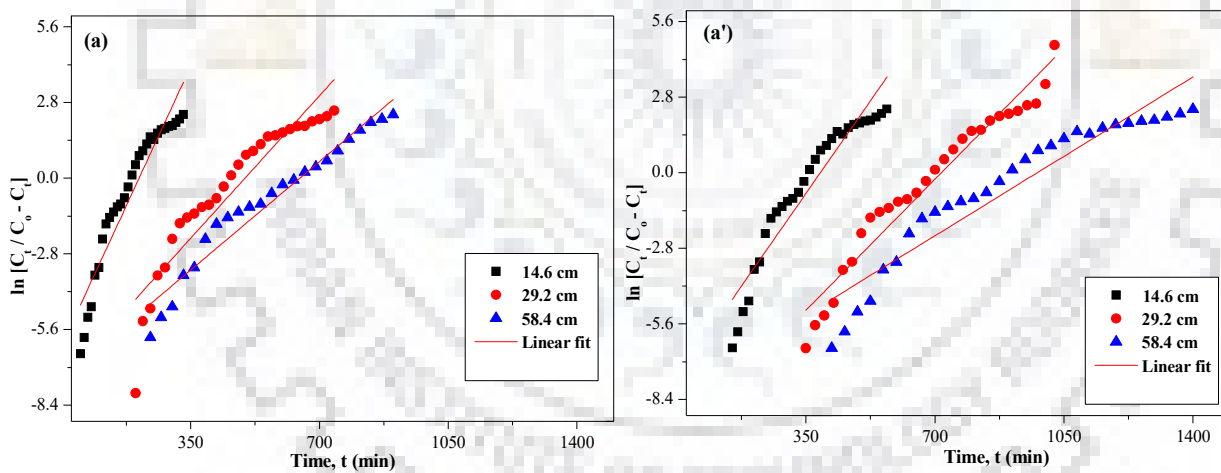


Figure 6.14. Linear plot of Yoon-Nelson model with experimental data at different fixed bed height(s) for (a) BIO NPs and (a') BIO-DW nanohybrids [$C_0 = 4.0 \text{ mg L}^{-1}$; $F_v = 8.0 \text{ ml min}^{-1}$].

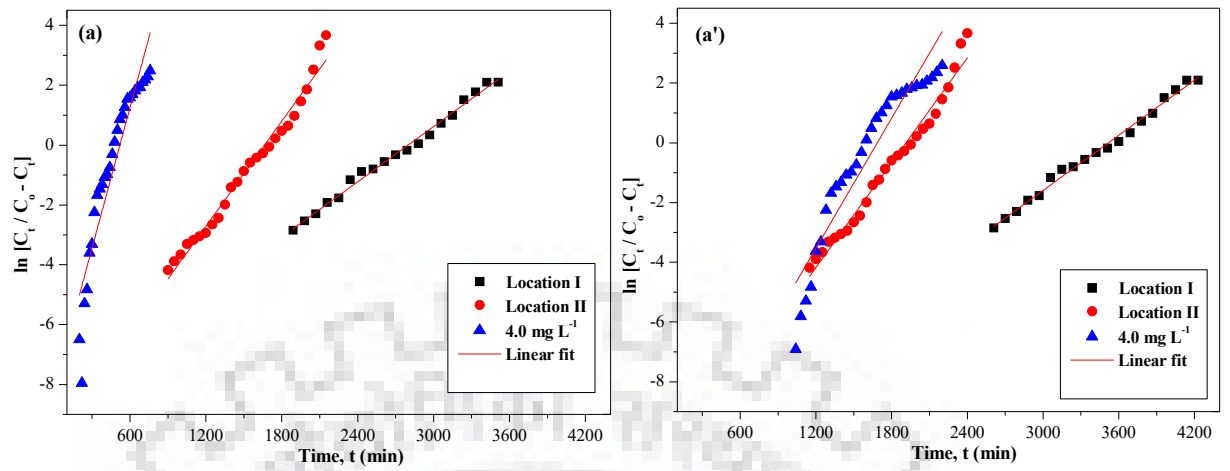


Figure 6.15. Linear plot of Yoon-Nelson model with experimental data at different As^V initial concentrations(s) for (a) BIO NPs and (a') BIO-DW nanohybrids [$F_v = 8.0 \text{ ml min}^{-1}$; $h_{tz} = 29.2 \text{ cm}$].

Table 6.2. Experimental parameters of adsorptive removal of As^V by as-synthesized BIO NPs in the fixed bed system(s).

Parameter	F_v ($ml\ min^{-1}$)	H_{rz} (cm)	C_o ($mg\ L^{-1}$)	T_b (min)	T_s (min)	$V_{effec.}$ (ml)	$q_{eq.}$ ($mg\ g^{-1}$)	$EBCT$ (min)	U_r ($g\ L^{-1}$)	η (%)
Volumetric flow rate	4	29.2	4.0	560	1610	6440	11.5	376.5	0.23	67.1
	8	29.2	4.0	220	740	5920	8.1	188.2	0.32	64.6
	12	29.2	4.0	140	400	4800	7.2	125.5	0.38	64.7
Reactive zone height	8	14.6	4.0	60	320	2560	3.9	47.1	0.59	59.3
	8	29.2	4.0	220	740	5920	8.1	188.2	0.25	64.6
	8	58.4	4.0	260	780	6240	11.1	752.9	0.24	64.6
Inlet solution	8	29.2	Location I	2270	3510	28080	1.0	188.2	0.04	77.3
	8	29.2	Location II	1200	2020	16160	2.2	188.2	0.10	81.8
	8	29.2	4.0	220	740	5920	8.1	188.2	0.25	64.6

Table 6.3. Experimental parameters for adsorptive removal of As^V by as-synthesized BIO-DW nanohybrids in the fixed bed system(s).

Parameter	F_v ($ml\ min^{-1}$)	H_{rz} (cm)	C_o ($mg\ L^{-1}$)	T_b (min)	T_s (min)	$V_{effec.}$ (ml)	$q_{eq.}$ ($mg\ g^{-1}$)	$EBCT$ (min)	U_r ($g\ L^{-1}$)	η (%)
Volumetric flow rate	4	29.2	4.0	1080	2140	8560	16.0	376.5	0.37	74.8
	8	29.2	4.0	375	925	7800	13.7	188.2	0.53	73.9
	12	29.2	4.0	195	585	7560	11.7	125.5	0.68	68.9
Reactive zone height	8	14.6	4.0	165	555	4440	7.7	47.1	0.27	64.8
	8	29.2	4.0	375	925	7800	13.7	188.2	0.20	73.9
	8	58.4	4.0	455	1365	10920	17.2	752.9	0.16	66.6
Inlet solution	8	29.2	Location I	2970	4140	33120	1.3	188.2	0.04	66.3
	8	29.2	Location II	1470	2280	18240	2.5	188.2	0.07	72.5
	8	29.2	4.0	375	925	7800	13.7	188.2	0.20	73.9

Table 6.4. Breakthrough parameters for various experimental conditions obtained during As^V adsorption using BIO NPs.

	Model	Volumetric flow rate			Adsorbent bed height			Inlet initial concentration		
		4	8	12	14.6	29.2	58.4	Location I	Location II	4.0
Breakthrough models	<i>(a) Adam -Bohart</i>									
	K_{AB} ($L\ mg^{-1}\ min^{-1}$)	1.331×10^4	2.810×10^4	5.421×10^4	1.983×10^3	5.5×10^4	2.56×10^4	1.46×10^3	1.52×10^3	5.5×10^4
	N_0	486.5	465.0	382.8	126.6	200.37	58.0	68.7	99.9	200.4
	R^2	0.73	0.69	0.71	0.74	0.69	0.81	0.93	0.95	0.69
	<i>(b) Thomas</i>									
	K_{TH} ($ml\ min^{-1}\ mg^{-1}$)	0.0002	0.001	0.003	0.003	0.001	0.0004	0.0025	0.0022	0.0001
	q_0 ($mg\ g^{-1}$)	21.2	17.3	14.1	20.2	36.2	48.8	15.3	35.2	90.3
	R^2	0.90	0.87	0.88	0.90	0.87	0.95	0.99	0.98	0.87
	<i>(c) Yoon - Nelson</i>									
	K_{YN} (min^{-1})	0.0170	0.0011	0.055	0.001	0.027	0.001	0.10	0.017	0.027
$T_{0.5}$	1102.2	529.4	280.2	239.7	529.4	673.4	2785.3	1598.1	529.4	
R^2	0.90	0.95	0.92	0.90	0.86	0.95	0.99	0.98	0.87	

Table 6.5. Breakthrough parameters for various experimental conditions obtained during As^V adsorption using BIO-DW nanohybrids.

Model	Volumetric flow rate			Adsorbent bed height			Inlet initial concentration		
	4	8	12	14.6	29.2	58.4	Location I	Location II	4.0
<i>(a) Adam -Bohart</i>									
K_{AB} ($L\ mg^{-1}\ min^{-1}$)	1.338	3.450	8.060	9.09×10^4	3.53×10^4	1.68×10^4	1.61×10^3	1.56×10^3	3.53×10^4
N_0	1184.0	331.1	196.7	454.3	403.9	182.1	121.7	139.8	403.9
R^2	0.72	0.77	0.77	0.74	0.77	0.74	0.92	0.95	0.77
<i>(b) Thomas</i>									
K_{TH} ($ml\ min^{-1}\ mg^{-1}$)	0.0001	0.001	0.003	0.003	0.0008	0.0004	0.0025	0.002	0.0008
q_0 ($mg\ g^{-1}$)	32.3	26.8	21.5	29.5	46.3	65.5	19.2	45.4	101.8
R^2	0.89	0.94	0.91	0.90	0.94	0.90	0.99	0.98	0.89
<i>(c) Yoon - Nelson</i>									
K_{YN} (min^{-1})	0.014	0.023	0.026	0.002	0.039	0.013	0.005	0.035	0.014
$T_{0.5}$	1658.8	711.9	412.3	397.1	674.3	961.4	3505.5	1697.7	1658.8
R^2	0.89	0.95	0.91	0.90	0.95	0.90	0.99	0.98	0.89

6.4.2 Sand-tank studies (3D)

It may be noted that the *in-situ* sand tank experiments have been performed to study remediation of As^{III} , and not As^{V} , which has been studied in batch/column experiments presented in earlier sections. In order to move ahead with sand tank experiments, preliminary batch adsorption experiments exploring remediation of As^{III} have first been conducted, the findings of which has been presented in the following section.

6.4.2.1 Batch Adsorption experiments for As^{III} removal

In the present work, the As^{III} adsorption has been attempted in the concentration range of 1-125 mg L^{-1} employing BIO NPs and BIO-DW nanohybrids for a dose concentration of 0.30 g L^{-1} . In near neutral pH conditions, these experiments have been performed at a temperature and shaking speed of 15 °C and 250 rpm, respectively. The samples have been allowed to shake for 24 hours to reach the equilibrium conditions. The adsorption capacity (mg g^{-1} -Fe) has been found to be 203.5 and 345.1 for BIO NPs and BIO-DW nanohybrids, respectively. The obtained value of removal capacity (mg g^{-1} -Fe) against the different concentrations of As^{III} for both of these nanosystems has been plotted and shown in Figure 6.16 below:

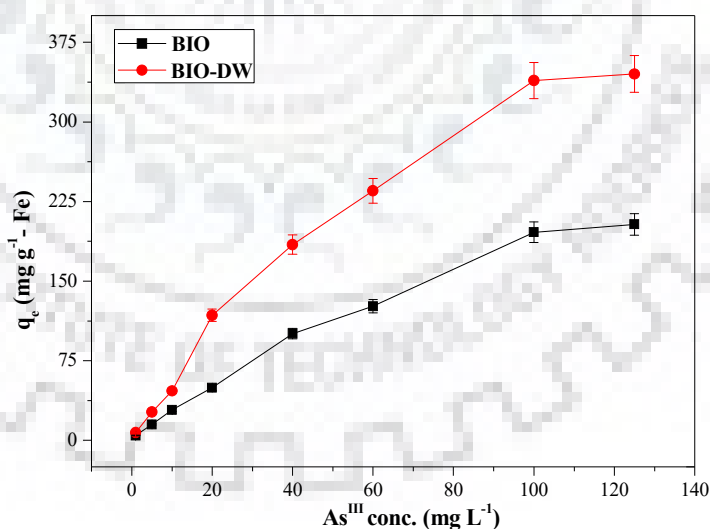


Figure 6.16. Adsorption isotherm plot for As^{III} onto BIO NPs and BIO-DW nanohybrids.

6.4.2.2 Tracer transport experiments

Tracer transport experiments have been performed first to estimate vertical dispersivity coefficient of the porous media. These experiments were conducted by maintain the constant head space of 0.5 cm in in the tank. The inlet flow of tap water has been controlled through peristaltic pump. The tracer solution was injected from the injection port (x: 15 cm; Y: 15 cm; Z: 30 cm) at a flow rate of 50 ml min^{-1} . Simultaneously, the flow of inlet solution from the tap has been maintained at the $< 25 \text{ ml min}^{-1}$. In all experiments, the flow of tap water (utilizes as to maintain the constant head difference) was kept 2 times lower as compared to those of injected tracer solution. This is because of to overcome the dilution factor which has been contributed due to the addition of tap water having the electrical conductivity lower as compared to tracer solution.

For this, the NaCl solution having the electrical conductivity of $5760 \mu\text{S cm}^{-1}$ has been injected from the above mentioned port location. The samples were collected at the 30 min intervals of time and analyzed for electrical conductivity (EC) measurements. The maximum value of EC has been determined to be $3235 \mu\text{S cm}^{-1}$ at the outlet after the 24.8 h. Further, these observations have been utilized for the calculation of longitudinal dispersivity of the medial using the equation mentioned earlier (Equation 19). The results outcomes of tracer experiments are shown below:

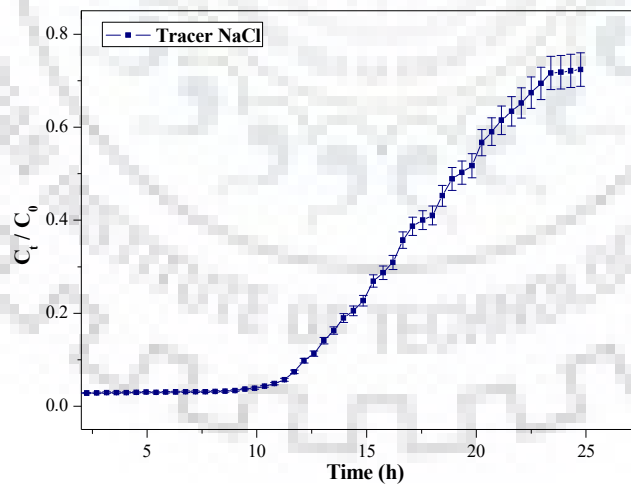


Figure 6.17. Tracer breakthrough curve (longitudinal) observed at constant head and flow conditions.

6.4.2.3 Determination of retardation coefficient of nanoparticles

It is an important parameter which signify the distribution of nanoparticles in porous media. Generally, it calculates the loss of nanoparticles in terms of their transport to a desired level. In present study, the retardation value for both of BIO NPs and BIO-DW nanohybrids have been calculated through a series batch experiments. For this, the nanoparticle dose ranging from 0.1-1.0 g have been allowed to react/adsorbed onto fixed mass (50 g) of porous media at shaking speed of 200 rpm. The double distilled water has been added to this mixture. The maximum time of contact has been kept of about 12 h. Thereafter, the samples in terms of iron content retained in the supernatant, which estimates the amount of iron retained by soil particles. From the experiments, the retardation coefficient has been observed to be 0.0101 g m⁻³ and 0.0142 g m⁻³ for BIO NPs and BIO-DW nanohybrids, respectively.

6.4.2.4 Governing equation, boundary conditions and input parameters for nanoparticle transport modelling

The COMSOL Multiphysics software (subsurface module) explains the transport of solute in subsurface conditions by incorporating four processes such as advection (driven by water flow), dispersion (caused by heterogeneity), reaction (kinetic equation) and adsorption to the soil (attachment of particle to media). It is generally expressed as an equation mentioned below:

$$1 + \left[\frac{K_d \rho}{\eta} \right] \frac{dc}{dt} = -\mu_L \frac{dc}{dL} + E \frac{d^2C}{dL^2} + r \quad (6.22)$$

Where, dc/dt is change in concentration of solute with time at a certain location, μ_L flow velocity (m time⁻¹), dc/dL is Concentration gradient, E dispersion coefficient, K_d distribution coefficient, density of porous media, porosity of porous media.

The boundary conditions and solute transport parameters for present sand tank experiments utilized for simulations are presented in Tables 6.6 and 6.7. These parameters have been applied to simulations by forming an extra fine mesh for the tank, as shown in Figure 6.18. The boundary conditions representing the zero flow, inflow and outflow of the tank is shown in Figure 6.19.

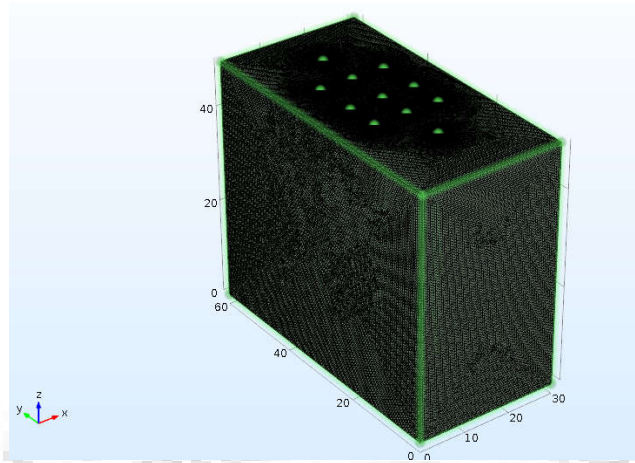


Figure 6.18. A fine mesh of 3-D model for simulation of nanoparticles transport in homogenous saturated porous media.

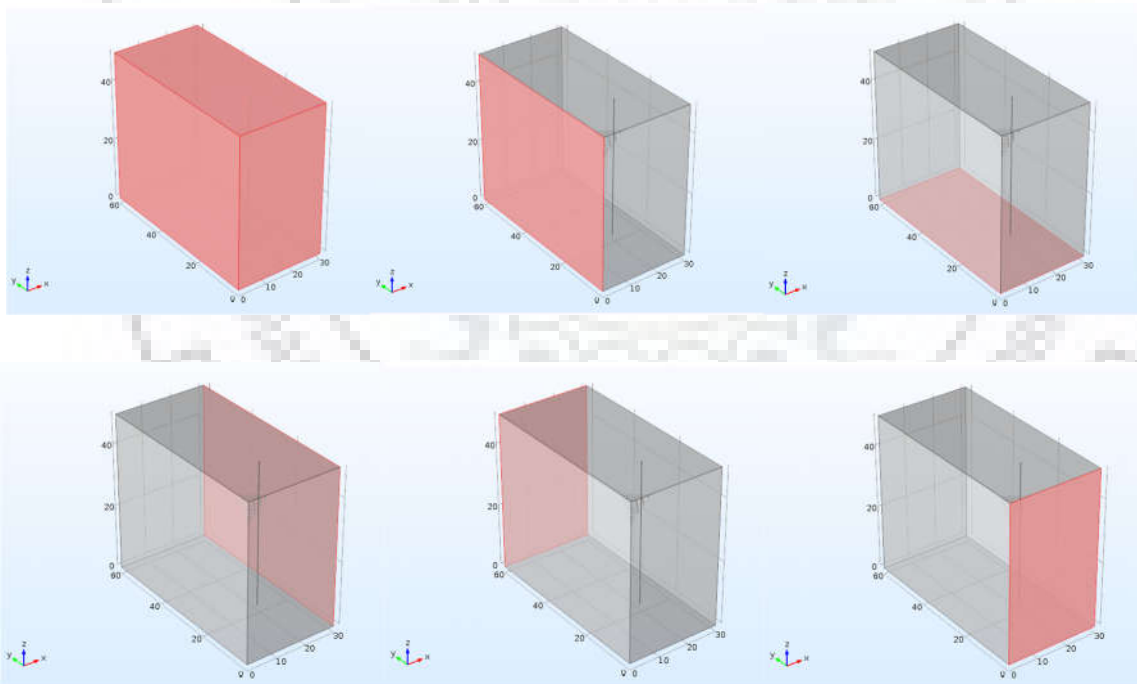


Figure 6.19. Diagrams showing the zero flow, no flow and out flow boundary conditions for simulation experiments.

Table 6.6. Overview of Boundary Conditions used to simulate arsenic fate and transport in subsurface.

Types	Formulation	Descriptions
Initial Conditions	$\theta(z, t) = \theta_i(z, 0)$ $h(z, t) = h_i(z, 0)$ $C(z, t) = C_i(z, 0)$	Initial conditions characterizing the initial state of the system can be specified either in terms of water content, pressure head, and zero concentration gradients.
<i>System-Independent Boundary Conditions</i>		
Type-1/Dirichlet/pressure head boundary condition	$h(z, t) = h_o(z, t)$	When the pressure head at the boundary is known, one can use when simulating ponded infiltration, to specify the water table.
Types-2/Neumann/Flux boundary condition	$-K(h) \left(\frac{\partial h}{\partial z} + 1 \right) = J_o(z, t)$	This boundary condition is often referred when flux is known, and used to recharge well etc.
Gradient types boundary condition	$\frac{\partial h}{\partial z} + 1 = J_o(z, t)$	Commonly used to specify a unit vertical hydraulic gradient simulating free drainage from bottom of a soil profile.
<i>System-dependent Boundary Conditions</i>		
Atmospheric boundary conditions	$\left K(h) \left(\frac{\partial h}{\partial z} + 1 \right) \right \leq E,$ $h_A \leq h \leq h_s$	The h_A is determined from the equilibrium condition between soil water and atmospheric water vapour, whereas h_S is usually set to zero.
Seepage Face	$J_o(z, t) = 0 \text{ for } h(z, t) < 0$ $h(z, t) = 0 \text{ for } h(z, t) \geq 0$	This boundary conditions states that there is no flux across the boundary as long as the boundary is unsaturated and that the pressure head change to zero once saturated. This boundary condition used at the bottom of certain types (finite) lysimeters, 2/3D sand tanks, along tile drains or at seepage faces.
Deep Drainage	$Q(n) = \text{With. } \partial h(n) * A$ $* \exp(B h - \text{GWLOL})$ <p>Where GWLOL= Reference position of the groundwater table</p>	The flux depends upon the potion of the groundwater table.

Free Drainage/Zero pressure head gradient

$$h(z,t) = 0$$

A free drainage boundary condition is its use as a bottom outflow boundary condition for situations where the water table is situated far below the domain of interest.

Variable Flux

$$J(z,t) = J_n, n=1,2,3,\dots,n$$

Variable pumping or fluid injection, and variable sprinkler irrigation, provide examples of a variable flux boundary condition.

Variable pressure head

$$h(z,t) = h_n \\ n=1,2,3,\dots,n.$$

A variable groundwater level is an example of a variable pressure head boundary condition.

No Flux

$$J(z,t) = 0$$

No-flux boundary conditions are specified for impermeable boundaries where the flux is zero perpendicular to the boundary. Impermeable layers or walls of structures, which form the boundary of the flow domain, are examples of no-flow boundary conditions.

Constant Flux

$$J(z,t) = J_i$$

The value of a constant flux boundary condition at a particular node, n, is given by the initial value of the recharge/discharge flux, Q(n). Constant pumping and constant flux sprinkler irrigation are examples of constant flux boundary conditions.

Solute Boundary Conditions

No Flux

$$C(z,t) = 0$$

No-flux boundary conditions are specified for impermeable boundaries where the flux is zero perpendicular to the boundary. Impermeable layers or walls of structures, which form the boundary of the flow domain, are examples of no-flow boundary conditions.

Types-1

(Dirichlet, or concentration type)

$$C(z,t) = C_o(z,t)$$

A first-type boundary condition is used when the concentration along the boundary is specified. Note that this type of boundary condition is generally not mass conservative.

Types-2
(Cauchy, mixed, or solute flux)

$$-K(h) \left(\frac{\partial C}{\partial z} + 1 \right) = J_o(z, t)$$

A third-type boundary condition is used when the solute flux along a boundary is specified. This type of boundary condition is mass conservative.

Volatile Type

The usual third-type boundary condition by including an additional term to account for gaseous diffusion through a stagnant boundary layer of thickness d on the soil surface.

Table 6.7. Summary of water flow and solute transport parameters used in simulation experiments.

Parameters	Values	Units
Porosity (η)	0.34	-
Residual soil water content (θ_r)	0.0081	-
Saturated soil water content (θ_s)	0.33	-
Saturated hydraulic conductivity (K_s)	$5.8 \times 10^5 \text{ m s}^{-1}$	m s^{-1}
Average bulk density (ρ_b)	1.5	g cm^{-3}
Saturated longitudinal dispersivity (D_{Lv})	12.8	m
Saturated transverse dispersivity (D_{Tv})	4.3	m
Retardation factor (R)	0.0102	g m^{-3}

6.4.2.5 Simulations of nanoparticles transport in homogenous fully saturated media

Figure 6.20 shows the predictive behaviour of transport of BIO NPs in homogenous and fully saturated porous media. The simulations have been performed for the two injection points (x: 15 cm; Y: 20 cm; Z: 30 cm) and (x: 25 cm; Y: 40 cm; Z: 30 cm). The boundary conditions and input parameters for present simulations are given in Tables 6 and 7. These results revealed that the plume of nanoparticles transport is increases with an increase in the injection time. From Figure 6.20, it can be observed that the nanoparticles concentration is reaching to the outlet of sand tank model at time of about 240 min. Based on the simulation results, the nanoparticles have been injected from the two injection ports having variable depth at the flow rate of 1.2 L h^{-1} for 4 h at constant head space (0.5 cm), maintained using peristaltic pump. The results of simulations are presented in Figure 6.20. After the injection of nanoparticles, the porous media samples have been collected from some selected locations, which further analyzed for iron concentrations. A fairly good correlation has been observed between the simulated NPs transport outcomes and calculated values. Further, the removal experiments for As^{III} has been performed using the synthetic water representing the groundwater composition equivalent to those of samples collected from the field. Their details are discussed earlier in Chapter 5.

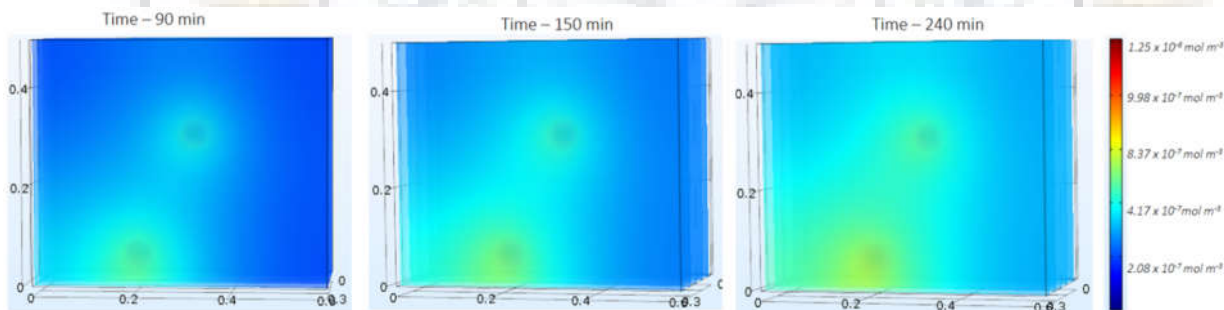


Figure 6.20. Predictive analysis of nanoparticles transport through simulations using COMSOL.

6.4.2.6 Arsenic removal experiments in 3-D sand tank model

During these experiments, the synthetic water has been prepared utilizing the methodology as disused earlier. The injected water contained the As^{III} concentration of $200 \mu\text{g L}^{-1}$ along with other co-existing ions. The flow rate was kept at 350 ml min^{-1} . The samples have been collected from the outlet and different intervals of time, which further measured for arsenic concentration using ICP-MS. Form the breakthrough, the calculated time at which the concentration of arsenic reached beyond the limit to WHO permissible limit is 31 h. The treated volume of water has been

demined to be 10.85 L for this synthetic water. The breakthrough curve observed during this analysis is presented below:

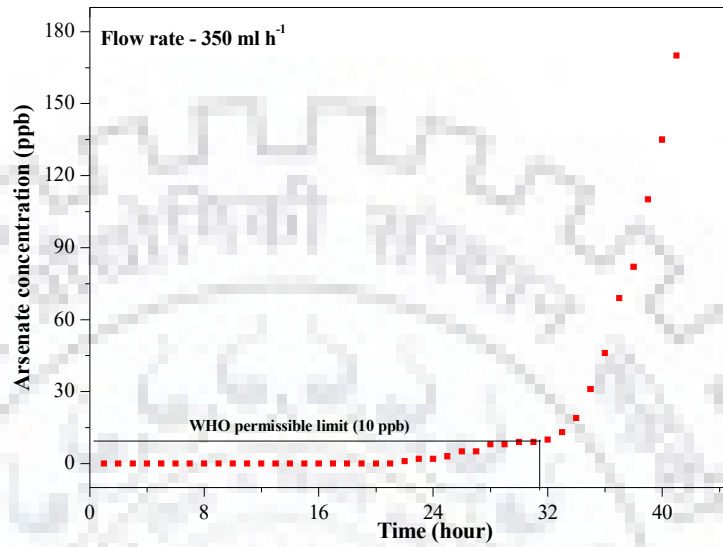


Figure 6.21. The breakthrough curve for As^{III} removal in sand-tank experiments using as-synthesized BIO NPs.



Conclusions and recommendations

7.1 Outcomes of the study

The addressing of the twin problem(s) i.e. the utilization of industry waste as a source of nanoadsorbent production and their usage for arsenic removal is a novel approach, especially in terms of cost-effective production of nanomaterial for water remediation as well as resource recovery from the waste.

A successful attempt has been performed in synthesizing the functionalized nanostructures of γ -Fe₂O₃ NPs, which are capped with the organic moieties sourced from industry waste (-NH, -OH and -CO). A reduction in the size of iron^{III} oxide nanocluster(s) has been observed associated with the increase in surface area of nanohybrids. A percent increase of 38.5 % in the surface area is demonstrated during the functionalization of maghemite NPs. In UV-spectra, the shifting of peak(s) in BIO-DW NPs, as compared to those of BIO NPs, indicate the variations in particle size and morphology during the functionalization. The present approach of synthesis has apparently allowed to conserve the crystallinity and phase of concerned polymorph of iron^{III} oxide, which has been analysed through XRD, Raman and XPS analyses. A decrease of 13.5 % in average particle size has been observed for BIO-DW nanohybrids in comparison to BIO NPs, which is beneficial in terms of enhancing the surface area as well as increasing the reactive moieties. The generation of organic functional moieties onto BIO-DW nanohybrids such as C-O-C, C=S, CC alicyclic, CH₂ and CH₃ (asym.), C=C, C-NO₂ (asym.), N=N aliphatic, C=O, and CH stretch has been found to develop well, which has got confirmed through FTIR spectroscopy. These organic moieties lead in providing several kind of interactions with the oxyanions of arsenic and might enhance removal capabilities of functionalized nanostructures in groundwater effectively. Moreover, the superparamagnetic behaviour of these nanosystem are considered to be reliable in their extraction from the treatment system even by applying magnets of low magnetization potential.

The above as-synthesized nanomaterials have demonstrated significant potential towards As^V removal as reflected by the Batch studies conducted to optimize the arsenic removal process along

with modeling of removal kinetics and adsorption isotherms. These experiments have been performed for different operational variables in the identified ranges to optimize the contact time for As^V removal utilizing both BIO and BIO-DW NPs. For BIO NPs (at desirability 0.983), the optimum contact time and removal capacity have been calculated as 272 min. and 16.1 mg g-Fe⁻¹, respectively. For BIO-DW nanohybrids (at desirability 1.0), the optimum contact time and removal capacity have been calculated as 151 min. and 24.83 mg g-Fe⁻¹, respectively. A decrease in the time from 272 min to 151 min with an enhanced removal capacity clearly indicates a quick adsorption onto the functionalized nanostructures. From RSM plots, it has been observed that the BIO-DW nanohybrids provide additional adsorption sites which enhance the adsorption capacity at high temperature and high pH conditions. This is due to the functional groups available onto the surface of these nanohybrids, which undergo an increase in the covalent interactions with As^V oxyanions. The adsorption behaviour has been examined to follow second-order-kinetic model and Langmuir isotherm model with high correlation coefficient values ($R^2 > 0.99$). Upon examination, the removal apparently has been observed to occur through primarily chemisorption along with the involvement of partial physisorption.

Both of the as-synthesized nanosystems have demonstrated significant potential in As^V removal for the groundwater representing real world conditions (test water sample composition simulating real ground water) without causing any appreciable leaching of iron. Taguchi design of experimental methodology has been applied to explore the effects of the experimental variables along with the interactions among them on the removal of As^V. The optimum shaking speed of removal was found to be 170 rpm for both of these nanosystems. The coexisting ions have been followed to influence the adsorption behaviour of As^V largely for BIO NPs as compared to those of BIO-DW nanohybrids. The adsorption is predominantly followed by physisorption and chemisorption in case of BIO NPs and BIO-DW nanohybrids, respectively. The interactions between the As^V oxyanions surface functionalities are quicker in BIO-DW nanohybrids as compared to those of BIO NPs. The high concentration of coexisting ions has been examined to provide generation of more secondary sites to interact with As^V in BIO-DW nanohybrids. The inter-variable interaction studies have revealed that the removal of As^V has largely occurred through the formation of surface complexes onto both of BIO NPs and BIO-DW nanohybrids. The charge distribution multi-sites complexation (CD-MUSIC) model and 2pk-Three-Plane-Model (TPM) have been explored as a function of pH for both BIO NPs and BIO-DW nanohybrids. The CD-MUSIC model along with 2pk-TPM has adequately explained the behaviour of As^V adsorption onto BIO NPs, which involves the reactivity of singlet

($\text{FeOH}^{-0.5}$) and triplet ($\text{Fe}_3\text{O}^{-0.5}$) species of iron. Additionally, the deprotonated surface specie FeO^- has been observed to follow the adsorption in near neutral pH conditions in case of BIO-DW nanohybrids. It got possibly involved to form the dominant complex ($= \text{FeOHAsO}_4^{3-}$) between surface moiety and As^{V} ions. The ANN tool has also been found effective in predicting the adsorption behaviour for both of as-synthesized nanosystems.

Both of these nanosystems have demonstrated a significant potential in the removal of arsenic under the dynamic flow conditions. The 1-D columns representing the height of reactive zone as 14.8 cm, 29.2 cm and 58.4 cm were designed having an internal diameter of 1.5 cm. The porosity of these have been maintained using the analytical grade sand soil of particles size ranging from 0.5 - 1 mm. The maximum adsorption capacity ($\text{mg g}^{-1}\text{-Fe}$) of 11.5 and 16.0 has been observed for BIO NPs and BIO-DW nanohybrids, respectively. Using synthetic water, the maximum adsorption capacity has been observed to be 2.2 and 2.5 $\mu\text{g g}^{-1}\text{-Fe}$. An increase in the effective volume (V_{eff}) and breakthrough time (T_b) for treated water employing BIO-DW nanohybrids indicates their higher efficiency as compared to those of BIO NPs. The experiments exploring the *in-situ* injection of nanomaterials implies that the functionalized nanostructures get transported quickly as compared to BIO NPs in porous media. The outcomes of COMSOL Multiphysics software (subsurface flow module) have revealed the significance of this in exploring the behaviour of nanoparticle transport under homogenous saturated conditions.

7.2 Recommendations for further study

Although arsenic removal through adsorption is a widely acceptable technology, however, few gaps and challenges still exist for the scientific communities to address. In future, the following efforts are proposed for further development/deployment of nanoadsorbents along with the improvement in laboratory based experiments for analyzing their comparative efficiency.:

1. For deployment at a larger and wider scale, the green approach of synthesis is required for upscaling the bulk production of nanoadsorbents by adopting the use of industrial and available natural wastes as precursor materials, depending upon their local/regional availability.
2. Comprehensive investigations related to the removal capabilities of nanoadsorbents under varied experimental conditions are recommended for such remediation studies, such as consideration of aerobic and anaerobic zones; presence of other inorganic and organic contaminants and redox

species; and use of representative test water samples in both batch and column (appropriately designed) experimental studies.

3. Assessment of the durability of system through time series analyses under different environmental conditions using laboratory scale experiments.
4. Management of toxic sludge generated after the exhaustion of treatment unit.
5. Attempting techno-financial analysis of the laboratory process to get an insight into further possible upscaling.



References

- [1] World Health Organization, "Exposure to arsenic: A major public health concern," *Report*, vol. World Heal, 2010.
- [2] N. M. F. *et al.*, "The Broad Scope of Health Effects from Chronic Arsenic Exposure: Update on a Worldwide Public Health Problem," *Environ. Health Perspect.*, vol. 121, no. 3, pp. 295–302, Mar. 2013.
- [3] P. Pal *et al.*, "Contamination of groundwater by arsenic: a review of occurrence, causes, impacts, remedies and membrane-based purification," *J. Integr. Environ. Sci.*, vol. 6, no. 4, pp. 295–316, Dec. 2009.
- [4] World health organisation, *Guidelines for drinking-water quality: fourth edition incorporating the first addendum*. 2017.
- [5] Office of Water U.S. Environmental Protection Agency, "Edition of the Drinking Water Standards and Health Advisories Tables," *EPA 822-F-18-001 Off.*, no. March, 2018.
- [6] D. Chatterjee, D. Halder, S. Majumder, and A. Biswas, "Assessment of arsenic exposure from groundwater and rice in Bengal Delta Region , West Bengal , India," *Water Res.*, vol. 44, no. 19, pp. 5803–5812, 2010.
- [7] S. Bhowmick, S. Pramanik, P. Singh, P. Mondal, D. Chatterjee, and J. Nriagu, "Science of the Total Environment Arsenic in groundwater of West Bengal , India : A review of human health risks and assessment of possible intervention options," *Sci. Total Environ.*, vol. 612, pp. 148–169, 2018.
- [8] J. Ahmed *et al.*, "Ecotoxicology and Environmental Safety Speciation and evaluation of Arsenic in surface water and groundwater samples : A multivariate case study," *Ecotoxicol. Environ. Saf.*, vol. 73, no. 5, pp. 914–923, 2010.
- [9] D. K. Nordstrom, "Worldwide Occurrences of Arsenic in Ground Water," *Science*, vol. 296, no. 5576, pp. 2143–2145, 2002.
- [10] J. C. Ng, J. Wang, and A. Shraim, "A global health problem caused by arsenic from natural sources," *Chemosphere*, vol. 52, no. 9, pp. 1353–1359, 2003.
- [11] M. A. Ali *et al.*, "Groundwater dynamics and arsenic contamination in Bangladesh," *Chem. Geol.*, vol. 228, no. 1–3, pp. 112–136, 2006.
- [12] K. Ueda and F. Furukawa, "Skin manifestations in acute arsenic poisoning from the Wakayama curry-poisoning incident," *Br. J. Dermatol.*, vol. 149, no, pp. 757–762, Oct. 2003.

- [13] M. M. Rahman, J. C. Ng, and R. Naidu, "Chronic exposure of arsenic via drinking water and its adverse health impacts on humans," *Environ. Geochem. Health*, vol. 31, no. 1, pp. 189–200, 2009.
- [14] A. H. Smith *et al.*, "Cancer risks from arsenic in drinking water," *Environ. Health Perspect.*, vol. 97, pp. 259–267, Jul. 1992.
- [15] E. J. Tokar, B. A. Diwan, J. M. Ward, D. A. Delker, and M. P. Waalkes, "Carcinogenic Effects of 'Whole-Life' Exposure to Inorganic Arsenic in CD1 Mice," *Toxicol. Sci.*, vol. 119, no. 1, pp. 73–83, Oct. 2010.
- [16] X. Qu, J. Brame, Q. Li, and P. J. J. Alvarez, "Nanotechnology for a Safe and Sustainable Water Supply: Enabling Integrated Water Treatment and Reuse," *Acc. Chem. Res.*, vol. 46, no. 3, pp. 834–843, Mar. 2013.
- [17] S. Lata and S. R. Samadder, "Removal of arsenic from water using nano adsorbents and challenges: A review," *J. Environ. Manage.*, vol. 166, pp. 387–406, 2016.
- [18] I. Ali, "New Generation Adsorbents for Water Treatment," *Chem. Rev.*, vol. 112, no. 10, pp. 5073–5091, Oct. 2012.
- [19] J. T. Nurmi *et al.*, "Characterization and Properties of Metallic Iron Nanoparticles: Spectroscopy, Electrochemistry, and Kinetics," *Environ. Sci. Technol.*, vol. 39, no. 5, pp. 1221–1230, Mar. 2005.
- [20] C. K. Jain and R. D. Singh, "Technological options for the removal of arsenic with special reference to South East Asia," *J. Environ. Manage.*, vol. 107, pp. 1–18, 2012.
- [21] S. Sarkar *et al.*, "Evolution of community-based arsenic removal systems in remote villages in West Bengal, India: Assessment of decade-long operation," *Water Res.*, vol. 44, no. 19, pp. 5813–5822, 2010.
- [22] S. R. A. J. Kanel, "Arsenic (V) Removal from Groundwater Using Nano Scale Zero-Valent Iron as a Colloidal Reactive Barrier Material," no. V, pp. 2045–2050, 2006.
- [23] K. Lee, Y. Lee, J. Yoon, S. Kamala-Kannan, S. Park, and B. Oh, "Assessment of zero-valent iron as a permeable reactive barrier for long-term removal of arsenic compounds from synthetic water," *Environ. Technol.*, vol. 30, no. 13, pp. 1425–1434, Dec. 2009.
- [24] M. Vahter, "Health Effects of Early Life Exposure to Arsenic," *Basic Clin. Pharmacol. Toxicol.*, vol. 102, no. 2, pp. 204–211, 2008.
- [25] J. D. Rimstidt, P. M. Dove, D. K. Nordstrom, G. A. Parks, and R. G. Robins, "Solubility and stability of scorodite, $\text{FeAsO}_4 \cdot 2\text{H}_2\text{O}$: Discussion," *Am. Mineral.*, vol. 72, p. 852, 1987.

- [26] D. Langmuir, J. Mahoney, A. MacDonald, and J. Rowson, "Predicting arsenic concentrations in the porewaters of buried uranium mill tailings," *Geochim. Cosmochim. Acta*, vol. 63, no. 19–20, pp. 3379–3394, 1999.
- [27] A. K. Singh, "Chemistry of arsenic in groundwater of Ganges-Brahmaputra river basin," *Curr. Sci.*, vol. 91, no. 5, pp. 599–606, 2006.
- [28] Δ. H, T. Δ. S, and Δ. G, "0 -20 -40," *Arsen. poisoning Ganges delta*, vol. 40, no. mM, p. 1049, 1999.
- [29] M. Kumar, A. L. Ramanathan, A. Mukherjee, S. Verma, M. M. Rahman, and R. Naidu, "Hydrogeo-morphological influences for arsenic release and fate in the central Gangetic Basin, India," *Environ. Technol. Innov.*, vol. 12, pp. 243–260, 2018.
- [30] R. T. Nickson, J. M. McArthur, P. Ravenscroft, W. G. Burgess, and K. M. Ahmed, "Mechanism of arsenic release to groundwater, Bangladesh and West Bengal," *Appl. Geochemistry*, vol. 15, no. 4, pp. 403–413, 2000.
- [31] L. A. Richards *et al.*, "High resolution profile of inorganic aqueous geochemistry and key redox zones in an arsenic bearing aquifer in Cambodia," *Sci. Total Environ.*, vol. 590–591, pp. 540–553, 2017.
- [32] C. A. J. Appelo, M. J. J. Van Der Weiden, C. Tournassat, and L. Charlet, "Surface complexation of ferrous iron and carbonate on ferrihydrite and the mobilization of arsenic," *Environ. Sci. Technol.*, vol. 36, no. 14, pp. 3096–3103, 2002.
- [33] J. Diwakar, S. G. Johnston, E. D. Burton, and S. Das Shrestha, "Arsenic mobilization in an alluvial aquifer of the Terai region, Nepal," *J. Hydrol. Reg. Stud.*, vol. 4, pp. 59–79, 2015.
- [34] C. L. Lockwood *et al.*, "Mobilisation of arsenic from bauxite residue (red mud) affected soils: Effect of pH and redox conditions," *Appl. Geochemistry*, vol. 51, pp. 268–277, 2014.
- [35] P. Bhattacharya, D. Chatterjee, and G. Jacks, "Occurrence of Arsenic-contaminated Groundwater in Alluvial Aquifers from Delta Plains, Eastern India: Options for Safe Drinking Water Supply," *Int. J. Water Resour. Dev.*, vol. 13, no. 1, pp. 79–92, Mar. 1997.
- [36] M. Chakraborty, A. Mukherjee, and K. M. Ahmed, "A Review of Groundwater Arsenic in the Bengal Basin, Bangladesh and India: from Source to Sink," *Curr. Pollut. Reports*, vol. 1, no. 4, pp. 220–247, 2015.
- [37] R. J. Poreda, C. B. Dowling, A. R. Basu, P. K. Aggarwal, and S. L. Peters, "Geochemical study of arsenic release mechanisms in the Bengal Basin groundwater," *Water Resour. Res.*,

vol. 38, no. 9, pp. 12-1-12-18, 2002.

- [38] L. Rodríguez-Lado *et al.*, “Groundwater Arsenic Contamination Throughout China,” *Science*, vol. 341, no. 6148, p. 866 LP-868, Aug. 2013.
- [39] J. Bundschuh *et al.*, “One century of arsenic exposure in Latin America: A review of history and occurrence from 14 countries,” *Sci. Total Environ.*, vol. 429, pp. 2–35, 2012.
- [40] B. Cancès *et al.*, “Changes in arsenic speciation through a contaminated soil profile: A XAS based study,” *Sci. Total Environ.*, vol. 397, no. 1–3, pp. 178–189, 2008.
- [41] E. Terlecka, “Arsenic speciation analysis in water samples: A review of the hyphenated techniques,” *Environ. Monit. Assess.*, vol. 107, no. 1–3, pp. 259–284, 2005.
- [42] P. L. Smedley and D. G. Kinniburgh, “A review of the source, behaviour and distribution of arsenic in natural waters,” *Appl. Geochemistry*, vol. 17, no. 5, pp. 517–568, 2002.
- [43] P. A. O.; Day, D. Vlassopoulos, R. Root, and N. Rivera, “The influence of sulfur and iron on dissolved arsenic concentrations in the shallow subsurface under changing redox conditions,” *Proc. Natl. Acad. Sci. U. S. A.*, vol. 101, no. 38, p. 13703 LP-13708, Sep. 2004.
- [44] P. L. Smedley *et al.*, “Arsenic associations in sediments from the loess aquifer of La Pampa, Argentina,” *Appl. Geochemistry*, vol. 20, no. 5, pp. 989–1016, 2005.
- [45] M. F. Ahmed, “An Overview of Arsenic Removal Technologies in Bangladesh and India,” *Civ. Eng.*, pp. 251–269, 2001.
- [46] V. S. T. Ciminelli, M. Gasparon, J. C. Ng, G. C. Silva, and C. L. Caldeira, “Dietary arsenic exposure in Brazil: The contribution of rice and beans,” *Chemosphere*, vol. 168, pp. 996–1003, 2017.
- [47] R. Bondu, V. Cloutier, E. Rosa, and M. Benzaazoua, “Mobility and speciation of geogenic arsenic in bedrock groundwater from the Canadian Shield in western Quebec, Canada,” *Sci. Total Environ.*, vol. 574, pp. 509–519, 2017.
- [48] M. Berg *et al.*, “Magnitude of arsenic pollution in the Mekong and Red River Deltas — Cambodia and Vietnam,” *Sci. Total Environ.*, vol. 372, no. 2–3, pp. 413–425, 2007.
- [49] P. Pino *et al.*, “Chile Confronts its Environmental Health Future After 25 Years of Accelerated Growth,” *Ann. Glob. Heal.*, vol. 81, no. 3, pp. 354–367, 2015.
- [50] E. E. Adomako, P. N. Williams, C. Deacon, and A. A. Meharg, “Inorganic arsenic and trace elements in Ghanaian grain staples,” *Environ. Pollut.*, vol. 159, no. 10, pp. 2435–2442, 2011.
- [51] É. Sugár, V. G. Mihucz, and G. Záray, “Determination of arsenic in drinking water and several food items,” *Elelmiszervizsgalati Kozlomenyek*, vol. 60, no. 2, pp. 163–176, 2014.

- [52] O. Navarro, J. González, H. E. Júnez-Ferreira, C. F. Bautista, and A. Cardona, “Correlation of Arsenic and Fluoride in the Groundwater for Human Consumption in a Semiarid Region of Mexico,” *Procedia Eng.*, vol. 186, pp. 333–340, 2017.
- [53] L. A. Richards, D. Magnone, B. E. van Dongen, C. J. Ballentine, and D. A. Polya, “Use of lithium tracers to quantify drilling fluid contamination for groundwater monitoring in Southeast Asia,” *Appl. Geochemistry*, vol. 63, pp. 190–202, 2015.
- [54] S. Das, S. S. Bora, R. N. S. Yadav, and M. Barooah, “A metagenomic approach to decipher the indigenous microbial communities of arsenic contaminated groundwater of Assam,” *Genomics Data*, vol. 12, pp. 89–96, 2017.
- [55] D. Chakraborti, M. M. Rahman, S. Ahamed, R. N. Dutta, S. Pati, and S. C. Mukherjee, “Arsenic groundwater contamination and its health effects in Patna district (capital of Bihar) in the middle Ganga plain, India,” *Chemosphere*, vol. 152, pp. 520–529, 2016.
- [56] K. S. Patel *et al.*, “Groundwater arsenic and fluoride in Rajnandgaon District, Chhattisgarh, northeastern India,” *Appl. Water Sci.*, vol. 7, no. 4, pp. 1817–1826, 2017.
- [57] A. Rana, S. K Bhardwaj, M. Thakur, and S. Verma, *Assessment of Heavy Metals in Surface and Ground Water Sources under Different Land Uses in Mid-hills of Himachal Pradesh*, vol. 7. 2016.
- [58] M. O. Alam, W. A. Shaikh, S. Chakraborty, K. Avishek, and T. Bhattacharya, “Groundwater Arsenic Contamination and Potential Health Risk Assessment of Gangetic Plains of Jharkhand, India,” *Expo. Heal.*, vol. 8, no. 1, pp. 125–142, 2016.
- [59] S. Sharma, J. Kaur, A. K. Nagpal, and I. Kaur, “Quantitative assessment of possible human health risk associated with consumption of arsenic contaminated groundwater and wheat grains from Ropar Wetland and its environs,” *Environ. Monit. Assess.*, vol. 188, no. 9, 2016.
- [60] A. K. Chandrashekhar, D. Chandrasekharam, and S. H. Farooq, “Contamination and mobilization of arsenic in the soil and groundwater and its influence on the irrigated crops, Manipur Valley, India,” *Environ. Earth Sci.*, vol. 75, no. 2, pp. 1–15, 2016.
- [61] R. A. Olea, N. J. Raju, J. J. Egozcue, V. Pawlowsky-Glahn, and S. Singh, “Advancements in hydrochemistry mapping: methods and application to groundwater arsenic and iron concentrations in Varanasi, Uttar Pradesh, India,” *Stoch. Environ. Res. Risk Assess.*, vol. 32, no. 1, pp. 241–259, 2018.
- [62] S. Bhowmick, S. Pramanik, P. Singh, P. Mondal, D. Chatterjee, and J. Nriagu, “Arsenic in groundwater of West Bengal, India: A review of human health risks and assessment of

- possible intervention options,” *Sci. Total Environ.*, vol. 612, pp. 148–169, 2018.
- [63] M. a. Armienta, R. Rodríguez, and O. Cruz, “Arsenic content in hair of people exposed to natural arsenic polluted groundwater at Zimapan, Mexico,” *Bull. Environ. Contam. Toxicol.*, vol. 59, no. 4, pp. 583–589, 1997.
- [64] V. S., “Riesgo sanitario ambiental por la presencia de arsénico y fluoruros en los acuíferos de México,” *Com. Nac. del Agua. Gerenc. Saneam. y Calid. del Agua*, p. 15, 2002.
- [65] D. Chakraborti *et al.*, “Groundwater arsenic contamination in Manipur, one of the seven North-Eastern Hill states of India: A future danger,” *Environ. Geol.*, vol. 56, no. 2, pp. 381–390, 2008.
- [66] J. Matschullat, R. Perobelli Borba, E. Deschamps, B. R. Figueiredo, T. Gabrio, and M. Schwenk, “Human and environmental contamination in the Iron Quadrangle, Brazil,” *Appl. Geochemistry*, vol. 15, pp. 181–190, 2000.
- [67] J. Buschmann, M. Berg, C. Stengel, and M. L. Sampson, “Arsenic and manganese contamination of drinking water resources in Cambodia: Coincidence of risk areas with low relief topography,” *Environ. Sci. Technol.*, vol. 41, no. 7, pp. 2146–2152, 2007.
- [68] D. R. Boyle, R. J. W. Turner, and G. E. M. Hall, “Anomalous arsenic concentrations in groundwaters of an island community, Bowen Island, British Columbia,” *Environ. Geochem. Health*, vol. 20, no. 4, pp. 199–212, 1998.
- [69] P. M. Ashley and B. G. Lottermoser, “Arsenic contamination at the Mole River mine, northern New South Wales,” *Aust. J. Earth Sci.*, vol. 46, no. 6, pp. 861–874, 1999.
- [70] G. Sun, S. Liu, B. Li, X. Li, and X. Sun, “Current Situation of Endemic Arsenicosis in China,” p. 476, 2001.
- [71] M. Berg, H. C. Tran, T. C. Nguyen, H. V Pham, R. Schertenleib, and W. Giger, “Arsenic contamination of groundwater and drinking water in Vietnam: a human health threat,” *Environ. Sci. Technol.*, vol. 35, no. 13, pp. 2621–6, 2001.
- [72] R. T. Nickson, J. M. McArthur, B. Shrestha, T. O. Kyaw-Myint, and D. Lowry, “Arsenic and other drinking water quality issues, Muzaffargarh District, Pakistan,” *Appl. Geochemistry*, vol. 20, no. 1, pp. 55–68, 2005.
- [73] A. Contamination and E. A. Countries, “Towards a More Effective Operational Response Arsenic Contamination of Groundwater in South and East Asian Countries,” vol. I, no. 31303, 2005.
- [74] M. Castro de Esparza, “The presence of arsenic in drinking water in Latin America and its

- effect on public health,” *Intern. Congr. Nat. Arsen. Groundwaters Lat. Am.*, no. June, pp. 20–24, 2006.
- [75] A. Mukherjee *et al.*, “Arsenic contamination in groundwater: A global perspective with emphasis on the Asian scenario,” *J. Heal. Popul. Nutr.*, vol. 24, no. 2, pp. 142–163, 2006.
- [76] D. Chakraborti, “Arsenic calamity in the Indian subcontinent What lessons have been learned,” *Talanta*, vol. 58, no. 1, pp. 3–22, 2002.
- [77] O. X. Leupin and S. J. Hug, “Oxidation and removal of arsenic (III) from aerated groundwater by filtration through sand and zero-valent iron.,” *Water Res.*, vol. 39, no. 9, pp. 1729–40, 2005.
- [78] D. Mohan and C. U. Pittman, “Arsenic removal from water/wastewater using adsorbents—A critical review,” *J. Hazard. Mater.*, vol. 142, no. 1–2, pp. 1–53, 2007.
- [79] X. Luo, C. Wang, S. Luo, R. Dong, X. Tu, and G. Zeng, “Adsorption of As (III) and As (V) from water using magnetite Fe₃O₄-reduced graphite oxide–MnO₂ nanocomposites,” *Chem. Eng. J.*, vol. 187, pp. 45–52, 2012.
- [80] X. Luo *et al.*, “Nanocomposites of graphene oxide-hydrated zirconium oxide for simultaneous removal of As(III) and As(V) from water,” *Chem. Eng. J.*, vol. 220, pp. 98–106, 2013.
- [81] X. Meng, G. P. Korfiatis, C. Christodoulatos, and S. Bang, “Treatment of arsenic in Bangladesh well water using a household co-precipitation and filtration system,” *Water Res.*, vol. 35, no. 12, pp. 2805–2810, 2001.
- [82] A. S. Sheoran and V. Sheoran, “Heavy metal removal mechanism of acid mine drainage in wetlands: A critical review,” *Miner. Eng.*, vol. 19, no. 2, pp. 105–116, 2006.
- [83] J. E. Greenleaf, J. C. Lin, and A. K. Sengupta, “Two novel applications of ion exchange fibers: Arsenic removal and chemical-free softening of hard water,” *Environ. Prog.*, vol. 25, no. 4, pp. 300–311, 2006.
- [84] R. Ning, “Arsenic removal by reverse osmosis,” *Desalination*, vol. 143, no. 3, pp. 237–241, 2002.
- [85] S. R. Wickramasinghe, B. Han, J. Zimbron, Z. Shen, and M. N. Karim, “Arsenic removal by coagulation and filtration: comparison of groundwaters from the United States and Bangladesh,” *Desalination*, vol. 169, no. 3, pp. 231–244, 2004.
- [86] M. F. Ahmed, “An Overview of Arsenic Removal Technologies in Bangladesh and India,” *Technol. Arsen. Remov. from Drink. water a Compil. Pap. Present. Int. Work. Technol. Arsen.*

Remov. from Drink. Water, pp. 251–269, 2001.

- [87] G. L. Ghurye, D. A. Clifford, and A. R. Tripp, “Combined arsenic and nitrate removal by ion exchange,” *J. / Am. Water Work. Assoc.*, vol. 91, no. 10, pp. 85–96, 1999.
- [88] P. Brandhuber and G. Amy, “Alternative methods for membrane filtration of arsenic from drinking water,” *Desalination*, vol. 117, no. 1, pp. 1–10, 1998.
- [89] P. Westerhoff, D. Highfield, M. Badruzzaman, and Y. Yoon, “Rapid Small-Scale Column Tests for Arsenate Removal in Iron Oxide Packed Bed Columns,” *J. Environ. Eng.*, vol. 131, no. February, pp. 262–271, 2005.
- [90] K. D. Hristovski, P. K. Westerhoff, T. Möller, and P. Sylvester, “Effect of synthesis conditions on nano-iron (hydr)oxide impregnated granulated activated carbon,” *Chem. Eng. J.*, vol. 146, no. 2, pp. 237–243, 2009.
- [91] M. Grassi, G. Kaykioglu, and V. Belgiorno, “Emerging Compounds Removal from Wastewater,” pp. 15–38, 2012.
- [92] S. Shankar, U. Shanker, and Shikha, “Arsenic contamination of groundwater: a review of sources, prevalence, health risks, and strategies for mitigation,” *ScientificWorldJournal.*, vol. 2014, p. 304524, 2014.
- [93] S. A. Baig, T. Sheng, Y. Hu, J. Xu, and X. Xu, “Arsenic Removal from Natural Water Using Low Cost Granulated Adsorbents: A Review,” *CLEAN - Soil, Air, Water*, vol. 43, no. 1, pp. 13–26, 2015.
- [94] H. Zhang and H. M. Selim, “Kinetics of arsenate adsorption-desorption in soils,” *Environ. Sci. Technol.*, vol. 39, no. 16, pp. 6101–6108, 2005.
- [95] H. Genc-Fuhrman, J. C. Tjell, and D. McConchie, “Adsorption of arsenic from water using activated neutralized red mud,” *Environ. Sci. Technol.*, vol. 38, no. 8, pp. 2428–2434, 2004.
- [96] Z. Gu, J. Fang, and B. Deng, “Preparation and evaluation of adsorbents for arsenic removal,” *Environ. Sci. Technol.*, vol. 39, no. 10, pp. 3833–3843, 2005.
- [97] M. P. A.-M. Elizalde-Gonzalez J. AU3 - Einicke, W.D. AU4 - Wennrich, R., “Sorption on natural solids for arsenic removal: RN - Chem. Eng. J., v. 81, p. 187-195,” vol. 81, pp. 187–195, 2001.
- [98] G. P. Gillman, “A simple technology for arsenic removal from drinking water using hydrotalcite,” *Sci. Total Environ.*, vol. 366, no. 2–3, pp. 926–931, 2006.
- [99] A. H. Malik, Z. M. Khan, Q. Mahmood, S. Nasreen, and Z. A. Bhatti, “Perspectives of low cost arsenic remediation of drinking water in Pakistan and other countries,” *J. Hazard. Mater.*,

vol. 168, no. 1, pp. 1–12, 2009.

- [100] E. J. Sullivan, R. S. Bowman, and I. a Legiec, “Sorption of arsenic from soil-washing leachate by surfactant-modified zeolite.,” *J. Environ. Qual.*, vol. 32, no. 1997, pp. 2387–2391, 1997.
- [101] K. Yin, I. M. C. Lo, H. Dong, P. Rao, and M. S. H. Mak, “Lab-scale simulation of the fate and transport of nano zero-valent iron in subsurface environments: Aggregation, sedimentation, and contaminant desorption,” *J. Hazard. Mater.*, vol. 227–228, pp. 118–125, 2012.
- [102] P. K. Tandon, R. C. Shukla, and S. B. Singh, “Removal of Arsenic(III) from Water with Clay-Supported Zerovalent Iron Nanoparticles Synthesized with the Help of Tea Liquor,” *Ind. Eng. Chem. Res.*, vol. 52, no. 30, pp. 10052–10058, 2013.
- [103] M. Bhaumik, H. J. Choi, R. I. McCrindle, and A. Maity, “Composite nanofibers prepared from metallic iron nanoparticles and polyaniline: high performance for water treatment applications.,” *J. Colloid Interface Sci.*, vol. 425, pp. 75–82, 2014.
- [104] M. Mosafiri, S. Nemati, A. Khataee, S. Nasserri, and A. A. Hashemi, “Removal of Arsenic (III, V) from aqueous solution by nanoscale zero-valent iron stabilized with starch and carboxymethyl cellulose.,” *J. Environ. Heal. Sci. Eng.*, vol. 12, no. 1, p. 74, 2014.
- [105] D. De, S. M. Mandal, J. Bhattacharya, S. Ram, and S. K. Roy, “Iron oxide nanoparticle-assisted arsenic removal from aqueous system.,” *J. Environ. Sci. Health. A. Tox. Hazard. Subst. Environ. Eng.*, vol. 44, no. 2, pp. 155–162, 2009.
- [106] Y. Wang, G. Morin, G. Ona-Nguema, F. Juillot, G. Calas, and G. E. Brown, “Distinctive arsenic(V) trapping modes by magnetite nanoparticles induced by different sorption processes,” *Environ. Sci. Technol.*, vol. 45, no. V, pp. 7258–7266, 2011.
- [107] Y. F. Lin, J. L. Chen, C. Y. Xu, and T. W. Chung, “One-pot synthesis of paramagnetic iron(III) hydroxide nanoplates and ferrimagnetic magnetite nanoparticles for the removal of arsenic ions,” *Chem. Eng. J.*, vol. 250, pp. 409–415, 2014.
- [108] Z. Özlem Kocabaş-Atakli and Y. Yürüm, “Synthesis and characterization of anatase nanoadsorbent and application in removal of lead, copper and arsenic from water,” *Chem. Eng. J.*, vol. 225, pp. 625–635, 2013.
- [109] M. I. Danish, I. A. Qazi, A. Zeb, A. Habib, M. A. Awan, and Z. Khan, “Arsenic Removal from Aqueous Solution Using Pure and Metal-Doped Titania Nanoparticles Coated on Glass Beads: Adsorption and Column Studies,” *J. Nanomater.*, vol. 2013, pp. 1–17, 2013.
- [110] K. Gupta *et al.*, “Arsenic(III) sorption on nanostructured cerium incorporated manganese

- oxide (NCMO): A physical insight into the mechanistic pathway,” *J. Colloid Interface Sci.*, vol. 377, no. 1, pp. 269–276, 2012.
- [111] W. Sun, Q. Li, S. Gao, and J. K. Shang, “Exceptional arsenic adsorption performance of hydrous cerium oxide nanoparticles: Part B. Integration with silica monoliths and dynamic treatment,” *Chem. Eng. J.*, vol. 185–186, pp. 136–143, 2012.
- [112] a. Goswami, P. K. Raul, and M. K. Purkait, “Arsenic adsorption using copper (II) oxide nanoparticles,” *Chem. Eng. Res. Des.*, vol. 90, no. 9, pp. 1387–1396, 2012.
- [113] K. J. Reddy, K. J. McDonald, and H. King, “A novel arsenic removal process for water using cupric oxide nanoparticles,” *J. Colloid Interface Sci.*, vol. 397, pp. 96–102, 2013.
- [114] N. Sahiner, O. Ozay, N. Aktas, D. a. Blake, and V. T. John, “Arsenic (V) removal with modifiable bulk and nano p(4-vinylpyridine)-based hydrogels: The effect of hydrogel sizes and quarternization agents,” *Desalination*, vol. 279, no. 1–3, pp. 344–352, 2011.
- [115] B. Davodi and M. Jahangiri, “Determination of optimum conditions for removal of As (III) and As (V) by polyaniline/polystyrene nanocomposite,” *Synth. Met.*, vol. 194, pp. 97–101, 2014.
- [116] Y. S. Han, T. J. Gallegos, A. H. Demond, and K. F. Hayes, “FeS-coated sand for removal of arsenic(III) under anaerobic conditions in permeable reactive barriers,” *Water Res.*, vol. 45, no. 2, pp. 593–604, 2011.
- [117] A. Piquette, C. Cannon, and A. W. Apblett, “Remediation of arsenic and lead with nanocrystalline zinc sulfide,” *Nanotechnology*, vol. 23, p. 294014, 2012.
- [118] J. Milewska-Duda, J. T. Duda, G. Jodłowski, and M. Kwiatkowski, “Model for multilayer adsorption of small molecules in microporous materials,” *Langmuir*, vol. 16, no. 18, pp. 7294–7303, 2000.
- [119] T. R. Holm and S. D. Wilson, “Chemical Oxidation for Arsenic Removal from Drinking Water, pp. 6–7, 2002.
- [120] D. Fan *et al.*, “Sulfidation of Iron-Based Materials: A Review of Processes and Implications for Water Treatment and Remediation,” *Environ. Sci. Technol.*, vol. 51, no. 22, pp. 13070–13085, 2017.
- [121] S. Sarkar and L. E. E. M. Blaney, “Arsenic Removal from Groundwater and Its Safe Containment in a Rural Environment : Validation of a Sustainable Approach,” vol. 42, no. 12, pp. 4268–4273, 2008.
- [122] H. Crabbe *et al.*, “Hazard ranking method for populations exposed to arsenic in private water

- supplies: Relation to bedrock geology,” *Int. J. Environ. Res. Public Health*, vol. 14, no. 12, 2017.
- [123] Tanveer Ahsan, “Technologies for arsenic removal from groundwater Tanveer Ahsan,” *SamSam Water*, 2010.
- [124] S. Khettab and N. Chabbi-Chemrouk, “Sense of place in the coastal town of Tipaza in Algeria: Local-community’s socio-cognitive representations,” *Int. J. Sustain. Built Environ.*, vol. 6, no. 2, pp. 544–554, 2017.
- [125] S. K. Singh, “An analysis of the cost-effectiveness of arsenic mitigation technologies: Implications for public policy,” *Int. J. Sustain. Built Environ.*, vol. 6, no. 2, pp. 522–535, 2017.
- [126] A. A. Shahraki, “Urban planning and design in unauthorized neighborhoods using case studies,” *Int. J. Sustain. Built Environ.*, vol. 6, no. 2, pp. 273–284, 2017.
- [127] S. Tahura, S. M. Shahidullah, T. Rahman, and A. H. Milton, “Evaluation of An Arsenic Removal Household Device : Bucket Treatment Unit (BTU),” *Technol. Arsen. Remov. from Drink. Water*, pp. 158–170, 1998.
- [128] P. F. Souter *et al.*, “Evaluation of a new water treatment for point-of-use household applications to remove microorganisms and arsenic from drinking water,” *J. Water Health*, vol. 1, no. 2, pp. 73–84, 2003.
- [129] O. X. Leupin, S. J. Hug, and a. B. M. Badruzzaman, “Arsenic Removal from Bangladesh Tube Well Water with Filter Columns Containing Zerovalent Iron Filings and Sand,” *Environ. Sci. Technol.*, vol. 39, no. 20, pp. 8032–8037, 2005.
- [130] A. Hussam, “Contending with a Development Disaster: SONO Filters Remove Arsenic from Well Water in Bangladesh (Innovations Case Discussion: SONO Filters),” *Innov. Technol. Governance, Glob.*, vol. 4, no. 3, pp. 89–102, Jul. 2009.
- [131] S. H. Shah, Q. Mahmood, I. A. Raja, A. Pervez, and A. Kalsoom, “Bio-Sand filter to treat arsenic contaminated drinking water,” *Desalin. Water Treat.*, vol. 53, no. 11, pp. 2999–3006, 2015.
- [132] M. M. Ahammed and K. Davra, “Performance evaluation of biosand filter modified with iron oxide-coated sand for household treatment of drinking water,” *Desalination*, vol. 276, no. 1–3, pp. 287–293, 2011.
- [133] A. A. L. S. Duarte, S. J. A. Cardoso, and A. J. Alçada, “Emerging and innovative techniques for arsenic removal applied to a small water supply system,” *Sustainability*, vol. 1, no. 4, pp.

1288–1304, 2009.

- [134] H. Chen, M. M. Frey, D. Clifford, L. S. McNeill, and M. Edwards, “Arsenic treatment considerations,” *J. Am. Water Works Assoc.*, vol. 91, no. 3, pp. 74–85, Mar. 1999.
- [135] C. C. Azubuikwe, C. B. Chikere, and G. C. Okpokwasili, “Bioremediation techniques—classification based on site of application: principles, advantages, limitations and prospects,” *World J. Microbiol. Biotechnol.*, vol. 32, no. 11, 2016.
- [136] M. Limmer and J. Burken, “Phytovolatilization of Organic Contaminants,” *Environ. Sci. Technol.*, vol. 50, no. 13, pp. 6632–6643, 2016.
- [137] Y. Spira, J. Henstock, P. Nathanail, D. Müller, and D. Edwards, “A European approach to increase innovative soil and groundwater remediation technology applications,” *Remediat. J.*, vol. 16, pp. 81–96, 2006.
- [138] A. Fiúza, A. Futuro, A. Silva, A. Ferreira, and F. Guimarães, “in-Situ Removal of Arsenic From Groundwater Using Permeable Reactive Barriers With Iron Based Sorbents,” no. January 2015.
- [139] D. G. Beak and R. T. Wilkin, “Performance of a zerovalent iron reactive barrier for the treatment of arsenic in groundwater: Part 2. Geochemical modeling and solid phase studies,” *J. Contam. Hydrol.*, vol. 106, no. 1–2, pp. 15–28, 2009.
- [140] D. Zhou *et al.*, “Column test-based optimization of the permeable reactive barrier (PRB) technique for remediating groundwater contaminated by landfill leachates,” *J. Contam. Hydrol.*, vol. 168, pp. 1–16, 2014.
- [141] R. T. Wilkin, C. Su, R. G. Ford, and C. J. Paul, “Chromium-removal processes during groundwater remediation by a zerovalent iron permeable reactive barrier,” *Environ. Sci. Technol.*, vol. 39, no. 12, pp. 4599–4605, 2005.
- [142] K. R. Waybrant, D. W. Blowes, and C. J. Ptacek, “Selection of reactive mixtures for use in permeable reactive walls for treatment of mine drainage,” *Environ. Sci. Technol.*, vol. 32, no. 13, pp. 1972–1979, 1998.
- [143] S. Alp *et al.*, “Chemical composition and antioxidant activity *Ziziphora clinopodioides* ecotypes from Turkey,” *Rom. Biotechnol. Lett.*, vol. 21, no. 2, pp. 11298–11303, 2016.
- [144] S.-O. Ipsen, J. Gerth, and U. Förstner, *Identifying and testing materials for arsenic removal by permeable reactive barriers*. 2005.
- [145] N. Oikawa, Y. Nakagawa, K. Nishimura, T. Ueno, and T. Fujita, “Quantitative structure-activity studies of insect growth regulators X. Substituent effects on larvicidal activity of 1-

- tert-butyl-1-(2-chlorobenzoyl)-2-(substituted benzoyl)hydrazines against *Chilo suppressalis* and design synthesis of potent derivatives,” *Pesticide Biochemistry and Physiology*, vol. 48, no. 2. pp. 135–144, 1994.
- [146] I. M. C. Lo, R. Surampalli, and K. C. K. Lai, “Zero-valent iron reactive materials for hazardous waste and inorganics removal,” *Zero-Valent Iron React. Mater. Hazard. Waste Inorganics Remov.*, 2007.
- [147] J. Morris *et al.*, “Nanotechnology white paper,” *Environ. Prot. Agency (EPA), U.S., 2007. Sr. Policy Counc. Nanotechnol. White Pap. USEPA, Washington, DC.*, no. February, p. 136, 2007.
- [148] F. He, D. Zhao, and C. Paul, “Field assessment of carboxymethyl cellulose stabilized iron nanoparticles for in situ destruction of chlorinated solvents in source zones,” *Water Res.*, vol. 44, no. 7, pp. 2360–2370, 2010.
- [149] D. I. Kaplan, K. J. Cantrell, T. W. Wietsma, and M. A. Potter, “Retention of Zero-Valent Iron Colloids by Sand Columns: Application to Chemical Barrier Formation,” *J. Environ. Qual.*, vol. 25, pp. 1086–1094, 1996.
- [150] R. Baxter, N. Hastings, A. Law, and E. J. Glass, “Methods and Techniques for cleaning up contaminated sites”, *Animal Genetics*, vol. 39, no. 5. 2008.
- [151] W. C. Hung, S. H. Fu, J. J. Tseng, H. Chu, and T. H. Ko, “Study on photocatalytic degradation of gaseous dichloromethane using pure and iron ion-doped TiO₂ prepared by the sol-gel method,” *Chemosphere*, vol. 66, no. 11, pp. 2142–2151, 2007.
- [152] G. Jegadeesan, S. R. Al-Abed, V. Sundaram, H. Choi, K. G. Scheckel, and D. D. Dionysiou, “Arsenic sorption on TiO₂ nanoparticles: Size and crystallinity effects,” *Water Res.*, vol. 44, no. 3, pp. 965–973, 2010.
- [153] H. Takanashi, A. Tanaka, T. Nakajima, and A. Ohki, “Arsenic removal from groundwater by a newly developed adsorbent,” *Water Sci. Technol.*, vol. 50, no. 8, pp. 23–32, 2004.
- [154] Y. Masue, R. H. Loeppert, and T. A. Kramer, “Arsenate and Arsenite Adsorption and Desorption Behavior on Coprecipitated Aluminum:Iron Hydroxides,” *Environ. Sci. Technol.*, vol. 41, no. 3, pp. 837–842, Feb. 2007.
- [155] K. Hristovski, A. Baumgardner, and P. Westerhoff, “Selecting metal oxide nanomaterials for arsenic removal in fixed bed columns: From nanopowders to aggregated nanoparticle media,” *J. Hazard. Mater.*, vol. 147, no. 1–2, pp. 265–274, 2007.
- [156] M. J. Haron, F. Ab Rahim, A. H. Abdullah, M. Z. Hussein, and A. Kassim, “Sorption removal

- of arsenic by cerium-exchanged zeolite P,” *Mater. Sci. Eng. B Solid-State Mater. Adv. Technol.*, vol. 149, no. 2, pp. 204–208, 2008.
- [157] S. Hering, J. G., Chen, P. Y., Wilkie, J. A., Elimelech, M., & Liang, “Arsenic removal by ferric chloride,” *Journal-American Water Work. Assoc.*, vol. 88, no. 4, pp. 155–167, 1996.
- [158] S. P. Pande, L. S. Deshpande, P. M. Patni, and S. L. Lutade, “Arsenic removal studies in some ground waters of West Bengal, India,” *J. Environ. Sci. Heal. . Part A Environ. Sci. Eng. Toxicol.*, vol. 32, no. 7, pp. 1981–1987, 1997.
- [159] W. Yang, Q. Li, S. Gao, and J. K. Shang, “High efficient As(III) removal by self-assembled zinc oxide micro-tubes synthesized by a simple precipitation process,” *J. Mater. Sci.*, vol. 46, no. 17, pp. 5851–5858, 2011.
- [160] S. Saridag, O. Tak, and G. Alniacik, “Basic properties and types of zirconia: An overview,” *World J. Stomatol.*, vol. 2, no. 3, pp. 40–47, 2013.
- [161] H. Zhang, F. Huang, B. Gilbert and JF Banfield, Molecular dynamics simulations, thermodynamic analysis, and experimental study of phase stability of zinc sulphide nanoparticles,” *J. of Phys. Chem C*, vol. 107, pp. 13051-13060, 2003.
- [162] S. B. Qadri *et al.*, “Size-induced transition-temperature reduction in nanoparticles of ZnS,” *Phys. Rev. B*, vol. 60, no. 13, pp. 9191–9193, Oct. 1999.
- [163] Z. W. Pan, “Nanobelts of Semiconducting Oxides,” *Science*, vol. 291, no. 5510, pp. 1947–1949, 2001.
- [164] S. Ram and C. Mitra, “Formation of stable Cu₂O nanocrystals in a new orthorhombic crystal structure,” vol. 306, pp. 805–809, 2001.
- [165] R. A. Evarestov and V. A. Veryazov, “The Electronic Structure of Copper Oxide Crystalline Compounds. II. Chemical Bonding in Copper–Oxygen Crystals,” *Phys. status solidi*, vol. 158, no. 1, pp. 201–212, Mar. 1990.
- [166] S. R. Kanel, J.-M. Grenèche, and H. Choi, “Arsenic(V) Removal from Groundwater Using Nano Scale Zero-Valent Iron as a Colloidal Reactive Barrier Material,” *Environ. Sci. Technol.*, vol. 40, no. 6, pp. 2045–2050, 2006.
- [167] M. E. Morgada, I. K. Levy, V. Salomone, S. S. Farooq, G. Lopez, and M. I. Litter, “Arsenic (V) removal with nanoparticulate zerovalent iron: Effect of UV light and humic acids,” *Catal. Today*, vol. 143, no. 3–4, pp. 261–268, 2009.
- [168] A. Robaldis, G. M. Naja, and M. Klavins, “Highlighting inconsistencies regarding metal biosorption,” *J. Hazard. Mater.*, vol. 304, pp. 553–556, 2016.

- [169] N. Arancibia-Miranda, S. E. Baltazar, A. García, A. H. Romero, M. A. Rubio, and D. Altbir, "Lead removal by nano-scale zero valent iron: Surface analysis and pH effect," *Mater. Res. Bull.*, vol. 59, pp. 341–348, 2014.
- [170] W. Yan, M. A. V Ramos, B. E. Koel, and W. X. Zhang, "As(III) sequestration by iron nanoparticles: Study of solid-phase redox transformations with X-ray photoelectron spectroscopy," *J. Phys. Chem. C*, vol. 116, no. 9, pp. 5303–5311, 2012.
- [171] W. Yan, R. Vasic, A. I. Frenkel, and B. E. Koel, "Intraparticle reduction of arsenite (As(III)) by nanoscale zerovalent iron (nZVI) investigated with in situ X-ray absorption spectroscopy," *Environ. Sci. Technol.*, vol. 46, no. 13, pp. 7018–7026, 2012.
- [172] B. Calderon and A. Fullana, "Heavy metal release due to aging effect during zero valent iron nanoparticles remediation," *Water Res.*, vol. 83, pp. 1–9, 2015.
- [173] M. a V Ramos *et al.*, "Simultaneous Oxidation and Reduction of Arsenic by Zero-Valent Iron Nanoparticles: Understanding the Significance of the Core-Shell Structure," *Society*, no. Iii, pp. 2–5, 2009.
- [174] X. Li, Y. Cen, H. Liu, Y. Xu, and L. Guangle, "Thermal stability of Wüstite structure modified with calcium cations," *React. Kinet. Catal. Lett.*, vol. 81, no. 2, pp. 313–320, 2004.
- [175] S. Stølen, R. Glöckner, F. Grønvold, T. Atake, and S. Izumisawa, "Heat capacity and thermodynamic properties of nearly stoichiometric wüstite from 13 to 450 K," *Am. Mineral.*, vol. 81, no. 7–8, pp. 973–981, 1996.
- [176] D. Bruce and P. Hancock, "Note on the Temperature Stability of Wüstite in Surface Oxide Films on iron," *Br. Corros. J.*, vol. 4, no. 4, pp. 221–222, Jul. 1969.
- [177] F. Schrettlea, C. Kant, P. Lunkenheimer, F. Mayr, J. Deisenhofer, and A. Loidl, "Wüstite: Electric, thermodynamic and optical properties of FeO," *Eur. Phys. J. B*, vol. 85, no. 5, pp. 1–13, 2012.
- [178] H. Fjellvåg, F. Grønvold, S. Stølen, and B. Hauback, "On the Crystallographic and Magnetic Structures of Nearly Stoichiometric Iron Monoxide," *J. Sol. Stat. Chem.*, vol. 124, no. 124, pp. 52–57, 1996.
- [179] H. Fjellvåg, B. C. Hauback, T. Vogt, and S. Stølen, "Monoclinic nearly stoichiometric wüstite at low temperatures," *Am. Mineral.*, vol. 87, no. 511, p. 347, 2002.
- [180] M. Yin, Z. Chen, B. Deegan, and S. O'Brien, "Wüstite nanocrystals: Synthesis, structure and superlattice formation," *J. Mater. Res.*, vol. 22, no. 7, pp. 1987–1995, 2007.
- [181] G. Perversi, A. M. Arevalo-Lopez, C. Ritter, and J. P. Attfield, "Frustration wave order in

- iron(II) oxide spinels,” *Commun. Phys.*, vol. 1, no. 1, p. 69, 2018.
- [182] N. Compounds, “Longevity of Granular Iron in Groundwater Treatment Processes : Solution Composition,” pp. 1–9, 2001.
- [183] R. L. Rebodos and P. J. Vikesland, “Effects of oxidation on the magnetization of nanoparticulate magnetite,” *Langmuir*, vol. 26, no. 22, pp. 16745–16753, 2010.
- [184] M. L. Hunt and C. Amrhein, “Arsenic (III) and Arsenic (V) Reactions with Zerovalent Iron Corrosion Products,” vol. 36, no. 24, pp. 5455–5461, 2002.
- [185] G. F. Goya, T. S. Berquó, F. C. Fonseca, and M. P. Morales, “Static and dynamic magnetic properties of spherical magnetite nanoparticles,” *J. Appl. Phys.*, vol. 94, no. 5, pp. 3520–3528, Aug. 2003.
- [186] G. F. Goya, T. S. Berquó, F. C. Fonseca, and M. P. Morales, “Static and dynamic magnetic properties of spherical magnetite nanoparticles,” *J. Appl. Phys.*, vol. 94, no. 5, pp. 3520–3528, 2003.
- [187] C. T. Yavuz *et al.*, “Low-Field Magnetic Separation of Monodisperse Fe₃O₄ Nanocrystals,” *Sci.*, vol. 314, no. 5801, pp. 964–967, Nov. 2006.
- [188] V. Chandra, J. Park, Y. Chun, J. W. Lee, I. Hwang, and K. S. Kim, “Removal,” vol. 4, no. 7, pp. 3979–3986, 2010.
- [189] R. M. Cornell, A. M. Posner, and J. P. Quirk, “Crystal morphology and the dissolution of goethite,” *J. Inorg. Nucl. Chem.*, vol. 36, no. 9, pp. 1937–1946, 1974.
- [190] X. Zhao, X. Guo, Z. Yang, H. Liu, and Q. Qian, “Phase-controlled preparation of iron (oxyhydr)oxide nanocrystallines for heavy metal removal,” *Journal of Nanoparticle Research*, vol. 13, no. 19, pp. 2853–2864, 2011.
- [191] J. A. Arcibar-Orozco, M. Avalos-Borja, and J. R. Rangel-Mendez, “Effect of Phosphate on the Particle Size of Ferric Oxyhydroxides Anchored onto Activated Carbon: As(V) Removal from Water,” *Environ. Sci. Technol.*, vol. 46, no. 17, pp. 9577–9583, Sep. 2012.
- [192] X. Sun, C. Hu, X. Hu, J. Qu, and M. Yang, “Characterization and adsorption performance of Zr-doped akaganéite for efficient arsenic removal,” *Journal of Chemical Technology and Biotechnology*, vol. 88, no. 4, pp. 629–635, 2013.
- [193] P. K. Raul, R. R. Devi, I. M. Umlong, A. J. Thakur, S. Banerjee, and V. Veer, “Iron oxide hydroxide nanoflower assisted removal of arsenic from water,” *Mater. Res. Bull.*, vol. 49, pp. 360–368, 2014.
- [194] M. C. S. Faria *et al.*, “Arsenic removal from contaminated water by ultrafine δ -FeOOH

- adsorbents,” *Chem. Eng. J.*, vol. 237, pp. 47–54, 2014.
- [195] S. Fendorf, M. J. Eick, P. Grossl, and D. L. Sparks, “Arsenate and chromate retention mechanisms on goethite. 1. Surface structure,” *Environ. Sci. Technol.*, vol. 31, no. 2, pp. 315–320, 1997.
- [196] H. I. Adegoke, F. A. Adekola, O. S. Fatoki, and B. J. Ximba, “Sorptive interaction of oxyanions with iron oxides: A Review,” *Polish J. Environ. Stud.*, vol. 22, no. 1, pp. 7–24, 2013.
- [197] L. H. Liu, H. Dietsch, P. Schurtenberger, and M. Yan, “Photoinitiated coupling of unmodified monosaccharides to iron oxide nanoparticles for sensing proteins and bacteria,” *Bioconjug. Chem.*, vol. 20, no. 7, pp. 1349–1355, 2009.
- [198] J. C. Liu, P. J. Tsai, Y. C. Lee, and Y. C. Chen, “Affinity capture of uropathogenic *Escherichia coli* using pigeon ovalbumin-bound $\text{Fe}_3\text{O}_4@ \text{Al}_2\text{O}_3$ magnetic nanoparticles,” *Anal. Chem.*, vol. 80, no. 14, pp. 5425–5432, 2008.
- [199] R. M. Cornell and U. Schwertmann, *The Iron Oxides*, vol. 39, no. 8. 2003.
- [200] C. van der Zee, D. R. Roberts, D. G. Rancourt, and C. P. Slomp, “Nanogoethite is the dominant reactive oxyhydroxide phase in lake and marine sediments,” *Geology*, vol. 31, no. 11, pp. 993–996, 2003.
- [201] H. D. Ruan, R. L. Frost, and J. T. Kloprogge, “The behavior of hydroxyl units of synthetic goethite and its dehydroxylated product hematite,” *Spectrochimica Acta - Part A: Molecular and Biomolecular Spectroscopy*, vol. 57, no. 13. pp. 2575–2586, 2001.
- [202] R. M. Cornell and U. Schwertmann, “Introduction to the Iron Oxides,” in *The Iron Oxides*, Wiley-VCH Verlag GmbH & Co., 2004, pp. 1–7.
- [203] J. E. Post and V. F. Buchwald, “Crystal structure refinement of akaganeite,” *American Mineralogist*, vol. 76. pp. 272–277, 1991.
- [204] K. E. Garcia, A. L. Morales, C. A. Barrero, C. E. Arroyave, and J. M. Greneche, “Magnetic and crystal structure refinement in akaganeite nanoparticle,” *Physica B: Condensed Matter*, vol. 354, no. 1–4 SPEC. ISS. pp. 187–190, 2004.
- [205] R. M. Cornell and U. Schwertmann, *Also of interest Iron Oxides in the Laboratory*. 2003.
- [206] J. Scheck, T. Lemke, and D. Gebauer, “The Role of Chloride Ions during the Formation of Akaganéite Revisited,” *Minerals*, vol. 5, no. 4. pp. 778–787, 2015.
- [207] J. Saiz, E. Bringas, and I. Ortiz, “Functionalized magnetic nanoparticles as new adsorption materials for arsenic removal from polluted waters,” *J. Chem. Technol. Biotechnol.*, vol. 89,

no. 6, pp. 909–918, 2014.

- [208] L. M. Rossi, N. J. S. Costa, F. P. Silva, and R. Wojcieszak, “Magnetic nanomaterials in catalysis: advanced catalysts for magnetic separation and beyond,” *Green Chem.*, vol. 16, no. 6, p. 2906, 2014.
- [209] M. Kaloti, A. Kumar, and N. K. Navani, “Synthesis of glucose-mediated Ag- γ -Fe₂O₃ multifunctional nanocomposites in aqueous medium – a kinetic analysis of their catalytic activity for 4-nitrophenol reduction,” *Green Chem.*, vol. 17, no. 10, pp. 4786–4799, 2015.
- [210] M. Kaloti and A. Kumar, “Synthesis of Chitosan-Mediated Silver Coated γ -Fe₂O₃ (Ag- γ -Fe₂O₃@Cs) Superparamagnetic Binary Nanohybrids for Multifunctional Applications,” *J. Phys. Chem. C*, vol. 120, no. 31, pp. 17627–17644, 2016.
- [211] G. E. Brown *et al.*, “Metal Oxide Surfaces and Their Interactions with Aqueous Solutions and Microbial Organisms,” *Chem. Rev.*, vol. 99, no. 1, pp. 77–174, Jan. 1999.
- [212] H. Guo and A. S. Barnard, “Thermodynamic modelling of nanomorphologies of hematite and goethite,” *J. Mater. Chem.*, vol. 21, no. 31, pp. 11566–11577, 2011.
- [213] P. Fenter, L. Cheng, S. Rihs, M. L. Machesky, M. J. Bedzyk, and N. C. Sturchio, “Electrical Double-Layer Structure at the Rutile-Water Interface as Observed in Situ with Small-Period X-Ray Standing Waves,” *Journal of colloid and interface science*, vol. 225, pp. 154–165, 2000.
- [214] a S. Templeton, T. P. Trainor, S. J. Traina, a M. Spormann, and G. E. Brown, “Pb(II) distributions at biofilm-metal oxide interfaces,” *Proceedings of the National Academy of Sciences of the United States of America*, vol. 98, no. ii, pp. 11897–11902, 2001.
- [215] T. P. Trainor *et al.*, “Structure and reactivity of the hydrated hematite (0 0 0 1) surface,” *Surface Science*, vol. 573, pp. 204–224, 2004.
- [216] J. R. Bargar, S. N. Towle, G. E. Brown, and G. A. Parks, “XAFS and Bond-Valence Determination of the Structures and Compositions of Surface Functional Groups and Pb(II) and Co(II) Sorption Products on Single-Crystal α -Al₂O₃,” *J. Colloid Interface Sci.*, vol. 185, no. 2, pp. 473–492, 1997.
- [217] R. Zboril, M. Mashlan, and D. Petridis, “Iron(III) Oxides from Thermal Processes: Synthesis, Structural and Magnetic Properties, Mössbauer Spectroscopy Characterization, and Applications,” *Chem. Mater.*, vol. 14, no. iii, pp. 969–982, 2002.
- [218] L. Machala and R. Zbo, “Polymorphous Transformations of Nanometric Iron (III) Oxide : A Review,” no. iii, pp. 3255–3272, 2011.

- [219] T. Danno *et al.*, “Crystal Structure of β -Fe₂O₃ and Topotactic Phase Transformation to α -Fe₂O₃,” *Cryst. Growth Des.*, vol. 13, no. 2, pp. 770–774, 2013.
- [220] P. Brázda, J. Kohout, P. Bezdička, and T. Kmječ, “ α -Fe₂O₃ versus β -Fe₂O₃: Controlling the Phase of the Transformation Product of ϵ -Fe₂O₃ in the Fe₂O₃/SiO₂ System,” *Cryst. Growth Des.*, vol. 14, no. 3, pp. 1039–1046, Mar. 2014.
- [221] T. Chen, H. Xu, Q. Xie, J. Chen, J. Ji, and H. Lu, “Characteristics and genesis of maghemite in Chinese loess and paleosols: Mechanism for magnetic susceptibility enhancement in paleosols,” *Earth Planet. Sci. Lett.*, vol. 240, no. 3–4, pp. 790–802, 2005.
- [222] R. Grau-Crespo, A. Y. Al-Baitai, I. Saadoune, and N. H. De Leeuw, “Vacancy ordering and electronic structure of γ -Fe₂O₃ (maghemite): a theoretical investigation,” *J. Phys. Condens. Matter*, vol. 22, no. 25, p. 255401, 2010.
- [223] Z. Somogyi *et al.*, “Vacancy ordering in nanosized maghemite from neutron and X-ray powder diffraction,” *Appl. Phys. A Mater. Sci. Process.*, vol. 74, no. SUPPL.II, pp. 1077–1079, 2002.
- [224] J.-E. Jørgensen, L. Mosegaard, L. E. Thomsen, T. R. Jensen, and J. C. Hanson, “Formation of γ -Fe₂O₃ nanoparticles and vacancy ordering: An in situ X-ray powder diffraction study,” *J. Solid State Chem.*, vol. 180, no. 1, pp. 180–185, 2007.
- [225] T. Tuutijärvi, J. Lu, M. Sillanpää, and G. Chen, “As(V) adsorption on maghemite nanoparticles,” *Journal of Hazardous Materials*, vol. 166, no. 2–3, pp. 1415–1420, 2009.
- [226] S. Lin, D. Lu, and Z. Liu, “Removal of arsenic contaminants with magnetic γ -Fe₂O₃ nanoparticles,” *Chemical Engineering Journal*, vol. 211–212, pp. 46–52, 2012.
- [227] M. Kilianová *et al.*, “Remarkable efficiency of ultrafine superparamagnetic iron(III) oxide nanoparticles toward arsenate removal from aqueous environment,” *Chemosphere*, vol. 93, no. 11, pp. 2690–7, 2013.
- [228] M. Martínez-Cabanas, M. López-García, J. L. Barriada, R. Herrero, and M. E. Sastre de Vicente, “Green synthesis of iron oxide nanoparticles. Development of magnetic hybrid materials for efficient As(V) removal,” *Chem. Eng. J.*, vol. 301, pp. 83–91, 2016.
- [229] L. Yu, X. Peng, F. Ni, J. Li, D. Wang, and Z. Luan, “Arsenite removal from aqueous solutions by γ -Fe₂O₃-TiO₂ magnetic nanoparticles through simultaneous photocatalytic oxidation and adsorption,” *J. Hazard. Mater.*, vol. 246–247, pp. 10–17, 2013.
- [230] H. Su, X. Lv, Z. Zhang, J. Yu, and T. Wang, “Arsenic removal from water by photocatalytic functional Fe₂O₃-TiO₂ porous ceramic,” *J. Porous Mater.*, vol. 24, no. 5, pp. 1227–1235, 203

2017.

- [231] A. D. Abid, M. Kanematsu, T. M. Young, and I. M. Kennedy, "Arsenic Removal from Water Using Flame-Synthesized Iron Oxide Nanoparticles with Variable Oxidation States," *Aerosol Sci. Technol.*, vol. 47, no. 2, pp. 169–176, 2013.
- [232] Y.-F. Lin and J.-L. Chen, "Synthesis of mesoporous maghemite (γ -Fe₂O₃) nanostructures with enhanced arsenic removal efficiency," *RSC Adv.*, vol. 3, no. 35, p. 15344, 2013.
- [233] J. Yang *et al.*, "High-Content, Well-Dispersed γ -Fe₂O₃ Nanoparticles Encapsulated in Macroporous Silica with Superior Arsenic Removal Performance," *Adv. Funct. Mater.*, vol. 24, no. 10, pp. 1354–1363, 2014.
- [234] R. He, Z. Peng, H. Lyu, H. Huang, Q. Nan, and J. Tang, "Synthesis and characterization of an iron-impregnated biochar for aqueous arsenic removal," *Sci. Total Environ.*, vol. 612, pp. 1177–1186, 2018.
- [235] M. Kilianová *et al.*, "Remarkable efficiency of ultrafine superparamagnetic iron(III) oxide nanoparticles toward arsenate removal from aqueous environment," *Chemosphere*, vol. 93, no. 11, pp. 2690–2697, 2013.
- [236] W. Tang, Y. Su, Q. Li, S. Gao, and J. K. Shang, "Superparamagnetic magnesium ferrite nano-adsorbent for effective arsenic (III, V) removal and easy magnetic separation," *Water Research*, vol. 47, no. 11, pp. 3624–3634, 2013.
- [237] C. M. Babu *et al.*, "Characterization of reduced graphene oxide supported mesoporous Fe₂O₃/TiO₂ nanoparticles and adsorption of As(III) and As(V) from potable water," *J. Taiwan Inst. Chem. Eng.*, vol. 62, pp. 199–208, 2016.
- [238] W. Tang, Q. Li, C. Li, S. Gao, and J. K. Shang, "Ultrafine γ -Fe₂O₃ nanoparticles grown in confinement of in situ self-formed 'cage' and their superior adsorption performance on arsenic(III)," *Journal of Nanoparticle Research*, vol. 13, no. 6, pp. 2641–2651, 2011.
- [239] D. Mukherjee, S. Ghosh, S. Majumdar, and K. Annapurna, "Green synthesis of α -Fe₂O₃ nanoparticles for arsenic(V) remediation with a novel aspect for sludge management," *J. Environ. Chem. Eng.*, vol. 4, no. 1, pp. 639–650, 2016.
- [240] A. Yürüm, Z. Ö. Kocabaş-Atakli, M. Sezen, R. Semiat, and Y. Yürüm, "Fast deposition of porous iron oxide on activated carbon by microwave heating and arsenic(V) removal from water," *Chemical Engineering Journal*, vol. 242, pp. 321–332, 2014.
- [241] C. Su and R. W. Puls, "In situ remediation of arsenic in simulated groundwater using zerovalent iron: Laboratory column tests on combined effects of phosphate and silicate,"

- Environ. Sci. Technol.*, vol. 37, no. 11, pp. 2582–2587, 2003.
- [242] S. Kundu and A. K. Gupta, “Analysis and modeling of fixed bed column operations on As(V) removal by adsorption onto iron oxide-coated cement (IOCC),” *J. Colloid Interface Sci.*, vol. 290, no. 1, pp. 52–60, 2005.
- [243] T. H. Wang, M. H. Li, and S. P. Teng, “Bridging the gap between batch and column experiments: A case study of Cs adsorption on granite,” *J. Hazard. Mater.*, vol. 161, no. 1, pp. 409–415, 2009.
- [244] R. F. Benenati and C. B. Brosilow, “Void fraction distribution in beds of spheres,” *AIChE J.*, vol. 8, no. 3, pp. 359–361, 1962.
- [245] A. Sharma, N. Verma, A. Sharma, D. Deva, and N. Sankararamakrishnan, “Iron doped phenolic resin based activated carbon micro and nanoparticles by milling: Synthesis, characterization and application in arsenic removal,” *Chem. Eng. Sci.*, vol. 65, no. 11, pp. 3591–3601, 2010.
- [246] C. Noubactep and S. Care, “Designing laboratory metallic iron columns for better result comparability,” *J. Hazard. Mater.*, vol. 189, no. 3, pp. 809–813, 2011.
- [247] T. X. Xd, D. X. Xd, and D. X. Xd, “Lignocellulosic biomass pyrolysis mechanism : A state-of-the-art review,” *Prog. Energy Combust. Sci.*, vol. 62, pp. 33–86, 2017.
- [248] N. Vigneshwaran, R. P. Nachane, R. H. Balasubramanya, and P. V Varadarajan, “A novel one-pot ‘green’ synthesis of stable silver nanoparticles using soluble starch,” *Carbohydr. Res.*, vol. 341, no. 12, pp. 2012–2018, 2006.
- [249] P. Calandra, M. Goffredi, and V. T. Liveri, “Study of the growth of ZnS nanoparticles in water/AOT/n-heptane microemulsions by UV-absorption spectroscopy,” in *Colloids and Surfaces A: Physicochemical and Engineering Aspects*, 1999, vol. 160, no. 1, pp. 9–13.
- [250] E. P. Elsukov, I. V Povstugar, A. V Protasov, G. A. Dorofeev, and A. N. Streletskii, “Determination of nanoparticle sizes by X-ray diffraction,” *Colloid J.*, vol. 74, no. 6, pp. 675–685, 2012.
- [251] T. Ghodselahi, M. A. Vesaghi, A. Shafiekhani, A. Baghizadeh, and M. Lameii, “XPS study of the Cu@Cu₂O core-shell nanoparticles,” *Appl. Surf. Sci.*, vol. 255, no. 5 PART 2, pp. 2730–2734, 2008.
- [252] H. Yao and K. Kimura, “Field Emission Scanning Electron Microscopy for Structural Characterization of 3-D Gold Nanoparticle Superlattices,” *Mod. Res. Educ. Top. Microsc.*, pp. 568–575, 2007.

- [253] C. Flouraki, M. Kaliva, I. T. Papadas, G. S. Armatas, and M. Vamvakaki, "Nanoporous polystyrene-porphyrin nanoparticles for selective gas separation," *Polym. Chem.*, vol. 7, no. 17, pp. 3026–3033, 2016.
- [254] M. Carrier *et al.*, "Thermogravimetric analysis as a new method to determine the lignocellulosic composition of biomass," *Biomass and Bioenergy*, vol. 35, no. 1, pp. 298–307, 2011.
- [255] E. Mansfield, K. M. Tyner, C. M. Poling, and J. L. Blacklock, "Determination of nanoparticle surface coatings and nanoparticle purity using microscale thermogravimetric analysis," *Anal. Chem.*, vol. 86, no. 3, pp. 1478–1484, 2014.
- [256] D. Maiti, U. Manju, S. Velaga, and P. S. Devi, "Phase evolution and growth of iron oxide nanoparticles: Effect of hydrazine addition during sonication," *Cryst. Growth Des.*, vol. 13, no. 8, pp. 3637–3644, 2013.
- [257] J. Sun *et al.*, "Synthesis and characterization of biocompatible Fe₃O₄ nanoparticles," *J. Biomed. Mater. Res. Part A*, vol. 80A, no. 2, pp. 333–341, Feb. 2007.
- [258] M. Hanesch, "Raman spectroscopy of iron oxides and (oxy)hydroxides at low laser power and possible applications in environmental magnetic studies," *Geophys. J. Int.*, vol. 177, no. 3, pp. 941–948, 2009.
- [259] G. Martínez *et al.*, "Use of a polyol liquid collection medium to obtain ultrasmall magnetic nanoparticles by laser pyrolysis," *Nanotechnology*, vol. 23, no. 42, p. 425605, 2012.
- [260] J. Wang *et al.*, "A platinum anticancer theranostic agent with magnetic targeting potential derived from maghemite nanoparticles," *Chem. Sci.*, vol. 4, no. 6, pp. 2605–2612, 2013.
- [261] G. Unsoy, S. Yalcin, R. Khodadust, G. Gunduz, and U. Gunduz, "Synthesis optimization and characterization of chitosan-coated iron oxide nanoparticles produced for biomedical applications," *J. Nanoparticle Res.*, vol. 14, no. 11, 2012.
- [262] M. B. Yang, R. Y. Bao, J. Cao, Z. Y. Liu, W. Yang, and B. H. Xie, "Towards balanced strength and toughness improvement of isotactic polypropylene nanocomposites by surface functionalized graphene oxide," *J. Mater. Chem. A*, vol. 2, no. 9, pp. 3190–3199, 2014.
- [263] G. K. Pradhan, K. H. Reddy, and K. M. Parida, "Facile fabrication of mesoporous α -Fe₂O₃/SnO₂ nanoheterostructure for photocatalytic degradation of malachite green," *Catal. Today*, vol. 224, pp. 171–179, 2014.
- [264] A. Sharma, D. Baral, K. Rawat, P. R. Solanki, and H. B. Bohidar, "Biocompatible capped iron oxide nanoparticles for *Vibrio cholerae* detection," *Nanotechnology*, vol. 26, no. 17, p.

175302, 2015.

- [265] D. Fiorani, A. M. Testa, F. Lucari, F. D’Orazio, and H. Romero, “Magnetic properties of maghemite nanoparticle systems: Surface anisotropy and interparticle interaction effects,” *Phys. B Condens. Matter*, vol. 320, no. 1–4, pp. 122–126, 2002.
- [266] A.-H. Lu, E. L. Salabas, and F. Schüth, “Magnetic Nanoparticles: Synthesis, Protection, Functionalization, and Application,” *Angew. Chemie Int. Ed.*, vol. 46, no. 8, pp. 1222–1244, Feb. 2007.
- [267] J. Yang *et al.*, “High-content, well-dispersed γ -Fe₂O₃ nanoparticles encapsulated in macroporous silica with superior arsenic removal performance,” *Adv. Funct. Mater.*, vol. 24, no. 10, pp. 1354–1363, 2014.
- [268] H. S. Li, “Reliability-based design optimization via high order response surface method,” *J. Mech. Sci. Technol.*, vol. 27, no. 4, pp. 1021–1029, 2013.
- [269] K. Sun and J. Zhou, “Response surface method and reliability calculation based on the generating function method,” in *2016 11th International Conference on Reliability, Maintainability and Safety (ICRMS)*, 2016, pp. 1–5.
- [270] D. Ba and I. H. Boyaci, “Modeling and optimization i: Usability of response surface methodology,” *J. Food Eng.*, vol. 78, no. 3, pp. 836–845, 2007.
- [271] A. Asfaram, M. Ghaedi, S. Hajati, M. Rezaeinejad, A. Goudarzi, and M. K. Purkait, “Rapid removal of Auramine-O and Methylene blue by ZnS: Cu nanoparticles loaded on activated carbon: A response surface methodology approach,” *J. Taiwan Inst. Chem. Eng.*, vol. 53, pp. 80–91, 2015.
- [272] G. Derringer and R. Suich, “Simultaneous Optimization of Several Response Variables,” *J. Qual. Technol.*, vol. 12, no. 4, pp. 214–219, Oct. 1980.
- [273] C. S. Aksezer, “On the sensitivity of desirability functions for multiresponse optimization,” *J. Ind. Manag. Optim.*, vol. 4, no. 4, pp. 685–696, 2011.
- [274] C. Moor, T. Lymberopoulou, and V. J. Dietrich, “Determination of heavy metals in soils, sediments and geological materials by ICP-AES and ICP-MS,” *Mikrochim. Acta*, vol. 136, no. 3–4, pp. 123–128, 2001.
- [275] S. Lagergren, “About the Theory of So-Called Adsorption of Soluble Substances,” *K. Sven. Vetenskapsakademiens Handl.*, vol. 24, no. 4, pp. 1–39, 1898.
- [276] Y. S. Ho, “Review of second-order models for adsorption systems,” *J. Hazard. Mater.*, vol. 136, no. 3, pp. 681–689, 2006.

- [277] Y. S. Ho and G. McKay, "Pseudo-second order model for sorption processes," *Process Biochem.*, vol. 34, no. 5, pp. 451–465, 1999.
- [278] J. Weber Jr., W.J., Morris, J.C. and Sanit, "Kinetics of Adsorption on Carbon from Solution," *J. Sanit. Eng. Div. Am. Soc. Civ. Eng.*, vol. 89, pp. 31–38, 1963.
- [279] C. Aharoni and F. C. Tompkins, "Kinetics of Adsorption and Desorption and the Elovich Equation," in *Advances in Catalysis*, vol. 21, no. C, D. D. Eley, H. Pines, and P. B. B. T.-A. in C. Weisz, Eds. Academic Press, 1970, pp. 1–49.
- [280] H. M. F. Freundlich, "Over the Adsorption in Solution," *J. Phys. Chem.*, vol. 57, pp. 385–371, 1906.
- [281] A. A. Khan, R. Ahmad, A. Khan, and P. K. Mondal, "Preparation of unsaturated polyester Ce(IV) phosphate by plastic waste bottles and its application for removal of Malachite green dye from water samples," *Arab. J. Chem.*, vol. 6, no. 4, pp. 361–368, 2013.
- [282] V. Temkin, M. and Pyzhev, "Kinetics of Ammonia Synthesis on Promoted Iron Catalysts," *Acta Physicochim. URSS*, vol. 12, pp. 217–22, 1940.
- [283] L. V. Dubinin, M.M. and Radushkevich, "The Equation of the Characteristic Curve of Activated Charcoal," *Proc. Acad. Sci. Phys. Chem. Sect.*, vol. 55, p. 331, 1947.
- [284] K. Kalantari, M. B. Ahmad, H. R. Fard Masoumi, K. Shameli, M. Basri, and R. Khandanlou, "Rapid and high capacity adsorption of heavy metals by Fe₃O₄/montmorillonite nanocomposite using response surface methodology: Preparation, characterization, optimization, equilibrium isotherms, and adsorption kinetics study," *J. Taiwan Inst. Chem. Eng.*, vol. 49, pp. 192–198, 2015.
- [285] M. Ghaedi, M. Yousefinejad, M. Safarpour, H. Z. Khafri, and M. K. Purkait, "Rosmarinus officinalis leaf extract mediated green synthesis of silver nanoparticles and investigation of its antimicrobial properties," *J. Ind. Eng. Chem.*, vol. 31, pp. 167–172, 2015.
- [286] D. Xiao *et al.*, "Two Novel Vanadium Tellurites Covalently Bonded with Metal-Organic Complex Moieties: M(phen)V₂TeO₈ (M = Cu, Ni)," *Inorg. Chem.*, vol. 42, no. 23, pp. 7652–7657, 2003.
- [287] D. Dey and P. Banerjee, "Toxic organic solvent adsorption by hydrophobic covalent polymer†," *New J. Chem.*, pp. 3769–3777, 2019.
- [288] K. Gupta, A. Maity, and U. C. Ghosh, "Manganese associated nanoparticles agglomerate of iron(III) oxide: Synthesis, characterization and arsenic(III) sorption behavior with mechanism," *J. Hazard. Mater.*, vol. 184, no. 1–3, pp. 832–842, 2010.

- [289] R. Goswami, P. Deb, R. Thakur, K. P. Sarma, and A. Basumallick, "Removal of As(III) from Aqueous Solution Using Functionalized Ultrafine Iron Oxide Nanoparticles," *Sep. Sci. Technol.*, vol. 46, no. 6, pp. 1017–1022, Mar. 2011.
- [290] S. Zhou, D. Wang, H. Sun, J. Chen, S. Wu, and P. Na, "Synthesis, characterization, and adsorptive properties of magnetic cellulose nanocomposites for arsenic removal," *Water. Air. Soil Pollut.*, vol. 225, no. 5, 2014.
- [291] Q. Liang, B. An, and D. Zhao, *Removal and Immobilization of Arsenic in Water and Soil Using Polysaccharide-Modified Magnetite Nanoparticles*. Elsevier B.V., 2013.
- [292] A. Asfaram, M. Ghaedi, A. Goudarzi, and M. Rajabi, "Response surface methodology approach for optimization of simultaneous dye and metal ion ultrasound-assisted adsorption onto Mn doped iron-NPs loaded on AC: Kinetic and isothermal studies," *Dalt. Trans.*, vol. 44, no. 33, pp. 14707–14723, 2015.
- [293] M. A. Tofighy and T. Mohammadi, "Adsorption of divalent heavy metal ions from water using carbon nanotube sheets," *J. Hazard. Mater.*, vol. 185, no. 1, pp. 140–147, 2011.
- [294] H. K. Boparai, M. Joseph, and D. M. O'Carroll, "Kinetics and thermodynamics of cadmium ion removal by adsorption onto nano zerovalent iron particles," *J. Hazard. Mater.*, vol. 186, no. 1, pp. 458–465, 2011.
- [295] R. Jolsterå, L. Gunneriusson, and A. Holmgren, "Surface complexation modeling of Fe₃O₄-H⁺ and Mg(II) sorption onto maghemite and magnetite," *J. Colloid Interface Sci.*, vol. 386, no. 1, pp. 260–267, 2012.
- [296] APHA, AWWA, and WEF, "Standard Methods for the Examination of Water and Wastewater Part 4000 INORGANIC NONMETALLIC CONSTITUENTS Standard Methods for the Examination of Water and Wastewater," *Am. Water Work. Assoc.*, p. 733, 1999.
- [297] M. C. Garg and H. Joshi, "A new approach for optimization of small-scale RO membrane using artificial groundwater," *Environ. Technol. (United Kingdom)*, vol. 35, no. 23, pp. 2988–2999, 2014.
- [298] G. Adams and P. M. Bubucis, "Calculating an artificial sea water formulation using spreadsheet matrices," *Aquarium Sci. Conserv.*, vol. 2, no. 1, pp. 35–41, 1998.
- [299] APHA, AWWA, and WEF, "Standard Methods for the Examination of Water and Wastewater Part 1000," 1999.
- [300] W. Environment, "Standard Methods for the Examination of Water and Wastewater Part 4000 Inorganic nonmetallic constituents Standard Methods for the Examination of Water and

Wastewater,” *Public Health*, 1999.

- [301] I. Asiltürk and S. Neşeli, “Multi response optimisation of CNC turning parameters via Taguchi method-based response surface analysis,” *Meas. J. Int. Meas. Confed.*, vol. 45, no. 4, pp. 785–794, 2012.
- [302] V. C. Srivastava, I. D. Mall, and I. M. Mishra, “Multicomponent Adsorption Study of Metal Ions onto Bagasse Fly Ash Using Taguchi’s Design of Experimental Methodology,” *Ind. Eng. Chem. Res.*, vol. 46, no. 17, pp. 5697–5706, 2007.
- [303] J. Zolgharnein, N. Asanjarani, and T. Shariatmanesh, “International Biodeterioration & Biodegradation Taguchi L 16 orthogonal array optimization for Cd (II) removal using *Carpinus betulus* tree leaves : Adsorption characterization,” *Int. Biodeterior. Biodegradation*, vol. 85, pp. 66–77, 2013.
- [304] I. Smičiklas, A. Onjia, S. Raičević, and D. Janačković, “Authors’ response to comments on ‘Factors influencing the removal of divalent cations by hydroxyapatite,’” *J. Hazard. Mater.*, vol. 168, no. 1, pp. 560–562, 2009.
- [305] M. Kilianová *et al.*, “Remarkable efficiency of ultrafine superparamagnetic iron(III) oxide nanoparticles toward arsenate removal from aqueous environment,” *Chemosphere*, vol. 93, no. 11, pp. 2690–2697, 2013.
- [306] A. Yürüm, Z. Ö. Kocabaş-Atakli, M. Sezen, R. Semiat, and Y. Yürüm, “Fast deposition of porous iron oxide on activated carbon by microwave heating and arsenic (V) removal from water,” *Chem. Eng. J.*, vol. 242, pp. 321–332, 2014.
- [307] P. Khare and A. Kumar, “Removal of phenol from aqueous solution using carbonized *Terminalia chebula*-activated carbon: process parametric optimization using conventional method and Taguchi’s experimental design, adsorption kinetic, equilibrium and thermodynamic study,” *Appl. Water Sci.*, vol. 2, no. 4, pp. 317–326, 2012.
- [308] A. B. Engin, Ö. Özdemir, M. Turan, and A. Z. Turan, “Color removal from textile dyebath effluents in a zeolite fixed bed reactor: Determination of optimum process conditions using Taguchi method,” *J. Hazard. Mater.*, vol. 159, no. 2–3, pp. 348–353, 2008.
- [309] S. Mandal, S. S. Mahapatra, M. K. Sahu, and R. K. Patel, “Artificial neural network modelling of As(III) removal from water by novel hybrid material,” *Process Saf. Environ. Prot.*, vol. 93, no. November 2013, pp. 1–16, 2014.
- [310] P. Roy, N. K. Mondal, and K. Das, “Modeling of the adsorptive removal of arsenic: A statistical approach,” *J. Environ. Chem. Eng.*, vol. 2, no. 1, pp. 585–597, 2014.

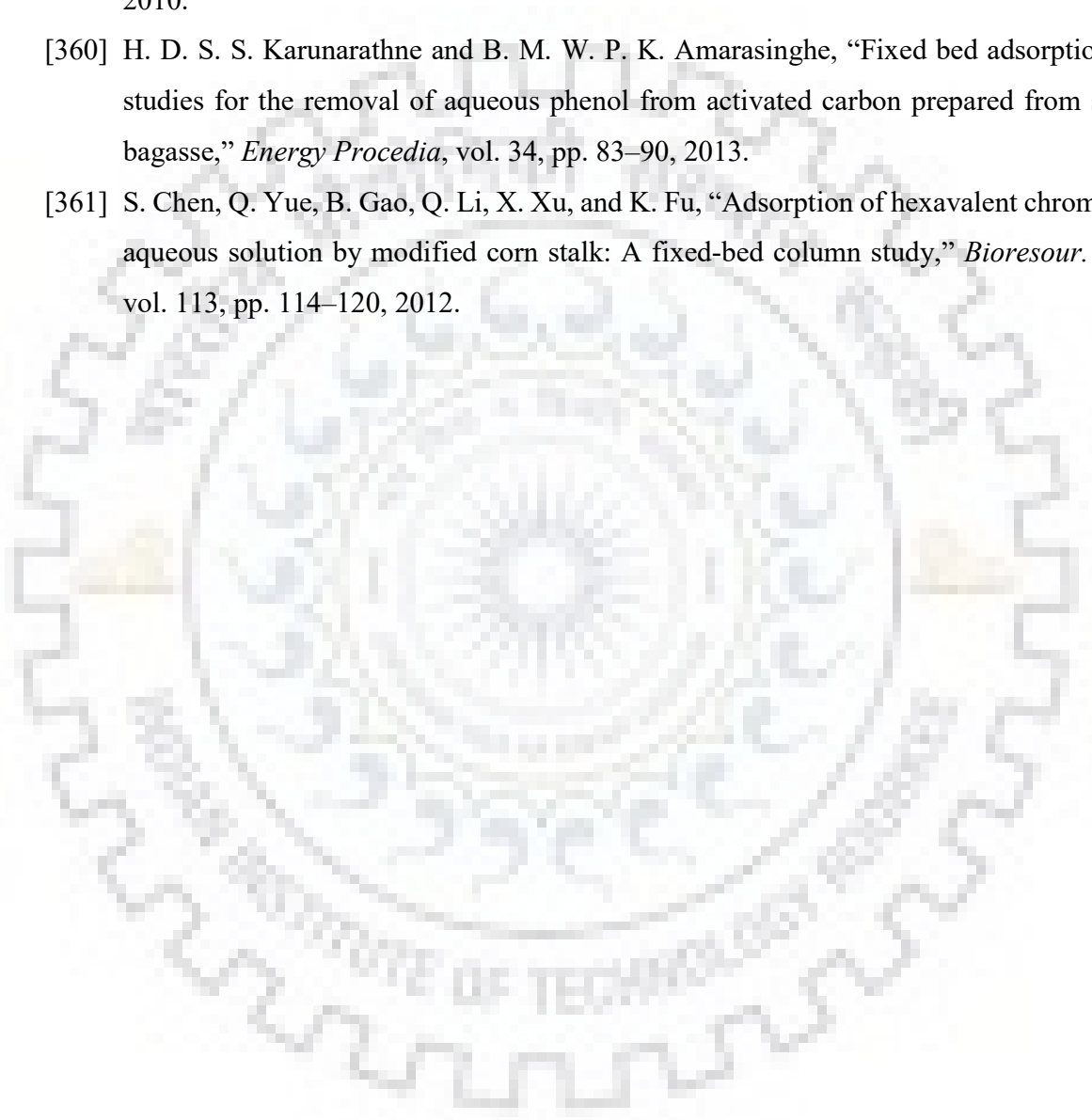
- [311] M. Nadeem, A. Mahmood, S. A. Shahid, S. S. Shah, A. M. Khalid, and G. McKay, "Sorption of lead from aqueous solution by chemically modified carbon adsorbents," *J. Hazard. Mater.*, vol. 138, no. 3, pp. 604–613, 2006.
- [312] J. Zhou, S. Yang, J. Yu, and Z. Shu, "Novel hollow microspheres of hierarchical zinc-aluminum layered double hydroxides and their enhanced adsorption capacity for phosphate in water," *J. Hazard. Mater.*, vol. 192, no. 3, pp. 1114–1121, 2011.
- [313] S. Lin, D. Lu, and Z. Liu, "Removal of arsenic contaminants with magnetic γ -Fe₂O₃ nanoparticles," *Chem. Eng. J.*, vol. 211–212, pp. 46–52, 2012.
- [314] J. P. Gustafsson, "Visual MINTEQ 3.1," *KTH, Sweden*. Stockholm, Sweden, 2016.
- [315] T. Hiemstra, P. Venema, and W. H. Van Riemsdijk, "Intrinsic proton affinity of reactive surface groups of metal (Hydr)oxides: The bond valence principle," *J. Colloid Interface Sci.*, vol. 184, no. 2, pp. 680–692, 1996.
- [316] D. Schröder, S. Shaik, and H. Schwarz, "Two-State Reactivity as a New Concept in Organometallic Chemistry," *Acc. Chem. Res.*, vol. 33, no. 3, pp. 139–145, Mar. 2000.
- [317] Sheryl D. Smith and Marc Edwards, "The influence of silica and calcium on arsenate sorption to oxide surfaces," *J. Water Supply Res. Technol.*, vol. 54, no. 4, pp. 201–211, 2005.
- [318] A. Restrepo, C. Ibarguen, E. Flórez, N. Y. Acelas, and C. Hadad, "Adsorption of Nitrate and Bicarbonate on Fe-(Hydr)oxide," *Inorg. Chem.*, vol. 56, no. 9, pp. 5455–5464, 2017.
- [319] S. L. Saalfield and B. C. Bostick, "Synergistic effect of calcium and bicarbonate in enhancing arsenate release from ferrihydrite," *Geochim. Cosmochim. Acta*, vol. 74, no. 18, pp. 5171–5186, 2010.
- [320] I. A. Katsoyiannis, "ScienceDirect - Water Research : Removal of arsenic from contaminated water sources by sorption onto iron-oxide-coated polymeric materials," *Water Res.*, vol. 36, pp. 5141–5155, 2002.
- [321] Y. Deng *et al.*, "Influence of calcium and phosphate on pH dependency of arsenite and arsenate adsorption to goethite," *Chemosphere*, vol. 199, pp. 617–624, 2018.
- [322] R. P. J. J. Rietra, T. Hiemstra, and W. H. Van Riemsdijk, "Interaction between calcium and phosphate adsorption on goethite," *Environ. Sci. Technol.*, vol. 35, no. 16, pp. 3369–3374, 2001.
- [323] R. Jolsterå, L. Gunneriusson, and W. Forsling, "Adsorption and surface complex modeling of silicates on maghemite in aqueous suspensions," *J. Colloid Interface Sci.*, vol. 342, no. 2, pp. 493–498, 2010.

- [324] A. Roy and J. Bhattacharya, "Removal of Cu (II), Zn (II) and Pb (II) from water using microwave-assisted synthesized maghemite nanotubes," *Chem. Eng. J.*, vol. 211–212, pp. 493–500, 2012.
- [325] H. K. Boparai, M. Joseph, and D. M. O'Carroll, "Cadmium (Cd²⁺) removal by nano zerovalent iron: Surface analysis, effects of solution chemistry and surface complexation modeling," *Environ. Sci. Pollut. Res.*, vol. 20, no. 9, pp. 6210–6221, 2013.
- [326] M. C. Garg and H. Joshi, "A new approach for optimization of small-scale RO membrane using artificial groundwater," *Environ. Technol. (United Kingdom)*, vol. 35, no. 23, pp. 2988–2999, 2014.
- [327] R. L. Coble, "Sintering Crystalline Solids. II. Experimental Test of Diffusion Models in Powder Compacts," *J. Appl. Phys.*, vol. 32, no. 5, pp. 793–799, May 1961.
- [328] A. Felinger and G. Guiochon, "Optimization of the experimental conditions and the column design parameters in displacement chromatography," *J. Chromatogr. A*, vol. 609, no. 1, pp. 35–47, 1992.
- [329] C. P. V. *et al.*, "Enhanced dispersion in cylindrical packed beds," *Philos. Trans. R. Soc. London. Ser. A Math. Phys. Eng. Sci.*, vol. 360, no. 1792, pp. 497–506, Mar. 2002.
- [330] C. J. Gommers, S. Blacher, J. H. Dunsmuir, and A. H. Tsou, "Practical Methods for Measuring the Tortuosity of Porous Materials from Binary or Gray-Tone Tomographic Reconstructions," *AIChE J.*, vol. 55, no. 8, pp. 2000–2012, 2012.
- [331] H. C. Thomas, "Heterogeneous ion exchange in a flowing system," *J. Am. Chem. Soc.*, vol. 66, no. 2, pp. 1664–1666, 1944.
- [332] Z. Saadi, R. Saadi, and R. Fazaeli, "Fixed-bed adsorption dynamics of Pb (II) adsorption from aqueous solution using nanostructured γ -alumina," *J. Nanostructure Chem.*, vol. 3, no. 1, p. 48, 2013.
- [333] A. Ghosh, S. Chakrabarti, and U. C. Ghosh, "Fixed-bed column performance of Mn-incorporated iron(III) oxide nanoparticle agglomerates on As(III) removal from the spiked groundwater in lab bench scale," *Chem. Eng. J.*, vol. 248, pp. 18–26, 2014.
- [334] J. Salas-García, L. Bibiano-Cruz, H. Llanos, J. Garfias, and R. Martel, "Batch and column test analyses for hardness removal using natural and homoionic clinoptilolite: breakthrough experiments and modeling," *Sustain. Water Resour. Manag.*, vol. 2, no. 2, pp. 183–197, 2016.
- [335] S.-T. Song *et al.*, "Process analysis of mercury adsorption onto chemically modified rice straw in a fixed-bed adsorber," *J. Environ. Chem. Eng.*, vol. 4, no. 2, pp. 1685–1697, 2016.

- [336] S. A. Chaudhry, T. A. Khan, and I. Ali, "Zirconium oxide-coated sand based batch and column adsorptive removal of arsenic from water: Isotherm, kinetic and thermodynamic studies," *Egypt. J. Pet.*, vol. 26, no. 2, pp. 553–563, 2017.
- [337] Z. Asif and Z. Chen, "Removal of arsenic from drinking water using rice husk," *Appl. Water Sci.*, vol. 7, no. 3, pp. 1449–1458, 2015.
- [338] R. Han *et al.*, "Adsorption of methylene blue by phoenix tree leaf powder in a fixed-bed column: experiments and prediction of breakthrough curves," *Desalination*, vol. 245, no. 1, pp. 284–297, 2009.
- [339] G. S. Bohart and E. Q. Adams, "Some Aspects of the Behavior of Charcoal With Respect To Chlorine.1," *J. Am. Chem. Soc.*, vol. 42, no. 3, pp. 523–544, 1920.
- [340] M. A. Martín-Lara, G. Tenorio, G. Blázquez, F. Hernáinz, and M. Calero, "Sorption of Cr (VI) onto Olive Stone in a Packed Bed Column: Prediction of Kinetic Parameters and Breakthrough Curves," *J. Environ. Eng.*, vol. 136, no. 12, pp. 1389–1397, 2010.
- [341] R. Dobson, M. H. Schroth, and J. Zeyer, "Effect of water-table fluctuation on dissolution and biodegradation of a multi-component, light nonaqueous-phase liquid," *J. Contam. Hydrol.*, vol. 94, no. 3, pp. 235–248, 2007.
- [342] S. Mohan and G. Sreelakshmi, "Fixed bed column study for heavy metal removal using phosphate treated rice husk," *J. Hazard. Mater.*, vol. 153, no. 1–2, pp. 75–82, 2008.
- [343] A. Pachathu, K. Ponnusamy, and S. K. V. R. Srinivasan, "Packed bed column studies on the removal of emulsified oil from water using raw and modified bagasse and corn husk," *J. Mol. Liq.*, vol. 223, pp. 1256–1263, 2016.
- [344] Z. Ren, C. Chen, H. Xu, Y. Long, D. Lei, and J. Ni, "Packed bed column studies on lead(II) removal from industrial wastewater by modified *Agaricus bisporus*," *Bioresour. Technol.*, vol. 152, pp. 457–463, 2013.
- [345] Y. Li, B. Zhao, L. Zhang, and R. Han, "Biosorption of copper ion by natural and modified wheat straw in fixed-bed column," *Desalin. Water Treat.*, vol. 51, no. 28–30, pp. 5735–5745, 2013.
- [346] X. Li, Z. Liu, and J. Y. Lee, "Adsorption kinetic and equilibrium study for removal of mercuric chloride by CuCl₂-impregnated activated carbon sorbent," *J. Hazard. Mater.*, vol. 252–253, pp. 419–427, 2013.
- [347] V. Sriram, Z. Liu, and J.-Y. Lee, "Modeling of mercuric chloride removal in ductwork and fabric filter by raw activated carbon injection," *Fuel*, vol. 188, pp. 223–231, 2017.

- [348] A. Öztürk and E. Malkoc, "Cationic Basic Yellow 2 (BY2) adsorption onto manure ash: surface properties and adsorption mechanism," *Desalin. Water Treat.*, vol. 54, no. 1, pp. 209–226, 2015.
- [349] S. Netpradit, P. Thiravetyan, and S. Towprayoon, "Evaluation of metal hydroxide sludge for reactive dye adsorption in a fixed-bed column system," *Water Res.*, vol. 38, no. 1, pp. 71–78, 2004.
- [350] G. Mckay, D. C. K. Ko, J. F. Porter, and G. Mckay, "Optimised correlations for the fixed-bed adsorption of metal ions on bone char metal ions on bone char," vol. 55, no. December 2000, 2014.
- [351] S. Patel, J. Han, W. Qiu, and W. Gao, "Synthesis and characterisation of mesoporous bone char obtained by pyrolysis of animal bones, for environmental application," *J. Environ. Chem. Eng.*, vol. 3, no. 4, Part A, pp. 2368–2377, 2015.
- [352] A. P. Lim and A. Z. Aris, "Continuous fixed-bed column study and adsorption modeling: Removal of cadmium (II) and lead (II) ions in aqueous solution by dead calcareous skeletons," *Biochem. Eng. J.*, vol. 87, pp. 50–61, 2014.
- [353] V. Sarin, T. S. Singh, and K. K. Pant, "Thermodynamic and breakthrough column studies for the selective sorption of chromium from industrial effluent on activated eucalyptus bark," *Bioresour. Technol.*, vol. 97, no. 16, pp. 1986–1993, 2006.
- [354] M. A. E. de Franco, C. B. de Carvalho, M. M. Bonetto, R. de P. Soares, and L. A. Féris, "Removal of amoxicillin from water by adsorption onto activated carbon in batch process and fixed bed column: Kinetics, isotherms, experimental design and breakthrough curves modelling," *J. Clean. Prod.*, vol. 161, pp. 947–956, 2017.
- [355] M. Tamez Uddin, M. Rukanuzzaman, M. Maksudur Rahman Khan, and M. Akhtarul Islam, "Adsorption of methylene blue from aqueous solution by jackfruit (*Artocarpus heterophyllus*) leaf powder: A fixed-bed column study," *J. Environ. Manage.*, vol. 90, no. 11, pp. 3443–3450, 2009.
- [356] D. M. Saad, E. Cukrowska, and H. Tutu, "Column adsorption studies for the removal of U by phosphonated cross-linked polyethylenimine: modelling and optimization," *Appl. Water Sci.*, vol. 5, no. 1, pp. 57–63, 2014.
- [357] Z. Aksu and F. Gönen, "Binary biosorption of phenol and chromium(VI) onto immobilized activated sludge in a packed bed: Prediction of kinetic parameters and breakthrough curves," *Sep. Purif. Technol.*, vol. 49, no. 3, pp. 205–216, 2006.

- [358] H. Patel and R. T. Vashi, "Fixed bed column adsorption of Acid Yellow 17 dye onto Tamarind Seed Powder," *Can. J. Chem. Eng.*, vol. 90, no. 1, pp. 180–185, 2012.
- [359] A. A. Ahmad and B. H. Hameed, "Fixed-bed adsorption of reactive azo dye onto granular activated carbon prepared from waste," *J. Hazard. Mater.*, vol. 175, no. 1–3, pp. 298–303, 2010.
- [360] H. D. S. S. Karunaratne and B. M. W. P. K. Amarasinghe, "Fixed bed adsorption column studies for the removal of aqueous phenol from activated carbon prepared from sugarcane bagasse," *Energy Procedia*, vol. 34, pp. 83–90, 2013.
- [361] S. Chen, Q. Yue, B. Gao, Q. Li, X. Xu, and K. Fu, "Adsorption of hexavalent chromium from aqueous solution by modified corn stalk: A fixed-bed column study," *Bioresour. Technol.*, vol. 113, pp. 114–120, 2012.





Work Recognition

Patent

[1]. Joshi H., Kumar A., **Kumar A.**, Reflux method for the synthesis of nanohybrid using Industrial waste as a precursor material in the removal of arsenic, **File No., SSCPL/IITR/2017-18/CRN030.**

International Journals

[1]. **Kumar A.**, Joshi H., Kumar A., Remediation of Arsenic by Metal/ Metal Oxide Based Nanocomposites/ Nanohybrids: Contamination Scenario in Groundwater, Practical Challenges and Future Perspectives, Separation and Purification Reviews, Taylor and Francis [under review].

[2]. **Kumar A.**, Joshi H., Kumar A., Exploring the removal characteristics of As^V using maghemite nanoparticles in groundwater of Ballia, Uttar-Pradesh, India, Journal of Environmental Engineering, ASCE [under review].

Book chapter

[1]. Kumar A., **Joshi H.**, **Kumar A.**, 'Exploring the scope of nanoparticles for arsenic removal in groundwater, Arsenic in the Environment, CRC Press, ISBN: 9781138486096, September 2019, doi.org/10.1201/9781351046633.

International Conferences

[1]. **Kumar A.**, Joshi H., Kumar A., 'Exploring the scope of nanoparticles for arsenic removal in groundwater, paper presented (oral) to 7th International Congress on Arsenic in the Environment (As2018) organized by International Society of Groundwater for Sustainable Development at Beijing, China from 1st to 6th July, 2018.

[2]. **Kumar A.**, Joshi H., Kumar A., An approach of utilizing the industry waste in the development of maghemite functionalized nanostructures for arsenic removal, paper presented (oral) to Water Security and Climate Change Conference organized by International Network on Sustainable Water Management in Developing Countries (SWINDON) at Nairobi, Kenya from 3rd to 5th December, 2018.

National Conferences

[1]. **Kumar A.**, Joshi H., Kumar A., Assessing the maghemite ($\gamma\text{-Fe}_2\text{O}_3$) nanoparticles in As^{V} removal using laboratory scale batch and column experiments, paper presented (oral) to 7th International Groundwater Conference- Groundwater Vision 2030 organized by NIH and CGWB at New Delhi, India from 11th to 13th December, 2017.

[2]. Saxena S., **Kumar A.**, Joshi H., Arsenic occurrence and interactions between Ganga river; sediments and adjoining aquifers in the upper and middle Ganga basin, India' paper presented to 7th International Groundwater Conference- Groundwater Vision 2030 organized by NIH and CGWB at New Delhi from 11th to 13th December, 2017.